Development of Fusion Motion Capture for Optimisation of Performance in Alpine Ski Racing

A thesis presented in fulfilment of the requirements for the degree of

Doctor of Philosophy
in
Science

at Massey University, Wellington, New Zealand

Matthew Andrew Dalhousie Brodie

2009

Abstract

Fusion Motion Capture (FMC), a wearable motion capture system was developed, and applied to the optimisation of athlete performance in alpine ski racing. In what may be a world first, the three-dimensional movements of a skilled athlete (with less than 20 FIS[1] points) skiing through a complete training giant slalom racecourse were analysed.

FMC consists of multiple light weight sensors attached to the athlete including inertial measurement units (IMUs), pressure sensitive insoles and a global position system (GPS) receiver. The IMUs contain accelerometers, gyroscopes, and magnetometers. Limb orientation and location are obtained by mathematically combining the most reliable data from each sensor using fusion algorithms developed by the author. FMC fuses the signals from the IMUs and GPS without the need for the post filtering, usually applied to motion capture data, and therefore, maintains maximum bandwidth. The FMC results were stable and relatively independent of motion type and duration unlike other inertial systems available in 2005, when the research was initiated.

Analysis of data collected from an athlete skiing giant slalom contradict the traditional „going straight turning short" race strategy. The shortest path may not always be the fastest. Instead each gate has a different optimum approach arc. Optimum turn radius increases with both increasing speed and increasing terrain slope. The results also contradict laboratory measurements of ski/snow sliding friction and suggest that snow resistance in giant slalom is of similar importance to wind drag. In addition to gravity, the athlete increased speed using the techniques of „lateral projection" and „pumping".

Race performance was determined from the analysis of the athlete skiing through the entire course. FMC proved, therefore, to be more suitable than traditional optical systems that are practically limited to capturing small sections of a race course.

The athlete experienced high and rapidly fluctuating torques about all three axes of the lower joints. This information could be useful in designing training programmes racecourses and equipment to reduce knee injuries. Data driven animations and colour coded force vector diagrams were developed to enhance athlete feedback. Inline skating data was also analysed.

[1] Federation International Ski (FIS), the ruling body in ski racing. Less than 20 FIS points means it is likely the athlete will be ranked within the top few hundred athletes world wide.

To Emily, Reuben, and Douglas who are more precious than sunshine

Preface

The preface tells a story about a research journey. Along the road a brief summary of part of this research became an entry to the 2008 New Zealand MacDiarmid Young Scientists of the Year Awards. The 90 second competition entry video and poster provide a useful overview of the research suitable for all audiences. After the success in these awards the Foundation for Research Science and Technology made a short professional video which also provides and interesting introduction to the thesis. The videos and poster from the competition are available on the accompanying CD (**Appendices\MacDiarmid 2008\Stage 2 Gold_Science.mpg**) and the video entry is also available on YouTube at the following address:

www.youtube.com/BrodieMAD

The project was originally titled „The Optimisation of Athlete Movements in Alpine Ski Racing" but was changed to reflect the shift in focus of the research to the development of Fusion Motion Capture. At the start there were many obstacles to overcome. There was no funding, a suitable motion capture system was not available, ski racing was not a high priority in New Zealand, and the nearest ski area was several hours drive away. It soon became apparent that motion capture of giant slalom racing in the harsh alpine environment was not an easy proposition. Several times, contrary to the weather forecast, conditions were favourable. If all the hidden obstacles had been known in advance then a different path might have been chosen, but then ignorance was bliss.

One by one the obstacles fell, but like the heads of the serpent Hydra from Greek mythology more keep appearing. Fortunately, most of Hydra"s heads eventually represented the possibility of novel contributions to the body of knowledge and so the mantra was adopted, „every cloud has a silver lining (and a publication)".

The research for this PhD resulted in several peer-reviewed publications in journals, books and conferences. It also generated a lot of mainstream media interest, including TV appearances, radio interviews and articles in magazines, newspapers and on the internet.

There is a saying: "May you live in interesting times." It has been and still is an interesting journey.

Acknowledgements

The author gratefully acknowledges the support that made this project possible.

The following people, in alphabetical order, contributed to this project through the research, the funding applications and the thesis preparation: Prof Geoffrey Anneson, Dr Bobby Cheema, Prof Philip Dickinson, Mr David Graham, Mr Ben Griffin, Mr Angus Howden, Dr Edmond Lai, Dr Rachel Page, Dr Wyatt Page, Dr John Ruck, Mr Rhys Thorpe, Mrs Judy Thorpe, Mr Mike Turner, and Dr Alan Walmsley.

This research was supported by the following institutions: The Institute of Food Nutrition and Human Health, Massey University, Mt Ruapehu Alpine Lifts, the New Zealand Academy of Sport, Sport and Recreation New Zealand, and Volkswagen New Zealand.

This research was supported by the following awards and grants: The Foundation for Research Science and Technology, for the 2008 MacDiarmid Overall Runner Up New Zealand Young Scientist of the Year Award and Future Science and Technology Award. The Federation International Ski, for an Innovation award at the 4th International Congress on Science in Skiing. The Royal Society of New Zealand, for the R.H.T Bates award and the James G. Hay travel award. Education New Zealand, for a postgraduate study travel abroad award. Sport and Exercise Science New Zealand (SESNZ), for the 2005 Emerging Scientist Award. The Vice Chancellors Committee, for a Claude McCarthy travel award.

Approval for the skiing experiments in this thesis was obtained from the Massey University Human Ethics Committee, Palmerston North Application 05/105.

Table of Contents

List of Illustrations

List of Videos

The supplementary videos are available on the accompanying CD (**Appendices/FMC Video**). In order to view these videos using the hyperlinks in the electronic version of this thesis first ensure that the supplementary material and the thesis are in the same folder. It may also be necessary to set the default media player to Windows Media Player.

Glossary

AP	Anterior Posterior axis of the human body or segment, pointing forwards and generally parallel to the ground.
ASIS	Anterior Superior Iliac Spine, bony landmarks on the front of the sacrum
Bias	1. GPS clock bias or error, both satellite and receiver, because of the unstable receiver clock bias four satellites instead of three are required to fix receiver location in three dimensions. 2. IMU accelerometer, magnetometer or gyroscope low frequency error.
C7	Posterior bony landmark, 7^{th} cervical vertebra, close to the neck joint centre
Carrier-frequency	GPS data and the signal used to measure relative velocity between satellites and receivers.
CI	Confidence interval, usually 95%
CoM	Centre of Mass, the single point in space that represents the mean location an athlete‟s distributed mass. A force acting though the centre of mass of a body causes no torque or rotation of that body.
CoP	Centre of Pressure, two meanings. 1. The weighted mean location of pressure measurements taken with separate measurement cells that are part of a pressure sensitive insole. 2. An imaginary point between the modelled ski and snow surfaces. If the multiple ground reaction forces acting on different parts of the ski were approximated by a single force, then that combined force would act through the CoP.
DOP	Dilution of precision, 50% of GPS measurements fall within the stated DOP usually in metres. It is different from absolute accuracy.
Differential GPS	Use of a fixed base station to reduce GPS roving receiver errors
Drift	The rate of change of GPS clock bias, because of clock drift four satellites instead of three are required to fix GPS receiver velocity.
ECEF	Earth Centred Earth Fixed coordinate system in which GPS operates. The origin is the Earth‟s centre. The Z-axis refers to a north-pointing vector through the geographic poles of the earth and the X-axis intersects the Greenwich meridian (where longitude = 0°).
EMG	Electromyography, a measurement of muscle activity.
FMC	Fusion Motion Capture, a prototype wearable motion capture system that combines multiple data streams developed in this thesis.
GPS	Global Positioning System, consists of multiple satellites orbiting the earth and receivers on Earth‟s surface
GRF	Ground Reaction Forces, forces between the athlete‟s skis and the snow surfaces
IMU	Inertial Measurement Unit, a motion tracking sensor, in this thesis the IMUs contain accelerometers, gyroscopes and magnetometers.

Inverse dynamic	Analysis when differentiation of positional data is used to obtain rates and accelerations.
IPAQ	A portable handheld computer used as a data logger in this thesis
Kinematic analysis	Analysis of visual parameters such as location or limb angles
Kinetic analysis	Analysis of accelerations, forces, rates and torques, which cannot be determined from a single video frame
MATLAB	A technical computing language used in this thesis to develop fusion motion capture algorithms, to develop data visualisations and analyse the skiing data.
MEMS	Micro-Electro-Mechanical-Sensors, very small electromechanical devices such as sensors and actuators with integrated electronics
MID	Message Identification number in binary communication protocol
MT9B	A type of IMU sensor from XSens Technology
ML	Medio Lateral axis of the human body or segment, generally parallel to the ground and pointing laterally.
PSIS	Posterior Superior Iliac Spine, a bony landmark on the rear of the sacrum
PS	Pubic symphisis, a bony landmark on the front of the sacrum
PCMCIA	Communication slot used to connect the GPS to the IPAQ
Pseudo-range	GPS time of flight data used to measure relative distance between satellites and receivers.
RMS	Root Mean Square, used in this thesis to determine noise in a signal
VMA	Video Motion Analysis
XBus	A communication hub to which multiple IMUs can be attached

Symbols

Bold font represents a vector or matrix quantity and normal or *italic* font represents a scalar value. Subscripts often denote the source or owner of the parameter.

A	Acceleration
A_c	Cross sectional area normal to the relative wind velocity
bo	IMU sensor bias
bT	IMU sensor temperature bias
C_d	Wind drag coefficient
CF	Carrier Frequency
c	Speed of light constant used internally by the SiRF2 GPS chip ($299{,}792{,}458 ms^{-1}$), (SiRF Technology Inc, 2005)
E	Estimated error in a measurement
F	GPS signal frequency (1575420000 Hz) used by the SiRF2 GPS chip (SiRF Technology Inc, 2005)
F	Force, a subscript if present denotes the type of force
F_N	Normal force, applied perpendicularly to the ski base
g	Gravity
Go	IMU sensor gain correction
GRF	Ground Reaction Forces
GT	IMU sensor temperature gain compensation
H, h	Earths magnetic vector (in the GLOBAL and local reference systems)
HGRF	Horizontal ground reaction forces
I	1. Identity Matrix. 2. An Inertial Tensor describing the rotational inertia of a body segment.
$K_{Friction}$	Lumped inline skating bearing friction coefficient
K_{Drag}	Lumped wind drag coefficient
m	Mass
PR	Pseudo Range
Q	Quaternion representation of orientation consists of four elements Q0 to Q3, it describes orientation in terms of a rotation of $\cos(\theta/2)$ about a vector $\mathbf{U}\sin(\theta/2)$. More information is provided in Chapter 4.1.1
R	A Rotation matrix (3 by 3) that describes three degree of freedom orientations relative to a global reference system. Each element is a cosine of one of nine angles between the axes of the reference and local body system.
$\mathbf{R_{LG}}$	A rotation from the local sensor to the global reference system as denoted by the order of the subscripts
Re	Reynolds number, a dimensionless quantity that describes the characteristics of the airflow about the skier as he descends the snow slope
S	Calibrated IMU data
T	Torque or moment
T	Temperature
To	Temperature offset

U	1. Raw binary IMU data. 2. A unit vector describing the axis of rotation used in defining quaternions
V, V, Vel	Velocity
X, Y, Z	Global axes, Z is always vertical and X generally points in the direction of travel and Y floats. Sometimes however X points towards magnetic north.
x, y ,z	Local axes of a body segment, y points along the limb caudally, z is mediolateral and x floats
×	Cross product of two three element vectors
α	Angular acceleration
ε	Residual errors
θ	Angle of rotation
ρ	Density of air
σ	Standard deviation
μ, μ_F, μ_V	Snow/ski friction or resistance coefficients, static and velocity dependent
ν	Kinematic viscosity of air
ω	Angular velocity
⊥	Normal to a surface or perpendicular
|F|	Magnitude of a force vector

1.Introduction

Figure 1.1: Marey's white heron, in motion capture from 1884[Ψ]

1.1. Why…

…"Many skiers do not take advantage of the way modern equipment has been designed to facilitate carving turns"…(Stenmark, 1990)

From 1974-1989, Ingemar Stenmark won an incredible 86 FIS (Federation International Ski) and World Cup races. Regardless of the course conditions Stenmark would adapt his movements to the course. What can be learnt from him? In the 18 years since publication of Stenmark"s article there has been a revolution in materials science and alpine ski design. Most important among many factors is the side cut radius of the „carving" ski. (Lind & Sanders, 1997).

Do Stenmark"s comments still hold true today? Do today"s skiers take advantage of modern equipment design? Stenmark"s comments were the motivation to begin this research because they highlighted a gap in the understanding of the scientific base for the different ski methodologies adhered to by athletes from different countries. Why did people from different countries ski differently? Was there a faster, easier or safer way to ski? How could this be proven scientifically? What makes one athlete the fastest, is it science or art?

In between working as a technical development engineer and starting this research, the author spent eight consecutive winters working in ski race schools, in ski patrols, as a ski instructor, and as a snowboard instructor in both New Zealand and Japan. During his endless winter he observed subjective differences in the ski technique of athletes from different countries and became interested in how the task of skiing was learned.

Skiing may be taught by the modelling system of imitation. The rhythmical negotiation of gates in a FIS regulation course could be considered as an escapement system, like a pendulum clock, and so is similar to walking gait. Consequently, once skiing technique is well learned, it may be almost impossible to change.

The need to question the status quo of ski technique against the backdrop of rapidly changing ski design was further encouraged by comments in a recent book by a Slovenian ski race coach: „Therefore the basic ski technique is unchanged relative to ski design" (Matijevec, 2003). Questions that motivated this thesis included: "Which comes first, ski design or ski technique?" Ski designers use feedback from the top athletes to design new prototypes; an athlete adapts their technique to current ski design. The recreational skier is exposed to recreational versions of this technique and equipment design. Is it possible that developments are slowly approaching a local optimal solution, but different and better optimal solutions could exist that are dependent on individual physiology?

The initial questions for consideration were very broad and a multidisciplinary approach including biomechanics, physics and engineering was going to be required in order to attempt

to address these questions. This study is limited to measuring the athletes‟ movements and how they are affected by the external forces of gravity, wind drag, snow resistance and ground reaction. From all the disciplines of skiing alpine ski racing was chosen for two reasons: Firstly, it has an objective goal, to pass between the course gates and complete the course in the minimum time. Secondly, athletes are competitive and will naturally perform near their perceived limits and so the data collected may ultimately give general new insights into limitations of human performance. The implicit assumption underlying this thesis is that, in ski racing, style is not judged, so ultimately the external forces acting on the athlete completely determine the outcome of the race.

Biomechanics includes the science of athletic movement. Biomechanists use motion capture data as one of many tools to further the understanding of athletic movement. This thesis has two key components; the motion capture of alpine ski racing, and the analyses of forces and effects in alpine ski racing.

1.2. Chronology of motion capture and skiing

Both motion analysis and skiing have a long history. Skiing pre-dates motion capture by perhaps thousands of years. The earliest known ski was excavated from a Swedish bog and dates back to between 2500BC and 4500BC. One of the oldest surviving written accounts of skiing is by Olaus Magnus in his 1555 book, „A Description of the Northern Peoples‟.

Figure 1.2: Rampant Lioness: Photograph by Luca Galuzzi – www.galuzzi.it

Although humans have been skiing for a long time, they have been obsessed even longer with the visual representation and artistic appearances of athletic performances. Ancient rock carvings (petroglyphs) demonstrate early attempts at capturing, representing and recording

motion, such as the „Mœrcatz‟ or Rampant Lioness rock carving found in libya (Figure 1.2). The oldest known etched rock art dates back to the Neolithic and Upper Palaeolithic boundary, approximately 10,000 years ago.

Possibly this kinematic obsession (obsession with the way something looks) led a photographer to become a scientist and complete the first motion capture of a galloping horse in 1877. Eadweard Muybridge, an Englishman learnt photography while recovering from a stage coach accident. After the civil war Muybridge returned to America and Leland Stanford, former Governor of California, employed Muybridge to capture the motion of his race horses. Muybridge helped to develop an ingenious system that could photograph a horse in fast motion using a number of cameras arranged parallel to the track and triggered by a succession of trip wires (Figure 1.3). His still shots settled a long standing dispute about whether a galloping horse‟s hooves are ever simultaneously clear of the ground (they are) and showed that the illustrators of the time had things hopelessly wrong (Figure 1.4). This success later led the University of Pennsylvania to employ Muybridge where he worked on his ground breaking book, Animal Locomotion (Muybridge, 1887).

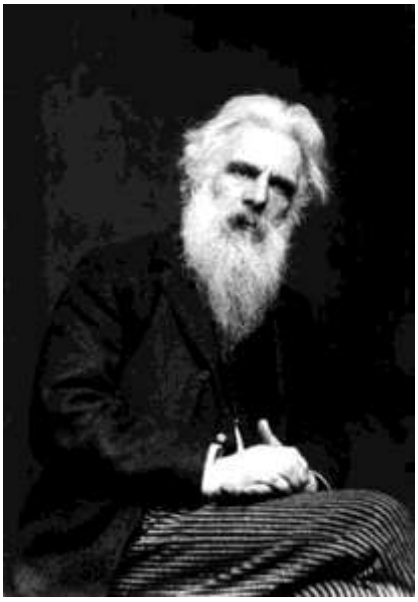

Figure 1.3: Eadweard Muybridge first used cameras for motion capture in 1877[Ψ]

Around the same time in 1882 Étiennes-Jules Marey, a brilliant scientist interested in human and animal locomotion developed a portable motion capture gun. Marey was the first to photograph the flight of birds (Figure 1.1). Marey was at the forefront of the biomechanical analysis of human and animal movements as well as having many other scientific interests.

Until very recent times most motion analysis was carried out in a way Marey or Muybridge would recognise, using cameras in the controlled environment of the laboratory, athletics track, or motion capture studio (for animation in film and video).

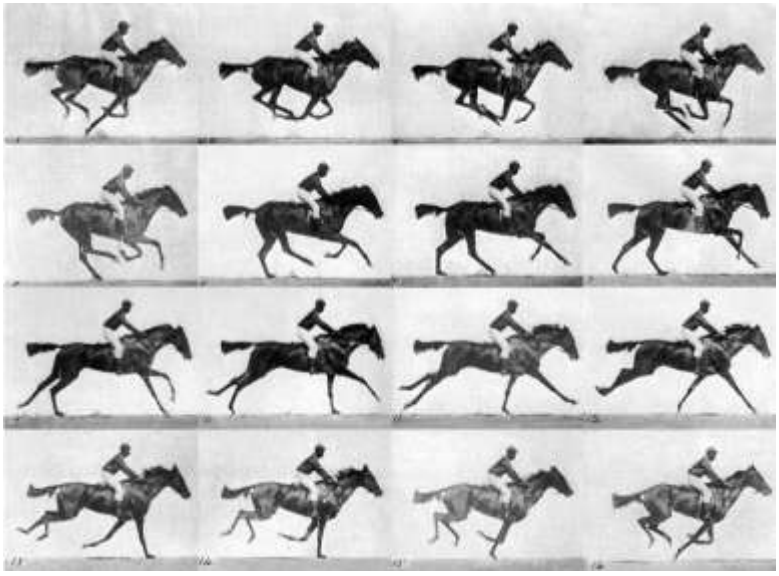

Figure 1.4: Woodcut of Muybridge's motion capture

Parallel with the 19th century advances in science and motion capture, skiing was also making significant leaps forward. Around 1870 Sondre Norhiem introduced Telemark skiing to the world. Norhiem from the Telemark district of Norway introduced the Telemark ski, a narrow waist ski which overtime has evolved into the modern carving skis with side-cut. Soon after Slalåm (Slalom) skiing also emerged from the Telemark region (sla is Norwegian for slope and låm means „track down the slope").

From the cradle of skiing in Norway, ski racing took over forty years to reach New Zealand, the author's home country. In 1923 the Ruapehu Ski Club organised the first ski races in New Zealand. The founders Bill Mead and Bernard Drake had imported two sets of skis into New Zealand earlier in 1913.

While New Zealanders were enjoying their first ski races more serious scientific work was being undertaken in Russia. Professor Nicholas Bernstein was working in Russia on the material for his book „The Co-ordination and Regulation of Movements" which was first published in English after his death (Bernstein, 1967). In 1934 technology had advanced a long way from 1887. In Bernstein's book it was estimated that Muybridge could capture motion at about 24 frames per second (not equi-temporal sampling), but in 1934 with the latest Zeiss system up to 1500 frames per second was possible for short durations.

Bernstein used a cyclogramatic method developed earlier by Marey and similar to modern strobe photography where multiple frames of movement were captured as a sequence on fixed film. The sequential movements of bright strips attached to the subject's limbs were recorded on a single image. He also developed kymocyclography for the recording of repetitive movements when the subject had little or no global movement. Incandescent light bulbs were attached to the subject and the movement was recorded on a slowly moving film. These methods allowed for derived measurements of limb angles, velocity, and acceleration, and, ultimately, forces. Using these methods changes in limb movement coordination over time

were represented as curves on a single page and were useful for characterising changes associated with fatigue in factory workers for example. He also employed mirrors to capture and synchronise motion from multiple angles with a single camera. This was used for 3D motion capture. Since Bernstein‟s research, digital cameras and computers have replaced film and analogue measurements. This has made biomechanics research less time consuming, but the basic principles and the accuracy of optical motion capture systems have remained relatively unchanged.

In 1992 many years after Bernstein‟s work, Annelise Coberger won New Zealand‟s first Olympic alpine skiing medal, silver in Slalom. Over one hundred years since the name (Slalåm) was coined in Telemark, Norway, New Zealand had come of age as a skiing nation.

1.2.1. Biomechanical analysis and skiing

In recent years, the number of published papers based on the motion capture of skiing using video cameras has increased dramatically. So much so that when Erich Müller and Hermann Schwameder published a paper in 2003 that included a „brief‟ description of the history of biomechanical analysis of alpine skiing, their paper included over 90 references (Erich Müller & Schwameder, 2003).

Müller and Schwameder‟s paper contains reference to many important contemporary and historical papers, which show both the depth and high quality of previous research. Müller and Schwameder characterise the development of the biomechanics of skiing into three phases:

- 1930 – Present, Qualitative descriptions
- 1957 – Present, Quantitative
- 1980 – Present, Optimisation of Technique and Injury Prevention

The first phase contains studies that provide qualitative descriptions of skiing such as the recording of motion sequences of skilled athletes or the discussion of forces during skiing. Some contributors to the first phase include (Brandenberger, 1934; Hatze, 1966; Howe, 1983; Lind & Sanders, 1997).

The second phase contains studies that make use of biomechanical analyses in order to make objective measurements that describe the technique of skiing. The first study of this type measured ground reaction forces during skiing (Möser, 1957). Some other significant contributors to the second phase include (Eric Müller, 1994; Raschner, et al., 2001).

The third phase is characterised by using biomechanical analyses and mathematical modelling in order to measure, predict and sometimes suggest improvements. Some studies have looked at reducing course time through better aerodynamic position (Kaps, Nachbauer, & Mossner, 1996) and run line. Other studies have investigated how ski geometry affects run line (Casolo, Lorenzi, Vallatta, & Zappa, 1997; Margane, Trzecinski, Babiel, & Neumaier, 1998). Further

studies have analysed musculoskeletal loading often for the purpose of injury prevention (Herzog & Read, 1992; Nachbauer & Kaps, 1994; Quinn & Mote, 1992; Senner, Lehner, Wallrapp, & Schaff, 2000).

Müller and Schwameder then presented biomechanical data including; electromyography (EMG, muscle activity), kinematic data (such as knee angles), and kinetic (force) data (Erich Müller & Schwameder, 2003). They summarised the differences between traditional parallel skiing and „new" carving technique, commonly employed to control modern shaped skis. Some conclusions included; smaller radius turns were possible with the new skis, better sagittal plane (fore/aft) balance control and movement was required and a more equal inside/outside foot loading ratio was used. Their summary demonstrates that ski technique and equipment design are both developing and intertwined.

1.3. Is optical motion capture suitable for skiing?

Only a few researchers have questioned the suitability of optical motion capture for the biomechanical analysis of skiing, possible because there were no other practical options available. The short literature review below illustrates some of the issues with the use of video and/or cinematic cameras for the biomechanical analysis of alpine ski racing and how those issues were overcome. Some of issues that are discussed below include:

- Practical constraints on the use of contemporary video motion capture systems limit the biomechanical analysis of skiing to one or two discrete turns.
- Race performance does not depend on the performance about an isolated turn. It depends on the complete race strategy of both past and future turns.
- Video data are almost always smoothed before analysis and higher frequency components are lost, portraying human movements to be composed of smooth low frequency functions.
- Velocities, accelerations and forces are not measured directly; instead discrete locations are measured often by attaching visible markers to anatomical reference points on the athlete.
- The three dimensional motion analyses require long post processing times for skiing. The harsh alpine environment, high speeds of the athlete and aggressive race strategies make automated marker tracking of visible markers difficult. Time-consuming manual digitising of estimated anatomical reference points on the athlete is often required.
- Many calculation steps separate the forces and torques (the factors underlying the control of human movement) from the raw data (digitised estimates of the athletes anatomical reference points).
- It is difficult to achieve high accuracy of the derived parameters such as limb angle, velocity and acceleration.
- Surveyed control points, required to calibrate the cameras, may impinge on the athlete"s safety.

It took many years for motion capture and the biomechanical analysis of skiing to come together. Initially a single fixed camera was used to track the motion of individual points on the athlete such as the toe piece of the outside ski (Förg-Rob & Nachbauer, 1988). In 1988 Förg-Rob and Nachbauer were limited to capturing the planar 2D-trajectory of the outside ski in a single slalom turn.

The Förg-Rob and Nachbauer paper raised three issues: Using fixed cameras it was only possible to measure isolated turns. A single camera did not measure 3D motion and the digitized data were noisy. To overcome these issues the authors assumed the performance around a single gate was representative of the complete run. The authors assumed the motion took place in a single plane and so they could use mathematics to rotate two-dimensional measurements from the camera coordinate system onto the snow surface plane. The noisy digitised data were smoothed using an approximating cubic spline „for an approximate description of the curve" (Förg-Rob & Nachbauer, 1988).

Förg-Rob and Nachbauer made two assumptions before using cubic spline smoothing on the noisy positional data.

(a) The force of gravity is constant with respect to time, and the gradient of the slope does not change abruptly.
(b) The contractions of the muscles are not abrupt but continuous." (Förg-Rob & Nachbauer, 1988)

Förg-Rob"s and Nachbauer"s assumptions were based on the fact they used a smooth, constant gradient and well prepared testing slope. It is possible some higher frequency components of the motion were lost but because they were primarily interested in the outside ski spatial trajectory the losses might not have adversely affected their analyses.

In 1989 Yeadon captured the 3D motion of ski jumping using two pan and tilt cameras to overcome the fixed camera trade off between resolution and field of view (Yeadon, 1989). Yeadon used two surveyed reference markers in each frame to calculate the changing camera orientation angles and pseudo focal length. Data smoothing was again required and Yeadon used a method of repeated digitisations and quintic (5^{th} order) splines based on a previous discussion of data smoothing (Wood & Jennings, 1979). Yeadon claimed his method produced very accurate results (1° error in limb orientation angle). Yet the system had many practical limitations including; the relatively large fields of camera view used (10-14 metres), the distance of the camera from the athlete (100-180 metres), the fact only two cameras were used, and the difficulty in identifying unmarked joint centres in video frames.

Unfortunately, the accuracy reportedly achieved by Yeadon in his research was not possible using the video equipment available to the author of this thesis. Prior to this research the author experimented with optical motion capture for ski racing (collecting data from the New Zealand North Island Championships) and his estimated error (unpublished) was considerable more than that of a recent study using a 12 camera Vicon system (Schwartz, Trost, & Wervey,

2004). In these ideal laboratory conditions the standard deviation of knee flexion/extension error between expert therapists was between 3° and 5° depending on the percentage of the gait cycle. These results possibly infer the 95% confidence interval for knee flexion/extension might be greater than 6°.

The research questions the author is attempting to answer require the analysis of data from athlete movements through an entire racecourse. How long would this take using manual digitisation? Yeadon took up to 3 hours to digitise 12 landmarks for less than 3 seconds of data from each camera. Both camera views were digitised twice so the whole process might have taken around 12 hours per trial. The extrapolated time commitment for the digitisation of a complete ski run, of over 30 seconds, using 12 cameras, (which is not going to be enough) and a complete body model, could be up to two months per run! Today automated tracking algorithms are available to save time but they perform poorly in the alpine conditions, under direct sunlight, and would require the athlete to wear active markers, which could easily be dislodged during gate contacts.

In 1992 Herzog and Read completed one of the first inverse dynamic analyses (analysis of forces and moments from positional data) of downhill ski landings (Herzog & Read, 1992). Herzog and Read computed one-dimensional flexion-extension knee moments during alpine ski race landings for the purpose of understanding and reducing knee injuries. Herzog and Read chose to use a fixed single camera with its optical axis approximately orthogonal to the plane of athlete‟s motion. The knee forces and torques were then calculated from the video data. Without additional data Herzog and Read were forced to assume either symmetrical loading over the skis or a unipedal stance to calculate knee loading (net joint forces and net joint torques). Quintic smoothing splines were used to smooth the digitised data.

Herzog and Read were investigating injury mechanics in jump landings that occur during rapid changes in movement but they were forced to use data smoothing because of the intrinsic noise in their optical motion capture system. Their approach could have had a detrimental effect on their results, as the many important high frequency components during the impacts of landings, are likely to be lost.

In 1994 Nachbauer et al completed a full 3D analysis of downhill ski jump landings and recoveries at the Winter Olympics (Nachbauer, et al., 1996). Two panning and tilting cameras were used. Six to ten control points per frame were required to calibrate each camera‟s parameters. Nachbauer reported that accuracy improved with the increased number of control points but noted that it was difficult to place the control points without adversely affecting the athlete‟s safety. Nachbauer required more control points than Yeadon‟s earlier experiments because he used a direct linear transformation method (DLT) that also accommodated changing camera zoom. Without data smoothing Nachbauer reported large oscillating acceleration errors of magnitude 10,000 m/s^2. To improve the results, cubic spline smoothing was used on the digitised data, which resulted in the very smooth „knee loading‟ curves in which many of the high frequency components during impact might have been lost.

Nachbauer states they were „well aware of the limitations of the inverse dynamics approach" but at the time there was not a viable alternative (Nachbauer, et al., 1996). There are at least two issues with cubic spline smoothing for inverse dynamic analysis of ski injuries: First the underlying assumptions that supported the use of cubic spline smoothing made earlier were unlikely to hold true for the impacts in jump landings (assumption of smooth movement trajectories, (Förg-Rob & Nachbauer, 1988)). Secondly the smoothed cubic spline data were likely to result in questionable second order derivatives from which forces and moments were calculated.

Since 1996 incremental improvements to the motion capture of alpine ski racing have been made. Müller & Schwameder completed a 3D comparative analysis of parallel and carving ski turns using three cameras simultaneously, along with pressure sensitive insole data and electromyography (Erich Müller & Schwameder, 2003). Pozzo and colleagues undertook the motion analysis of three gates from a world cup giant slalom race using four cameras capable of panning, tilting and zooming to cover the action (Pozzo, Canclini, Cotelli, & Baroni, 2005). Pozzo and colleagues used gates, safety fences, and other landmarks as control points in the subsequent analysis, thus overcoming the problem of interfering with the athlete"s performance and safety.

It appears intrinsically that smoothing of video data is still necessary and the search for better methods continues. An alternative to spline smoothing is digital frequency filtering. Low-pass Butterworth filters, designed by Ludwig Septmeyer, are designed to pass the wanted low frequency components while attenuating the high frequency (unwanted) noise. The selection of an optimum cut-off frequency is difficult without actually knowing the range of wanted frequencies and so cut-off frequency selection and filter order remain a contentious issue. In 1991 David Winter proposed an objective method to optimise the cut-off frequency of Butterworth filters based on a root mean square error (RMSE) analysis such that the noise passed was approximately equal to the good signal lost supposedly maximising the signal to noise ratio (Winter, 1991). Other work has shown that the optimum cut-off frequency is different for each body segment, and for each higher order derivative, such as velocity and acceleration (Angeloni, Riley, & Krebs, 1994; Giakas & Baltzopoulos, 1997). More recently it was suggested wavelet transform based filtering may be better than Butterworth filters (Ismail & Asfour, 1999). Wavelets work over multiple resolutions (scales) simultaneously, which minimises the limitations of resolution in both the temporal and the frequency dimensions of the transform (Macey, 2000). Also, wavelet shape can be optimised for a particular data set. This means, wavelet filtering should be able to adapt better than Butterworth filters to any changing signal or changing noise characteristics in digitised marker data. It is still not practical to use optical motion capture for the biomechanical analysis of a complete ski run.

Biomechanists have already realised that in order to increase the understanding of alpine ski racing outcomes, data from multiple consecutive turns are required. Supej noted through an energy analysis that turn performance was dependant on the previous turn (Supej, Kugovnik, & Nemec, 2005). In a recent paper it was further hypothesised; „if turn strategy is dependent

on both past and future turns, then, unfortunately, race outcome, and ultimately athlete performance, cannot be predicted from the analysis of an isolated turn sequence" (Brodie, Walmsley, & Page, 2008b). In the same paper evidence was provided for this by analysing estimated split times through a ten-gate giant slalom course. The evidence is also presented in Chapter 8, page 195 of this thesis.

By 2005 biomechanists were looking for alternative ways to capture the movements of alpine ski racing and the global positioning system (GPS) was proposed as a practical solution (Ducret, Ribot, Vargiolu, Lawrence, & Midol, 2005). Ducret synchronised GPS (to approximately measure the athlete speed and position on the course) with strain gauges (to measure forces normal to the ski base).

1.4. Motion capture using new sensing technology

The potential of a new wearable motion capture system that used small sensors attached to the athlete was investigated. The system was based on inertial measurement units (IMUs), small sensors that contain accelerometers, gyroscopes and magnetometers. More details about the system that was purchased for this research and the internal components of the IMUs, are in Chapter 2.

This approach was new in 2005 and there were no previous papers detailing the use of IMU based systems for the motion capture or biomechanical analysis of skiing. While the limitations of 3D optical motion capture were well documented, the limitations of the new wearable motion capture system were, at the time, difficult to determine from the literature.

The original idea for IMU based motion capture may have come from previous research into inertial navigation of ships, submarines or aircraft (Broxmeyer, 1964). IMUs usually contain linear accelerometers and gyroscopes that measure rate of rotation. To get the IMU orientation the gyroscope data are integrated, but without alternative data streams the initial orientation of the IMU is unknown and the accumulated integration error becomes unacceptably large. Additional data from GPS, radar, magnetometers or barometers can be used to improve accuracy. The process of combining several streams of data like this is known as *„data fusion"*; the different data streams are fused together (joined mathematically) to improve accuracy. Kalman filters are most commonly used as real-time fusion algorithms (Kalman, 1960). In navigation literature this mathematical compensation process is also known as strap down integration. Prior to strap down integration mechanical methods were used that employed a series of rotating gimbals[2] to provide a quasi-inertial global reference frame.

Human motion capture presents different challenges from vehicle navigation. The dynamics of human movement are less predictable than the dynamics of a large vehicle with considerable mass and better-defined inertial properties. Also, the sensor technology for

[2] A gimbal is a pivoted support that allows the rotation of an object such as a spinning globe.

human motion capture needs to be smaller, lighter, and less expensive. Low cost, light weight sensors are currently less accurate that those used in precision vehicle navigation.

Bogert, Read and Nigg suggested that accelerometers (one component of IMUs) might have future potential for motion capture in skiing because of the large global motion experienced in skiing (van den Bogert, Read, & Nigg, 1996). Over thirty years ago accelerometers were used to analyse forces and moments during tennis racket impacts (Kane, Hayes, & Priest, 1974). This method was later adapted for trunk segment motion and hip joint torques using four tri-axial accelerometers (van den Bogert, et al., 1996). Significant improvements in IMU motion capture systems were made when miniature gyroscopes were combined with the accelerometer data using Kalman filters to obtain more accurate inclination data (Luinge, 2002; Luinge, Veltink, & Baten, 1999; Matsuda, 2003). In the later papers, the accelerometer data were used to reduce the accumulated pitch and roll errors from the integrated gyroscope data. The accelerometer data were used to determine the resultant acceleration vector that was assumed over long periods of time to approximate the gravity vector and hence the vertical axis of the global coordinate system.

Finally, additional data were required to reduce IMU heading drift in the integrated gyroscope data. This was typically obtained from a magnetometer and correction was reported to be accurate if the movement took place through a relatively homogeneous magnetic field (XSens, 2004a) and (Bachmann, 2000). The magnetometers measured the resultant magnetic field, which, provided the movement was in an environment free of magnetic disturbances, was a constant vector. In most places on Earth except near the poles, the magnetic field vector and the gravity vector are distinct. Provided the sensor was stationary and far enough from the poles, data from the accelerometers and magnetometers could provide a unique second estimate of IMU orientation. All three data channels (accelerometers, gyroscopes and magnetometers) were fused using Kalman filters and stable estimates of 3D orientation became possible.

In his thesis Luinge developed a Kalman filter for the inertial measurement of trunk inclination and reported errors of less than 2° (Luinge, 2002). This was similar to the errors reported to be associated with the optical motion capture systems (Schwartz, et al., 2004). Such low errors appeared to make IMUs very appropriate for the biomechanical analysis of alpine ski racing.

In hindsight Luinge"s brief comment in the introduction to his thesis should have been considered more seriously:

> *...„œccuracy of the estimated kinematics depends on the particular movement to be performed."...*(Luinge, 2002)

Luinge"s comment should have been considered more seriously because the athletic movements in alpine ski racing are very different from the quasi static trunk movements in box stacking. But every cloud has had a silver lining and each problem documented in this

thesis has resulted in the opportunity to improve our capacity to study complex human motion.

1.5. Forces and optimum trajectories in alpine ski racing

In ski racing all athletes start with the same gravitational potential energy relative to their mass, so all should theoretically (in a frictionless environment) finish with the same final velocity. The winning athlete makes efficient use of gravity and has a global strategy that balances the shortest path between gates against maintaining a high velocity and avoiding injury.

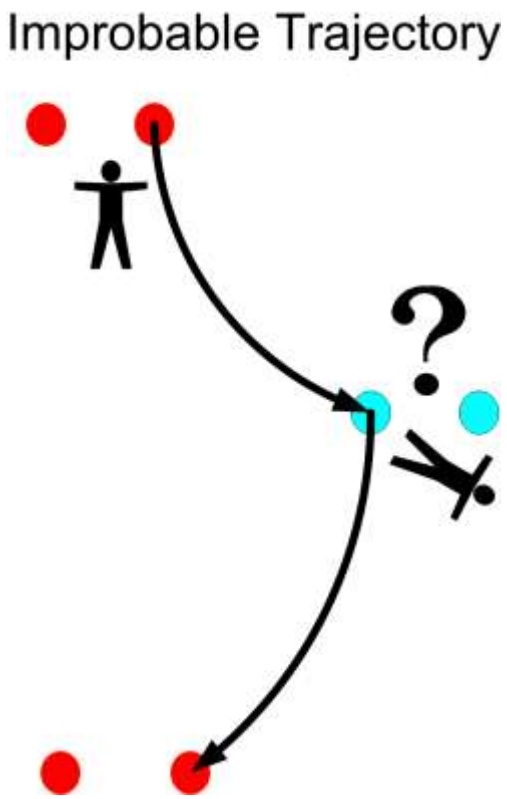

Figure 1.5: Improbable solution to the brachistocrone problem

Some research has focused on the path of shortest descent time commonly termed the *brachistocrone* problem (from Greek meaning shortest time). The fastest path between gates is not a straight line but the research suggests the athlete should start skiing close to the fall line to increase speed early in the trajectory (Figure 1.5). The analysis was done first without frictional forces (Reinisch, 1991) and later with „snow cutting" forces included (Hirano, 2002).

Neither of these papers considers how the athlete should change direction at each gate. The analyses results in infinite forces required at each gate to change direction. Reinisch"s and

Hirano‟s results support one accepted tactic for skiing fast „going straight turning short‟ (Lind & Sanders, 1997) and this might have impacted on the design of modern racing skis.

In these cases the models used to optimise the trajectories did not consider the athletes physical limitations and so they predicted trajectories that were not possible when skiing through a continuous sequence of gates. The optimum strategy for passing through a series of gates is unknown. The optimum ski design for a particular gate set is unknown. The optimum envelopes of athlete movements through complete gate sets are also unknown. Steps towards finding these answers require measurements, models, and estimations of the external forces acting on the athlete. Simulations of performances during a ski races are required based on estimations of the athlete‟s physical limitations.

Fortunately, considerable research has been undertaken into the analyses of the external forces acting on the athlete. External forces include gravity, wind drag, ground reaction, and snow resistance. Because style does not decide race outcome the external forces uniquely define the athlete‟s performance and so it follows that a survey of what is known about the external forces acting on the athlete during ski racing is required.

1.5.1. Gravity

In alpine skiing athletes travel downhill so the primary accelerating force is gravity. Gravitational potential energy is turned in kinetic energy as the athlete descends the slope. It was assumed that the gravitational acceleration was constant and equal to $9.81 ms^{-2}$, which is not exactly true at different parts of the Earth‟s surface but any variation in gravity should not significantly affect the research.

1.5.2. Ground reaction forces measurement

Ground reaction forces (GRFs) are generated between the athlete‟s skis and the snow surface. Athlete technique directly affects ground reactions forces, which accelerate or decelerate the athlete, changing the magnitude and/or direction of the resultant velocity vector. Ground reaction forces are therefore very important in ski racing.

The earliest reference to measuring ground reaction forces in skiing is from a PhD thesis in 1957 (Möser, 1957). Muller and Schwameder reported that in 1957 a dynamograph was developed and mounted to a ski so that forces could be recorded on paper strips (Erich Müller & Schwameder, 2003).

In more recent times both pressure sensitive insoles, and miniature force plates have been used to measure ground reaction forces. Also, inverse dynamic analysis of video data has been used to estimate ground reaction forces. Ground reaction force data from a single turn were measured using all three methods and the data were recently published (Lüthi, et al., 2005). Lüthi‟s paper demonstrates the relative accuracy of each method very well.

Miniature force plates are the most reliable, but these are expensive to build and, because of their size, may be unacceptable to athletes. Force plates can measure both ground reaction forces and moments but a common mistake is to assume the measured forces between the foot and the boot or the boot and the ski is the same as the ground reaction force between the ski and the snow, without accounting for the extra mass of the ski. Lüthi‟s force plate measurements were drift free and sensitive to the high frequency fluctuations in ground reaction forces as the skis vibrate across the snow surface.

Pressure sensitive insoles are easy to use but are inherently less accurate than force plates and can only measure pressure, which, given the known area of the sensors can be turned into a force measurement perpendicular to the insole. Pressure sensitive insoles are unable to measure the forces transmitted through the boot shank, the forces parallel to the boot sole, or the ground reaction force moments. Lüthi‟s data show between 7% and 10% of the ground reaction forces were in the plane of the ski surface and so could not be measured by pressure sensitive insoles. The ground reaction forces perpendicular to the ski bases that were measured by the pressure sensitive insoles did not contain the rapid changes in forces measured by the miniature force plates.

One issue with both pressure sensitive insoles and miniature force plates is that the measurements are in the local frame of the ski or boot and, without additional data, they cannot be used to predict changes in the athlete‟s global trajectory. This problem can be overcome by simultaneously completing a 3D kinematic analysis with multiple cameras.

Inverse dynamic analyses are usually based on video data. The athlete does not need to wear additional measuring equipment but the post processing required may produce unreliable results as discussed previously in Section 1.3. Lüthi‟s data show the ground reaction forces calculated by inverse dynamic were over smoothed and peak forces were underestimated.

1.5.3. Wind resistance

Wind drag force opposes the athlete‟s movements through the air as they descend the slope. Barelle et al suggested that, at high speeds (>25ms^{-1}), wind drag is the most important dissipative force (Barelle, Ruby, & Tavernier, 2004). This is because wind drag forces in ski racing are usually considered to be proportional to the athlete‟s speed squared.

It is not possible to measure wind drag directly during alpine ski racing so it has to be estimated from models. Equation 1.1 is the most commonly used model. In the past wind drag force was calculated from force platform measurements in wind tunnels. The athletes adopted many different stationary poses on force platforms and different wind speeds were used; the horizontal reaction forces measured by the force platform were equal and opposite to the wind drag force. Some of these previous measurements have been summarised in a paper by (Kaps, et al., 1996).

Laboratory experiments report wind drag in terms of the drag coefficient (C_d) or drag area (A_c*C_d the drag coefficient multiplied by the cross sectional area). These coefficients are then used to estimate wind drag force using Equation 1.1. Reported values for drag area range from 0.15m^2 for the „egg posture" (crouching with arms in front and poles tucked beside the torso) in skiing at 28ms^{-1} (Barelle, et al., 2004) to 0.73m^2 for an upright posture in cross country skiing at less than 11ms^{-1} (Spring, Savolainen, Erkkila, Hamalainen, & Pihkala, 1988).

Equation 1.1 $$F_{Drag} = \frac{1}{2}\rho A_c C_d V^2$$

In Equation 1.1 the symbols have the following meanings: (ρ) Density of air, (V) Relative wind velocity between the athlete's centre-of-mass (CoM) and the air, (Ac) Cross sectional area normal to the relative wind velocity, (Cd) The coefficient of wind drag.

How do the measurements made on static poses relate to wind drag when the athlete is moving between gates? It seems that any model used to estimate instantaneous wind drag is going to have inherent errors. Barelle proposed a method to extrapolate the controlled laboratory measurements of wind drag to the athlete's performance during a ski race (Barelle, et al., 2004). Joint angles, such as the ankle, knee, and hip, which could be filmed in the sagital plane, were measured together with wind tunnel measurements of wind drag force. Barrelle then constructed an empirical model to predict the wind drag during ski races based on joint angles measured from video data.

1.5.4. Snow resistance

Snow resistance opposes the athlete's skis as they move over and through the surface layers of snow. The ski/snow interaction is very complicated and a satisfactory model that can accurately predict the snow resistance forces during ski racing remains to be discovered. Snow resistance is a component of the ground reaction forces but in this thesis it is separated from the ground reaction forces normal to the ski bases because it may be modelled.

Federolf et al. state: „More than 40 scientific papers discuss ski-snow friction" (Federolf, et al., 2007) and they have provided a good discussion about them. One theory is that the initial contact between the ski and the snow is dry friction, which melts some snow providing a thin fluid layer for the rest of the ski to run on. If this is the case, snow sliding friction might depend on the thickness of the fluid film, the pressure at the contact points, and the contact area. The linear model most often used is the Coulomb friction model Equation 1.2 and friction coefficients are reported to be μ=0.003-0.007 for ice and μ=0.04-0.2 for hard and soft snow respectively (Shimbo, 1971; van Ingen Schenau, 1982).

Equation 1.2 predicts increased ski/snow sliding friction as a function of increased normal force (F_N). At high speed when the athlete turns normal force can increase between four and six fold so when turning sliding friction is predicted (as a result of increased normal forces) to increase with increased speed. While running smoothly in a straight line the Coulomb friction model predicts sliding friction remains unchanged.

Equation 1.2 $$F_{Frict} = \mu F_N$$

Unfortunately in ski racing the skis do not sit flat on the snow surface, but move from edge to edge between gates. The skis bend and the snow is displaced as it compresses and fractures. Federolf et al. provided evidence for a threshold process for the ski edge penetration and snow fracture in which the maximum pressure at the ski edge must exceed the mechanical strength of the snow (Federolf, et al., 2007). While Equation 1.2 may be acceptable for ski/snow sliding models it is unlikely it can accurately predict snow resistance forces when the skis penetrate into the snow surface and snow is displaced.

In 1996 Kaps tried to incorporate velocity effects into a simple model and used data from skiing to fit empirical snow resistance coefficients (Kaps, et al., 1996).

Equation 1.3 $$F_{Snow} = F_N(\mu_F + \mu_V V)$$

If Kaps's equation (Equation 1.3) is a more reliable model for ski racing than the Coulomb model (Equation 1.2) it means snow resistance increases with velocity and it should possibly not be ignored at high speeds (>25ms^{-1}) as has been previously suggested (Barelle, et al., 2004).

More work is required to build an accurate model of snow resistance. Chapter 7, Forces in Giant Slalom, contains a more detailed discussion about snow resistance, the methods used to estimate snow resistance in ski racing, and reasons why those methods were chosen.

1.6. Thesis objectives

Which comes first, ski design or ski technique? Is there a faster, easier or safer way to ski? Do Stenmarks's comments („Many skiers do not take advantage of the way modern equipment has been designed to facilitate carving turns") still hold true today? Seeking answers to these questions led to the original thesis objective:

"Optimisation of athlete movement in alpine ski racing"

The conciseness of the stated objective disguises the complexity of the objective and so it is separated it into five milestones.

1. To accurately capture the motion of ski racing over a complete race course
2. Measure or model the different forces exerted on the athletes through their interactions with their environment
3. To analyse complex whole body motion through a large 3D volume
4. To present the analysis in a way intuitive to the athlete
5. To optimise the athlete‟s essential movements through simulations based on athlete specific performance parameters

The milestones are in a sequential order and to complete them multiple experiments were required. The lessons learnt from each experiment were applied to the subsequent experiments. The sequential nature of the milestones dictates that the best structure for this thesis is to present the information in the order it was realised.

To meet the thesis objective, the measurements should be from simulated race conditions. The measurements should be completed on steep alpine terrain, in winter and with minimal interference with the athlete‟s technique.

1.7. Chapter Summary

Chapter 2 contains initial tests carried out on a wearable motion capture system. In this chapter the IMU based motion capture system (as purchased) is shown to unlikely to be suitable for alpine ski racing. Custom fusion algorithms are developed by the author, which combine raw data from the different sensing elements within the IMU.

Chapter 3 presents Fusion Motion Capture (FMC) for the first time. FMC consists of a GPS receiver and IMUs attached to the athlete. The prototype FMC system is used to successfully measure free skiing at Coronet Peak ski area, New Zealand. Colour coded force vector analysis, is developed, a novel tool used to visualise the effects of forces on athlete performance.

Chapter 4 contains further development of FMC. New FMC algorithms that combine the GPS and IMU data are developed and validated against video analysis data. A method for measuring a subject‟s bony landmarks in three-dimensions is developed and subsequently used to create a subject specific body model.

Chapter 5 covers the developments to FMC made through the motion capture and analysis of inline skating. The FMC data is used to measure, calculate and model the external forces acting on the athlete. Power and work analyses are used to investigate the effects of the different forces on performance. New ways to visualise these performance effects through data driven animations are developed. Variability in performance is analysed resulting in a theory about how an athlete could construct performances using global checkpoints and an

open radius turn strategy. Finally, the athlete‟s optimum performance through the course is simulated using constraints based on athlete specific performance parameters measured from the FMC data.

Chapter 6 describes the motion capture of giant slalom ski racing at Mt Ruapehu in 2006 and the improvements made to FMC for skiing. The accuracy of the GPS receiver pseudo-range and carrier-frequency data is investigated. A method to measure and construct the variable course terrain is also developed. Soft tissue artefacts are discussed and methods to reduce their adverse effects on FMC accuracy are implemented.

Chapter 7 describes the calculations developed for the biomechanical analysis of alpine ski racing. The effects of different external forces on ski racing performance are investigated including; gravity, wind drag, snow resistance and ground reaction forces.

In Chapter 8 the athlete performance in alpine ski racing is optimised using the FMC data from Mt Ruapehu. Analyses of the data show that performance cannot be determined from the analysis of a single turn. The traditional „going straight turning short‟ race strategy is disproved. The results indicate that the athlete could have improved his performance through both changes to turn technique and changes to global race strategy.

Chapter 9 presents the conclusions to the thesis. The material in the thesis is critically reviewed to determine how it compares to the original thesis objectives and milestones and where it fits into past literature. Some major findings of the thesis are highlighted and avenues for future work are discussed.

2. IMU Laboratory Tests

Figure 2.1: Subject with ten IMUs and an XBus models the IMU placement

In Chapter 1 traditional methods for optical motion capture were discussed and they were found not to be ideal for capturing athlete movements through a complete racecourse. In this chapter, a wearable motion capture system based on inertial measurement units (IMUs) is investigated for accuracy during dynamic movements. The system, consisting of twenty IMUs and three XBus interface modules, that were purchased from the vendor (XSens, 2004c).

This chapter contains the initial tests done on the IMUs to assess their suitability to meet the first milestone of the thesis:

"To capture the motion of alpine ski racing over a complete race course"

This chapter assesses the ability of the motion capture system to accurately measure a variety of movements. In the first test, ten IMU sensors are attached to a subject to drive a body model called Nancy (Section 2.1). The results were mixed and so further investigations into IMU motion capture and the development of custom algorithms for IMU motion capture were completed in two situations:

- Section 2.2, pendulum swing tracking
- Section 2.3, static orientation and calibration of the sensors.

Further information and the background to these experiments is available on the accompanying CD (Brodie, Walmsley, & Page, 2008a, 2008d).

2.1. Animating Nancy

The ability of an IMU based motion capture system to measure a variety of human movements in a laboratory was tested. Accuracy was qualitatively assessed from a real time image of the subject projected behind the subject during movements. Data from IMUs attached to the subject were used to drive an open source body model (Nancy). The 3D body model was projected as a 2D image in real time behind the subject. The subject"s slow motions appeared relatively accurate compared to dynamic movements. The algorithm provided by the vendor to obtain orientation from the IMUs performed poorly in the dynamic situations. Skiing is a dynamic activity, and so this test indicated that the system as purchased was not directly applicable to the biomechanical analysis of skiing.

2.1.1. Methods

IMUs are integrated electronic devices that contain accelerometers, magnetometers and gyroscopes. The raw data from the IMUs can be processed using an algorithm supplied by the vendor to provide orientation expressed as a rotation matrix, quaternions, or Euler angles, (XSens, 2004a)

All the IMUs used in the experiments reported here were MT9 sensors from XSens Technologies. The MT9 housing measures 53.5mm long by 38.5mm wide by 28.7mm high

and the unit weighs 35 grams. Further technical details about the MT9 units are provided on the accompanying CD (Brodie, et al., 2008d).

Ten IMUs attached to ten body segments were connected to a single XBus. The XBus combined the IMU data into a single stream and relayed it to a computer. The IMUs were attached to the subject with double sided tape and medical tape (Figure 2.1). The ten segments animated were; Thorax, sacrum, thighs, shanks, upper-arms and forearms. Because 10 IMUs were used to animate 15 body segments, the head was rigidly attached to the thorax, the hands were rigidly attached to the forearms and the feet were rigidly attached to the shanks. The locations of the IMUs were:

- Thorax: Over the third thoracic vertebra between the scapular spines.
- Arm: Lateral aspect of the arm between biceps and triceps brachii on flattest section of humerus midway between shoulder and elbow.
- Forearm: Posterior aspect of the wrist with the lower edge of the IMU on the line between the styloid processes of radius and ulna.
- Sacrum: Over the mid-point of the line joining the posterior iliac spines.
- Thigh: Lateral aspect of thigh on a flat section of the quadriceps tendonous sheath, midway between the greater trochanter and the lateral femoral condyle.
- Shank: Medial aspect of the tibia just inferior to the tibial tuberosity, on flat section of the tibia.

Data were collected from the XBus Master (the vendor‟s interface to the IMUs) via a three-metre serial cable to a personal computer. Data from the XSens system were used to drive a body model and the animation was projected in real time on a wall behind the subject so the motion capture could be qualitatively validated.

The recommended settings for the vendor fusion algorithm were used to obtain an orientation measurement from each IMU, (XSens, 2004b). Nancy was a body model provided by Cindy Ballreich (copyright 1997) and modified for MATLAB (an extensible technical computing and visualization environment with a high performance programming language) by Ben Tordoff and Walterio Mayol. Nancy is provided with the vendor‟s software, but can be downloaded for non-commercial use from:

http://www.robots.ox.ac.uk/~wmayol/3D/nancy_matlab.html

Details about the data driven animation

Nancy was animated using MATLAB code adapted from code supplied by the vendor, (version 1.0, XM MT9-B © 2003, Xsens Technologies B.V.author, Per Slycke). Two changes were made to the code. The first change extended the animation from a five-segment upper body model to a ten-segment whole body model. The second improvement allowed the IMUs to be attached to the body segments in the most practical places to avoid skin artefacts. In the original code the IMUs had to be precisely placed with the local z-axis of each IMU aligned with the subject‟s antero-posterior (AP) axis in the anatomical position. The original code

posed problems for the IMU that was to be attached to the posterior aspect of the sacrum. The original code was also required the IMU to be attached to the anterior surface of biceps brachii, which could exacerbate skin artefacts.

First each IMU was mapped to the subject‟s limbs. Mapping is generally required because the orientation of each sensor, defined by the alignment of the internal components, is different from the orientation of each limb segment defined by bony landmarks. A constant rotation aligns each sensor with the limb to which it is attached. A three-by-three matrix is used to describe the constant rotation..

Mapping was completed with the subject standing stationary in a calibration position at the start of the test. The anatomical position (subject standing upright with arms straight down beside the body and palms facing forward) was used as the calibration position.

IMUs can provide information about the local limb orientation but not location. To produce the data driven animations, therefore, each limb segment was linked to the known location of its proximal joint centre. The animation had to have an external constraint; in this case the C6-7 cervical joint centre in the animation, was constrained to a fixed location. This gave the subject‟s recreated movements the appearance of being suspended from this joint, or being „hung from a coat hanger‟ even though the subject‟s true movements were unconstrained. This type of sequential process results in measurements of the distal body segments such as the feet, shanks, hands and forearms being less accurate than the measurements of the proximal body segments such as the thorax and sacrum.

Assumptions of IMU motion capture

Three assumptions were required. The first assumption was that the heading of the z-axis of the IMU attached between the subject‟s shoulder blades was physically aligned with the heading of the anterior-posterior (AP) axes of the subject‟s body segments while standing in the anatomical position. The second assumption was that the subject was in a homogenous magnetic field. The heading correction required between the magnetic north of the IMU reference system and the anterior-posterior axis of the subject could therefore be calculated. In this thesis heading generally refers to the projection of a vector onto the horizontal plane. These two assumptions seemed reasonable because the flat housing of the IMU was fixed onto a flat section of the athlete‟s back with little soft tissue artefacts and because the calibration mapping was performed away from any highly magnetic objects.

If the anterior-posterior axes of the limb segments had been inconsistent (because one or other of the first two assumptions were incorrect) then although the subject might be accurately represented in the calibrated position, subsequent limb rotations might be animated about the wrong local limb axes. This might cause for example, some flexion/extension to be erroneously recorded as abduction/adduction.

The third assumption was that the body model accurately represented the subject‟s dimensions and that the calibrated position adopted by the subject was accurate. More

technical details about creating data driven animations from IMU data are provided in Appendix A and on the accompanying CD (**Appendices\Example Code\Nancy\More about Nancy.pdf**).

2.1.2. Experimental

The IMUs were calibrated to each body segment with the subject standing in the anatomical position. The calibration procedure aligned the avatar pose with the subject pose, and the subject local axes of limb rotation with the avatar local axes of limb rotation. From the calibrated position three types of movement were carried out:

1. Walking.
2. Dancing.
3. Rotating on an office chair.

2.1.3. Results

The results of the experiment are based on qualitative comparison of subject motion and the resulting animation (Figure 2.2). The captured movements were displayed as a real time data driven animation behind the subject using a data projector.

Figure 2.2: The Subject dancing, Nancy, the real time data driven animation is visible

Movement one: Walking

Initially the captured motion appeared to be closely related to the motion of the subject. After about twenty seconds the captured motion deteriorated. Parts of limbs appeared to pass through each other and uniaxial joints such as the knee and elbow appeared to bend unnaturally. When the data driven animation periodically deteriorated the subject was made to return to the calibration pose for re-calibration, which improved the motion capture.

Movement two: Dancing

Motion Capture of slow artistic movements closely resembled those of the subject. Whenever the subject landed from jumps or moved rapidly the motion capture deteriorated briefly; once again uniaxial joints appeared to bend unnaturally. Once the impact abated, the data driven animation recovered within a short time.

Movement three: Rotating on a chair

The motion capture of subject limb movement while sitting on a chair appeared to be closely related to the actual motion. When the chair was rotated about the vertical axis the captured motion exhibited characteristics that were clearly not present in the actual motion. The motion capture showed elevation of shanks and forearms even though the segments did not actually move. The faster the chair was rotated the greater the elevation of the shanks and forearms.

Video of a slow moving trial

A video of selected movements is provided on the accompanying CD and by the following link.

Video 2.1: Appendices/FMC Video/Nancy 2005.AVI

2.1.4. Discussion

The results indicate that it is possible to use IMUs to capture some types of motion. It is not possible to determine absolute accuracy quantitatively from this experiment, but qualitative analysis of the motion is possible. For slow, short movements the captured motion appeared to resemble the actual motion. The slow dance movements were successfully captured, (Figure 2.2 and Video 2.1). The method successfully mapped each sensor to the subject"s correct body segment and converted the numerical data into to a real time animation.

The system unfortunately failed to accurately capture the motion of rapid movements. Of concern with regard to ski racing motion capture, are the results from the rotating chair. The centripetal acceleration experienced by the distal limb segments while rotating on the chair caused the erroneous motion in the animation. The hypothesis that centripetal acceleration is an issue is corroborated by the fact that the limb segments became erroneously more elevated when they experienced more centripetal acceleration as a result of the chair being rotated faster.

The algorithm provided by the vendor was unable to adapt to the dynamic movements of the subject, possibly because of incorrect assumptions made in the vendor‟s algorithm. In the vendor‟s algorithm the acceleration, measured by the IMU accelerometers, was assumed to approximate the global Z-axis (reaction to Earth‟s gravity) and was used to correct for the pitch and roll drift of the IMU, (XSens, 2004b). Unfortunately if an IMU is attached to a body segment undergoing continuous rotation, the acceleration, measured in the IMU local reference frame does not always converge to the global Z-axis.

For example, for the distal limb segments in the rotating chair test, the measured acceleration was a combination of reaction to gravity and centripetal acceleration and the resultant acceleration vector was deflected into the centre of rotation. Consequently, the acceleration measured in the IMU reference frame did not approximate the global Z-axis, which may have caused large errors in the calculated orientation. The vendor‟s algorithm was provided as a „black box‟, so it is not possible to confirm if this is the underlying reason for the high errors in IMU orientation observed.

In the walking tests the captured motion initially appeared realistic, but over time the solution deteriorated. It is not known why this occurred but possibly the long-term drift was a result of small magnetic disturbances in the laboratory, or instabilities in the motion capture system.

In skiing there are large accelerations of four to six times the gravitational acceleration when the athlete turns at speed. In skiing there may also be magnetic disturbances from the athlete‟s equipment and ski area infrastructure and a ski race is over a minute in duration. The system as purchased is therefore unsuitable for the biomechanical analysis of body segment orientation in skiing. The poor results were a serious setback for the project and, as a consequence, further investigations into the properties of the sensors were required.

2.2. The Pendulum

After the discovery that the IMU based motion capture system purchased was unlikely to provide accurate motion capture of skiing, two questions emerged:

- Could more be found out about the accuracy of IMUs in dynamic situations?
- Could better data fusion algorithms for dynamic motion be designed?

In order to attempt to answer these questions a simple pendulum experiment was devised. The motion of a simple pendulum is repeatable, predictable and continuous. If the pendulum swing orientation could be measured accurately with an IMU, then motion capture systems based on IMUs might be feasible for biomechanical research. Further information about this experiment is provided on the accompanying CD (Brodie, et al., 2008a).

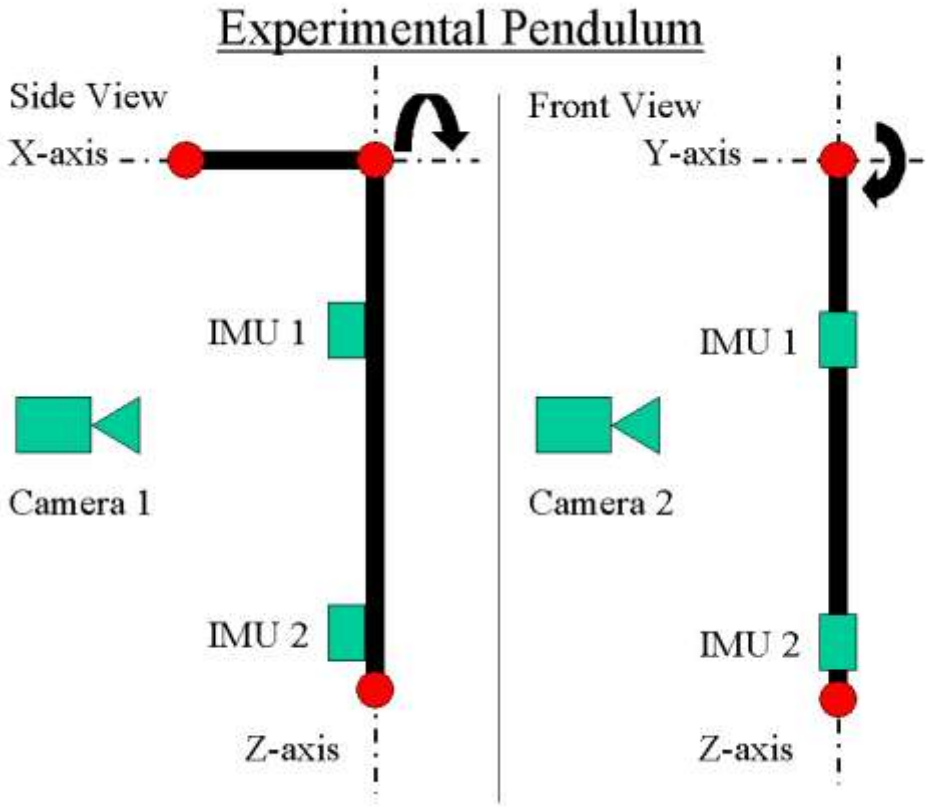

Figure 2.3: The pendulum set up

IMUs produce raw data in a local reference frame, and typically a Kalman filter is used to process the raw data to obtain orientation and measurements in the global reference frame. (Brodie, et al., 2008a, 2008d; Giansanti, Maccioni, Benvenuti, & Macellari, 2007; Luinge & Veltink, 2005; Luinge, Veltink, & Baten, 2007; Pfau, Witte, & Wilson, 2005; Waegli, Skaloud, Ducret, & Roland, 2007; XSens, 2004a)

The IMUs used in the experiments reported here were MT9 sensors from XSens Technologies. XSens provide no details about the internal workings of their Kalman filter supplied with the IMUs except that dynamic orientation accuracy is „less than 3º RMS" (XSens, 2004a). This is consistent with the results of other research (Luinge & Veltink, 2005):

> …„Although the problem of integration drift around the global vertical continuously increased in the order of $0.5^{o}s^{-1}$, the inclination estimate was accurate within 3º RMS."…

The vendor specification also came with the following fine print: "…may depend on the type of motion measured". More research was required therefore to determine what „type of motion" could be measured accurately. It was assumed that the Kalman filter implementation was similar to that used by Luinge and Veltink with the addition that the magnetometer data were used to prevent heading drift (integration drift around the global vertical).

2.2.1. Data processing

Fusion algorithm overview

Algorithms to determine global orientation were developed. The algorithms fuse a static estimate of orientation (from the accelerometers and magnetometers) with a continuous integral estimate of orientation (from the gyroscopes). The results are not required in real time and so the fusion algorithm is able to use the complete data set to estimate the orientation of the IMU at each point in time. A simple block diagram of a fusion algorithm is shown in Figure 2.4. The MATLAB code for the simple bi-directional fusion algorithm presented in this section is provided in Appendix A.

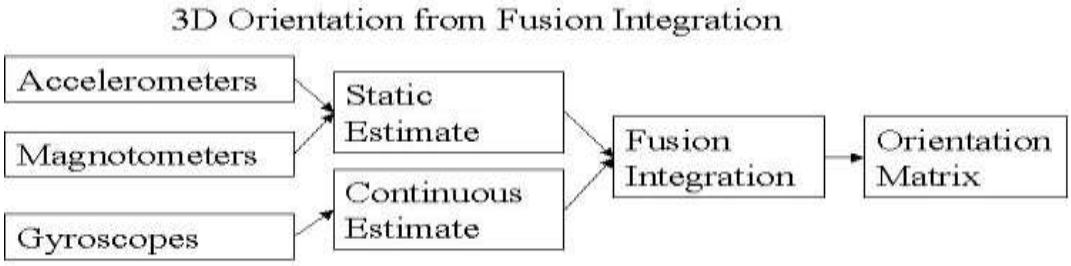

Figure 2.4: A general outline of the fusion integration process

Some example output of the fusion process for data from a pendulum swing is shown below (Figure 2.5). The static estimate of orientation was only accurate when the pendulum was stationary (5s>t>30s), during this time the static estimate (blue dots, Figure 2.5) are in close agreement with the fused estimate, (black line, Figure 2.5). The continuous estimate, (red line, Figure 2.5) based on the integration of the gyroscope data, contained integration drift. The fused estimate was obtained by correcting the low frequency drift of the gyroscope estimate with information from the static estimate. In terms of data fusion the static estimate was accurate over a long time period but contained noise, it displayed low frequency accuracy. The dynamic estimate was accurate over a short period of time but drifted over a long period of time, it displayed high frequency accuracy. In Figure 2.5 the quaternion representation of orientation has been used. The complete Quaternion representation of orientation consists of four elements, Q0 to Q3, but this would make the figure confusing and so arbitrarily only the second element, Q1, is visualised in order to illustrate the different properties of the three estimates. More details about quaternion representation are provided later in Chapter 4.1 on page 54 and on the accompanying CD (Brodie, et al., 2008d).

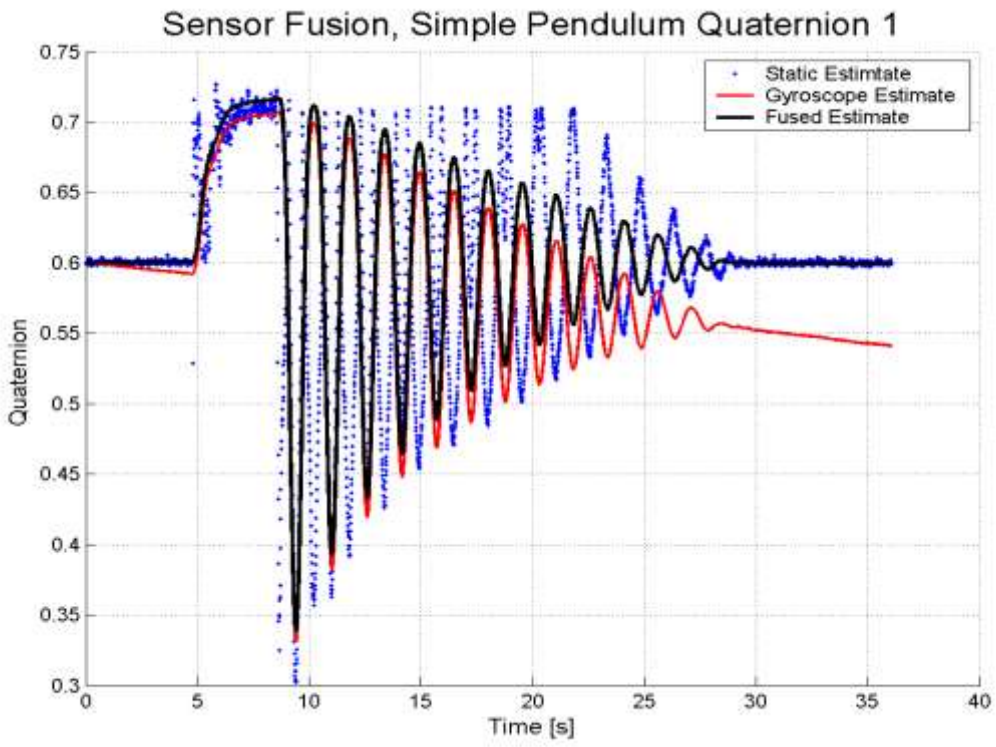

Figure 2.5: Pendulum swing in quaternion representation only Q1 is shown for clarity.

Obtaining a static estimate of orientation

An orientation measurement requires the rotation in each of three rotational degrees of freedom to be specified. The accelerometers provide information about pitch and roll while the magnetometers provide information about heading. The orientation matrix ($\mathbf{R}_{Global}$) that describes the sensor orientation in the global reference frame is obtained from the local axes, (Equation 2.1), which are derived from the IMU accelerometers and magnetometers and provide a static estimate of orientation.

Equation 2.1 $$\mathbf{R}_{Global} = \left[\mathbf{X}_{Local} \quad \mathbf{Y}_{Local} \quad \mathbf{Z}_{Local}\right]$$

In the global coordinate system used by the IMU, the Z-axis points vertically upwards. The X-axis points to magnetic north and is normal to the Z-axis, it is the projection of the magnetic vector (H, Figure 2.6) on the horizontal plane. The Y-axis is a floating axis, normal to both X and Z-axes, (Figure 2.6). In quasi-static situations and if the movement takes place through a homogeneous magnetic field, the orientation ($\mathbf{R}_{Global}$) is accurate. In dynamic situations, local acceleration of the sensor might affect the estimates of the Earth's gravitational field. More details about static orientation calculations and the IMU global reference frame are provided in Section 2.3 and on the accompanying CD (Brodie, et al., 2008a, 2008d).

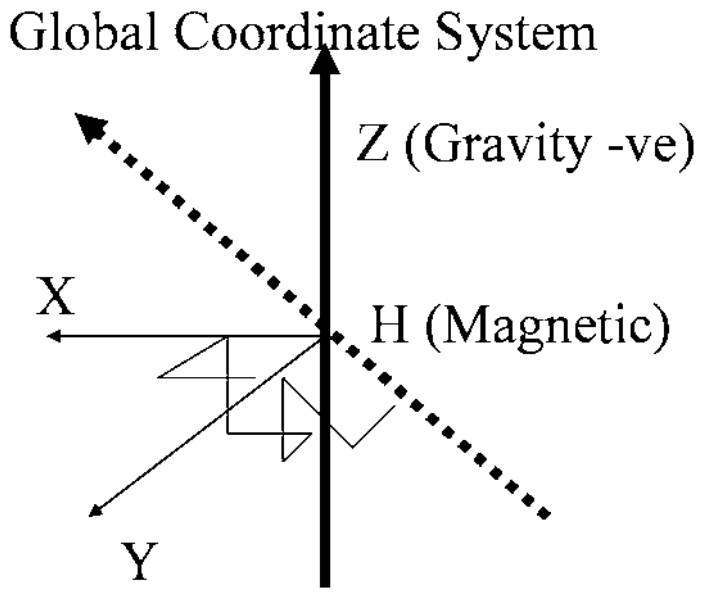

Figure 2.6: The IMU global coordinate system

Obtaining a dynamic estimate of orientation

A second estimate of IMU orientation is obtained by integrating the angular velocity data from the gyroscopes. Quaternion representation of orientation was used to reduce computation and avoid potential errors. More details are provided on the accompanying CD (Brodie, et al., 2008a, 2008d).

In this experiment the pendulum motion started and finished with stationary periods. It was therefore possible to estimate the initial and final orientation of the pendulum as well as the initial and final bias of the gyroscopes. The orientation during periods of motion was found by integrating the gyroscope channels between the static periods.

Bi-directional integration

To ensure that the pendulum motion started and finished in the correct orientation the gyroscope channels were integrated in both the forward and backward direction. The final estimated orientation was a weighted mean of the two continuous estimates. The „true" gyroscope measurements were then found by differentiating the „true" orientation. An estimate of the low frequency gyroscope bias was calculated and then the process iterated until both the forward and backward estimates of orientation converged. Example code is also available on the accompanying CD (see Appendix A).

The video system

The motion of the pendulum was also measured using two Sony DRV-940E camcorders shuttered at 1/500s. The digitising volume was calibrated using the static direct linear transformation procedure in the MaxTRAQ3D software (by Innovision Systems Ltd) that was used to manually digitise the motion of the pendulum. The MaxTRAQ software digitised individual fields giving a temporal resolution of 0.02s (50 pictures per second) and the digitised image was displayed at a resolution of 720x576 pixels.

2.2.2. Method

A wooden pendulum was constructed which rotated about a good quality cylindrical bearing (Figure 2.3). The pendulum was 900 mm long with a 500 mm transverse arm oriented along the axis of rotation. Two IMUs were attached to the pendulum 350 mm and 700 mm from the centre of rotation with the local IMU x-axis oriented along the pendulum shaft. The motion of the pendulum was recorded using two shuttered video cameras and the output of the IMUs was sampled at 100Hz. Two different pendulum conditions were tested:

1. Normal motion in which the pendulum was set in motion by rotation about the X-axis and allowed to come to rest naturally.
2. Stopped motion in which the pendulum rotation about the X-axis was stopped and started abruptly.

Three points on the pendulum, the centre of rotation, the end of the pendulum arm and the end of the transverse arm were tracked in three dimensions using the MaxTRAQ software package. The projected angles of the pendulum motion were calculated from the three digitised points. Pendulum orientation was also determined from the output of the IMUs.

Of the nine possible projected angles only three were required to completely define the pendulum orientation. The three projected angles chosen were equivalent to rotations about the X, Y and Z-axes as defined in the camera global coordinate system. The projected angle about the X-axis contained the majority of the pendulum motion. The projected angle about the Z-axis represented twists about the global vertical (or long axis of the pendulum when stationary) and should have been prevented by the pendulum design.

IMU accuracy was estimated by calculating the root mean square (RMS) difference between the three projected angles obtained from video motion analysis and the three projected angles obtained from the IMUs. The RMS difference between the projected angles of the two IMUs attached at different locations on the pendulum was calculated to estimate algorithm consistency. The Data from the IMUs were processed in two different ways:

1. Using the vendor‟s Kalman filter with the recommended settings; and
2. Using a custom bi-directional fusion integration algorithm.

2.2.3. Results

An example of the normal pendulum motion derived from video analysis is shown below (Figure 2.7). The pendulum swings are expressed in projected angles and rotations about the X, Y and Z axis are represented by blue, green and red lines respectively. The pendulum oscillated about the X-axis with very little motion about the Y or Z-axes.

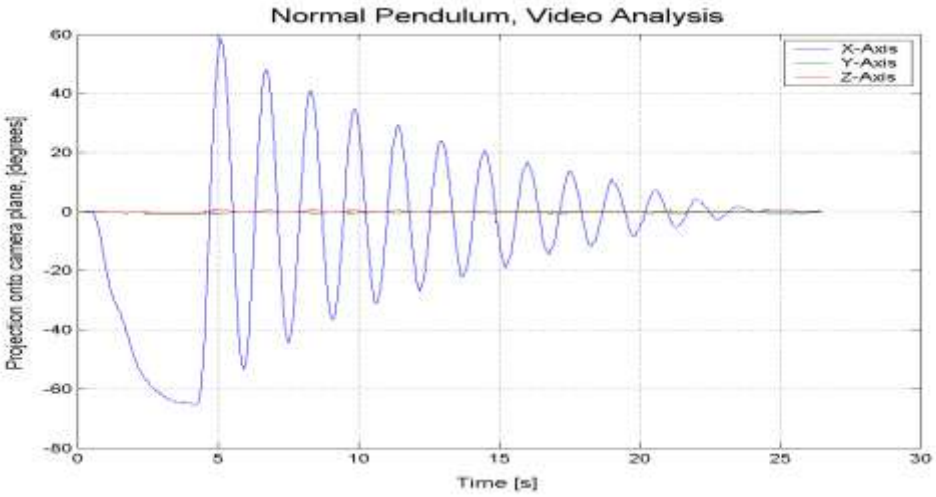

Figure 2.7: Video analysis of normal pendulum motion

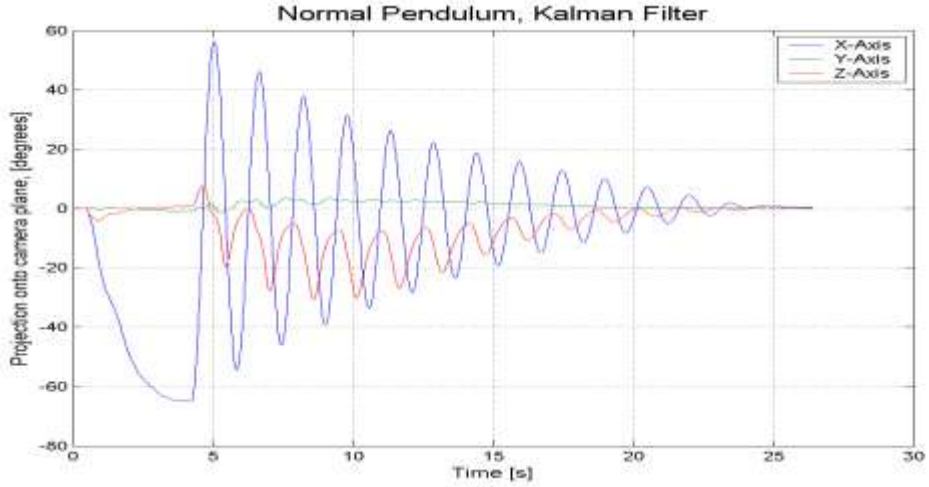

Figure 2.8: Kalman filter algorithm estimation of normal pendulum motion

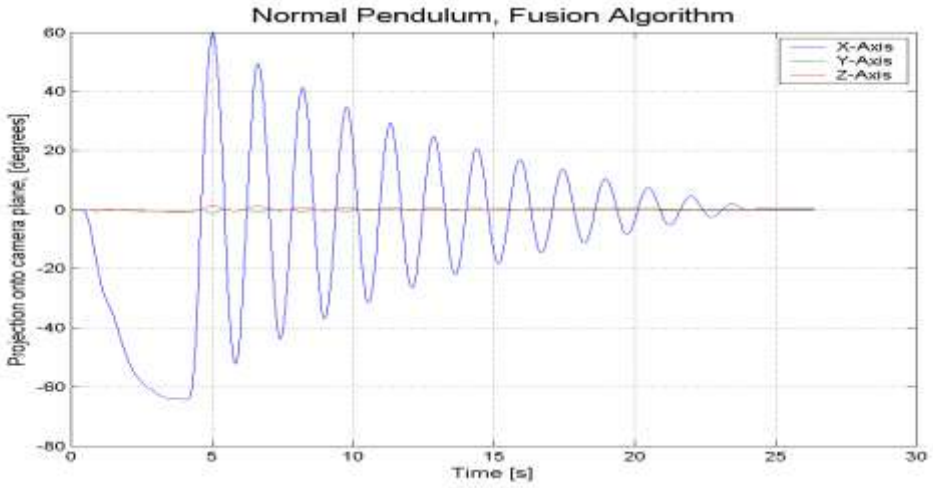

Figure 2.9: Fusion algorithm estimation of normal pendulum motion

The same pendulum swing was measured by IMU using the vendor supplied Kalman filter algorithm (Figure 2.8) and the custom fusion algorithm (Figure 2.9). Figure 2.8 shows the output of the Kalman filter solution contained erroneous motion about the Z-axis, which corresponds to rotations about the long axis of the pendulum when it is hanging at rest. The accuracy of pendulum position orientation using video analysis was estimated by considering the length of the transverse arm. The RMS transverse arm length error was 4mm, which corresponds to an estimated orientation error of <0.5°.

The RMS differences between the IMU estimates of pendulum orientation and the video analysis estimate of orientation are shown below (Table 2.1). The tables illustrate the larger error in the Kalman filter estimate of orientation. Table 2.2 shows the difference in pendulum orientation obtained from IMU1 and IMU2 using both the fusion integration algorithm and the Kalman filter, the lower the RMS difference the better the reliability.

Table 2.1: Accuracy: The RMS error of IMU estimates of orientation. Projected angles obtained from the video analysis are used as a reference.

Test Condition	Fusion IMU 1	Fusion IMU 2	Kalman IMU 1	Kalman IMU 2
Normal Pendulum	0.8º	0.9º	9.8º	11.7º
Stopped Pendulum	0.9º	1.3º	8.5º	8.6º

Table 2.2: Reliability: The RMS difference between estimates of orientation obtained from two IMUs attached to the same pendulum at different locations

Test Condition	Fusion IMU1vs IMU2	Kalman IMU1vs IMU2
Normal Pendulum	0.9º	4.0º
Stopped Pendulum	0.7º	3.3º

2.2.4. Discussion

A pendulum swing was used because it was repeatable and predictable. The cylindrical bearing substantially confined rotation to the X-axis, which was confirmed by the video analysis (Figure 2.7). There were however, small amounts of rotation about both the Y and Z-axes. The pendulum was also chosen because like skiing, it was a continuous movement and therefore, the attached IMU experienced both tangential and centripetal forces.

In a ski race the athlete experiences continuously changing forces while passing through consecutive course gates. Fortuitously, the gates are often spaced symmetrically and so part of

the athlete‟s motion, rotation about his anterioposterior axis, could be simply modelled by the motion of an inverted pendulum. The inverted pendulum is a commonly used model for some types of human motion.

The fusion algorithm performed very well. For test condition 1, the normal pendulum swing, the fusion algorithm output (Figure 2.9) was almost identical to the video output (Figure 2.7). The RMS error in orientation for the fusion algorithm was between 0.8º and 1.3º, which would be good enough for the analysis of alpine ski racing. The vendor‟s Kalman filter did not perform well; the RMS error was between 8.5° and 11.7º, and the peak orientation error was of the order of 30° about the Z-axis, which was significantly larger than the RMS error of 3º specified by the manufacturer. This type of motion capture equipment is relatively new and therefore, no agreed accuracy standard exists.

The fusion algorithm produced very similar results independent of the location of the IMU on the pendulum. The RMS difference was between 0.7º and 0.9º for the two locations on the pendulum (Table 2.2). The Kalman filter solution was less reliable for the two positions on the pendulum, producing significantly different estimations of orientation. The RMS error was between 3.3º and 4.0º.

The vendor‟s algorithm performed poorly for one of two reasons. The first possibility is that, during the periods of motion, the static estimate (Equation 2.1) was used to correct for the low frequency drift of the gyroscopes. The static estimate was biased during the pendulum swings because the centripetal acceleration was always measured along the same local axis of the IMU.

The second possibility is that the vendor‟s algorithm estimated the global acceleration using the method suggested by Luinge (Luinge & Veltink, 2005). This method requires that the orientation is accurately known. If the orientation error accumulates beyond a small threshold the global acceleration may be projected into the wrong axes and error may grow exponentially. Consequently, the threshold for stability may depend on the magnitude of acceleration experienced by the IMU. This would explain why the error decreased over the second half of the motion as the pendulum amplitude decreased (Figure 2.8).

In either case, if the calculation of orientation from the accelerometers and magnetometers data (Equation 2.1) was based on multiple cross products it might have given non-linear results as discussed elsewhere (Brodie, et al., 2008d). Consequently, even if the accelerometer and magnetometer data required to form the static orientation estimate were normally distributed about the true values, the resulting orientation estimate might be biased. The bias would appear worse in parts of the world where the magnetic dip angle was greater and when high accelerations were present. The magnetic dip in the lab is high (60º).

The fusion algorithm was good for short periods of motion (up to 30 seconds) provided there were short stationary periods before and after the action. The algorithm worked because the

orientation of the IMUs in the start and finish positions was the same and hence the magnetic field measured by the IMUs in both positions contained the same bias. In particular, this could be achieved for human motion in the laboratory by making the subject start and finish in the same calibrated position. The algorithm should work for all types of short motion provided the linear range of the sensors is not exceeded. The gyroscopes used in the IMUs have a linear range of $900^{o}s^{-1}$, which seems adequate for most human movements.

The results show it is possible to use small, light-weight and relatively inexpensive IMUs to accurately measure the orientation of body segments during dynamic motion. With such a system it may be possible to measure the biomechanics of alpine skiing with an acceptable degree of accuracy, but further development work is required.

2.3. Static accuracy

The previous pendulum experiment showed it was possible to obtain accurate dynamic measurements of orientation from an IMU. The vendor‟s data processing needs to be stripped away however, and the new system should, if possible, use the raw binary sensor data.

The purpose of the following research was to determine if it is possible to obtain accurate calibrated data from the XSens MT9 IMU raw binary data. Further information is provided on the accompanying CD (Brodie, et al., 2008d).

Raw data from the sensors within the IMUs are converted from binary representation to calibrated data by applying bias, gain, and temperature compensation. The calibrated data contain the acceleration, rate of rotation and magnetic field as measured in each of the three local axes of the IMU. The conversion process minimises any errors due to misalignment of the sensors within the IMU and any temperature effects.

Of particular interest is the performance specification of the unit as a whole. The static accuracy of orientation was reported to be <1.0º, the dynamic accuracy was reported to be 3º RMS, and orthogonality was reported to be 0.1º (XSens, 2004a). These specifications come with the caveat that data must be captured in a homogeneous magnetic environment and accuracy may depend on the type of motion measured. No detail were given about what is an acceptable „type of motion“ and so it appears that the manufacturer, at the time the manual was written, was unsure of what „type of motion“ could be measured accurately.

2.3.1. Method

The experiments were designed to determine the absolute and relative orientation accuracy of an IMU based on the accelerometer and magnetometer channels. The experiments tested:

1. The accuracy of the static orientation measurements.
2. Whether a custom calibration procedure would improve accuracy.
3. The stability of the custom calibration over twenty-two days.

The static calibration rig

A static calibration rig was required to test the accuracy of the IMUs and as part of the custom calibration procedure. A static calibration rig was constructed from non-magnetic material, (Figure 2.10). The rig allowed the IMU to be moved through 24 precisely known 90° rotations. The rig was levelled and the long axis of the rig was aligned with magnetic north or the global X-axis of the IMU coordinate system.

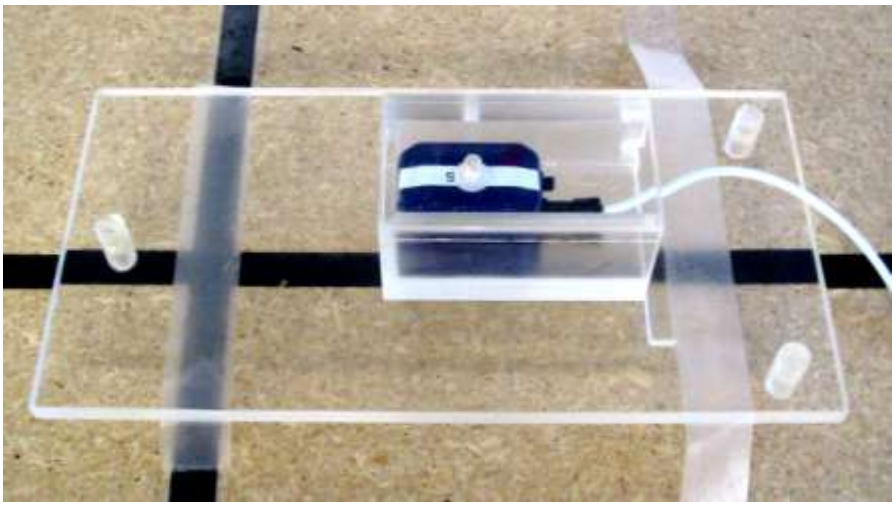

Figure 2.10: The static calibration rig

The Trials

Each trial consisted of the complete set of 24 orthogonal orientations of the sensor in the calibration rig. Each test measurement was separated by a 90 degrees rotation from any other measurement. Before each measurement the IMU was allowed to settle for 1s and then 1s of raw binary data were collected at 100Hz using a MATLAB programme. The raw binary data were converted to calibrated data using both the factory supplied calibration and the custom calibration. The measured calibrated data consisted of three accelerometer channels and three magnetometer channels.

Quaternion representation and error calculation

Quaternion representation was used to calculate the orientation error in terms of the magnitude of the smallest single rotation that separated the measured 3D orientation from the „true" orientation. Details of both quaternion representation and the error calculations are provided on the accompanying CD (Brodie, et al., 2008d).

Statistics

A trial consisted of 24 separate measurements from a single sensor at different orientations as described above. For each trial the root mean square (RMS) error was calculated. Where multiple trials with one or more sensors were grouped for analysis, the RMS values from each individual trial were averaged and reported as the Mean RMS error, representing the average performance over multiple trials for the experimental condition.

Calibration of the IMU raw data

The raw data from the IMU were output as a binary message (called MID50 by the manufacturer) in a specified format (XSens, 2005). The raw binary data were transformed into calibrated floating point data by:

1. Converting the measured binary data to an integer; and
2. applying the appropriate bias, gain, misalignment and temperature compensation.

This was done automatically in the MT9 firmware, (Equation 2.2). The calibration parameters and raw binary data were also accessed directly from each sensor using the XSens binary communication protocol and then used directly in the experiment. A calibration algorithm was supplied with the MT9 software but it only re-calibrated the accelerometer and gyroscope bias and did not significantly improve the accuracy of the IMUs therefore the following custom calibration procedure was developed.

The custom calibration procedure solved for the accelerometer and magnetometer gain **Go**, bias **bo** and misalignment **R**. The IMU was placed in the calibration rig, and 24 known orthogonal orientations were measured. The expected measurements **S**, based on the 24 known calibration rig orientations were compared to the integer signal from each channel **U**. The residual error (from the over determined set of linear equations) was minimised by selecting the appropriate gain, bias and misalignment matrices. For example if the z-axis of the IMU was up in the calibration rig the expected accelerometer vector **S** = [0 0 9.81]′ $m.s^{-2}$ should be obtained from the raw sensor data **U** following application of Equation 2.2.

Equation 2.2 $$\mathbf{S} = \left[\mathbf{Go}(\mathbf{I} + \mathbf{GT}(\mathrm{T} - \mathrm{To}))\mathbf{R}\right]^{-1}\left[\mathbf{U} - \mathbf{bo} - \mathbf{bT}(\mathrm{T} - \mathrm{To})\right]$$

Where **bT** = temperature offset, **GT** = temperature gain, To = reference temperature (35ºC), T = sensor temperature and **I** = 3x3 identity matrix. Equation 2.2 can be reformulated to solve for the gains (**Go**), misalignment (**R**), and bias (**bo**), more details on the calibration procedure and how to calculate the required bias, gains and misalignment are given on the accompanying CD (Brodie, et al., 2008d).

2.3.2. Experiments

Experiments were performed to investigate IMU measurement accuracy, precision, and stability. The experiment presented below investigates the absolute accuracy of IMUs in determining orientation relative to the global reference frame. Further information can be found on the accompanying CD (Brodie, et al., 2008d).

The data from 5 different IMUs (serial numbers MT7315-MT7319) were collected at each of the 24 orthogonal orientations in the global reference system. Measurements of IMU orientation (120 in total) were compared against the known orientation of the IMU in the calibration frame to investigate the magnitude and spread of the error in absolute orientation.

2.3.3. Results

Table 2.3: The absolute accuracy of the IMU sensors, Experiment 1

n = 120 (5*24)	Factory Calibration		Re-Calibrated All Sensors			
	All Sensors	No MT7315	Day1	Day2	Day3	Day22
Mean (RMS º)	6.12	3.01	0.36	0.57	0.78	0.55
Standard deviation (º)	4.50	1.24	0.18	0.36	0.52	0.31
Maximum (º)	21.61	5.23	0.84	1.65	1.97	1.72
Minimum (º)	0.80	0.80	0.07	0.05	0.03	0.02
Component Angles (Mean RMS)						
X-Axis (Roll º)	2.22	0.92	0.06	0.14	0.13	0.16
Y-Axis (Pitch º)	2.18	0.92	0.09	0.15	0.13	0.15
Z-Axis (Yaw º)	5.19	2.68	0.34	0.53	0.76	0.51

Table 2.3, column 1, shows the orientation error of all sensors, it was calculated using the factory calibration to process the raw binary data. Columns 3-6 show the orientation error of all sensors from day 1 to day 22. Columns 3-6 were calculated using the custom calibration, from day 1, to process the raw binary data. The bottom three rows show the total error split into component rotations about the global axes to further understand the sources of the orientation error. Column 2 contains the orientation errors of all the sensors excluding sensor MT7315 based on the factory calibration. Sensor MT7315 was so poorly calibrated it skewed the results in Column 1.

2.3.4. Discussion

The orientation errors from five IMUs were measured (Table 2.3). Excluding sensor MT7315, the RMS error in orientation using the factory calibration was 3º and the maximum error was 5.2º. This is larger than the value published by the manufacturer of less than 1º in static situations. After recalibration of the accelerometers and magnetometers using the proposed method, the mean RMS error dropped to 0.36º and the maximum error dropped to 0.86º. The good results included sensor MT7315 and suggest that frequent recalibration of the accelerometers and magnetometers is required to achieve accurate results with IMUs. It was assumed that Sensor MT7315, using the factory calibration, was a statistical outlier; the poor accuracy was probably not a result of poor factory calibration, but was probably a result of impacts during shipping and handling.

The requirement for periodic recalibration over time was measured by retesting the IMUs 2, 3, and 22 days after the first experiment (Table 2.3). For each test on each day the binary data were processed using the custom calibration from day 1. The maximum error increased from 0.86° on day one (immediately following recalibration) to 1.97° on day three, before dropping to 1.72º on day 22. The RMS error went from 0.36º on day 1 to 0.55º on day 22. The results suggest that the custom calibration was valid for at least 22 days provided the sensor was not subjected to substantial impacts. The error increased slightly from day 1 to day 3, possibly a

consequence of the error (±1º) associated with misalignment of the x-axis of the calibration rig with magnetic north each day.

The orientation error was further broken down into component rotations about the global X, Y, and Z-axes to investigate the error source (bottom rows, Table 2.3). In all cases the major component of error was rotation about the global Z-axis (heading error), which was approximately three times the error about either the X or Y-axes.

From the results it would be easy to erroneously assume that the magnetometers, responsible for heading, were less accurate than the accelerometers. Heading was not however calculated only from the magnetometers, it was calculated from the cross product of the gravity vector and the local y-axis. The local y-axis was calculated as the vector mutually perpendicular to both the gravity vector and the magnetic field vector. The accuracy of the heading therefore depended on the three factors:

1. Data from the accelerometers.
2. Data from the magnetometers.
3. Sufficient angular separation between the magnetic field and the gravity vector to properly define the y-axis.

The results show that even if the sensor orthogonality was as low as claimed (0.1º), the error (up to 5.2º) depended on the non-linear interaction between the magnetometer and accelerometer bias.

In our laboratory the magnetic dip angle is approximately 64º (latitude 41° south) resulting in a 36º separation between the magnetic field vector and the gravity vector. A roll error of 1º therefore may produce an additional error in the heading of approximately 2º. The high angle of dip means that the horizontal component of the Earth‟s field is about 1/3 the total magnitude and so any magnetometer error will have a relatively greater effect on the heading measured in the horizontal plane. The magnetometers are sensitive to small fluctuations in the local magnetic field and these effects will be less significant if the angle of magnetic dip is closer to zero, as it is at lower latitudes.

Information on additional experiments are available on the accompanying CD (Brodie, et al., 2008d). Of particular interest is the „daisy chain effect‟; the order the sensors are connected together affects the magnetometer bias causing additional heading errors of up to 15°.

3. Free Skiing At Coronet Peak 2005

Figure 3.1: The author modelling the FMC system at Coronet Peak. (Photo Emily Ross)

In 2005 field tests were conducted on the motion capture of skiing using inertial measurement units (IMUs) at Coronet Peak Ski Resort. The testing lasted three weeks during which time a new motion capture system was developed and called „Fusion Motion Capture" (FMC). The prototype FMC consisted of a global positional system (GPS) receiver and IMUs attached to the athlete. In this chapter, some selected results from the testing period are presented.

In Chapter 2 the swing of a simple pendulum was successfully captured. To go from the motion of a simple pendulum to motion capture of multiple body segments in an alpine environment is a challenging step. The work in this chapter contributes to the first milestone:

"To accurately capture the motion of alpine ski racing over a complete race course"

In addition, methods are developed that contribute to the third and fourth milestones:

"To analyse complex whole body motion through a large 3D volume"
"To present the analysis in a way intuitive to the athlete"

From this research was produced the first example of 3D motion capture of skiing over a complete ski run (Brodie, Walmsley, & Page, 2005).

3.1. Fusion Motion Capture set up

The fusion motion capture set up included:

1. Five IMUs (MT9 Xsens Technologies), attached the sacrum, each thigh and shank, (Figure 3.2 and Figure 3.3). These were positioned at the same locations as described in the Animating Nancy experiment (Chapter 2, page 25). IMU data were recorded at 100 Hz.
2. A GPS receiver was attached to the subject"s helmet and a stationary GPS base station was set up in the ski area car park, (Figure 3.1). The GPS used was a single frequency L1 unit (SiRFstarIIe/LP chipset) with a reported accuracy of 15m RMS for horizontal position and within $0.1 m.s^{-1}$ 95% of the time for velocity. GPS data were at 1 Hz. Additional GPS chip specifications are available on the accompanying CD (**Appendices/GPS_Manual.pdf**).
3. A handheld computer (IPAQ running Windows CE4.0) and XBus master, to log the data on the athlete
4. A video camera for validation purposes
5. Bluetooth was used to communicate between the XBus and the IPAQ. The GPS receiver was plugged into the IPAQ PCMCIA card slot.

The IMU"s provided the orientation of each limb. The athlete"s global trajectory was measured by fusing the GPS signal with the double integral of the accelerometer signal after the removal of gravity. The resulting data were used to drive the animation of a body model that approximated the subject, based on height and weight. Because only five IMUs were

used, the upper body motion was approximated by the sacrum IMU and the ski motion was approximated by the IMUs attached to the shanks.

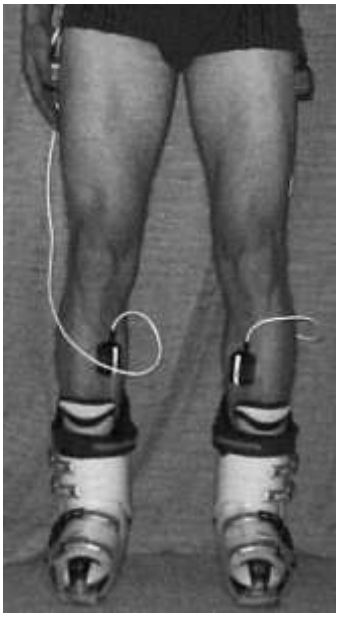

Figure 3.2: IMU placement on the thighs and shanks

Figure 3.3: Posterior view of the sacrum IMU placement between the PSIS

3.2. The FMC algorithm Version One

The calculation process is outlined in Figure 3.4. The algorithm is different from that used for the pendulum experiment in the previous chapter because the motion was longer than 30 seconds and global trajectory was required in addition to orientation.

To measure skiing movements the primary IMU data (in the case of the skiing experiment the sacrum sensor) are fused with the GPS data to get location and orientation. Two iterations are completed. The second iteration includes an estimate of global acceleration that improves the pitch/roll corrections.

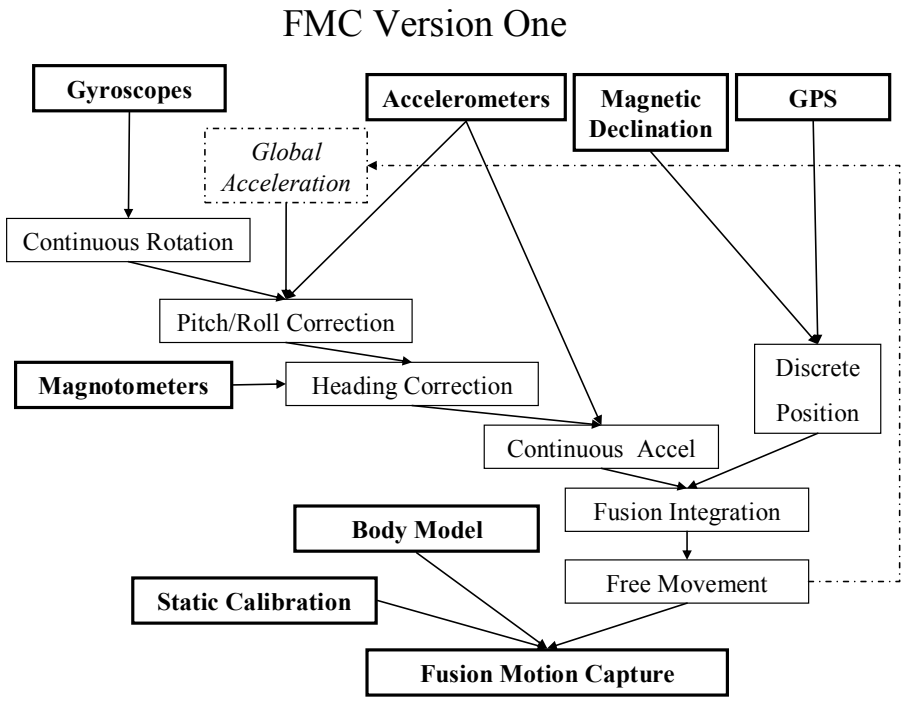

Figure 3.4: FMC Version One - Algorithm Diagram

The FMC – Version One algorithm can be broken down into the following smaller calculation steps:

1. The gyroscope channels are integrated over variable overlapping window lengths to get an orientation estimate.
2. The accelerometers are used to make a pitch and roll correction based on making the average measured global acceleration equal to the average „true" Global Acceleration, over the window of data. If the correction required is larger than the expected gyroscope bias (1°/s) then a larger window of data is used.
3. The magnetometers are used to make a heading correction based on a constant global magnetic field. Once again the window size is increased if the correction is too large.
4. The window of data is progressed and the process is repeated from step 2 until the end of the data set is reached.
5. The global trajectory is then computed by fusion integration, (Brodie, Walmsley, & Page, 2007). The high frequency trajectory is obtained from the IMU and the low frequency trajectory from the GPS.
6. The global trajectory is differentiated to get the global acceleration and the process is repeated in a second iteration.
7. The mean global acceleration is assumed to be equal for all the attached IMUs provided the window of data is long enough. Step 1 to step 4 are repeated for each additional IMU attached to the thighs and shanks.
8. The body model and static calibration data are used to map the IMU movement to the limb movement.

Using a laptop with a 1.5 GHz Celeron M processor, it takes about a minute to process all the data from a complete ski run.

The body model and static calibration

The subject‟s body model was estimated from standard anthropometric measurements of height, weight and limb lengths. The primary position (subject standing, with skis on, upright with arms straight and palms flat against the thighs) was used to calibrate the IMUs. This was done by recording five seconds of stationary data with the subject standing on flat snow. The same process as outlined in the Animating Nancy experiment (Chapter 2, page 25) was used to map the IMUs to each body segment. This still suffered from mapping errors because it was difficult for the subject to match the calibration positions as defined by the body model, in a repeatable way.

Synchronisation of the GPS and IMUs

The GPS receiver provided location information using latitude, longitude and height. Latitude and longitude (measured in degrees minutes and seconds) were converted into a horizontal distance (measured in metres) from the mean location by using trigonometry and an Earth radius of 6373 km.

The GPS location was then rotated about the vertical axis to align it with the IMU coordinate system using the known declination between magnetic north and grid north at Coronet Peak in 2005, (23.7º).

Because the GPS and IMU measurements were recorded independently they had to be synchronised post hoc. The synchronisation was found by minimising the residual error between the GPS and IMU velocity. GPS velocity at 1Hz was linearly interpolated to get GPS velocity at 100 Hz. IMU velocity was found by integrating the global acceleration. Global acceleration ($\mathbf{A}_{\mathbf{Global}}$) was found by rotating the local accelerometer ($\mathbf{A}_{\mathbf{Local}}$) channels to the global coordinate system and removing gravity ($\mathbf{g}$), (Equation 3.1). Where $\mathbf{R}_{\mathbf{LG}}$ is the first estimate of the orientation matrix from the IMU.

Equation 3.1 $$\mathbf{A}_{\mathbf{Global}} = \mathbf{R}_{\mathbf{LG}}\mathbf{A}_{\mathbf{Local}} - \mathbf{g}$$

3.3. Experimental

The subject completed multiple runs on the „Wall Street" trail at Coronet Peak. Five trials started from midway down the run and ended just above the executive car park. Each trial was approximately 300 metres long and consisted of thirty controlled turns down the slope. The snow condition was soft.

In a second experiment an eleven-gate racecourse was erected. The course was surveyed with GPS by skiing slowly through the course and stopping at each gate for five seconds. The course was then raced, both the GPS points of the athlete"s head and the fused trajectory of the athlete"s sacrum were recorded.

3.4. Results and Discussion from a Free Skiing Trial

Unfortunately because of the problems with Bluetooth serial communications and insufficient buffering in the XBus hub, data were lost from all but one run. This should still be considered a success because this is believed to be the first time that the motion of multiple body segments through a complete ski run has been captured.

Video 3.1: Appendices\FMC Video\Coronet Peak 2005.mpg

If the video footage (Video 3.1) is compared to the graphical representation of the athlete"s motion (Figure 3.5 to Figure 3.10) the FMC outputs appear consistent with the true motion.

Colour Coded Force Vector Analysis for skiing

The analysis shows the subject completed thirty turns down a three hundred metre ski slope and reached a peak speed of 50km/h (Figure 3.5, bottom panel). In ski racing athletes are interested in how to ski faster, so it is useful to know where they are accelerating and where they are braking. The data show a general pattern of accelerating between turns and braking at the turn apex (Figure 3.5, top panel). This is confirmed by the colour coded force vector analysis (Figure 3.6).

Colour coded force vector analysis were developed for the purpose of producing an intuitive analysis of complete runs for ski athletes. In the colour coded force vector analysis the continuous line represents the subject"s centre-of-mass trajectory while the coloured vectors represent both the magnitude and direction of the resultant external forces acting on the centre-of-mass. Dark red vectors represent periods of braking, blue for neutral and light green for periods of acceleration. The force vectors are scaled so that five metres equals the subject"s body weight. Examination of Figure 3.6 shows the athlete experienced the highest resultant horizontal forces at the apex of each turn and because the forces are red in colour the net result in addition to turning was to slow the athlete. Generally the athlete accelerated,

defined by the green vectors, between turn apexes, which can be confirmed by his changes in velocity (Figure 3.5, top panel).

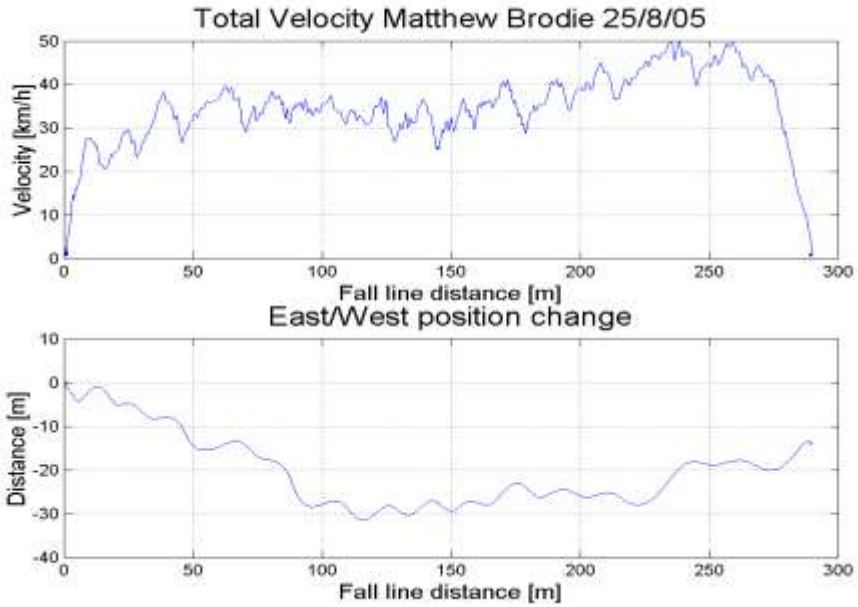

Figure 3.5: Velocity profile and CoM trajectory during the run

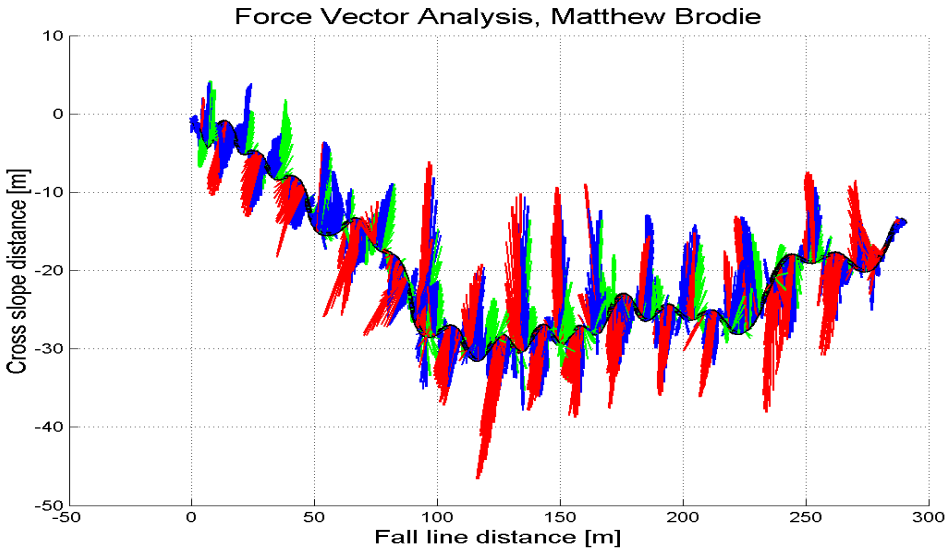

Figure 3.6: Colour Coded Force Vector Analysis

The subject did not always brake at the turn apex. At 50 metres on the fall line, horizontal axes of the figures, the subject completed a turn where there is net acceleration. For further analysis two turns, turns 7 and 8, 50 metres into the run were chosen. Figure 3.6 shows that these two turns are representative of the athlete's performances through the course. The first turn demonstrates braking technique while the second turn demonstrates accelerating technique. A close up inspection of these two turns follows (Figure 3.7 to Figure 3.10).

Data driven animation of skiing

In Figure 3.7 it is noticeable that the upper body appears to be rigid; this is because the orientation of the upper body was driven by the sacrum sensor. This does not affect the results because the skier travelled through a large volume and so his relative limb movements have little effect on the close up of the force vector analysis (Figure 3.8). Figure 3.7 shows that for the fast turn, accelerating forces acting on the athlete built up soon after the apex of the turn (52 m on the horizontal axis) and there was very little braking. In contrast the previous „braking" turn is characterised by more red „braking" forces.

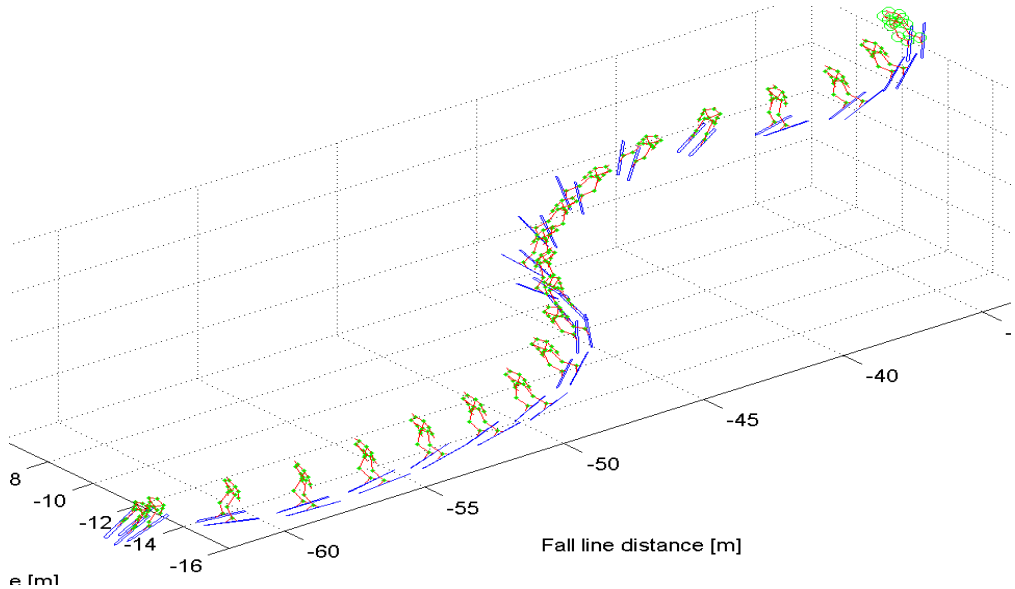

Figure 3.7: Data driven animation, five frames per second for clarity

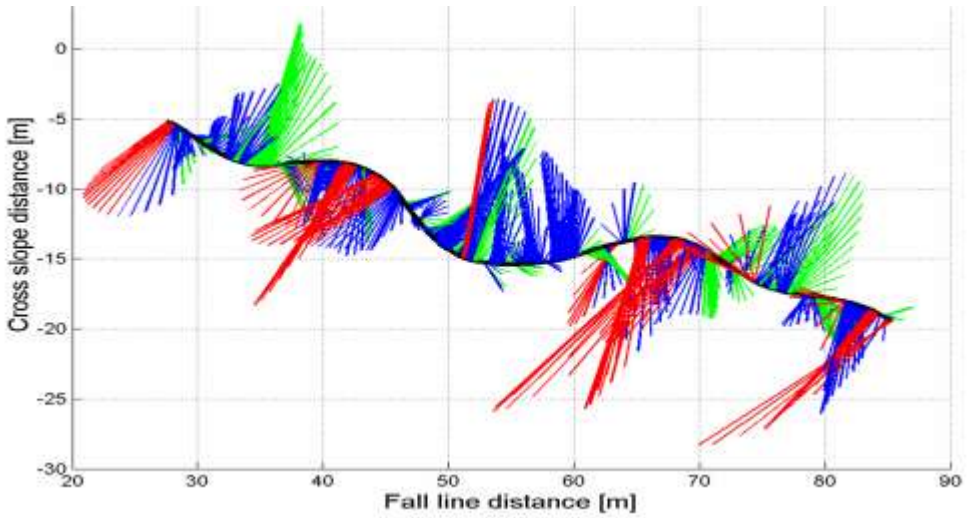

Figure 3.8: Close up of colour coded force vector analysis

One difference between the two turns was athlete stance. It is useful to view the action from a „bird"s eye view". During the accelerating turn the subject"s skis were more in line with the direction of motion than during the braking turn (Figure 3.9). From the side view another

difference between the two turns can be seen (Figure 3.10). From this view the subject‟s centre-of-mass appears behind the perpendicular projection of the subjects‟ boot centre during periods of braking. During periods of acceleration however, the subject‟s centre-of-mass was located more centrally.

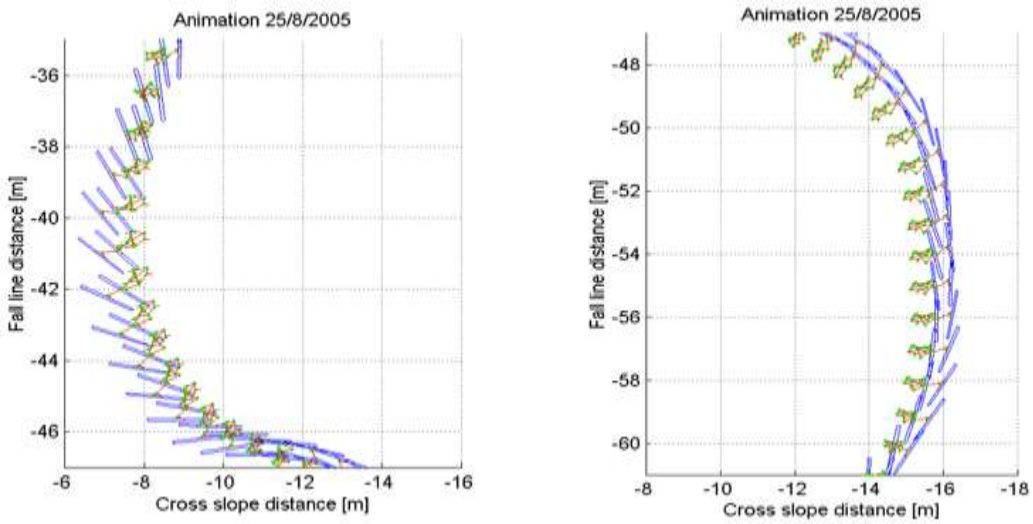

Figure 3.9: Birds eye view of turns. Left side - braking and right side - accelerating

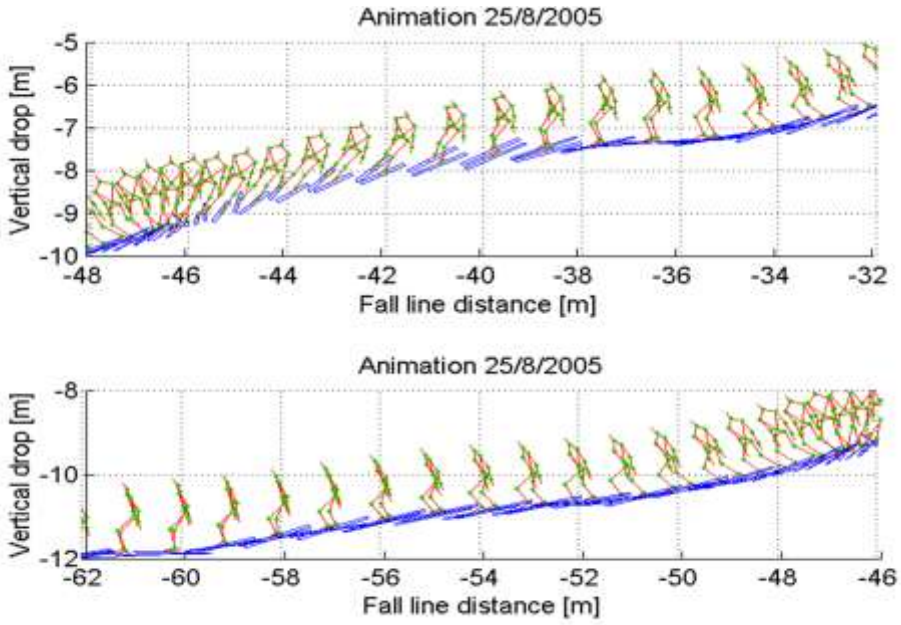

Figure 3.10: Side view of turns. Top panel - braking and bottom panel - accelerating

The analysis demonstrates the power of FMC to distinguish between techniques based on the external forces that ultimately drive acceleration or braking. Having first objectively categorised the athlete‟s performance using forces, velocity and trajectory, it is then possible to look for the underlying causes of the different techniques in terms of local body segment positions and movements.

Validation of GPS accuracy

To investigate the accuracy of the system we erected an eleven gate race course (Figure 3.11). The course was surveyed using just the GPS component of the FMC system. The subject slid slowly through the course stopping for at least five seconds at each gate, (cross markers in Figure 3.11). The approximate gate positions are identified by locations with a high density of GPS measurements. The subject then raced through the course. There was a large difference between the race line (continuous black line) and the surveyed course, indicating that the FMC global trajectory was less accurate than expected. The problem appears to be erroneous GPS measurements when the athlete travelled at speed (red/grey dots), which drifted as a result of systematic errors. At slow speed the GPS survey appears more accurate, because the GPS measured gate positions are symmetrical (containing repeated spacing) and this agrees with the gate set which was symmetrical.

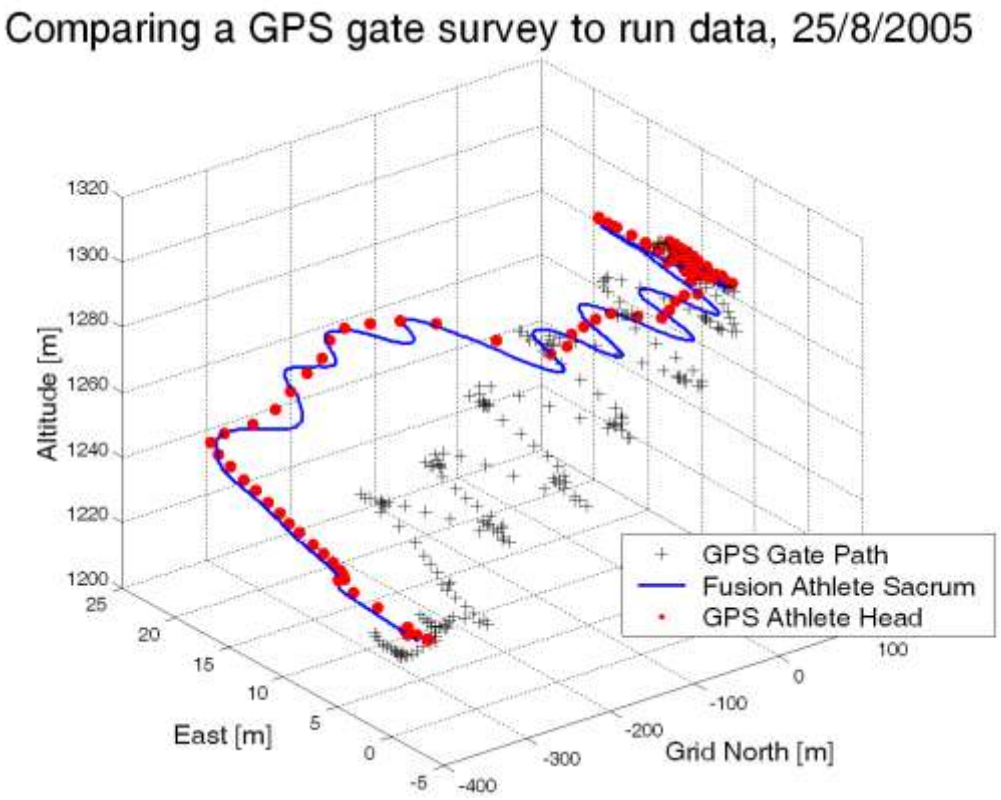

Figure 3.11: Comparing different measurements of a racecourse.

The GPS received error was much greater than the gate spacing of around 15m. The error was also much greater than the specification provided by the vendor of 15m RMS for horizontal position (see the supplementary CD, **Appendices\GPS_Manual.pdf**). It is likely the GPS error resulted from internal smoothing within the GPS chip that assumed relatively constant speed straight line trajectories over flat terrain, but more research is required. A post processing differential correction using the base station location data from the car park was also attempted, but this resulted in increased error as a result of discrepancy between the Kalman filter solutions of both GPS receivers used.

Validation of body segment orientation and visualisations

It was not possible to explicitly validate the on-snow prototype system in order to determine either the accuracy of the each body segment orientations or the accuracy of the data visualisations. It was not possible because as discussed in Chapter 1, no „gold standard" exists to capture the motion of alpine skiing. The tests done in Chapter 2, showed that dynamic orientation measurements with high accuracy (<2º RMS) using IMUs were possible. The validation is therefore subjective. The power of the subjective validation is however enhanced by several factors including, the process in which the animations were derived, the sensitive nature of the skis as a consequence of their long length to small errors in orientation, and the large data set with multiple turns available for comparison.

Subjectively, the body segment orientations visualised in Figure 3.7 to Figure 3.9 look plausible when compared to the video data (Video 3.1). In defining "plausible" the motion of uniaxial joints such as the knee were examined for off axis bending. The motion was examined for improbable artefacts such as the body segments moving through each other and the skis crossing. In skiing the motion and orientation of each ski is generally similar because the snow surface between the skis can be approximated by a flat plane connecting the skis. The ski orientations especially pitch and roll should therefore be similar throughout a ski run. No unusual artefacts were observed in visualisation of the data sets.

The skis are most sensitive to error because of their length. A 5º error in ski orientation measurement would cause ski tip to be displaced around 80mm and would be expected to manifest itself in some visual artefact such as the skis crossing. The skis are subjected to the highest vibrations. Skis are the most distal segment in the visualisation of IMU data as discussed in Chapter 2. Ski position is calculated from a chain of measurements and therefore contains the most error. The FMC visualisation of the ski motion looked both plausible and similar to the hand held video camera data and so the accuracy of the body segment orientation measured by the IMUs was estimated to be less than 5º and considered to be a good step towards satisfying the first thesis milestone.

"To accurately capture the motion of alpine ski racing over a complete race course"

Unlike video, where visual appearance is the primary measurement, in FMC the primary measurement is from accelerometers and gyroscopes. Body segment orientation is mainly derived from integration of the gyroscope data and location is mainly derived from either a fixed proximal joint centre or double integration of the accelerometer data. The least accurate parameter is therefore visual appearance. If visualisation of FMC data is free from visual artefacts when compared to independent video data then the underlying raw acceleration and angular velocity data should be accurate enough to have value in further analyses. Previous research demonstrates that the same argument can not be extended to the validation of traditional optical based motion capture systems. Even though the visual appearance of video data and optical motion capture data inherently look similar, as a result of the similar method of data capture, it does not mean the derived rate and acceleration data from optical motion capture are accurate. Without data smoothing Nachbauer reported large oscillating

acceleration errors of magnitude 10,000 m/s^2 (Nachbauer, et al., 1996). This discussion has highlighted the differences between the inherent properties of FMC data and the properties of optical motion capture data.

Other problems with the prototype FMC system

Other issues with the FMC system at Coronet Peak included:

1. No exact body model existed. The local limb movements were based on the assumption that the body model was accurate and the calibration position was able to be repeated by the subject.
2. Only five sensors were used, the full body model will require at least 15 IMUs to measure the individual body segment motion.
3. The kinetics and net joint torques of the lower limbs could not be determined because skiing is predominantly dual stance.
4. It was difficult to post synchronise the GPS and IMU data.
5. Bluetooth proved unreliable for communicating with the Xbus, (IMU hub) with on average 4 out of 5 data sets corrupted.
6. There was no guarantee that the magnetic field was homogeneous over the ski area, or that the local magnetic effects of the athlete"s equipment did not biased the results.

The FMC algorithm, version one (Figure 3.4) also had some theoretical issues. Because the magnetic dip is approximately 64º, any roll error that has accumulated from the gyroscope bias will subsequently cause twice the heading error when the magnetometers are used in the correction as previously discussed in Chapter 2, page 39. The pitch and roll error were corrected first using the accelerometer channels. If there was a heading error and horizontal global acceleration was present, then the roll correction might end up causing a pitch error and instead of reducing orientation error might increase it. The solution would be to apply both corrections simultaneously, but when the static estimate of orientation was used to do this, similar to the method previously discussed (Chapter 2, page 30) the errors were much larger than the results presented here.

4. Fusion Motion Capture Development

Figure 4.1: The Wand, three balls and an IMU located at the T-junction

The prototype FMC system was introduced in Chapter 3 and for the first time it became practical to capture the motion of an athlete skiing through a complete ski run. Several issues were raised during the experiments using the prototype system. In this chapter the FMC system is developed further by addressing four important issues:

1. Validation of system performance when alternative field measurements of alpine skiing are practically difficult to obtain.
2. Development of a more robust FMC algorithm that does not rely on the global magnetic field being constant or there being no local magnetic disturbances.
3. Improvement of the accuracy of the athlete‟s body model.
4. Mapping the inertial measurement units (IMUs) to the athlete‟s body segments using a repeatable procedure.

The first two issues are addressed by the experiments in Sections 4.1 and 4.2. The prototype FMC system is compared to a video motion analysis (VMA) system in an indoor trial.

The remaining two issues are addressed by the experiments in Section 4.3, where a 3D anthropometric frame is developed and used to measure the athlete. The frame data is tested against standard anthropometric measurements of limb length and the data are used to provide the IMU to body segment calibration.

4.1. Orientation accuracy of free movement

In Chapter 2 on page 27, it was established with the pendulum experiment that IMUs are capable of accurate orientation measurements. In Chapter 3 a prototype Fusion Motion Capture (FMC) system was used to successfully track a skier at Coronet Peak but some problems with accuracy and reliability were uncovered. In this section both the vendor supplied Kalman filter and the bi-directional fusion algorithm developed in Chapter 2 for the pendulum swing, are validated against a video motion analysis (VMA) system. The orientation of a wand moving freely through space is measured using all three systems. The video analysis system is assumed to be most reliable and accurate and is used to validate the IMU based motion capture systems.

This experiment is an extension of the pendulum swing experiment. The pendulum was constrained to a single axis of movement, but the wand movements are unconstrained, they take place over long durations and the period of the movement is similar to that period of gate passing in ski racing.

4.1.1. Method

The Wand

The orientation of a wand was tracked using an IMU and a MaxTRAQ two-camera VMA system. The T-shaped white aluminium wand had three black polystyrene balls and an IMU

attached to it (Figure 4.1). The balls were used as markers to be tracked by the VMA system as they were moved through 3D space. Because the balls were non-collinear, it was possible to obtain the orientation of the wand. The length of the wand cross bar, marker centre to marker centre was 60.4 cm, and the distance from the T-intersection to the 3rd ball was 30.1 cm. The IMU was attached at the T-intersection and its local axes were visually aligned to the local wand axes. The local axes of the wand are shown in Figure 4.2.

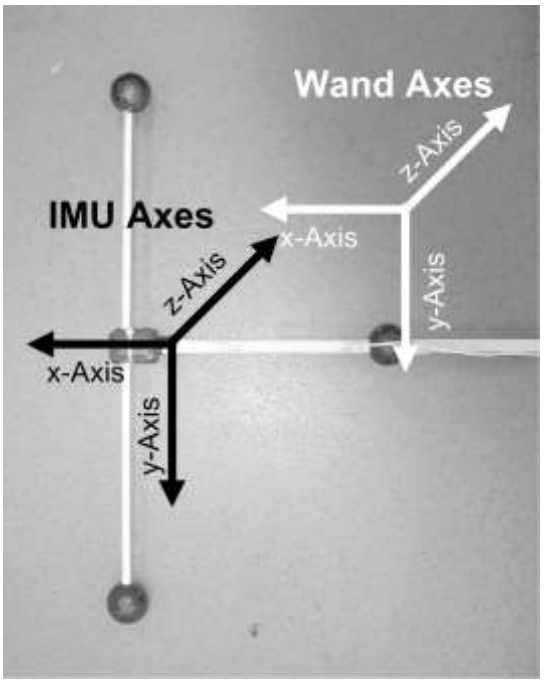

Figure 4.2: The wand, markers, and IMU with local axes shown

Differences between IMU and VMA estimates of orientation

To calculate the difference in measurements of orientation between the IMU and VMA measurements (θ_{VF}), the orientation measurements were first converted into quaternion form.

Quaternion representation of orientation has four components, one real and three imaginary, in vector form. The imaginary parts contain the x,y, and z components of a unit vector (**U**) while the real part of the quaternion defines a rotation (θ) about a vector (**U**, Equation 4.1).

Equation 4.1 $$\mathbf{Q} = \left[\cos(\theta/2) \quad Ux\sin(\theta/2) \quad Uy\sin(\theta/2) \quad Uz\sin(\theta/2)\right]$$

Equation 4.2 $$\mathbf{Q_{VF}} = \mathbf{Q_V}^{-1} * \mathbf{Q_F}$$

Equation 4.3 $$\theta_{VF} = 2 * \cos^{-1}\mathbf{Q_{VF}}(1)$$

The difference between the VMA and IMU orientation, $\mathbf{Q_{VF}}$, was calculated by „quaternion multiplication" of the inverse of $\mathbf{Q_V}$ by $\mathbf{Q_F}$, (Equation 4.2). Where $\mathbf{Q_V}$ and $\mathbf{Q_F}$ are the VMA and IMU measurements of orientation respectively. From the real element $\mathbf{Q_{VF}}(1)$, the smallest angle between the two quaternions was calculated (θ_{VF}, Equation 4.3). The VMA

measurements were initially assumed to contain no error and so θ_{VF} was assumed to be a good estimate of the IMU orientation error.

IMU to Wand Calibration

Although the IMU local axes were visually aligned to the wand axes, this did not account for the fact the IMU housing was not aligned with the internal sensors, and so a constant calibration matrix was used to map the IMU local axes to the wand local axes. The calibration matrix was defined by the mean angular separation between the FMC orientation and the VMA orientation over a 5-second trial, which resulted in a constant rotation of <2° that was applied to all results.

Experimental

Ten trials were completed ranging in duration from 5 to 120 seconds. Two test conditions were used:

1. The vendor supplied Kalman filter with recommend settings
2. The bi-directional fusion algorithm previously described (Chapter 2)

In each trial the wand was moved continuously through a volume measuring approximately 2m by 2m by 1m. Rapid direction changes such as might be experienced in slalom skiing were used.

4.1.2. Results and discussion

The resulting root mean square (RMS) differences from ten trials are shown in Figure 4.3. The estimated RMS difference in orientation between the VMA and the IMU motion capture systems (test conditions #1 and #2) was between 1.8° and 12.9°. Neither the vendor‟s Kalman filter nor the bi-directional fusion algorithms were accurate for long duration measurements.

Figure 4.3 shows the vendor‟s Kalman filter failed to report orientation accurately even for the short five-second trial (RMS difference approximately 6°). The bi-directional fusion algorithm was robust, displaying a relatively constant error of less than 3° RMS for trials of up to 50 seconds in duration.

Figure 4.3: The difference between VMA and IMU motion capture over ten trials

An orientation accuracy of less than 3° RMS should be suitable for skiing because it is less than that reported for some optical motion capture systems in a laboratory situation, as discussed in Chapter 1 on page 7. Even though the on-snow measurements in this thesis will probably be less than 50 seconds duration the results are still unsatisfactory for two reasons:

1. Ski races last longer than 50 seconds.
2. The bi-directional algorithm maximum measurement time, while maintaining accuracy, may depend on the type of movement. For some body segments, especially the ski/boot/foot segment undergoing high vibrations, the actual robust measurement time may reduce.

A better fusion algorithm is therefore required.

4.2. Free movement algorithm and accuracy

In Section 4.1 it was established that neither the IMU vendor's Kalman filter nor the bi-directional fusion algorithms were accurate enough to measure orientation during a complete ski race. In Chapter 3 a prototype Fusion Motion Capture (FMC) system was developed that combined global positioning system (GPS) and IMU data in order to track a skier at Coronet Peak. Several problems with the prototype system accuracy were also reported. In this chapter the development of the FMC algorithm is therefore continued and the FMC algorithm is validated against VMA measurements using the wand described in the previous section. The main purpose of this section is to improve the accuracy and reliability of FMC; this is achieved by the implementation of a new free movement fusion algorithm that combines GPS and IMU data.

Combining GPS and IMU data for accurate navigation is a well-established method (Brown, 2005; Broxmeyer, 1964), but its application to motion capture and biomechanical analysis of athletic performances was new and difficult to assess. A method was required to assess the quality of the FMC derived trajectory and orientation of an object undergoing free movement in a controlled laboratory environment.

Free movement is defined by 6 degrees of freedom (d-o-f); 3 d-o-f to describe the global X, Y, and Z-axes location of a body segment and 3 d-o-f to describe the orientation of the segment (eg roll, pitch, and yaw). Unfortunately, there appears to be no practical way to test the accuracy of the system for skiing directly because the spaces traversed are very large. Also, segment markers used for video tracking would not stay attached with an aggressive race strategy, and video auto-tracking algorithms do not work well under direct sunlight with a largely white background.

In order to objectively measure the accuracy of FMC the measurement of free movement in a laboratory setting is compared to a video motion analysis (VMA) system. The motion of a T-shaped wand, which represents the free motion of a single body segment, was tracked using both a video system and the FMC system. Because there was no GPS signal indoors, some additional data from the VMA system were substituted for GPS data that would normally be used in the fusion algorithm outdoors.

4.2.1. FMC algorithm Version Two

The free movement of body segments in global space was obtained from the fusion algorithm outlined in Figure 4.4.

In Figure 4.4 the new fusion algorithm solves for the global trajectory and orientation of the IMU over extended periods of time. Figure 4.4 illustrates the process used when GPS data are available. Estimates of discrete orientation and continuous rotation are derived from the IMU gyroscopes, accelerometers and magnetometers. In Figure 4.4 the [Bi-directional Fusion 1] process is the bi-directional fusion algorithm used for the pendulum experiment in Chapter 2.

In Figure 4.4 the [Orientation Fusion 2] process reduces the orientation error by minimising the residual between the continuous acceleration derived from the IMU data and the discrete acceleration derived by differentiation of the GPS velocity data. A rotational correction is applied to the IMU data over successive windows of data. The windows of data are long enough to ensure there is sufficient angular separation between the discrete GPS acceleration vectors, yet short enough so that a single orientation correction will account adequately for most of the changing accumulated integration errors.

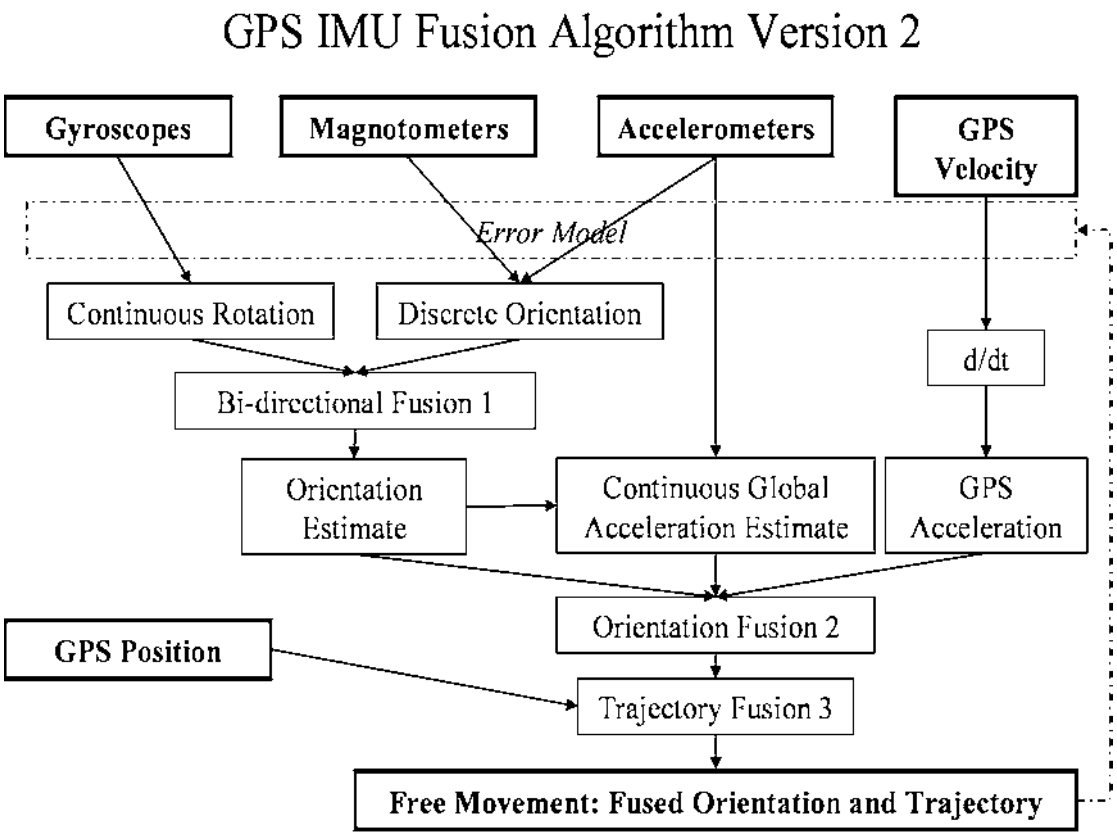

Figure 4.4: The FMC algorithm Version Two

In Figure 4.4 the [Trajectory Fusion 3] process combines two independent estimates of trajectory to give a final global trajectory. Discrete estimates of velocity and location are obtained from the differentially corrected GPS receiver raw data. The resulting GPS measurements of location and velocity are noisy but should have long-term accuracy (over a long enough time period the mean value should coverage to the true mean location and velocity). Continuous global velocity and location estimates are obtained by integration of the IMU based global acceleration. They are subject to integration drift as a result of both orientation error and accelerometer gain and bias errors, but are accurate in the short term. The „fused" translation movement is derived by combining the long term accuracy of the GPS velocity and location with the short term accuracy of the continuous estimates of velocity and location. An example output for vertical velocity after the [Trajectory Fusion 3] process is illustrated in Figure 4.5, the circles are simulated GPS velocity, the green/grey line is the integrated IMU acceleration and the black line is the fused velocity estimate. The [Trajectory Fusion 3] process is similar to the fusion integration process used to determine centre-of-mass (CoM) from a force platform (Brodie, et al., 2007).

Combining Different Coordinate Systems

The first estimation of orientation [Bi-directional Fusion 1] was based on the magnetic coordinate system described in Chapter 2. In the magnetic coordinate system, the global Z-axis is vertical while the X-axis points to magnetic north. The video system used the same global Z-axis but an arbitrary X-axis convenient for the laboratory layout. The substitute GPS

measurements (from the VMA system) were already in the VMA coordinate system and so the second part of the FMC algorithm [Orientation Fusion 2] rotated the IMU measurements into the VMA coordinate system automatically. The average angle between magnetic north and the VMA global X-axis was 14.5°, but the magnetic field appeared to be quite variable in our laboratory.

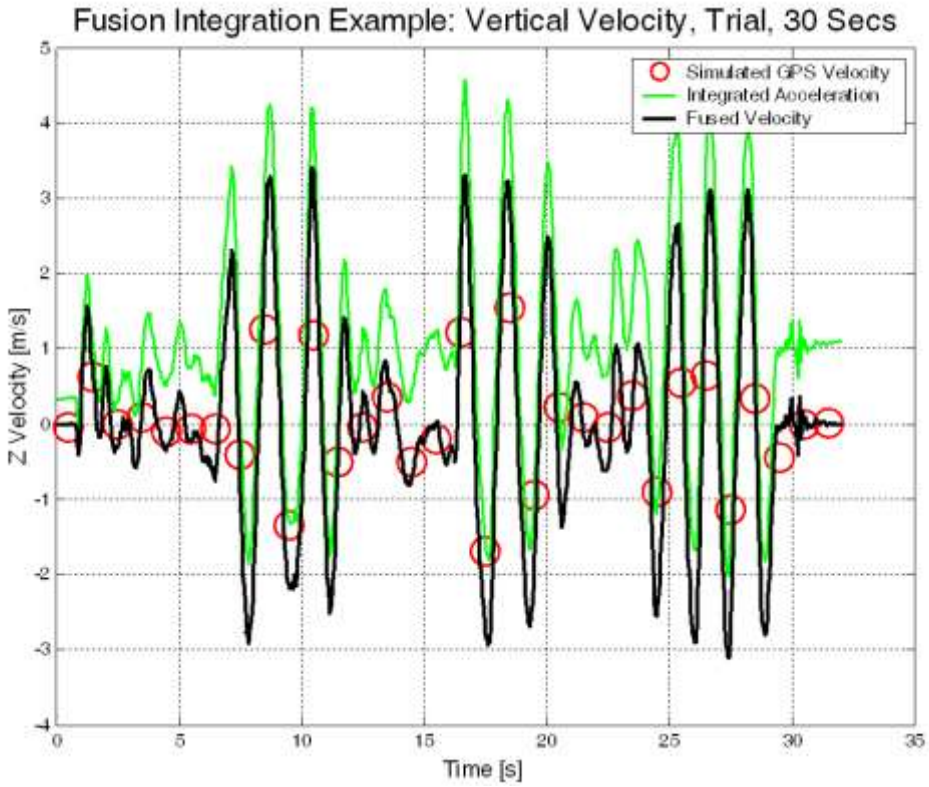

Figure 4.5: Fusion Integration estimation of vertical velocity

4.2.2. Method

The free movement of a wand was tracked using FMC and a MaxTRAQ two-camera VMA system. The same wand from Section 4.1 was used, but in addition the IMU was also tracked directly by the VMA system.

The FMC algorithm was implemented in MATLAB. The mean location and velocity of the wand T-intersection over each second (calculated from the MaxTRAQ VMA system data) was used as a substitute for the GPS data normally used outdoors. Suitably scaled Gaussian noise was added to the VMA location and velocity data. Because ski racers travel over 200m at about 20m.s^{-1}, compared with the wand moving 2m at speeds of about 2m.s^{-1} in the laboratory experiment, the standard deviation of the noise was scaled from <0.1m.s^{-1} and 15m, for velocity and location (from the GPS specifications of our receiver), to 0.01m.s^{-1} and 0.15m respectively. The scaling ensured the effect of the noise on the laboratory motion was similar to the effect of noise on skiing motion.

Experimental

Ten trials were completed ranging in duration from 5 to 120 seconds. Data from three conditions are presented in the results:

1. Video Internal Error - The estimated internal error of the VMA system based on the known distance between the marker balls of the wand.
2. FMC+VMA - The calculated the difference between VMA and FMC orientation and location. The mean location and velocity of the IMU over each second derived from the VMA system was input into the FMC algorithm as substitute GPS data.
3. „FMC+VMA+Noise - The calculated the difference between VMA and FMC orientation and location. Noise was added to the VMA data before being input into the FMC algorithm, which ensured it was a good substitute for GPS data.

In each trial the wand was moved continuously through a volume measuring approximately 2m by 2m by 1m. The movement exhibited rapid direction and orientation changes such as might be experienced in slalom skiing. The example trial in Figure 4.6 shows the wand location and orientation at 0.5s intervals from both VMA (blue) and FMC (red); there is no discernable difference between them. The example trial is also available as a video (Video 4.1).

Video 4.1: Appendices\FMC Video\Wand.avi

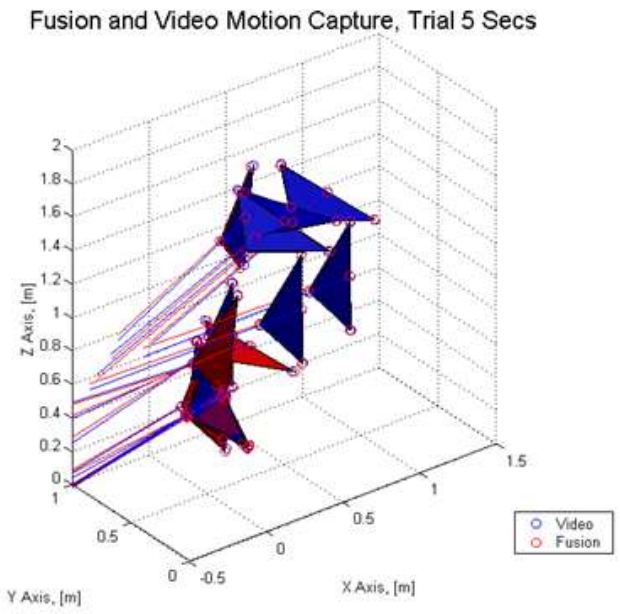

Figure 4.6: Experimental set up, the wand was moved through free space.

VMA system error

The internal location error in the VMA system was estimated by comparing the known distances between the black marker balls with the measured distances. Two location errors in the local orthogonal axes in the plane of the wand were calculated, Equation 4.4 and Equation 4.5. The third orthogonal axis error (E_3) was assumed to be the mean of the two

calculated errors, (E_1 and E_2). The location error was obtained from the error in each axis of movement using Equation 4.6.

Equation 4.4 $$E_1 = \left|marker_1 - marker_2\right| - 60.4$$

Equation 4.5 $$E_2 = \left|marker_3 - calculated\_T\_intersection\right| - 30.1$$

Equation 4.6 $$E_{Location} = \sqrt{\left(E_1^2 + E_2^2 + E_3^2\right)}$$

The internal orientation error of the VMA system was estimated from the arctangent of the ratio between the marker separation and location error, Equation 4.7 and Equation 4.8. The third orthogonal error ($E\theta_3$) was assumed to be the mean of the two calculated errors, ($E\theta_1$ and $E\theta_2$). The orientation error was obtained from the orientation error about each axis of movement using Equation 4.9.

Equation 4.7 $$E\theta_1 = arctan\left(\frac{E_1}{60.4}\right)$$

Equation 4.8 $$E\theta_2 = arctan\left(\frac{E_2}{30.1}\right)$$

Equation 4.9 $$E_{Orientation} = \sqrt{\left(E\theta_1^2 + E\theta_2^2 + E\theta_3^2\right)}$$

4.2.3. Results and discussion

The internal error of the VMA system, estimated from the known geometry of the wand and the RMS differences between VMA and FMC estimates of orientation and location for the ten trials are shown in Figure 4.7 and Figure 4.8.

The estimated root mean square (RMS) difference in orientation between the VMA and FMC systems was between 1.8° and 2.6°, which was similar to the estimated error range for the VMA system of 1.2º to 3.1º (Figure 4.7). The FMC measurement of wand orientation appeared robust because neither the addition of noise to the substituted GPS inputs nor increased measurement duration increased the RMS difference.

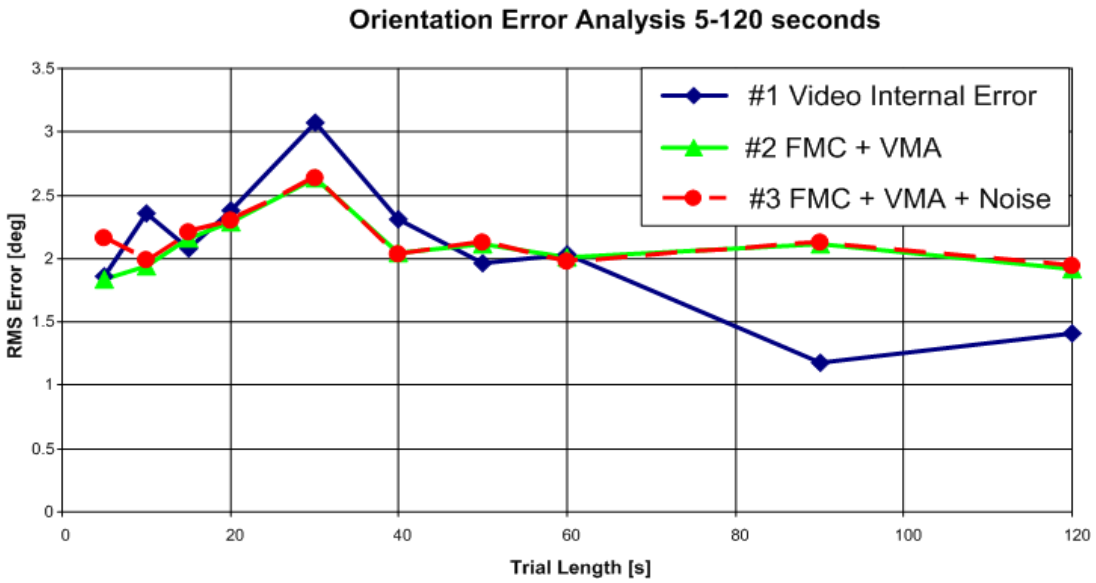

Figure 4.7: VMA Orientation Error and difference between VMA and FMC over trials

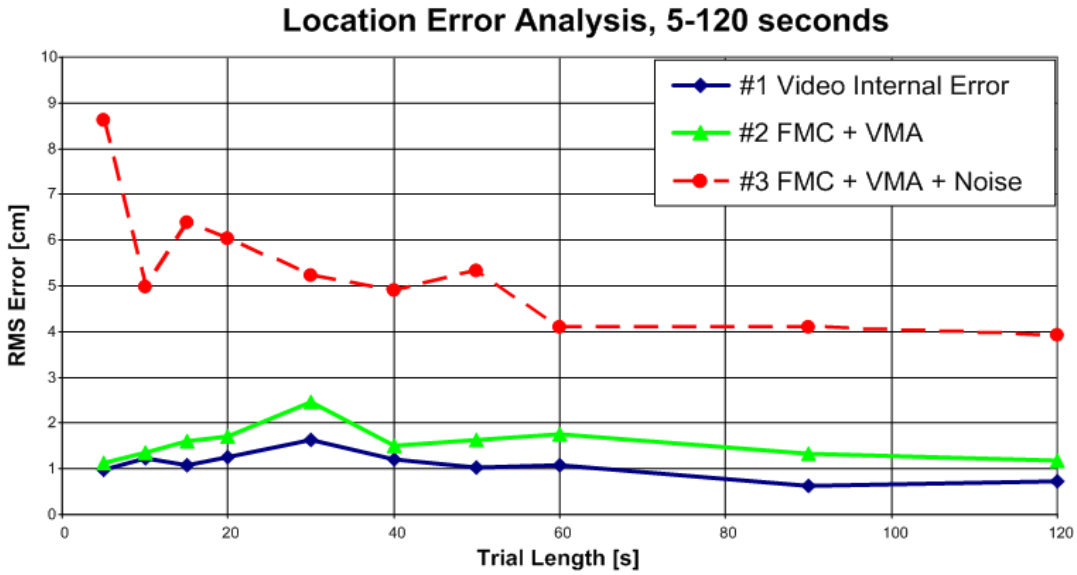

Figure 4.8: VMA Location Error and difference between VMA and FMC over trials

The RMS difference in location between the VMA and FMC systems ranged from 1.1cm to 2.5cm but was much more susceptible to noise in the substituted GPS data. In the presence of scaled Gaussian noise the RMS difference in location between the VMA and FMC systems ranged between 3.9cm and 8.6cm over the ten trials with a trend for difference in location to reduce as measurement duration increased (Figure 4.8). This was expected because, when discrete location measurements (such as GPS) contain noise, more points are required to obtain an accurate location.

The FMC algorithm performed at a similar level of accuracy to the VMA system, for both orientation and location. FMC has additional advantages, it may be used in motion capture tasks where camera based systems are not practical. FMC also has other advantages in some situations where, as part of a biomechanical analysis of movement, joint forces and torques

are important. Forces and torques are often derived from linear and angular segment acceleration and our IMUs contain accelerometers and gyroscopes that measure acceleration and angular velocity directly. The direct IMU measurement of acceleration and angular velocity removes the need for numerical differentiation processes that introduce noise.

In contrast, body segment angular velocity from VMA systems is derived from successive estimates of orientation, which in turn are derived from location measurements of three or more markers attached to body segments. As a result, the VMA measurement of angular velocity is likely to contain higher levels of noise compared with the IMU measurement of angular velocity

In Figure 4.9 the differences between VMA and FMC measurements of angular velocity are clearly visible. The VMA estimate of angular velocity contained more noise. The VMA estimate of angular velocity contained an estimated 13°.s^{-1} RMS of noise, which was 26% of the measured RMS angular velocity (50°.s^{-1}) during the trial.

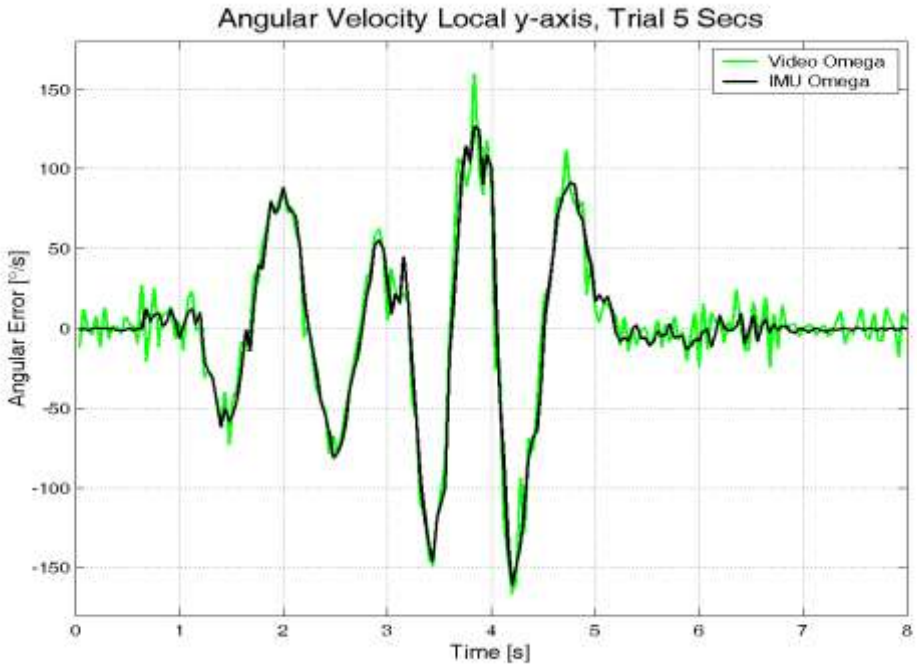

Figure 4.9: Local y-axis angular velocity of the wand (VMA) and the IMU gyroscope

Figure 4.9 shows a high level of noise in the VMA measurement of angular velocity. It is standard practise to use a low pass filter to reduce this type of VMA noise, but if this is done, then the high frequency components of the movement, especially during impacts, might be lost. A much better measurement of angular velocity is obtained directly from the IMU without additional filtering. As a consequence, estimates of angular acceleration from FMC measurements of angular velocity preserve more of the high frequency components of the motion because only a single numerical differentiation with minimal smoothing is required. In addition, because IMUs measure local linear acceleration directly, most of the high frequency components of linear motion are preserved when calculating net joint forces and torques.

So how might the fusion algorithm perform on the ski slope? The VMA and FMC spatial trajectory errors (around 0.04m) for the wand were made semi independent by the addition of scaled Gaussian distributed noise (0.15m for location). On the snow, if the GPS has a specified RMS error of 15m, FMC might locate the skier on the slope with a RMS error of 4m. If this level of error is unacceptable, it might be reduced further by starting the athlete from a known surveyed point on the slope, or using more accurate GPS modules.

On snow, errors in FMC measurements of orientation and heading should not increase significantly relative to the wand results because the accurate GPS velocity (calculated from the Doppler shift) is used as an input to the FMC algorithm. However because the wand movements in the laboratory were smooth, the effects of impacts or high frequency vibrations experienced while skiing are unknown. It is possible that the low frequency components of ski orientation measurements taken while chattering over an icy course will be less accurate than the low frequency components of the athlete‟s helmet orientation. FMC should however measure the high frequency components, within the linear range of the internal sensors, equally well in both cases.

4.3. 3D anthropometry and the Biomechanical Man

In FMC the motion of IMUs is used to drive a body model of the subject. In the previous section it was shown that it was possible to obtain accurate orientation and trajectory data from an IMU undergoing rapid direction changes such as might be experienced during skiing. If the IMUs cannot however be mapped accurately to the segments of the body model and/or the body model is not an accurate representation of the athlete, then accurate motion capture is still impossible. This section presents a method to construct an athlete specific body model, and then uses a ski specific reference position to map the IMUs to body model.

The orientation of the IMU is generally not the same as the orientation of the body segment to which it is attached. If soft tissue artefacts can be minimised then a constant rotation „maps“ the IMUs to the different body segments to which they are attached and a close approximation to the true limb orientation is possible. This mapping is described by a 3x3 rotation matrix. If the calibration is poor, all subsequent measurements will be poor. For accurate biomechanical analysis of skiing it is important to develop an accurate method to both define the athlete‟s body model and „map“ the IMUs to the individual body segments.

The body model contains information about body segment lengths, orientation in the reference position, and segment inertial properties such as, mass, location of segment centre-of-mass, and the inertia tensor. The body model is based on the body model proposed by Dumas and Reed (Dumas, Cheze, & Verriest, 2007; Reed, Manary, & Schneider, 1999). The model was selected because it defines the limb segments by using the known location of the joint centres in 3D space. The joint centres are defined from bony landmarks also measured in 3D space, which is useful because the locations of the joint centres are also very important for

driving the model with the IMU data. Further information is provided on the accompanying CD (Brodie, Walmsley, & Page, 2006a, 2006b; Brodie, et al., 2008b).

Figure 4.10: The 3D anthropometric frame Version One

4.3.1. Method

3D frame construction and development

A 3D anthropometric frame was constructed (Figure 4.10 and Figure 4.11). The entire frame was made from non-magnetic materials (aluminium, wood and plastic) as any distortion to the earth's magnetic field reduces the accuracy of the IMU to body segment calibration. The frame was designed to hold an athlete in a repeatable reference position while the measurement arms were used to measure the location of bony landmarks in 3D space. To our knowledge this was the first (and maybe the last) time such a frame has been constructed.

Figure 4.11: Mapping the local IMU coordinate systems to the local body segments

In the first version of the anthropometric frame (Figure 4.10) the athlete‟s reference position was determined by locating the feet in a self-selected position. Fixation of the PSIS and base of skull with measurement arms reduced the postural sway during measurements. Instructing the athlete to rest a bar on the upper thighs with fixed hand positions further reduced the superior limb degrees of freedom. Postural sway of 1-5cm was however still present, especially in the extremities, which could reduce measurement accuracy.

As a consequence improvements were made to the anthropometric frame to reduce postural sway (Figure 4.11). A calibration frame with seat was constructed to hold the athlete in place. Cross bars prevented movement of the athlete‟s feet, knees and hands, while measurement arms provided support for the sacrum, C7 and the base of skull.

In addition, the front section of the calibration frame could be removed and placed on the snow so the athlete could replicate the calibration position. This could provide additional reference positions at the start and finish of each run to improve the accuracy of FMC.

Special measurement arms were designed for specific bony landmarks. Each measurement arm had a scale fixed to it; the smallest division of the scale was 2mm. Because neither the

frame nor the measurement arms were perfectly machined the scale for each arm, in a typical measurement position, was calibrated against the 1mm square scale attached to the platform base. A plumb line was dropped from the end of the measurement arm onto the base grid; height was measured with a two metre ruler. Calibration was limited to the mean X, Y and Z offset from three typical measurements.

From bony landmarks to "The Biomechanical Man"

The body model was constructed from 42 measurements of the athlete and 11 measurements of the ski equipment (Table 4.1). A spreadsheet containing the full calculations is available on the accompanying CD (Appendix A). In the spreadsheet the 42 raw measurements are used to produce 52 anatomical landmarks, including the estimated joint centres. These were required to produce the body model named; „The Biomechanical Man" (Figure 4.12). The name was coined because the resulting avatar consists of the points of interest to a biomechanist. In Figure 4.12 the proximal joint centre and two distal landmarks are generally used to visualise each segment. The calculations of joint centre locations and body segment inertial parameters were completed using the method proposed by Dumas and Reed (Dumas, et al., 2007; Reed, et al., 1999).

First the athlete with skis and helmet was positioned in the frame so that all measurement arms could reach their targets. The seat height was adjusted for comfort (Figure 4.11). Thirty posterior measurement arms were adjusted to their target bony landmarks, starting with the helmet vertex and ending with the left calcaneus (the complete list is in the spreadsheet, Appendix A). While the athlete remained in the frame the height of five anterior bony land marks were measured; sellion, suprasternale, the anterior-superior iliac spines (ASIS) and pubic symphysis.

The athlete was then free to move out of the frame. Six additional calliper measurements were then taken to locate the anterior bony landmarks relative to the posterior bony landmarks including, base of skull to sellion, C7 to suprasternale, right posterior superior iliac spine (PSIS) to right ASIS, left PSIS to left ASIS, inter ASIS width, and right PSIS to pubic symphisis. The exact calculations are provided in the spreadsheet.

The 3D anthropometric frame measurements were adjusted to account for the measurement arm offset and then the 3D location of each joint centre was calculated. For the elbow this was simply the midpoint between the medial and lateral humeral epicondyles. For the hip and lumbar joint centres, the calculation required more steps. A local pelvic reference system was constructed using five bony landmarks; the left and right PSISs and ASISs and the pubic symphisis. The skin artefacts were removed, as suggested by Dumas, before a new pelvic coordinate system was constructed. The hip and lumbar joint centres were then located by scaling the characteristic pelvis width, depth and height to get an x, y and z offset from the pelvis origin. The pelvis origin was defined as the „new" ASIS midpoint.

Table 4.1: Measurements made in the 3D anthropometric frame

Number	Anatomical land mark			
1	Subject Mass	78 [kg]		
		Measurements [cm]		
Posterior Measurements		**Z**	**Y**	**X**
2	Vertex	180.2	43.8	24.3
3	Base of Skull	168.3	43.5	15
4	Right Acromion	152.7	63.6	21.8
5	C7	152.7	28	6
6	Left Acromion	152.7	23	20
7	Right Lateral Humeral Epicondyle	113.6	69.8	20.7
8	Right Medial Humeral Epicondyle	113.6	61.1	19.8
9	Left Medial Humeral Epicondyle	113.6	22.4	22.2
10	Left Lateral Humeral Epicondyle	113.6	15	22.9
11	Right Posterior-Superior Iliac Spine	103.8	32.2	9.1
12	Left Posterior-Superior Iliac Spine	103.8	22.6	9.6
13	Right Radial Styloid	92.5	74.7	37.1
14	Right Ulna Styloid	92.5	69.5	32.8
15	Left Ulna Styloid	92.5	13.3	32.5
16	Left Radial Styloid	92.5	9.8	36.8
17	Right 3rd Metacarpal Head	81	76	36.1
18	Left 3rd Metacarpal Head	81	8.4	34.2
19	Right Lateral Femoral Epicondyle	52.4	53.2	33.4
20	Right Medial Femoral Epicondyle	52.4	40.9	32.6
21	Left Medial Femoral Epicondyle	52.4	15.5	32
22	Left Lateral Femoral Epicondyle	52.4	3.2	32.8
23	Right Lateral Malleolus	15.4	52.9	16.2
24	Right Medial Sphyrion	15.4	41	16.4
25	Left Medial Sphyrion	15.4	14.4	16.5
26	Left Lateral Malleolus	15.4	2.7	15.6
27	Right Calcaneus	0	5.9	-2.1
28	Right 2nd Toe Tip	0	6.1	29
29	Left Calcaneus	0	-31.7	-1.7
30	Left 2nd Toe Tip	0	-33.3	29.4
Anterior Measurements				
31	Vertex	180.2	43.8	29
32	Sellion	168.3	44.4	16.6
33	Suprasternale	146	44.2	27.2
34	Right Anterior-Superior Iliac Spine	102.5	33.2	24.5
35	Left Anterior-Superior Iliac Spine	102.5	55.4	23.2
36	Pubic Symphysis	89.5	44.3	25.2
Caliper Measurements		**length [cm]**		
37	Base of Skull to Sellion	18.7		
38	C7 to Suprasternal	11.7		
39	Right PSIS to Right ASIS	15.8		
40	Right PSIS to Left ASIS	20.6		
41	Left PSIS to Left ASIS	15.6		
42	Left PSIS to Right ASIS	20.4		

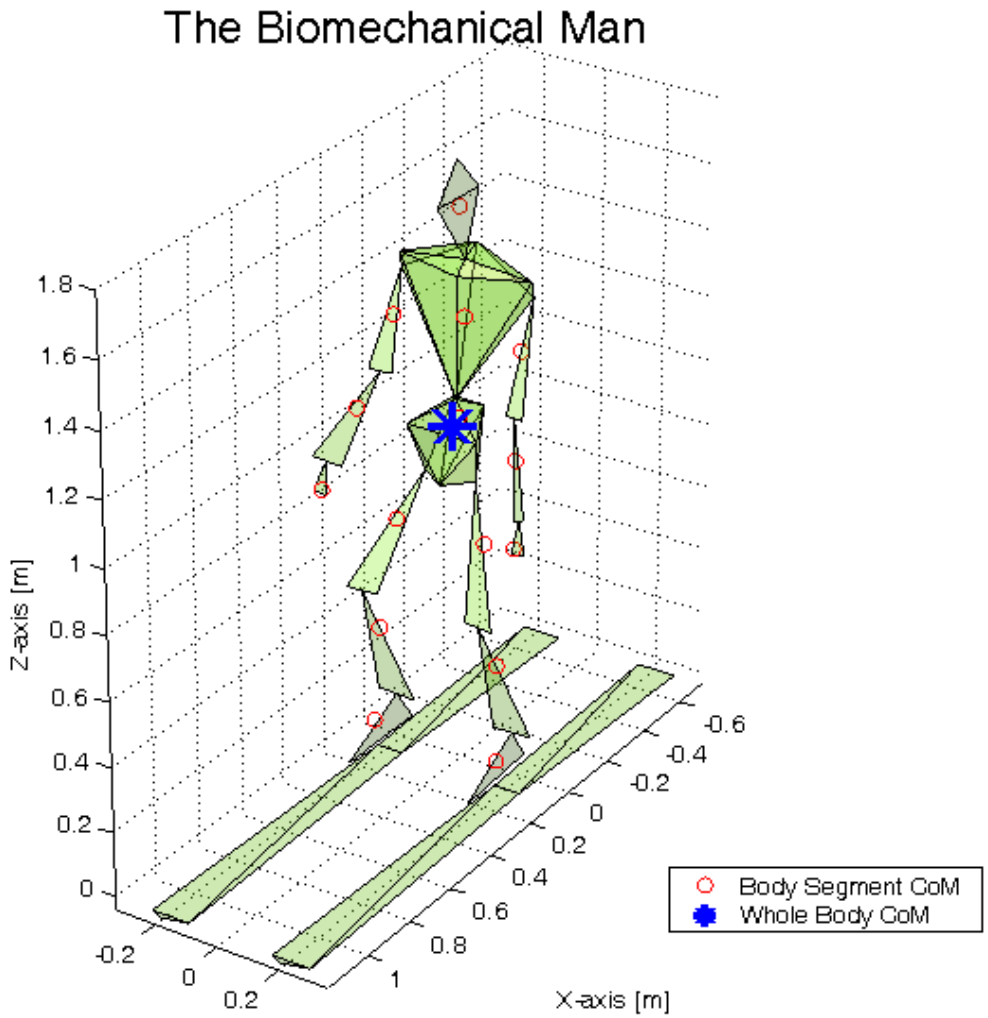

Figure 4.12: Visualisation of measurements from the 3D anthropometric frame

The Biomechanical Man in MATLAB

The previous calculations produced 52 biomechanical landmarks including joint centres that were then used to construct the biomechanical man body model in MATLAB (Figure 4.12). The biomechanical man visualisation was constructed entirely from triangles because triangles can be drawn efficiently in MATLAB. At each epoch an array of global points that described the subject's posture in the global coordinate system was calculated from the FMC data. Each triangular face was then rendered by connecting three specific global points with a planar surface. Details of the rendering process are provided in Appendix G and on the accompanying CD (**Appendices\Example Code\Biomechanical Man\More about the Biomechanical Man.pdf**).

Mapping the IMUs to the body segments

To drive the biomechanical man with real data, the local coordinate systems of the IMUs were mapped to the local coordinate systems of the body segments through the calibration procedure described below and pictured in (Figure 4.11).

In the calibration procedure if soft tissue artefacts are minimised, a constant rotation „maps" the IMUs to the different body segments and an accurate measurement of limb orientation is possible. The constant rotation is defined below by a 3-by-3 rotation matrix ($\mathbf{R}_{IL \rightarrow BL}$), which transforms the measurements from the IMU local (IL) to the body segment local (BL) coordinate systems. The calibration process requires five seconds of stationary data from the IMUs attached to the athlete. During calibration the athlete is precisely supported in the reference position by the 3D anthropometric frame (Figure 4.11) and the following four steps are completed:

1. The local orientations of the body segments with respect to the 3D anthropometric frame (F), and called ($\mathbf{R}_{BL \rightarrow F}$). Measurements of bony landmarks from the anthropometric frame are used.
2. The mean orientation of the IMUs ($\mathbf{R}_{IL \rightarrow G}$), are calculated from the IMUs accelerometer and magnetometer channels. The static orientation calculation described in Chapter 2 on page 30 is used.
3. The orientation of the anthropometric frame with respect to the IMU global coordinate system ($\mathbf{R}_{F \rightarrow G}$), is required. It is defined as the rotation about the vertical axis that brings the X-axis of the frame in line with magnetic north. This can be determined by using a compass to measure the frame X-axis heading.
4. The calibration matrix for each body segment can now be determined (Equation 4.10).

Equation 4.10 $$R_{IL \rightarrow BL} = R^{-1}_{BL \rightarrow F} * \left[R^{-1}_{F \rightarrow G} * R_{IL \rightarrow G} \right]$$

The procedures are now in place for FMC data from skiing to drive animations of the biomechanical man. In the future, the captured motion will be reconstructed by transforming the motion of each body segment into the global coordinate system. The body segment defined in the local body segment coordinate system will be rotated into the global coordinate system using the measured changing orientation of the body segment ($\mathbf{R}_{BL \rightarrow G}$, Equation 4.11). The body segments in the global coordinate system will then be connected together by their joint centres.

In Equation 4.11 $\mathbf{R}_{BL \rightarrow G}$ describes the rotation from the body local to global coordinate system at each epoch. $\mathbf{R}_{BL \rightarrow G}$ is found from the instantaneous IMU orientation ($\mathbf{R}_{IL \rightarrow G}$) and the constant calibration matrix ($\mathbf{R}_{IL \rightarrow BL}$) determined in equation Equation 4.10.

Equation 4.11 $$R_{BL \rightarrow G} = R_{IL \rightarrow G} * R^{-1}_{IL \rightarrow BL}$$

4.3.2. Experimental

Biomechanical analysis depends on human interpretation of data. Technology developments improve the amount of data available and its quality but the final analysis still rests with the biomechanist"s interpretation of the results. To interpret the results of FMC it is necessary to understand the different sources of error. The difficulty of constructing an accurate body model is one source of error. The approximate size of this error and its effects on future biomechanical analyses needs to be determined.

The 3D anthropometric frame measurements of six subjects were compared against criterion anthropometric measurements taken by a certified technician. Version one of the frame was used (Figure 4.10). Seventeen different measurements were compared. In the anthropometric frame the 3D lengths were calculated as the length between two separately measured bony landmarks in 3D space. A qualified anthropometrist used a standard anthropometric kit to measure the lengths directly.

Table 4.2: Comparison of measurements between criterion anthropometry and our 3D anthropometric frame.

Comparison of Error		Subject Error [cm]						Mean Error	Std Dev	Mean Length	Relative Error	CV
#	Anatomical Reference	1	2	3	4	5	6	[cm]	[cm]	[cm]	[%]	[%]
Right Side												
1	Acromiale-radiale	1.5	1.3	1.1	0.9	0.8	1.2	1.1	0.3	33.6	3	1
2	Radiale-stylion	0.8	-1.8	-0.8	-1.2	0.8	-1.0	-0.6	1.1	25.7	-2	4
3	Iliospinale ht	8.3	7.0	8.7	7.5	2.0	4.3	6.3	2.6	98.4	6	3
4	Trochanterion ht	-2.0	0.7	1.5	0.1	2.1	2.3	0.8	1.6	89.9	1	2
5	Trochanterion-tibiale laterale	-12.9	-1.0	-0.6	-1.7	0.7	-0.1	-2.6	5.1	43.3	-6	12
6	Tibiale laterale ht	10.5	1.2	0.6	0.1	-0.1	0.8	2.2	4.1	48.0	5	9
7	Foot length (ak-pt)	0.6	-0.3	-0.4	-0.5	0.1	2.4	0.3	1.1	26.5	1	4
Left Side												
8	Acromiale-radiale	4.0	0.7	0.6	-0.2	0.2	1.4	1.1	1.5	33.2	3	5
9	Radiale-stylion	2.5	0.6	-0.4	-1.6	-1.0	-1.1	-0.2	1.5	25.8	-1	6
10	Iliospinale ht	8.3	6.3	9.5	7.0	7.1	3.9	7.0	1.9	97.1	7	2
11	Trochanterion ht	0.7	0.3	0.8	0.8	1.0	1.7	0.9	0.5	88.6	1	1
12	Trochanterion-tibiale laterale	-10.1	-0.6	-0.4	-0.5	-0.2	0.0	-2.0	4.0	43.3	-5	9
13	Tibiale laterale ht	9.7	-0.5	-1.2	-0.6	-0.8	0.2	1.1	4.2	47.1	2	9
14	Foot length (ak-pt)	0.1	0.0	-0.2	-0.5	-0.2	0.3	-0.1	0.3	26.5	0	1
Breadths												
15	Biacromial breadth	6.8	1.9	0.5	3.1	3.2	2.6	3.0	2.1	39.6	8	5
16	Bi-iliocristal breadth	1.4	3.6	6.8	8.0	2.5	6.1	4.7	2.6	29.6	16	9
Height												
17	Vertex Height	-5.5	-11.7	-0.7	-0.1	-0.3	0.5	-3.0	4.8	174.7	-2	3
	Column Mean	**1.5**	**0.5**	**1.5**	**1.2**	**1.1**	**1.5**	**1.2**	**2.3**	**57.1**	**2.3**	**4.9**

4.3.3. Results and discussion

A method was presented previously to construct an athlete specific body model from 3D anthropometric measurements. A custom anthropometry frame was constructed and the accuracy of the frame measurements was tested by comparison to criterion measurements made by a certified anthropometrist. The body model is required in order to calculate the subject movements from the IMU data.

Creating a body model of the athlete with the 3D anthropometric frame was successful, but was a time consuming process, and it took an hour per subject. The process only needs to be completed once for each athlete. Additional motion capture sessions with the same athlete should only require a 5 second calibration of the IMUs while the athlete is constrained to a pre-measured reference position by the anthropometry frame measurement arms.

The calculated limb lengths for the athlete specific body model came from papers by Dumas and Reed (Dumas, et al., 2007; Reed, et al., 1999). The limb lengths were calculated from the position the joint centres, which were calculated from the underlying measurements of the bony landmarks. The possibility for error calculating limb lengths from bony landmarks was only discussed for the sacrum body segment by Dumas and Reed, which is probably, contains the most error because of the distance between the bony landmarks and the lumbar of hip joint centres. Based on an estimated vertical error in hip joint centre location of 3.5mm (the mean error from Reed‟s paper) and the mean sacrum segment length of 94 mm (from Dumas‟ paper) the estimated body segment limb length of 4% was chosen and adopted for all body segments. It was assumed this source of error would not affect the measured orientation of the body segments because orientation is generally calculated from the direction of vectors and not lengths.

The scaled inertial parameters used to create the athlete specific body model came from papers by Dumas and Reed (Dumas, et al., 2007; Reed, et al., 1999). The location of the body segment centre-of-mass and the inertia tensor were based on the characteristic dimensions of each body segment, which were inherently more accurate than some other approaches based on the regression of height and weight only. The underlying data came from McConville and Young and were based on 31 healthy males with a mean age of 27.5 years and a mean weight of 80.5 kg. McConville‟s mean age was about 5 years older than the mean age of the athletes and skiers have larger thighs than the average population. The inertial properties of the biomechanical man are therefore unlikely to be perfect for the athletes, but were the best estimate practically available. McConville used a stereo-photogrammetric technique that was reported to be within 6% error for CoM location measurements from cadavers, within 6% error for the principal moments of inertia and less than 10% error for body segment masses.

Criterion and 3D anthropometry differences

The differences between the criterion anthropometry and measurements derived from the 3D anthropometric frame were between 0cm and 12.9cm (Table 4.2). The largest differences

were from subject one. This was almost certainly a result of measurement protocol errors as the method of using the new frame became familiar.

Apart from measurements of subject one, the largest measurement error was contained in the measurement of Iliospinale height, both left and right side, with mean errors of 6.3cm and 7.0cm respectively. The large mean error highlights the systematic error that resulted from the difficulty in palpating and locating bony landmarks that were obscured by superficial soft tissue. It was likely the certified anthropometrist identified these bony landmarks differently. The error revealed that more practise in identifying and locating the bony landmarks in the frame was required. Often the same quantity was not being measured so it might have been better to consider the standard deviation of error instead of the mean error.

The standard deviation of error was up to 5.1cm (12% coefficient of variation, Table 4.2) for the distance between the greater trochanter and the tibiale laterale. The arcsine of the coefficient of variation represented a possible orientation error of nearly 7º in the definition of the thigh body segment, but fortunately the greater trochanter is not required to define the thigh body segment which instead uses bony landmarks of the sacrum. This type of error could also propagate into the calculation of the CoM location and the inertia tensor, and so also increase the error in any future kinetic analysis based on the body model.

Reasons for differences

Some additional reasons for the observed differences between the criterion and 3D anthropometry measurements are outlined below:

The frame measured the locations of two points in free space and the length was found by the difference. This type of calculation process, where two large quantities are subtracted to find a small quantity, exacerbates measurement error. If a length between two bony landmarks is required standard anthropometry will inherently be more accurate. For calculating an athlete specific body model the 3D positions of the athlete‟s joint centres were required, information that could not be obtained through standard measurements.

Postural sway was observed to be up to 5cm over the 30 minutes of measurement. To reduce postural sway a seat and front stabilisation frame were added to the frame. Unfortunately, the effect of these improvements in reducing error was not assessed.

In the measurement of bi-acromial breadth, the systematic error arose because the acromiale is defined differently by Reed and Dumas. The definition used was the undepressed most anterior corner of the lateral margin of the acromion process. This was different from the definition used by the anthropometrist, who used callipers to measure the distance between the superior-lateral aspects of the acromion processes. Often the same quantity was not being measured and so it might have been better to consider the standard deviation of error instead of the mean error.

If the first two subjects‟ data are assumed to contain statistical outliers as a consequence of the poor measurements made on the subjects during the process of learning to use the new frame, then the errors are reduced. The mean standard deviation of all 17 measurements drops to 1.0cm, the maximum standard deviation is 3.0cm (for iliospinale height). The standard deviation also drops and therefore the estimated orientation error also reduces to a more respectable mean value of 1.3º with a maximum value of 4.6º for the sacrum body segment.

Limitations for sacrum, thigh and thorax body segments

How might the potential for measurement error affect the derived body model? The correct measurement of sacrum body segment orientation is essential to building an accurate subject body model. The sacrum is used to define the hip and lumbar joint centres and so any errors also affect the measurement of thorax and thigh body segment parameters.

The criterion anthropometry bony landmarks used in this experiment were not exactly the same as those required to create a body model as specified by Dumas and Reed. The large estimated error (4.6º) in sacrum body segment orientation however highlights the difficulty in locating pelvis bony landmarks that are obscured by soft tissue. Dumas and Reed used instead the posterior superior iliac spines (PSIS), the anterior superior iliac spines (ASIS) and the pubic symphisis (PS), but these bony landmarks are equally if not more challenging to locate accurately.

The exact location of the shoulder joint centres within a single thorax body segment is another potential source of error. Movements of the scapular and clavicle and therefore the shoulder joint relative within the thorax body segment are not accounted for by the body model used.

Are the limitations of the body model acceptable?

The previous discussion covers some of the potential difficulties that might arise when creating an accurate body models of athletes. In a worst-case scenario; if the body model error (up to 7º) were added to the IMU orientation error discussed in Section 4.2 (<3º RMS) then the maximum possible orientation error of a body segment might exceed 10º. The analysis suggests however that if a skilled technician is used, conservatively body model errors of less than 5º for the sacrum body segment and 3º for the remaining body segments should be possible. This might result in the measurement of sacrum body segment orientation containing more error than distal body segments, but counteracting the higher body model error is the fact the IMU attached to the sacrum is exposed to less dynamic loading than the distal body segments and therefore produces more accurate measurements of orientation. Future FMC data should be examined carefully for such artefacts to prevent erroneous conclusions about human movement being made.

How do the limitations of our body model affect the future analyses of skiing? Fortunately the body model mapping from the anthropometric frame error will be constant. The dynamics and high frequency components of FMC should not therefore be affected. Such error may however manifest itself by making data driven animations appearing unnatural with a joint moving consistently beyond its healthy range of motion.

The errors may limit the kinetic analysis of joint torques because the positions of the external forces relative to the body model joint centres change the calculated net joint torque significantly. This is especially true if the subject is in an upright pose and the CoM is located very close to the hip, knee and ankle joints. In this stance a slight error in orientation would cause a positive torque to be calculated as a negative torque. Over the course of large changes in stance, the nature of the changes in joint torques should however be preserved.

Over an entire large scale movement like skiing, the error relative to the range of motion of each joint will be small. As long as these limitations in accuracy are considered during the analysis, FMC should be able to provide analysis of large-scale movements (like skiing) that was not previously practical. In this thesis, the whole body motion of the athlete and the net effect of different external forces are of interest. Any error in CoM location that may be a result of limb orientation error will be insignificant compared to the gross motion of the athlete‟s CoM through the ski racecourse. The methods presented in this chapter and used to construct the biomechanical man body model are therefore able to be used to produce useful information for the future analysis of alpine ski racing. In any future analysis of skiing potential sources of error arising from the difficulties associated with constructing an accurate body model should however be carefully considered.

5. Developments from inline skating

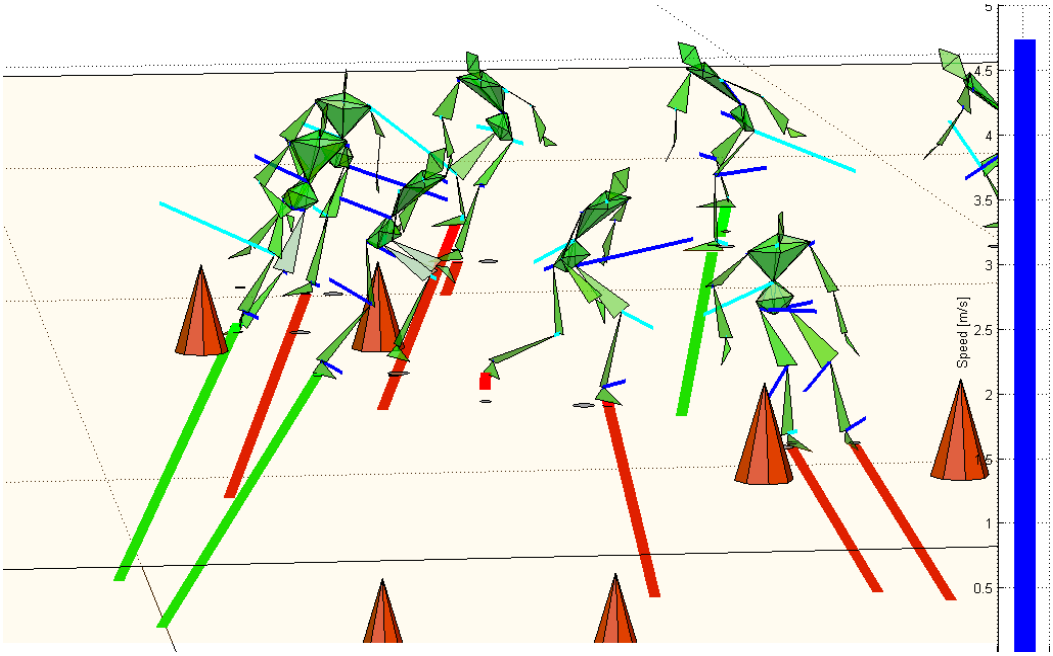

Figure 5.1: Biomechanical analysis of inline skating some forces and torques shown

In Figure 5.1 the ground reaction forces are colour coded, green for forces with a positive power (acting to accelerate the athlete) and red for forces with a negative power (acting to decelerated the athlete). The net joint torques are visualised according to the right hand rule. Dark blue for torques with a positive power (indicating concentric muscle action) and light blue for torques with a negative power (indicating eccentric muscle action).

Inline skating experiments were completed to test the revised prototype Fusion Motion Capture (FMC) system before taking it back onto the snow. As part of this work an opportunity was also taken to develop different ways to analyse and visualise the data because inline skating is commonly used for summer training of ski athletes and therefore parts of the analysis might be transferable to future skiing data.

There are both similarities and differences between skiing and inline skating (Kroll, Schiefermuller, Birkalbauer, & Muller, 2005). Kroll‟s paper analysed muscle activity, kinematic data and dynamic data from both inline skating and slalom skiing. Some differences reported include:

- The ground reaction forces in slalom skiing during cornering are higher (~1400N) than in inline skating (~600N).
- Slalom ski technique during turns uses the outside ski to take more of the load compared with inline skating technique where the load is spread evenly between the skates.
- The athlete steers the ski by applying more weight to the front of the ski compared with inline skating where the heel of the skate is favoured.

Kroll found that there were enough similarities between skiing and skating to suggest inline skating was a satisfactory dry land modality for ski racers. Similarities reported include:

- Kinematic data showed that the body positions and timing were similar, but that a combination of free skating and skating through gates might be required to reproduce more aspects of ski racing technique during any dry land training.
- Leg muscle activity data from the vastus lateralis, tibialis anterior and biceps femoris was recorded. The data show a large agreement between the muscle activation, timing and function of these muscle groups during both skiing and inline skating.

In section 5.1 FMC is adapted for indoor use when global positioning system (GPS) data are not available. Data driven animations and colour coded figures are developed to visualise the inline skating data. All calculations, figures and data driven animations are created in MATLAB using custom algorithms. In section 5.2 the external forces acting on the athlete: wind drag, bearing friction, and the ground reaction forces normal to each skate sole; are calculated. The force data are used to investigate how physical constraints limit the athlete‟s performance. In Section 5.3 the data from inline skating are used to investigate the question: What is variable and what is consistent within the athlete‟s global trajectory? In Section 5.4 simulations of the athlete‟s minimum time centre-of-mass (CoM) trajectory are developed from his measured dynamics. This chapter contains some developments most relevant to future analysis of ski racing. Further details of the analysis of inline skating are provided on the accompanying CD (Appendix B, **Appendices\Inline skating supplement.pdf**).

5.1. Capture and visualisation of inline skating

The athlete‟s motion through an inline slalom course around a set of cones was captured using FMC. The athlete, a retired ice hockey player from Canada, skated through the course multiple times. The instructions were to skate the course in as little time as possible. GPS was not available indoors so gate timings taken from a single video camera were used as a substitute. The results were analysed using MATLAB algorithms written by the author and are presented in this section by graphs and animations. The raw FMC output consists of large arrays of numbers and a major challenge was to make the data from complex 3D motion easier to understand and interpret. An example „strobe‟ animation is shown previously (Figure 5.1) with ground reaction forces and net joint torques visualised.

5.1.1. Methods

The Biomechanical Man - IMU to body segment mapping

The Biomechanical Man, a fifteen-segment body model of the athlete was constructed using the 3D anthropometric frame (Figure 5.2) and the methods presented in Chapter 4. The inertial parameters of the body model were scaled from the athlete‟s measured characteristic limb lengths and body mass (68kg). Ten IMUs were used in the motion capture. The five body segments without IMUs were the hands, feet and head, whose movements were determined by the IMUs attached to the forearms, shanks and thorax respectively.

The IMUs were mapped to each segment using a similar process to that used for the Animating Nancy experiment in Chapter 2, but there was one difference: The IMU global coordinate system required a heading correction, a rotation about the global vertical or Z-axis, from magnetic north (IMU coordinate system global X-axis) to the global X-axis of the gymnasium coordinate system (the long length of the course). The corrections were made using measurements of the sacrum IMU, aligning the X-axis of the 3D anthropometric frame with the X-axis of the gym and by assuming a homogeneous magnetic field. It was then assumed that the heading of the negative z-axis of the sacrum IMU was coincident with the heading of the local x-axis of the sacrum body segment as a result of the manual placement of the IMU. More details are provided in Appendix B.

Figure 5.2: Mapping the IMUs using the 3D frame

Creating the data driven animations from FMC data

Several MATLAB algorithms were developed to visualise the FMC data in different ways. The processes were very similar to rendering the biomechanical man, already described in Chapter 4. This time it was different because the biomechanical man‟s movements were driven by real skating data. The animations produced were saved as movie files in compressed form using the Cinepak codec (Radius co). This allowed the data to be viewed in Windows Media player without any special software. However some image quality was lost and the file sizes were generally large. Once captured it was possible to display the athlete‟s data in from any „virtual‟ camera position and this led to some interesting visual experiments in order to determine the most appropriate way to view the data. More details are provided in Appendix B.

Fusion Motion Capture algorithm Version Three

The FMC algorithm for inline skating (Figure 5.3) was very similar to the algorithm used to successfully capture to the motion of the wand in Chapter 4 on page 58. There were however four major changes, which are explained in this section.

Most importantly, GPS was not available so gate-crossing times were used as a substitute. The gate-crossing times were obtained from the video data by counting frames. The distance

between consecutive gates divided by the time was used to calculate the mean velocity between each gate. Velocity was further differentiated to give discrete estimates of the mean acceleration between two sets of gates. The discrete acceleration was then fed into the [Fusion Algorithm 2] process in Figure 5.3. The discrete acceleration data were used to correct for the low frequency accumulation of orientation error, a result of the gyroscope bias.

Using gate checkpoints as a substitute for GPS data should be reliable. The course gates should be close together with a period of between one and two seconds. Although the periods may be slightly longer than that commonly available with GPS (one second), the position of each check point should be near the turn apex which should have two advantages:

1. The bounds of the global trajectory should be defined well when integrating between the check points.
2. The mean velocity vector measured from the difference between subsequent gate check points should vary, which may improve the accuracy of the calculated body segment orientations in the [Fusion Algorithm 2] process.

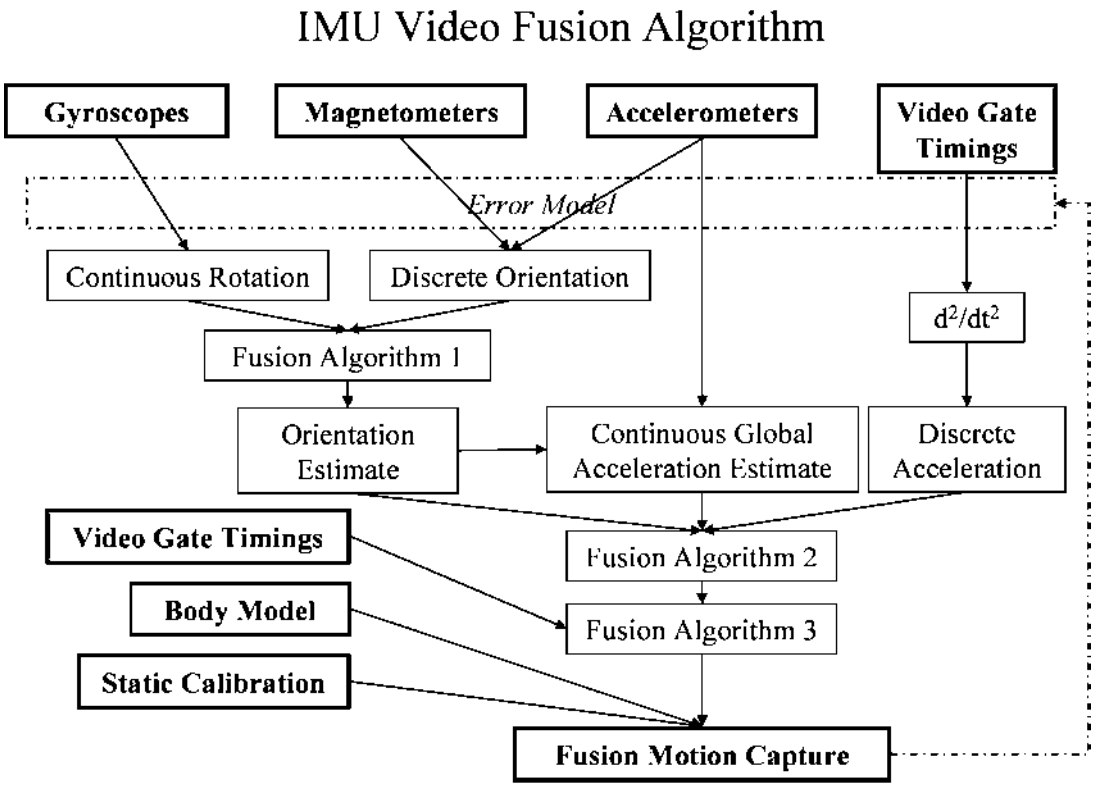

Figure 5.3: FMC Algorithm Version Three for indoor inline skating

Video gate-crossing times were then used a second time to correct for the accumulated integration error in global location estimate, the [Fusion Algorithm 3] process in Figure 5.3. This was similar to the process of Fusion Integration described elsewhere (Brodie, et al., 2007).

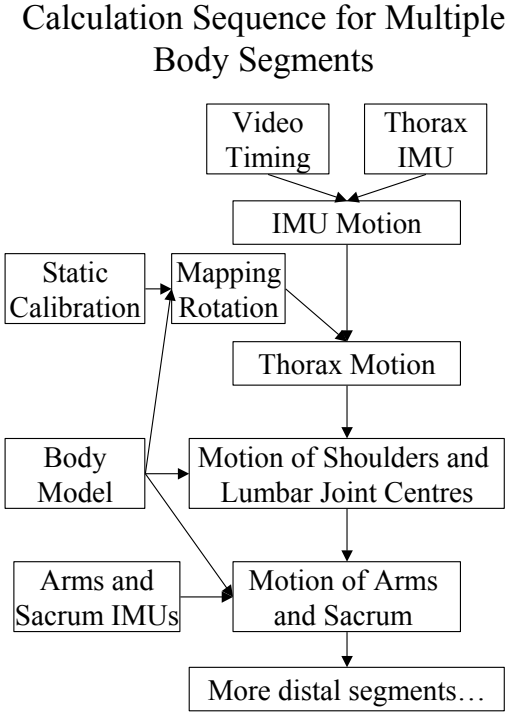

Figure 5.4: The proximal to distal calculation sequence for FMC

A second difference from the previous FMC algorithm used for the wand experiment was that the motion of multiple body segments was captured. The calculation sequence is represented in Figure 5.4. The motion of the IMU attached to the thorax was determined first as described previously. The body model and IMU to thorax mapping from a static calibration procedure were then used to drive the virtual motion of the athlete‟s thorax. It was then possible to calculate the trajectories of the athlete‟s shoulder, lumbar and cervical joint centres. The entire process was then repeated for the upper arm and sacrum body segments, except the acceleration of the proximal joint centres was used instead of the gate timing data. The process was then repeated moving from proximal to distal limb segments until all the body segment trajectories and orientations were determined.

A third difference from the previous FMC algorithm used for the wand experiment was that the gate crossing times could only give an approximate location of the athlete‟s cervical joint centre in the XY plane. The height (Z-axis) trajectory was unknown. Additional information was required and so the gymnasium floor was assumed to be flat and a variation of fusion integration was used to estimate the subject‟s height from the gymnasium floor (Figure 5.5). The pressure sensitive insoles were used to determine the airborne phase defined when measured mass of the athlete was less than 5% of true mass. During flight one estimate of the global trajectory was possible from the double integration of global acceleration, as measured by the thorax IMU. During ground contact the athlete height was estimated from both the stance height and the thorax IMU.

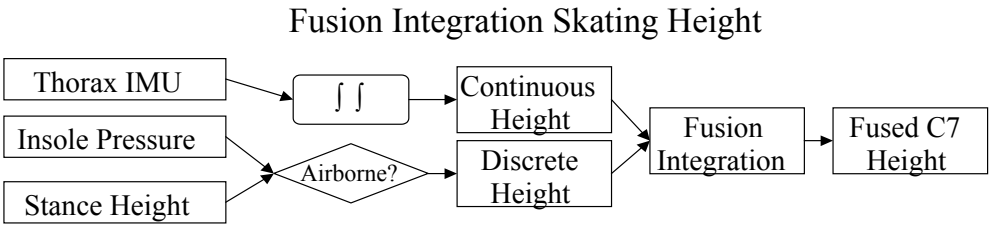

Figure 5.5: Calculation process for the cervical joint centre height

5.1.2. Experimental

The course

The athlete was instructed to skate quickly through six gates that defined a slalom course (Figure 5.6 and Figure 5.7).

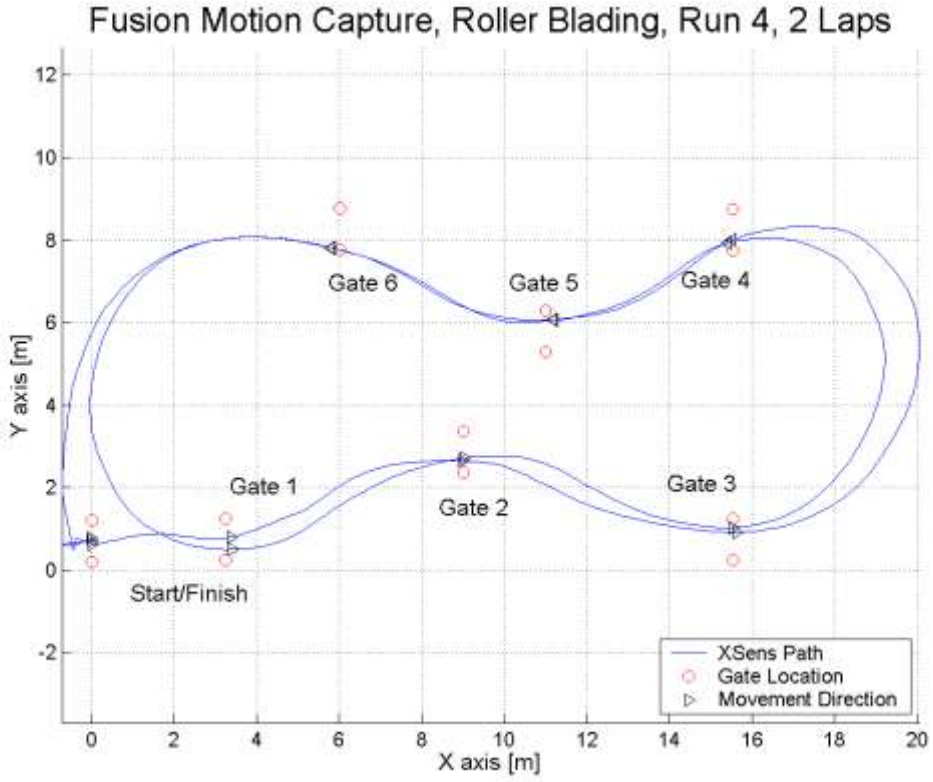

Figure 5.6: Run 4 shows the gate placement and global trajectory for two laps

Eight runs were completed; runs 1-3 were single laps while runs 4-8 were double laps. Each gate consisted of two cones placed 1.5 metres apart. Because skating was slower than skiing, the gates were more tightly spaced than is usual in skiing. Also, because the gymnasium was small, the gates were placed so that multiple laps of the course were possible.

Figure 5.7: Cones mark the course, the athlete, is held at the start position

Equipment

The motion capture set-up included:

1. Ten inertial measurement units (IMUs) attached to the athlete's limbs to measure orientation. The locations of the IMUs were consistent with the experiment in Chapter 2, on page 25.
2. Custom built elastic straps and double-sided tape to attach the IMUs to the limbs (Figure 5.8).
3. One Xbus controller with a Bluetooth communication unit to transmit the IMU data to a laptop computer.
4. A laptop with Bluetooth to record the data.
5. The 3D anthropometric frame to build an athlete specific body model, and map each IMU to its attached limb in the reference position (Figure 5.2).
6. Pressure sensitive insoles from RS-Scan to measure plantar pressures.
7. Cones to mark the course.
8. A tape to measure cone location.
9. A video to validate the local motion and measure approximate gate timings

Figure 5.8: IMUs being attached to the upper body

5.1.3. Results from data visualisation

The global trajectories of the athlete's CoM from runs 2, 4 and 5 are shown (Figure 5.9).

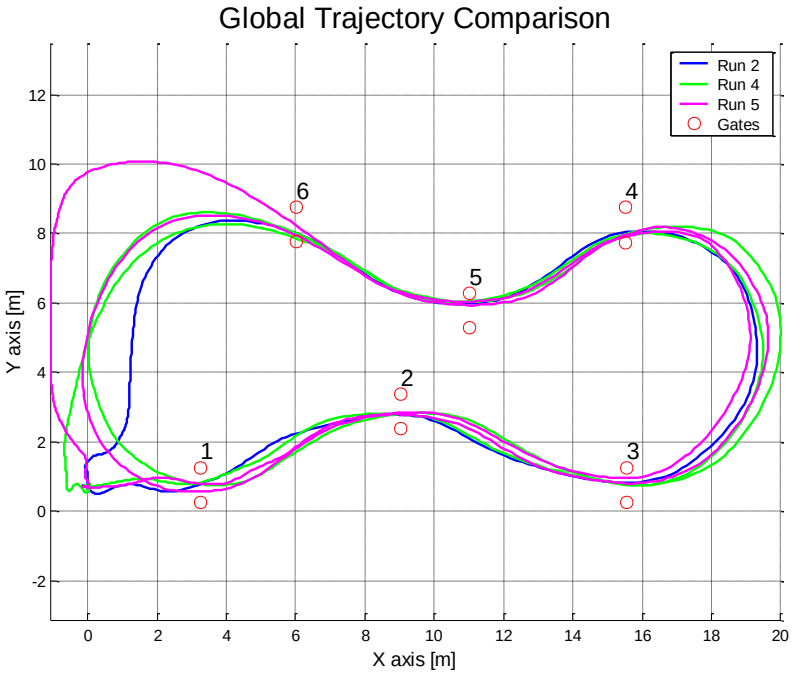

Figure 5.9: The global trajectories of athlete's CoM

The calculated local limb movements can be assessed against video footage by the reader in the first data driven animation (Video 5.1). All the data visualisations presented are from a single lap, Run 2.

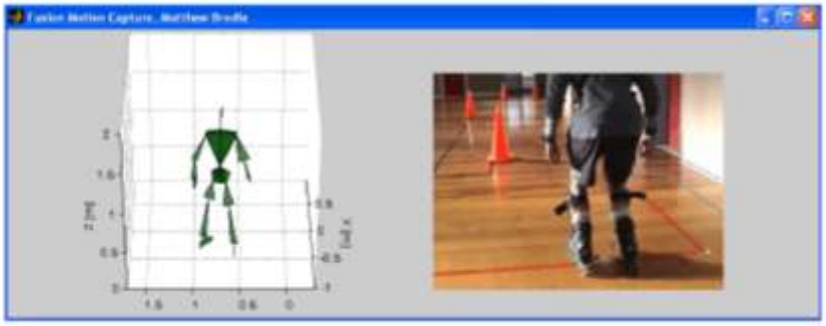

Video 5.1: Appendices/FMC Video/Skate_Local_Video_V1.avi

Two changes were then made to visual representations of the feet/skate segments which improved appearance. The feet were made parallel to the floor surface and the left foot was externally rotated by 25º so the skate blade would appear parallel to the motion. The improvement of these manual corrections to the visual appearance can be verified by the reader (Video 5.2).

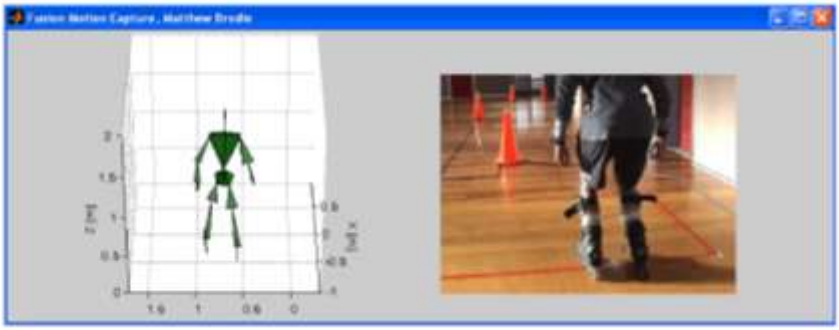

Video 5.2: Appendices/FMC Video/Skate_Local_Video_V2.avi

Simultaneous multiple views of the global action were created (Video 5.3).

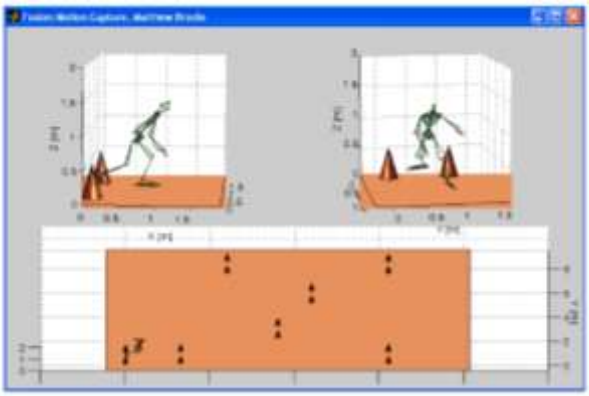

Video 5.3: Appendices\FMC Video\Skate_Multiviews.avi

Different virtual camera positions congruent with the athlete‟s perception of his motion were experimented with. The first attempt was unpleasant to view because of high frequency vibrations (Video 5.4). For the second attempt the congruent camera positions and camera targets were smoothed using a bi-directional low pass 3rd order Butterworth filter with a cut off frequency of less than 1 Hz (Video 5.5). Shadows were also projected on the floor under the athlete‟s CoM and feet.

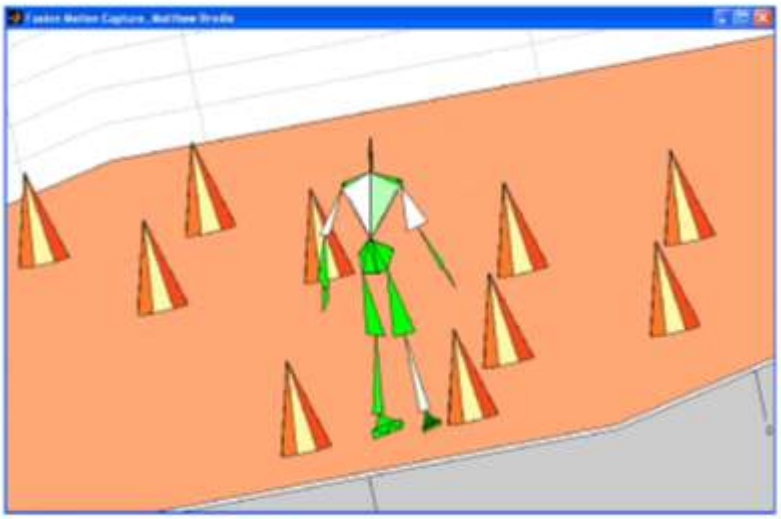

Video 5.4: Appendices\FMC Video\Skate_Congruence_V1.avi
Video 5.5: Appendices/FMC Video/Skate_Congruence_V2.avi

The final experiment into the visualisation of the FMC data used the athlete‟s CoM velocity vector to define the camera position. The virtual camera was placed in front of the athlete changing position as the athlete‟s CoM trajectory changed direction. The camera positions and camera targets were again filtered (Video 5.7)

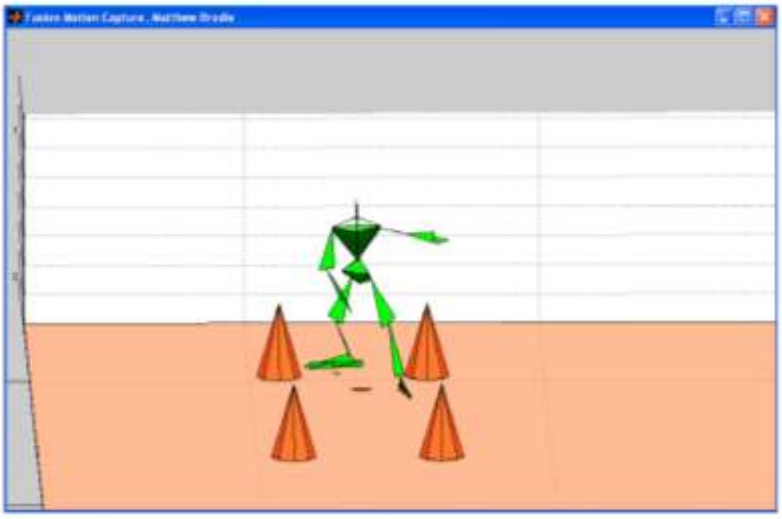

Video 5.6: Appendices\FMC Video\Skate_Front_Tracking.avi

5.1.4. Discussion about data visualisation

Although eight trials were completed only three complete data sets were recorded (runs 2, 4 and 5, Figure 5.9). Data from the incomplete data sets were lost because of the unreliable behaviour of the wireless Bluetooth connection between the Xbus master and the laptop computer, compounded by the fact that the Xbus master had insufficient memory buffering. Overall, the data collection was a success. Both the global motion of the athlete‟s CoM through multiple runs (Video 5.3) and the local motion were captured (Video 5.1 and Video 5.2). The author believes this is the first time that such a large data set on the motion of inline skating has been collected.

In the introduction it was discussed that, before FMC, it was not practical to complete the biomechanical analysis of athlete movements through a complete racecourse because of resource and time constraints. There were therefore no templates to use as a basis for presenting the data. The first data driven animations were similar in appearance to the animation of a galloping horse produced by Muybridge in 1877. Further developments soon led to substantial improvements in the data presentations, which were then able to simultaneously communicate both the large scale global movements through the inline skating course and the local limb movements.

Once the data were captured with FMC, any viewing angle was possible as demonstrated by Video 5.3. With this knowledge a virtual camera position that was more congruent with the athlete‟s perception of his motion was created (Video 5.5). The virtual camera tracked the athlete‟s CoM and was positioned 15 metres behind the athlete on a vector that connected the athlete‟s sellion and base of skull. It was assumed that the athlete might be looking along this vector as eye movements were not recorded.

The first congruent representation of the motion (Video 5.4) was jittery when the athlete‟s head rotated about the medial-lateral and longitudinal axes (as estimated from the thorax sensor). The motion also did not communicate adequately the lateral aspects of the global motion because the subject was always centred. The solution was to filter both the camera position and camera target using a bi-directional low pass 3rd order Butterworth filter with a cut-off frequency of less than 0.5 Hz (Video 5.5). The filtering allowed the data driven animation to move around the display space which better communicated the perception of global movement. The data driven animation was probably more congruent with the athlete‟s visual perception because high frequency head movements may be reduced by the vestibulo-ocular reflex. Camera roll angle defined by head segment y-axis (the vector connecting the cervical joint centre to head vertex) was not filtered as the eyes can not twist independently in their sockets to compensate for head rotations about the anterioposterior axis.

These novel data visualisations were a success; they made it possible to display the complex numerical data in a way the athlete could have easily interpreted, they displayed the data from virtual camera placement that are not practical to use with real cameras.

Limitations of global trajectory

How accurate are the calculated trajectories shown above in Figure 5.9 and visualised by the data driven animations? The accuracy of the FMC system for this inline skating analysis was estimated by qualitatively comparing the FMC data driven animations with frames from a video camera located near the course start in the gymnasium corner. This subjective approach was used previously to corroborate the accuracy of the skiing data from Chapter 3, where its validity was discussed.

At this stage the best estimate for the accuracy of the global trajectory is based on approximate gate passing measurements. Global trajectory accuracy was limited by the temporal resolution of the hand held video camera of 0.04s. As the athletes speed around the course was approximately 4.5m/s, the calculated error in the global trajectory will be around 0.18m, and the impact of this is discussed further in Section 5.3 on page 107.

Although 0.18m may seem large relative to the reported millimetre tolerances of optical motion capture systems, the estimated global trajectory error is less than 1% of the athlete‟s total trajectory. In spite of the estimated error, inspection of the athlete‟s centre-of-mass trajectories (Figure 5.9) reveals interesting trends such as the athlete passed close to the inside of each gate.

Limitations of the data driven animations

The inline skating results revealed a significant visual artefact. Initially there was a problem with the orientation of the athlete‟s left foot (Video 5.1). A heading correction of 25° anticlockwise fixed the problem (Video 5.2). The heading correction was applied to the matrix mapping the left shank IMU to the left foot. The correction was found by trial and error using the knowledge that the skates were parallel in the start position of run 2. The same correction was then used for all runs.

This error in left foot orientation could be traced back to errors during the construction of the body model or the mapping of the IMU to the left foot because the same constant correction was satisfactory for all runs. The required correction (25º) was much larger than the maximum estimate of body model error (7º) discussed in Chapter 4. The heading error was therefore likely to be a result of a non-uniform magnetic field near the left shank sensor during static calibration used to map the IMUs to the body segments. The non-uniform magnetic field could have been a consequence of the foot scan insole terminal attached to the athlete‟s shank, or the steel construction materials used to construct the gymnasium.

The accuracy of the remaining body segments (excluding the head, hands and feet, which did not have sensors attached) and the sacrum was likely to be less than 6º because there were no discernable visual artefacts in the data driven animations. The 6º upper limit was determined by addition of the potential body model errors (<3º, Chapter 4) with potential sensor orientation errors (<3º, Chapter 2). The 6º estimated error is greater than the error estimate of 5º from the skiing data in Chapter 3 but the same as the error estimate of 6º from an optical

motion capture system discussed in Chapter 1 (Schwartz, et al., 2004). The sacrum orientation error was estimated to be 8º and is bigger that for the other segments because of the greater potential for soft tissue artefacts to affect the body model errors.

It would have been difficult, because of practical constraints, to capture inline skating motion using optical motion capture. FMC can therefore provide valuable data for the biomechanical analysis of inline skating that could not practically be obtained any other way. Even if the error is as large as estimated (6º for limb orientation and 0.18m for trajectory) it does not reduce the potential effectiveness of the data driven animations to provide valuable interpretations of skating performances.

5.2. Analysis of external forces on slalom skating

Using FMC large amounts of data on inline skating were collected. The challenge is now to use these data in biomechanical analyses to understand more about the forces that drove the athlete‟s motion. Some material in this section is reproduced from a paper by the author with permission from the publisher (Brodie, et al., 2008b).

5.2.1. Methods

Defining ground reaction forces

By definition the total ground reaction forces include all forces acting on the skates from contact with the ground. In this thesis the total ground reaction forces were separated into friction terms ($\mathbf{F_{Frict\_R}}$ and $\mathbf{F_{Frict\_L}}$) and reaction force terms ($\mathbf{GRF_R}$ and $\mathbf{GRF_L}$) under the feet effects of technique changes on performance in skating and skiing could be investigated.

After the separation, the first components of the total ground reaction forces ($\mathbf{F_{Frict\_R}}$ and $\mathbf{F_{Frict\_L}}$) would be snow resistance in skiing or bearing friction in skating. The friction terms could be modelled and depended on factors such as the choice of ski wax, the quality of the skate wheel bearings, and running surface conditions. These factors were influenced more by race preparation than athlete technique.

The second components of the total ground reaction forces would be the remaining ground reaction forces under the feet after the friction terms have been removed. They were called ground reaction forces ($\mathbf{GRF_R}$ and $\mathbf{GRF_L}$) and they should act approximately normal to the ski bases or skate soles. Most of the ground reaction forces could be measured with pressure sensitive insoles and should be the result of the athlete pushing against the ground, which should be directly a consequence of the athlete‟s technique.

Calculation: Ground reaction forces, wind drag, and bearing friction

The FMC data from the previous inline skating experiment was used to calculate the different external forces acting on the athlete of; wind drag ($\mathbf{F_{Drag}}$), bearing friction ($\mathbf{F_{Frict}}$) and the ground reaction forces normal to both skate soles ($\mathbf{GRF_R}$ and $\mathbf{GRF_L}$). The equipment to

measure all of these forces directly was not available to the author so the forces were calculated using a combination of an inverse dynamic analysis of the athlete‟s CoM trajectory, the orientation of the skates, and force data from the Footscan insole system (RS-Scan International). Estimates of the coefficient of bearing friction and the coefficient of wind drag were made by minimising the residuals to a set of over-determined equations based on Newton‟s law applied to the skating (∑Forces = mass*acceleration, Figure 5.10 and Equation 5.1). The weight force ($\mathbf{F_g}$) was a constant (m*[0 0 -9.81] in the global coordinate system), the subject‟s mass (m) including skates was 68.85 kg.

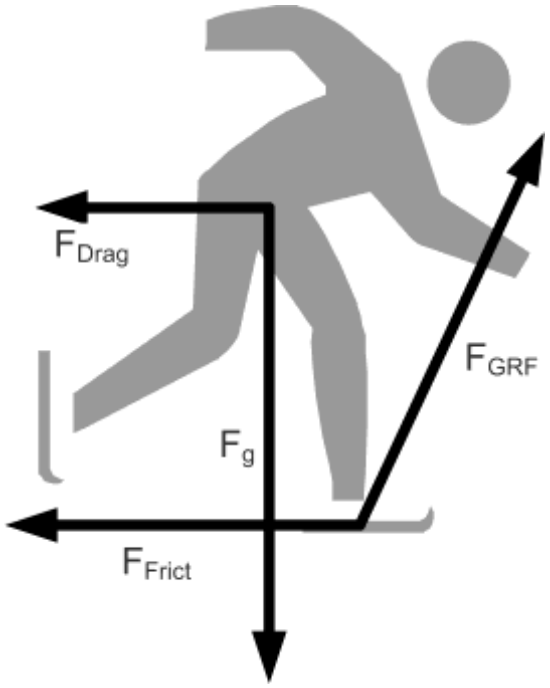

Figure 5.10: Free body diagram of skating

Equation 5.1 $$\mathbf{Residual} = m * \mathbf{A}_{CoM} - \mathbf{F}_g - \mathbf{GRF}_L - \mathbf{GRF}_R - \mathbf{F}_{Drag} - \mathbf{F}_{Frict}$$

RS-Scan insole measurement hysteresis and foot loading ratio

Initially it was assumed that the pressure sensitive insoles would give accurate ground reaction forces normal to each skate insole and this information could then be combined with the measured orientation of the skate to give the normal component of the ground reaction force. Unfortunately the pressure sensitive insoles suffered from severe hysteresis and were poorly scaled (Figure 5.11).

Our athlete‟s mass was 68.85kg, but his weight measured by the insoles at the start of the run was around 1100N, (about 400N over). By the end of the run his weight had apparently fallen to around 700N, which seemed impossible (unless there had been a nuclear reaction). In correspondence with the manufacturer, they explained this was because of hysteresis, and

suggested that the athlete take several steps at the start of the measurement, this was tried but it did not improve the accuracy significantly.

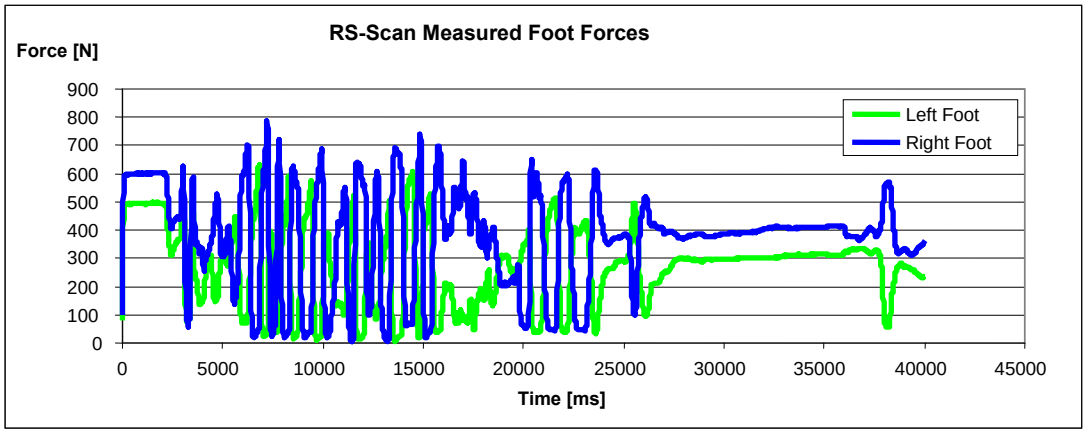

Figure 5.11: RS-Scan measured normal foot forces contain hysteresis

To get more accurate measurements from the insole data, some reasonable assumptions were made. It was assumed that the athlete was standing in a perfectly balanced stance at the start of the measurement; therefore the forces were scaled so each foot was taking half the athlete's weight at the start. It was further assumed that although the re-scaled force measurements were not accurate they would give an accurate ratio of the normal force magnitudes ($|\mathbf{GRF_R}|$ and $|\mathbf{GRF_L}|$) between the right and left feet (Equation 5.2). More accuracy could have been obtained with miniature force plates attached between the skis and bindings (or skate wheels and boot in this case), but at present the miniature force plates are too thick to pass an International Ski Federation (FIS) regulation based on athlete safety.

Equation 5.2
$$Ratio = \frac{|\mathbf{GRF_L}|}{|\mathbf{GRF_L}| + |\mathbf{GRF_R}|}$$

Ground reaction force calculations (GRF)

The following calculations and assumptions for the ground reaction forces refer to Figure 5.12. First the resultant force ($\mathbf{F_{Resultant}}$) was calculated by twice differentiating the CoM trajectory to get acceleration ($\mathbf{A_{CoM}}$), which was then multiplied by the athlete's mass (m) including skate equipment. No significant high frequency noise was introduced into the resultant force calculation in this step because:

1. The high frequency component of the CoM trajectory was based on the integral of the measurements from an accelerometer attached to the athlete's helmet and the rate of turn gyroscopes attached to the athlete's limbs.
2. The differentiation process was carefully chosen to be the mathematical inverse of the previous integration process.

The resultant force calculations were different from resultant force calculations based on optical measurements from conventional motion capture systems, which are often noisy and require significant filtering during the data processing.
Next the combined force from ground reaction forces, wind drag and bearing friction ($\mathbf{F_{GDF}} = m * \mathbf{A_{CoM}} - \mathbf{F_g}$, Figure 5.12) was calculated from the resultant force minus the weight force.

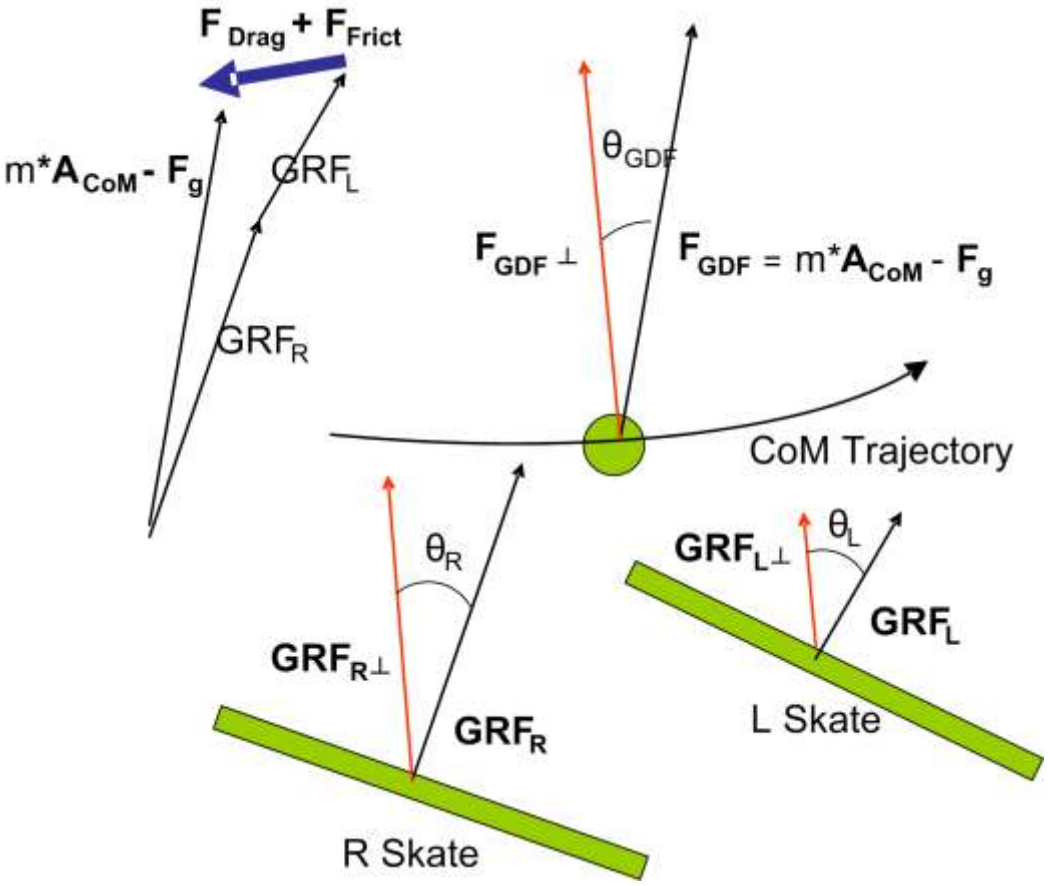

Figure 5.12: Ground reaction force calculations for skating

The projection of the combined force perpendicular to the CoM trajectory was calculated and called the combined perpendicular force ($\mathbf{F_{GDF\perp}}$). The normalised direction vector ($\mathbf{F_{GDF\perp}} / |\mathbf{F_{GDF\perp}}|$) was calculated by taking multiple cross products of the combined force vector ($\mathbf{F_{GDF}}$) and the CoM velocity vector (**Vel**, Equation 5.3 and Equation 5.4).

Equation 5.3
$$\mathbf{Floating\_Vector} = \frac{\mathbf{Vel}}{|\mathbf{Vel}|} \times \frac{\mathbf{F_{GDF}}}{|\mathbf{F_{GDF}}|}$$

Equation 5.4
$$\frac{\mathbf{F_{GDF\_\perp}}}{|\mathbf{F_{GDF\_\perp}}|} = \frac{\mathbf{Floating\_Vector}}{|\mathbf{Floating\_Vector}|} \times \frac{\mathbf{Vel}}{|\mathbf{Vel}|}$$

The magnitude ($|\mathbf{F_{GDF\perp}}|$) was calculated by multiplying $\mathbf{F_{GDF}}$ by the cosine of the angle (θ_{GDF}) between the vectors $\mathbf{F_{GDF}}$ and $\mathbf{F_{GDF\perp}}$. The cosine of the angle θ_{GDF} was found using the dot product (Equation 5.5).

Equation 5.5 $$\cos\theta_{GDF} = \frac{\mathbf{F_{GDF}}}{|\mathbf{F_{GDF}}|} \bullet \frac{\mathbf{F_{GDF\perp}}}{|\mathbf{F_{GDF\perp}}|}$$

The combined perpendicular force $\mathbf{F_{GDF\perp}}$ was assumed to be equal to the sum of the ground reaction forces perpendicular to the CoM trajectory ($\mathbf{GRF_L}\perp + \mathbf{GRF_R}\perp$, Equation 5.6). This assumption required that both wind drag and skate bearing friction acted mainly perpendicular to the CoM velocity vector. This assumption ignored the aerodynamic lift force and the fact the skate trajectories were not exactly the same as the CoM trajectory.

Equation 5.6 $$|\mathbf{F_{GDF\perp}}| = |\mathbf{GRF_R}\perp| + |\mathbf{GRF_L}\perp|$$

Next the magnitude of the right foot ground reaction force ($|\mathbf{GRF_R}|$, Equation 5.8) was calculated by rearranging Equation 5.7, which was derived from trigonometry (Figure 5.12) and substitution of a re-arranged Equation 5.2 into Equation 5.6. The cosines of the angles (θ_L and θ_R) were calculated by dot products using the vectors normal to the skate soles and the normalised combined perpendicular force vector ($\mathbf{F_{GDF\perp}}$ / $|\mathbf{F_{GDF\perp}}|$, found by Equation 5.4). Ratio is the ratio calculated from measurements made by the foot scan insole system (Equation 5.2).

Equation 5.7 $$|\mathbf{F_{GDF\perp}}| = |\mathbf{GRF_R}|\cos\theta_R + |\mathbf{GRF_R}|\frac{Ratio}{1-Ratio}\cos\theta_L$$

Equation 5.8 $$|\mathbf{GRF_R}| = \frac{|\mathbf{F_{GDF\perp}}|}{\cos\theta_R + \cos\theta_L \frac{Ratio}{1-Ratio}}$$

The magnitude of the left foot ground reaction force was then calculated (Equation 5.9) by once again re-arranging Equation 5.7.

Equation 5.9 $$|\mathbf{GRF_L}| = \frac{|\mathbf{F_{GDF\perp}}| - |\mathbf{GRF_R}| * \cos\theta_R}{\cos\theta_L}$$

Finally the directions of the ground reaction forces ($\mathbf{GRF_R}$ and $\mathbf{GRF_L}$) were defined as the vectors normal to the skate soles.

Dissipative force calculations: Wind drag and bearing friction

In slalom skating and ski racing the dissipative forces of wind drag and friction have a large effect on athlete performance ($\mathbf{F}_{\mathbf{Dissipative}} = \mathbf{F}_{\mathbf{Frict}} + \mathbf{F}_{\mathbf{Drag}}$). It was proposed that the dissipative forces could be estimated by minimising the residual to Equation 5.1, the residual between the estimated ground reaction forces (calculated in Equation 5.8 and Equation 5.9) and the resultant force ($\mathbf{F}_{\mathbf{GDF}} = m * \mathbf{A}_{\mathbf{CoM}} - \mathbf{F}_{\mathbf{g}}$) attributed to ground reaction forces, wind drag and bearing friction (based on Figure 5.12).

Bearing friction ($\mathbf{F}_{\mathbf{Frict}}$) is parallel to but opposing the direction of travel of the skate. It was modelled from Equation 5.10 using the ground reaction force component normal to the skate sole ($|\mathbf{GRF}|$), the co-efficient of friction ($K_{Friction}$), and the normalised velocity vector of the athlete's feet ($\mathbf{V}_{\mathbf{Foot}} / |\mathbf{V}_{\mathbf{Foot}}|$). In Equation 5.10 normalisation of the foot velocity produces a unit vector describing the direction of the instantaneous velocity of the skate and is required to transform the one dimensional friction force calculated in the local orientation of the skate into a three dimensional force acting in the global coordinate system.

Equation 5.10
$$\mathbf{F}_{\mathbf{Frict}} = -|\mathbf{GRF}|K_{Friction}\frac{\mathbf{V}_{\mathbf{Foot}}}{|\mathbf{V}_{\mathbf{Foot}}|}$$

Wind resistance was modelled from Equation 5.11 using the CoM velocity vector ($\mathbf{V}_{\mathbf{CoM}}$), the lumped coefficient of wind drag (K_{Drag}) and the normalised CoM velocity vector ($\mathbf{V}_{\mathbf{CoM}} / |\mathbf{V}_{\mathbf{CoM}}|$). In Equation 5.11 the athlete's cross sectional frontal area and air density are assumed to be constant and then halved to produce a lumped wind drag coefficient.

Equation 5.11
$$\mathbf{F}_{\mathbf{Drag}} = -|\mathbf{V}_{\mathbf{CoM}}|^2 K_{Drag}\frac{\mathbf{V}_{\mathbf{CoM}}}{|\mathbf{V}_{\mathbf{CoM}}|}$$

A set of equations representing a force balances for the inline skating data were set up in MATLAB. It was then possible to find the coefficients of friction and wind drag (K_{Drag} = 0.58Ns^{2}m^{-2} and $K_{Friction}$ = 0.016, Equation 5.10 and Equation 5.11) that minimised the sum of the squared residual forces (Equation 5.1). More calculations are available in Appendix B.

Component power calculations

During three dimensional movements such as skating and skiing where the athlete turns and changes direction, it is useful to calculate the power of each external force. A positive power means that the external force is acting to increase the athlete's CoM velocity at that instant in time. Power in Watts is a scalar quantity and from three dimensional forces power is calculated from the dot products of the component force vectors and the CoM velocity vector.

Component energy calculations

While the power developed by each external force shows the instantaneous effect on the resultant CoM motion, an energy analysis shows the net contribution of a particular force over an entire course, or sections of a course. Energy changes or work done by the external forces are calculated by the integral of the power. In this way different external forces that change throughout course can be given a scalar value describing the energy contribution to the motion in Joules. A positive energy means that the force has done work that has acted to increase the athlete"s kinetic energy, and therefore has acted to increase the athlete"s velocity.

5.2.2. Results and discussions

The data driven animations where enhanced to include calculated external forces acting on the athlete. These forces were scaled (1 metre = 500 Newton) and colour coded (green for a positive power and red for a negative power) and shown dynamically about their point of application. The side view of Run 2 is most appropriate for viewing the dissipative forces (Video 5.7) of wind drag and bearing friction, which are much smaller than the ground reaction and gravity forces. The enhanced data driven animation is a very effective way to display the affects of external forces on the athlete"s performance.

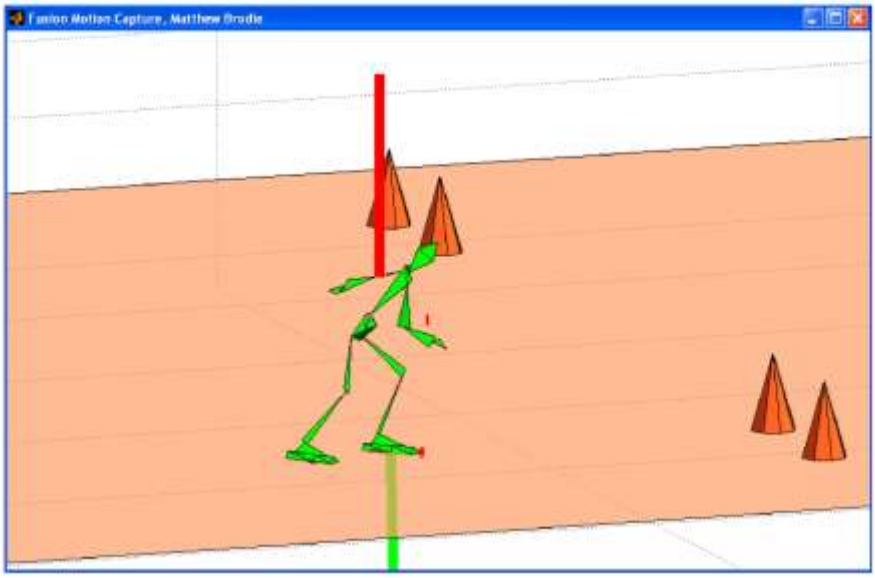

Video 5.7: Appendices\FMC Video\Skate_All_Force_Side.avi

Limitations of modelling the dissipative forces

The wind drag and bearing friction displayed in the data driven animation (Video 5.7) were modelled by two equations requiring two coefficients of friction (K_{Drag} = 0.58Ns^{2}m^{-2} and $K_{Friction}$ = 0.016, Equation 5.10 and Equation 5.11). The two coefficients were chosen in order to minimise the sum of the squared residual forces (Equation 5.1). Normally distributed noise in the measurement data would not have affected the selection of the coefficients of wind drag and bearing friction, but extreme statistical outlying data points might have. For this reason

the window of data used to calculate the coefficients was carefully chosen to exclude the start synchronisation jump and stationary periods. More discussion about how the dissipative force coefficients were calculated and the potential for error is provided (Appendix B).

How close were the modelled forces to the true bearing friction and wind drag forces? The approach taken suffered from several problems. Over the entire course it was unlikely that constant lumped coefficients (K_{Drag} and $K_{Friction}$) accurately modelled the true forces.

The bearing friction did not include any non-linear bearing friction arising from torsion applied to the bearing during a skating stroke. Maybe a viscous friction model (taking account of the compression of the soft plastic wheels and incorporating velocity dependency) should have been used as well. In any case the bearing friction coefficient used ($K_{Friction} = 0.016$) was greater than that of ice skating (0.003-0.007, (van Ingen Schenau, 1982) but less than that of skiing on both hard and soft snow (0.04-0.2, (Shimbo, 1971) and close to the value used for roller skis on asphalt (0.021, (Spring, et al., 1988).

The wind drag coefficient was dependant on both the cross sectional area of the athlete, which was not constant over the course, and Reynolds number. Reynolds number depends on effective wind speed. According to measurements made in a wind tunnel of speed skaters below $19ms^{-1}$, the wind drag coefficient is not constant, but as wind speed increases, the wind drag coefficient decreases (van Ingen Schenau, 1982). Schenau reported lumped wind drag coefficients of around $0.15Ns^2m^{-2}$ for speed of $12ms^{-1}$, but also reported that at $5ms^{-1}$ (close to the maximum speed of our athlete at $4.5ms^{-1}$) the lumped wind drag coefficient increased by around 2.5 times to approximately $0.40Ns^2m^{-2}$. Our athlete also used an upright stance which was reported to further increase the wind drag coefficient by a factor of 1.2-1.5. Considering all these factors, the value for the average wind drag coefficient used ($K_{Drag} = 0.58Ns^2m^{-2}$) seemed well within reason.

Comparing the effects of different external forces

Each external force acts in three dimensions but visually it is difficult to display this information. Since the X-axis was main axis of motion through the slalom course, only the X-axis components of the external forces are displayed. In Figure 5.13 the left and right foot forces have been combined. The magnitude of the X-axis ground reaction force (up to 450 N) is well over an order of magnitude greater than both the wind drag and bearing friction forces which are very similar (~10 N in magnitude). The athlete‟s direction of motion reversed between gates 3 and 4 accounting for the change in sign of the forces. The ground reaction X-axis forces were close to zero near each gate but fluctuated between the gates indicating the athlete accelerated and braked between the gates but maintained a relatively constant speed at each turn apex.

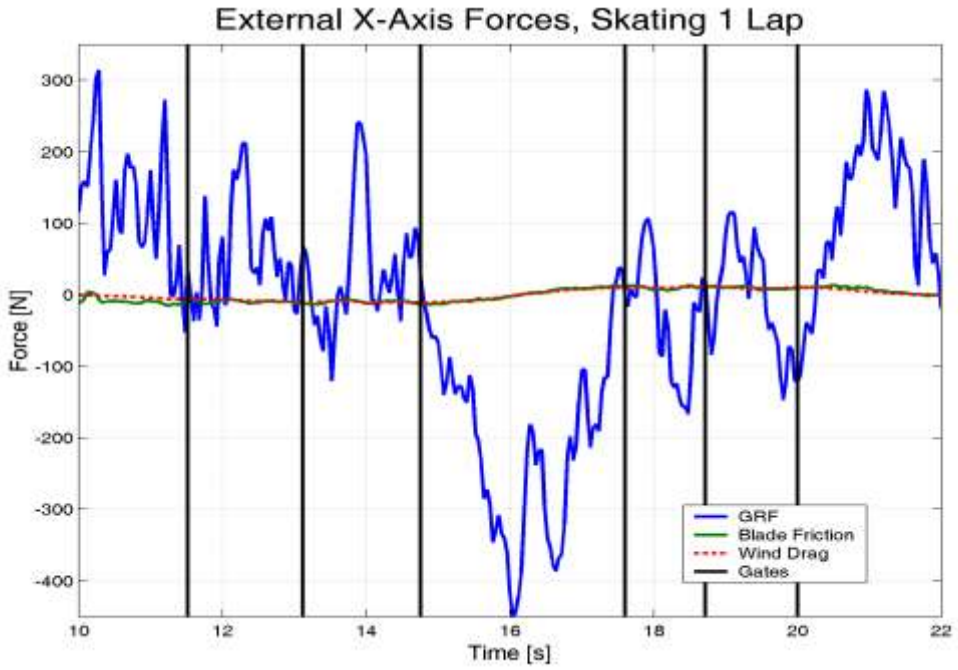

Figure 5.13: Calculated Forces in the X-Axis

Because the athlete‟s direction of motion changed, force vector diagrams are useful to visualise the effects of the forces on the athlete‟s CoM trajectory at different parts of the course. The first force vector diagram (Figure 5.14) shows the effect of the resultant forces on the athlete‟s CoM trajectory. The thick black line is the athlete‟s CoM trajectory while the thin coloured vectors show the resultant external forces acting on the athlete. Light green vectors indicate periods of acceleration while dark red vectors indicate periods of braking. The athlete accelerated from the start to gate 2 and then braked after gate 6. Once race pace was reached, approximately between gates 2 and 6, the athlete braked immediately before the turn apex and accelerated immediately after the turn apex. This suggests the athlete‟s performance was limited by the speed he took the corners, which was less than his skating speed between the gates.

The second force vector diagram (Figure 5.15) shows both left and right foot forces. In this figure bearing friction has been added to the ground reaction forces normal to each skate. The length of each skate stroke, when viewed in the global coordinate system, increases with the athlete‟s velocity. In five out of the six gates the athlete used the outside skate around the apex of each corner. Generally each stroke started with a braking phase when the skate was close to the athlete‟s CoM followed by an accelerative phase as the skate and CoM trajectories diverged rapidly.

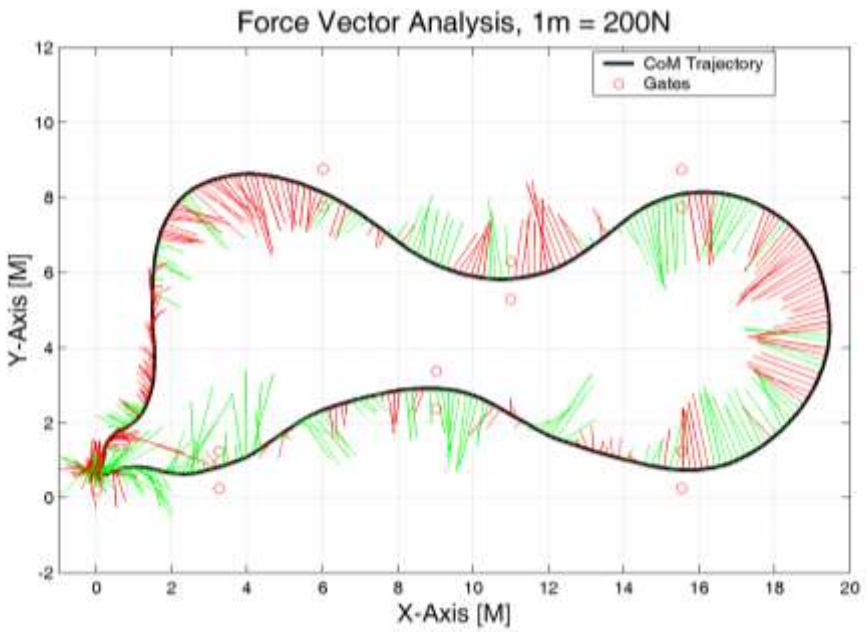

Figure 5.14: Resultant force vector diagram for skating

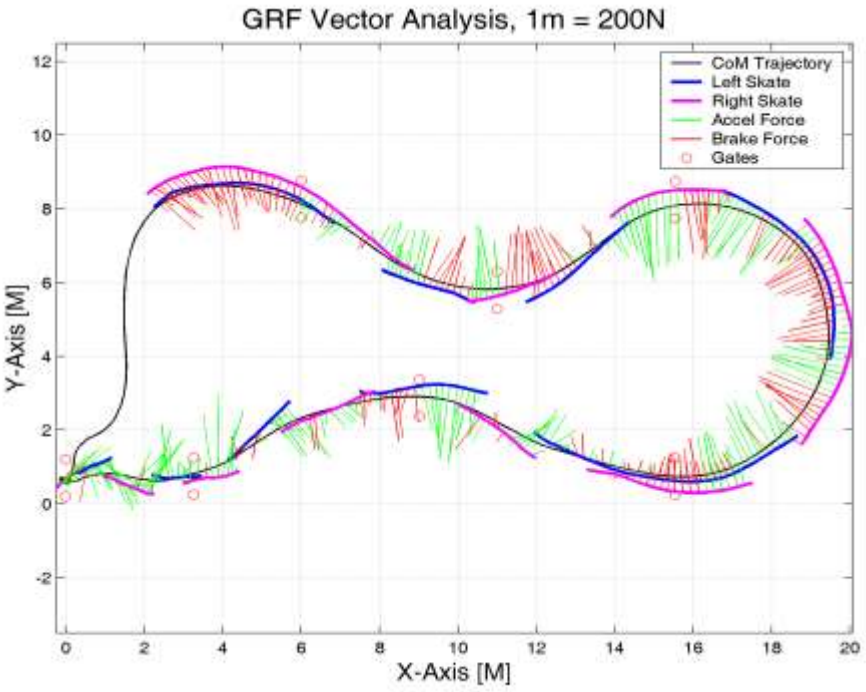

Figure 5.15: Ground Reaction Force vector diagram shows skate strokes

The athlete‟s minimum time over this course was limited in part by his maximum cornering speed and minimum turn radius, which in turn was limited by the horizontal ground reaction force perpendicular to the direction of travel. The horizontal ground reaction force was ultimately limited by the static sliding friction force between the skate wheels and the floor and/or the athlete‟s perception of how far he could lean into each turn. By plotting the vertical ground reaction forces against the horizontal ground reaction forces (Figure 5.16) a friction

cone was produced. The figure shows that 95% of the time the athlete was able to incline up to 31º from the vertical.

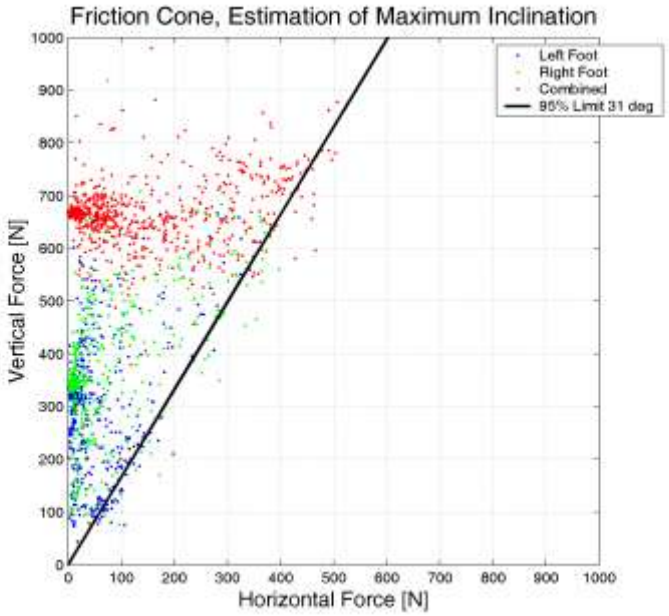

Figure 5.16: Friction cone based on calculated horizontal ground reaction forces

Limitations of the calculated forces

The calculations and analyses of forces apparently revealed some interesting factors that affected the athlete"s performances, but how reliable are the calculated data? In Chapter 3 on page 51, accuracy was discussed. Summarising this discussion, the FMC data were derived from rate and acceleration measurements and so if the FMC data were free of visual artefacts then the underlying rate and acceleration measurements would be accurate enough to have value in further biomechanical analyses. In section 5.1.4 on page 91 the skating data were assessed for visual artefacts. Visual artefacts were found only in the left shank segment and were corrected by adjusting the IMU to body segment mapping.

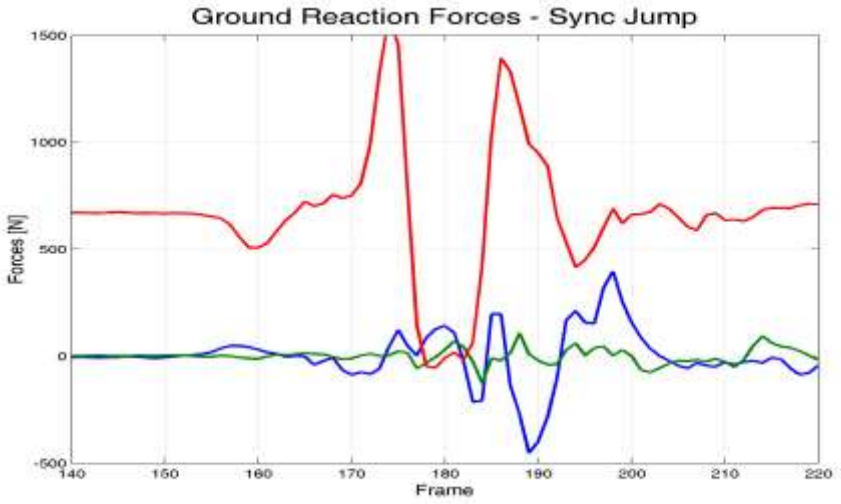

Figure 5.17: Airborne ground reaction forces

Reliability could have been decreased by measurement noise. The measurement noise could have been a consequence of body model error, IMU sensor error, soft tissue artefacts, and global trajectory error, which combined could have resulted in the calculated forces containing some high frequency noise. This noise was first estimated from the total ground reaction forces calculated during airborne phase of the start synchronisation jump (the reader is invited to view Video 5.7: **Appendices\FMC Video\Skate_All_Force_Side.avi** frame-by-frame) when the athlete is airborne there should be no ground reaction forces. There were forces observed, up to 150N (see Figure 5.17 around Frame 180).

The maximum measurement noise of 150N is an acceptable level of noise when compared to the total ground reaction forces which often exceeded 1000N. 150N is however a significant proportion of the X-axis ground reaction forces which peaked around 450N (see Figure 5.13). The measurement noise was estimated from the synchronisation jump that was performed when the athlete was nearly stationary before he passed through the start gate. This is the worst case scenario for two reasons. Firstly, before passing the start gate there were insufficient checkpoints to enable the fusion algorithm (Figure 5.3) to accurately determine the global trajectory. Secondly, the synchronisation jump is highly dynamic with an explosive take off and large landing impact.

If the measurement noise while skating quickly between the checkpoints was as high as 150N then the calculated forces displayed as lines in Figure 5.13 would have been swamped by high frequency fluctuations. The high frequency fluctuations visualised in Figure 5.13 appear to be around 25N and therefore it is likely the measurement noise while skating between the gates was less than 25N. The measurement noise for FMC might well be less than 25N because the athlete‟s true ground reaction forces should contain some high frequency content which should also be visualised in Figure 5.13.

The forces were not smoothed by filtering so even if the noise level was as high as 150N this is a large improvement on the error associated with unfiltered inverse dynamic solutions traditionally available from optical motion capture systems. These errors are reported to be as high as 10,000m/s^2 and further need to be multiplied by the subjects mass to get an estimated force error (Nachbauer, et al., 1996).

The measurement noise did not seem to significantly affect the force vector analyses (Figure 5.14 and Figure 5.15). The analyses show distinct periods of acceleration and breaking. The analyses also show consistent direction and magnitude of forces, directed into each turn. The measurement noise also did not affect the friction cone analysis which was based on the complete data set. This discussion has highlighted several differences between the properties of FMC data and traditional optical motion capture data. It has demonstrated how the reliability of the analyses of FMC data was enhanced by the large amounts of data it was practical to collect and how any measurement noise at a single point in time probably had little effect on the overall analysis.

Power analysis and the work of external forces

In this slalom skating experiment the direction of movement changed significantly through the course. Each external force affected the athlete‟s speed differently depending on both the magnitude of the force and the relative angle between the force and the athlete‟s velocity vector. Larger forces parallel to the athlete‟s trajectory affected speed more than small forces perpendicular to the athlete‟s trajectory. In order to quantify the effects of different forces on speed a power analysis could be useful (Figure 5.18).

In Figure 5.18 the greater the positive power of a force the more work the force is doing to increase the athlete‟s speed, while a negative power indicates the force is acting to reduce the athlete‟s speed. The power dissipated by both bearing friction and wind drag forces reached a minimum of around negative 60W. Ground reaction force power fluctuated. From gate 2 to gate 6, before the apex of each turn, it was negative and slowed the athlete but became positive and accelerated the athlete out of each turn.

The power analysis showed the instantaneous effect of each external force on the athlete‟s speed, but in order to quantify the effect of each force over the duration of the course a work/energy analysis could also be useful (Figure 5.19). The energy analysis shows the athlete did significantly more work with his right foot until 20 seconds and then also favoured his right foot for braking from 20-25 seconds.

Although the forces of wind drag and bearing friction were small in Figure 5.13, they did a significant amount of negative work equal to the amount of positive work done by the ground reaction forces over the course and so should also be considered limiting factors to the athletes performance. Over the speed range of the athlete (0-4.5 m/s) bearing friction dissipated slightly more energy than wind drag. Gravity did positive work when the athlete‟s CoM was lowered by a more aerodynamic stance, but over the course had no net effect.

Validity of power and work analyses

The power analysis is formed by the dot product of the force vector and velocity vectors and so any measurement noise in the force data set (~25N while skating) is likely to be scaled by the athlete‟s velocity (around 4m/s) and so is probably less than 100W. The work analysis contains very little measurement noise because it is obtained by integrating the calculated powers, a step which reduces the high frequency measurement noise. Measurement noise is unlikely to have affected the conclusions drawn from either the work or power analyses because the trends over several turns were analysed.

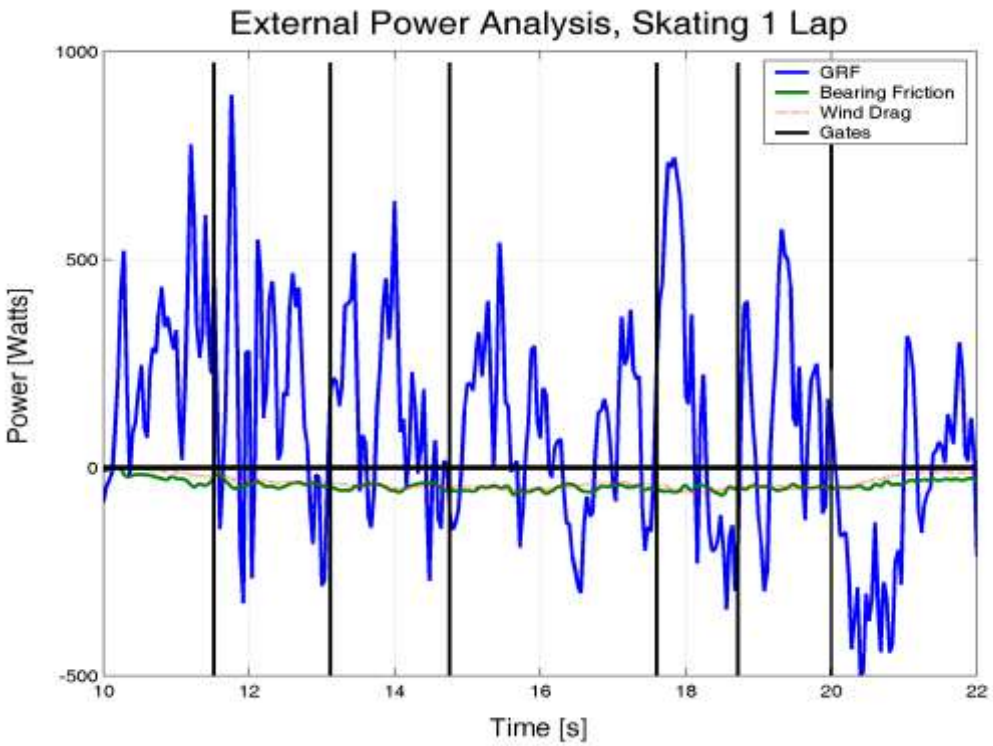

Figure 5.18: Power analysis of external forces

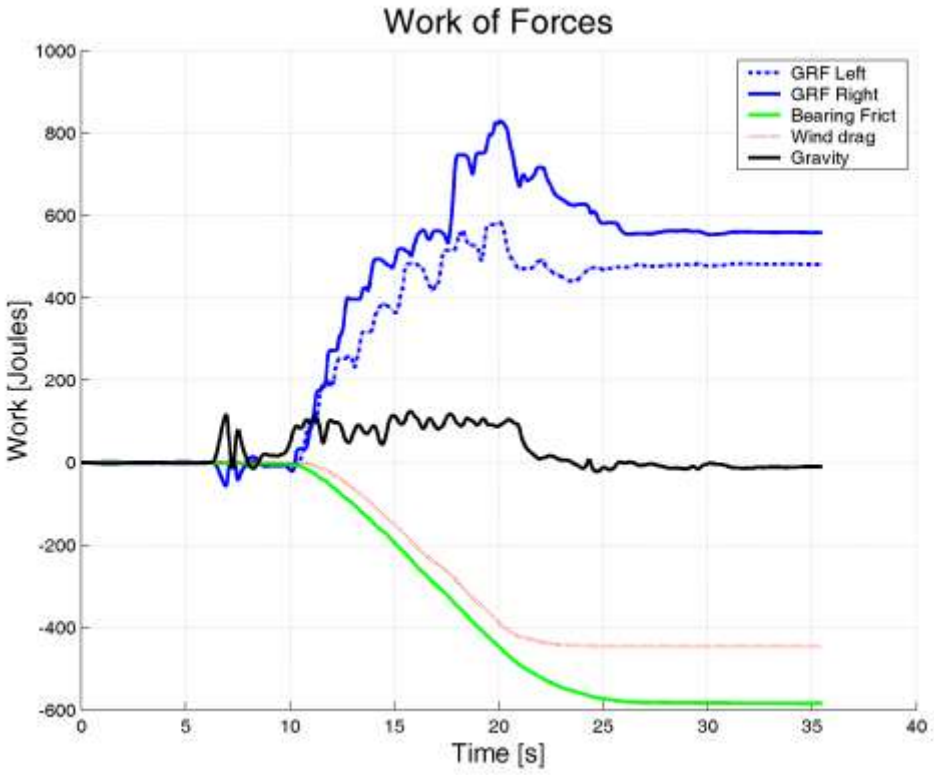

Figure 5.19: Work done by different external forces

5.3. Variability of inline skating global trajectory

Human movement contains natural variability, even for simple tasks. For example, when standing stationary in bipedal stance, natural postural sway is unavoidable (Zatsiorsky & Duarte, 2000). The athlete skated five laps through a six-gate slalom course described but no two laps were identical (Figure 5.20), and the variability in the CoM trajectory changed in different parts of the course. The hypothesis to be investigated in the section is that the variability in CoM trajectory through the course is related to how the athlete plans and executes his movements.

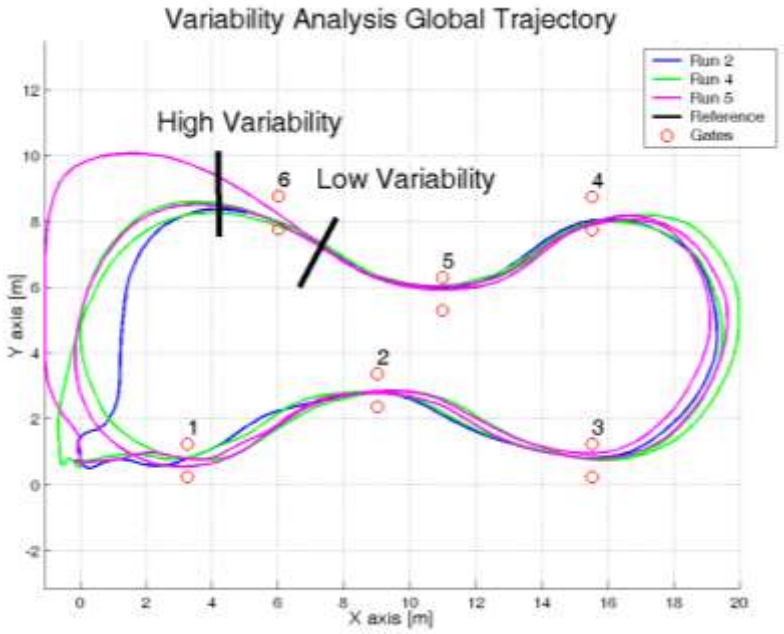

Figure 5.20: Analysis of variability in global trajectory

5.3.1. Methods and calculations

Variability in global trajectory

Variability in global trajectory is a measure of how spread-out in space the trajectories from different laps are. Visual inspection of the data spread reveals there is less variability before gate 6 than after gate 6 (Figure 5.20). A quantitative measurement of variability in space was developed for inline skating trajectory called the root mean squared (RMS) variability. First the mean trajectory was defined based on the mean location at each point on the course for all laps skated. Then for each point on the mean trajectory the closest point to the vector normal to the mean trajectory from each lap skated was measured. Finally for each point on the mean trajectory the root mean squared (RMS) distance was calculated.

5.3.2. Results and discussion

Variability in trajectory around the course was measured and is displayed below (Figure 5.21). Where the variability in Figure 5.21 is low the trajectories of different laps are tightly grouped in Figure 5.20.

Global trajectory accuracy

The variability results have an important implication for the accuracy of the global trajectory estimated in section 5.1.4 on page 91. Based on the temporal resolution of the video camera used to make a comparison, the error was previously estimated to be around 0.18m. The variability analysis suggests however that the error may be as low as 0.05m while skating between the gates. Between gates 5 and 6 in Figure 5.21 the variability of the five trajectories remains below 0.05m over a distance of around 5m. This measured convergence of multiple trajectories would be impossible if the error was as high as 0.18m as was previously estimated. This highlights how the fusion algorithm, presented in Figure 5.3, may produce results that are more accurate than the raw data, by combining multiple data streams of complimentary data. FMC exploits the properties of the signals from IMUs and GPS, fusing them without the need for post low-pass filtering and so ensures maximum derived signal bandwidth.

Variability in trajectory

In Figure 5.21 the RMS variability ranges from less than 3cm just before gate 2 to over half a metre after gate 6. In general variability is least just before each gate and on the „finish straight" between gates 5 and 6. It is proposed that where the trajectory variability increased (such as between the gates in Figure 5.20 and Figure 5.21) the athlete"s control of his trajectory decreased and where the variability decreased the athlete"s control increased, such as near each gate.

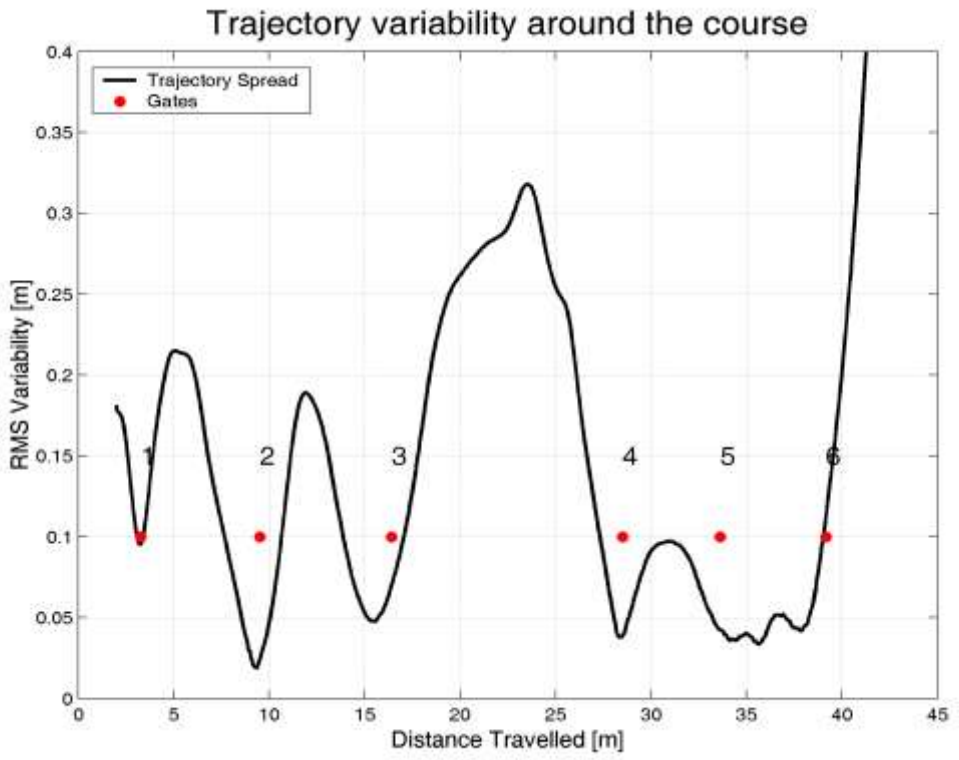

Figure 5.21: Trajectory variability around the course

The results suggest that specific checkpoints on the course were very important and the athlete controlled his movements in an attempt to pass close to these points. The checkpoints were generally just before and close to the inside marker of each gate, these check points would have allowed the athlete to pass efficiently through each gate. The low variability between gates 5 and 6 shows that the fastest path between the gates on the finish straight was more important than setting up for the end turn after gate 6. These results show that the athlete was capable of using different strategies on different parts of the course, depending on the situation. It is believed that this type of analysis could also reveal interesting information about how racing trajectories are constructed by the athlete.

Open radius slalom gate passing strategy

The turn radii of the athlete's turns were calculated by dividing his velocity squared in the XY-plane (V^2_{XY}) by his acceleration perpendicular to the velocity vector ($A_{XY\perp}$, Equation 5.12).

Equation 5.12 $$Radius = \frac{V_{XY}^2}{A_{XY\_}}$$

Unexpectedly the turn radius analysis (Figure 5.22) shows that the athlete did not make the tightest turn either at the gate or at the turn apex. Figure 5.22 shows the athlete used a mean turn radius of around 6 metres through gates 2 and 5 (zero distance on the x-axis) and the

tightest part of the turn (mean radius of 2-3 metres) generally occurred at lease one metre before and after the gate.

Based on these results it appears that in the approach to the turn the athlete aimed not for the gate or the turn apex. This is because the least variability was not at the gate or turn apex but just before the gate. The athlete appears to have aimed for the start of a repeatable approach arc beginning between one and two metres before the turn apex, which takes him between the gates. The proposed approach arc starts with a tight turn (mean radius 2-3 metres, Figure 5.22) about 1.5 metres before the gate, which sets the athlete up so he can pass safely through the gates with a more open turn (mean radius ~6 metres). The proposed approach open gate passing strategy also takes the athlete close to a „check point" generally just before the gate where global variability is least in Figure 5.21.

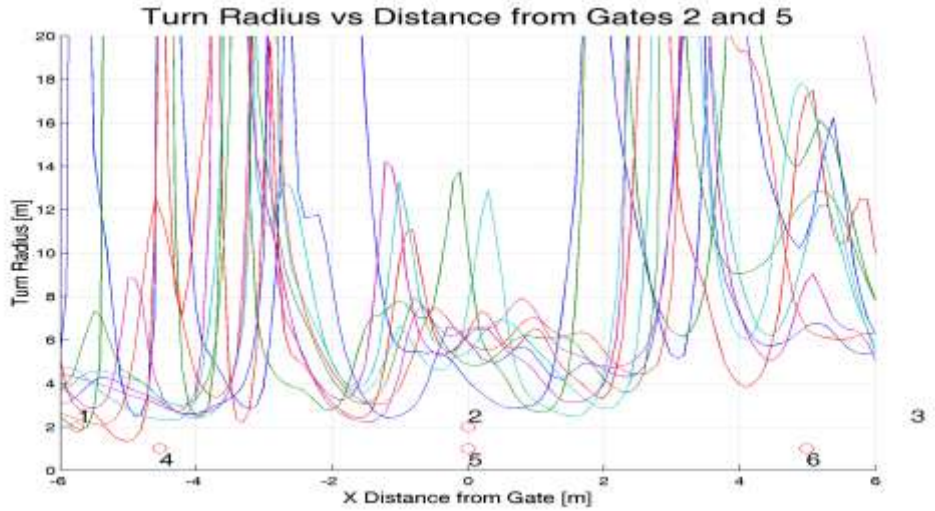

Figure 5.22: Analysis of turn radius

As a result of the open gate passing strategy the athlete did not use maximum force inclination (and therefore minimum radius) while passing the gates and this enabled him to create enough external torque about the anterior posterior axis to rotate quickly between the turns and onto the opposite skate edge before the next turn.

The idea of a repeatable approach arc that the athlete is both capable of and aware of has been previously suggested as a way that the global trajectory could be constructed by the athlete (LeMaster, 1999). But until now there has been very little data available to investigate these ideas. The open radius gate passing strategy may be slower than the theoretical optimum turn radius; logically it seems it would be faster to make a tighter turn at the gate while maintaining speed.

The athlete"s performance may have been limited by his pre-determined perception of a safe passing trajectory through each gate. If so, he might improve by some training that focuses on decreasing his perceived limits of turn radii and increasing the inclination angle he used. During training non-uniform gate spacing could also be used to challenge the athlete to use a

variety of strategies and turn radii/inclination angle dependant on the course position, this type of control is possible as demonstrated by our athlete who used a straight finish to gate 6. Markers could be placed on the course to help the athlete identify the optimum location to start the entry arc to each turn and to identify any global checkpoints over which he should pass.

Final caveats

It should be noted that the athlete while encouraged to skate quickly through the gates he was not instructed to skate as quickly as possible and his strategy may also have been influenced by the high capital value of the fusion motion capture system components. It is therefore possible minimum course time was not his only consideration. In this section turn radius was analysed but it is possible that other parameters such as inclination angle (leaning angle) into the turn are of equal if not more importance to the athlete.

5.4. Simulation of athlete specific optimum trajectories

Inline skating through a set of slalom gates has several similarities to skiing. It is also easier to simulate because the modelled athlete does not have to choose either a carving turn or a skidding turn and can make turns of almost any radius on the skates. The optimum (fastest) global trajectory of our athlete through the course was modelled. Constraint parameters measured from the athlete‟s performance on the course were used to drive the simulation. The athlete was modelled as a single ridged body using the mean measured inertial properties of the athlete. A turn apex location and turn radius for each gate were chosen as control parameters. Turn apex location and turn radius completely defined the simple model of the athlete‟s trajectory and agrees with the observations of what might have been „important‟ to the athlete from the analysis of global trajectory variability in the previous section.

5.4.1. Methods

Simulation constraints

The simulated trajectory was based on a simplified model of the athlete‟s whole body motion. The effects of individual limb motions or foot strokes were not considered. Instead the following parameters were extracted from the athlete‟s performance to drive the simulation using the fusion motion capture data:

1. Maximum inclination while cornering (~31°). The maximum inclination and the athlete‟s mass (68kg) determine the maximum horizontal forces (*HGRF* ~ 440N) the athlete can produce and therefore the maximum speed (*Speed*) he can make a turn of any given radius (*Radius*, Equation 5.13). The maximum inclination was based on the „friction cone‟, the relationship between the horizontal and vertical ground reaction forces described previously (Figure 5.16).

Equation 5.13 $$Speed = \sqrt{\frac{HGRF * Radius}{Mass}}$$

2. Maximum angular acceleration about the direction of travel (α~5 rad.s^{-2}); The angular acceleration determines how quickly the athlete can rotate from edge to edge between left and right turns. „Bang bang" control was assumed (the athlete accelerates and brakes his rotation with no rest to move from edge to edge) to calculate minimum time of rotation (*Rot_Time*) based on the change in inclination angle between two consecutive turns (θ_{Start} and θ_{End}, Equation 5.14). The turn inclination angles were dependant on the athlete's turn speeds and turn radii and gravity (g, Equation 5.15). The maximum angular acceleration was determined by the root mean square of the angular acceleration about the direction of travel, which was calculated by dividing the previously calculated rate of change of angular momentum by the instantaneous whole body moment of inertia.

Equation 5.14 $$Rot\_Time = 2\sqrt{\frac{\theta_{Start} + \theta_{End}}{\alpha}}$$

Equation 5.15 $$\theta = \tan^{-1}\left(\frac{Speed^2}{Radius * g}\right)$$

3. The calculated coefficients of wind drag and bearing friction (K_{Drag} = 0.58 Ns^{2}m^{-2} and $K_{Friction}$ = 0.016) from the previous analysis.

4. The athlete's power curve defined by the force-velocity relationship (Equation 5.16); the figure of the fusion motion capture data shows the faster the athlete skated the less force was available to increase his speed. This relationship was approximated by a linear equation fitted to the athlete's FMC data (Figure 5.23).

Equation 5.16 $$Force = 716 - 133 * Velocity \text{ (N)}$$

5. The final constraint was the location of the course gates, through which the trajectory was required to pass.

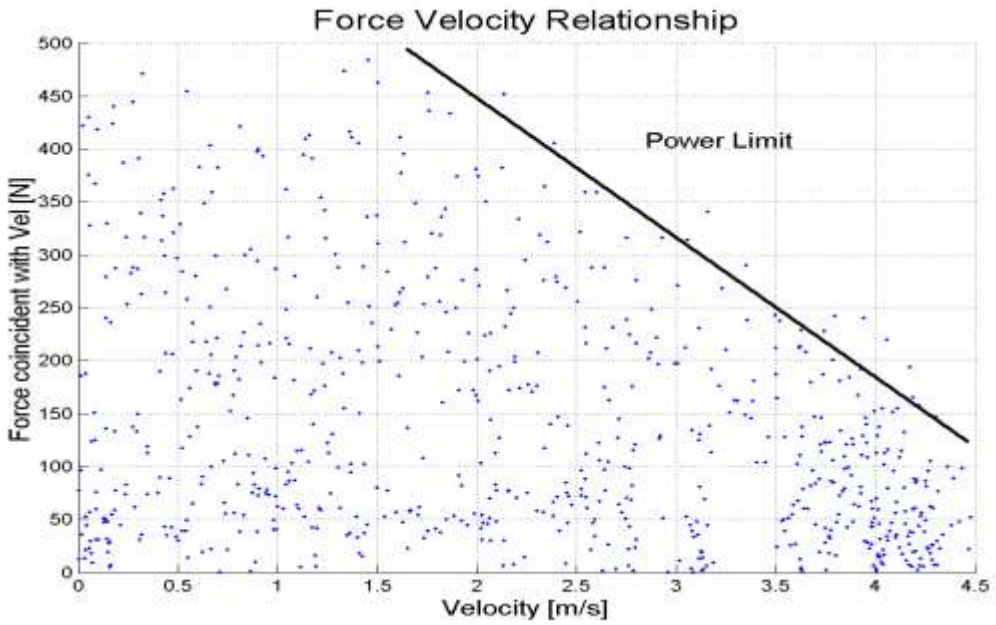

Figure 5.23: The force-velocity relationship

Optimisation of the global trajectory

MATLAB's constrained non-linear minimisation function was used to find the minimum time trajectory that passed between the course gates. The trajectory was found using MATLAB functions written by the author to calculate the time through the course with different combinations of turn apexes and turn radii.

MATLAB's constrained non-linear minimisation function passed the control parameters of turn apexes and radii to the trajectory functions, which returned a course time and information about whether or not the course constraints were exceeded. The starting guess was a trajectory that passed through the inside of each gate with a turn radius of two metres. After 22 iterations of the minimisation function and 786 executions of the trajectory functions the minimum time trajectory was found. It took about 120 seconds using a laptop (Celeron M 1.60GHz processor) to solve for the turn apexes and radii that produced a minimum time trajectory. A variety of starting guesses were used but this was the best result.

The MATLAB functions used to calculate course time used the following procedures: Given the set of turn apexes and turn radii the global trajectory was solved piecewise from turn apex to turn apex. The global trajectory between consecutive apexes was approximated by two circular arcs connected by a straight line (Figure 5.24).

Figure 5.24: Simulated trajectory between two apexes

The maximum speed at about each arc was limited by the simulated athlete‟s ability to incline and therefore produce horizontal ground reaction forces (Equation 5.13). The simulated athlete‟s speed between the arcs was limited by the length of the connecting line and the minimum time required rotating from edge to edge between the arcs according to Equation 5.14. Furthermore, the simulated athlete‟s speed had to be continuous. Starting from the „slowest maximum speed constraint‟, bang-bang control was used to either accelerate the simulated athlete using available ground reaction force power or decelerate the athlete due to wind drag and bearing friction. If during the calculation process the simulated athlete could not brake fast enough to meet a speed constraint, then calculations were re-iterated starting from the new „slowest maximum speed constraint‟ to ensure the simulated speed profile was continuous.

5.4.2. Results and discussion

The simulation was successful in defining a minimum time trajectory through the course. The simulated athlete was able to pass through the course in 10.87 seconds (black line, Figure 5.25). This time was less than the best lap time by our athlete of 13.60 seconds, and represents a 2.73 second or 20% improvement.

In a surprise result: the simulated athlete achieved the improvement by skating slower, which enabled him to take a shorter path with tighter turns. The simulation consisted of eight turns through six gates because two extra turns were required to make the end turns possible. The two extra turns will be named end turn 1 and 2 for the purposes of this discussion. The main difference between the simulated athlete and the real athlete is in the execution of the end turns. For turns 1, 3, 4 and 6 the simulated athlete moved the turn apexes horizontally closer to the centre of the course and this allowed both end turns to be moved inwards and the trajectory shortened (Figure 5.25). The trade-off was a slower maximum speed (4.2 m/s for the simulation reduced from 4.6m/s for the real athlete) limited by his maximum inclination angle (31°) and the tighter turns. It appears the athlete could achieve the resulting 20% time reduction with less effort because less skating power would be required to reach the slower optimum speed, but tighter trajectory control would be required.

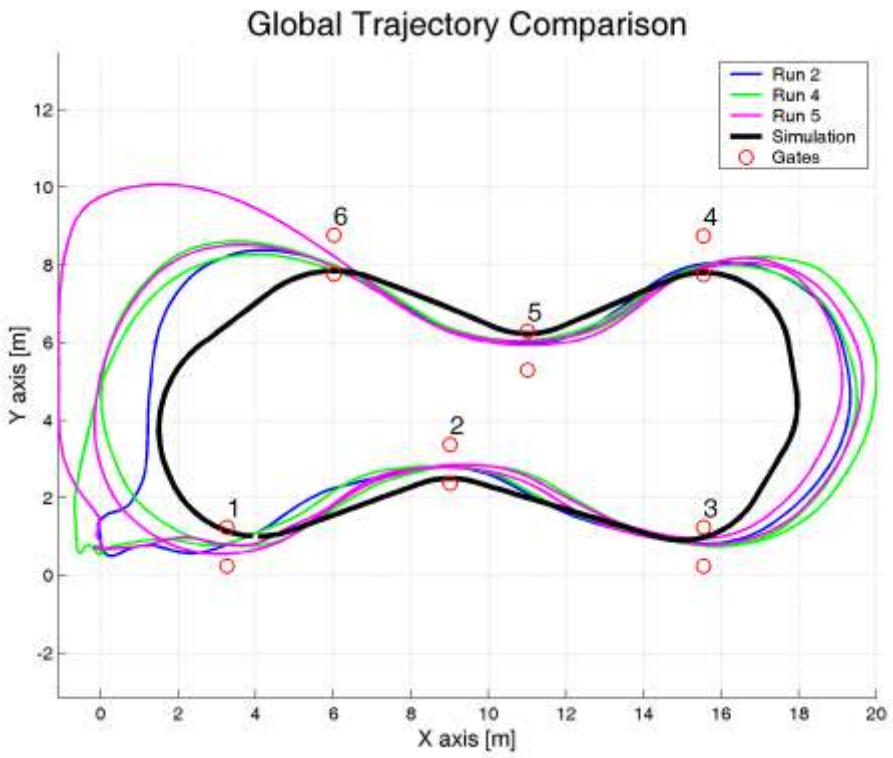

Figure 5.25: Simulated trajectory vs. five actual laps through the course

The simulated athlete's trajectory consisted of a slow section (between gate 2 and gate 5, mean speed 3.7 m/s) and a fast section (between gate 6 and gate 1, mean speed 4 m/s). The turn radii through the slow turns are consistently tighter (2.18-2.27, Table 5.1) than the turn radii through the fast section (2.45-2.76 m).

Turn	Gate 1	Gate 2	Gate 3	End 1	Gate 4	Gate 5	Gate 6	End 2
Radii [m]	2.45	2.19	2.19	2.27	2.21	2.18	2.74	2.76

Table 5.1: Simulated trajectory turn radii

The simulated optimum solution (black line, Figure 5.25) was asymmetric in comparison to the athlete's trajectories (coloured lines, Figure 5.25). From this limited data it could be speculated that humans prefer symmetrical solutions to complex tasks, but the optimum solution may be asymmetrical because the gate spacing was asymmetrical. The simulated results are interesting but care should be taken in interpreting these results because: The solution may be a local optimum, and not the absolute minimum time trajectory. The solution may also be a result of artefacts introduced because of the simplicity of the model, which did not model the individual foot strokes or how the athlete created external torque to rotate from edge to edge between the turns. Unfortunately the optimised solution was not tested on the athlete because of the long time delay between the data collection and the data analysis. The optimised solution was also not tested on the athlete because ski racing and not inline skating is the main focus of the thesis.

6. FMC at Mt. Ruapehu October 2006

Figure 6.1: System diagnostics using a laptop from (Brodie, Walmsley, & Page, 2008c)

Fortune favours the brave; after waiting through two weeks of poor weather and in spite of an inclement weather forecast for the closing week of the winter season, it was decided that an attempt should be made to collect some data at Mount Ruapehu. Fortunately everything worked out, the weather cleared unexpectedly, the equipment was ready, and, the volunteer athlete, a member of a national ski team was available.

This is a technical chapter, it contains the data collection methods used for the motion capture of alpine ski racing at Mt Ruapehu in 2006 (Section 6.1) and some improvements made to the FMC system (Sections 6.2 to 6.7). The results of these improvements on the FMC output are then presented in Section 6.8 which is then followed in Section 6.9 by a discussion about accuracy and errors.

This work contributes significantly to reaching the first milestone:

"To accurately capture the motion of ski racing over a complete race course"

This is, to the author"s knowledge the first time both the local limb segment movements and global trajectory while skiing through a complete giant slalom training course have been accurately captured. In Chapter 3 the motion of an athlete free skiing over a 300 metre course was captured. From the analysis of this data it was possible to determine that limb orientation error was less than 5º, however, the analysis of global trajectory error through a giant slalom course showed errors of greater than 15m and so significant improvements were still required.

In Chapter 5 significant improvements to the system were made. Chapter 5 began with a prototype FMC system that had been developed through laboratory experiments using, the pendulum experiment in Chapter 2, field tests in Chapter 3, and the wand experiments in Chapter 4. It was not known how the new fusion algorithms and biomechanical man body model would perform for slalom skating. It was not known how to display the data in an understandable way or where to start the biomechanical analysis. Chapter 5 was successful in answered all these questions. Global trajectory error was reduced to around 0.05m by the use of a new improved fusion motion capture algorithm. Data driven animations and other data visualisation techniques were developed, biomechanical analyses and simulations of the motion were conducted and therefore, significant steps were made towards the thesis objective.

There are however, many differences between Fusion Motion Capture (FMC) of skiing in this chapter and the FMC of inline skating in Chapter 5. For a start the terrain is not flat, global positioning system (GPS) data are required, the centripetal accelerations and vibrations are much higher, and the environment is a lot more challenging. These problems resulted in some novel solutions that are documented in this chapter. Test data from runs at Mt Ruapehu in 2006 is used to illustrate the improvements made the FMC system.

6.1. Ski racing data collection

The motion of a highly skilled athlete (less than 20 FIS points in their best discipline and mass of 78kg) was captured using the revised prototype FMC system. The athlete completed five runs through a ten-gate giant slalom training course at Mt. Ruapehu Ski Area in 2006 (Video 6.1). The course was over 300 metres in length. The athlete‟s body segment kinematics, including angular velocity and local acceleration were obtained from thirteen IMUs attached to the following body segments; head, torso, pelvis, upper and lower arms, thighs, shanks, and ski boots.

Video 6.1: Appendices\FMC Video\Ruapehu_R3_Video.avi

6.1.1. Instrumentation

IMU placement

The IMUs were attached to each body segment in such a way to reduce skin artefacts. The placement was different from the placement used for the inline skating experiment in order to prevent direct impacts of the IMUs with the course gates. A lycra bodysuit was constructed to contain the connecting wires. The suit had apertures at the location of each IMU so the IMU could be attached directly to the athlete‟s skin with double-sided tape. In addition, each IMU was fastened with a firmly fitting elastic strap attached with Velcro to the suit.

Figure 6.2: Lycra motion capture suit to contain the connecting wires

The exact position of each IMU was specific to alpine ski racing as the IMUs would be damaged by aggressive race strategy if they were attached to the outside of the limbs or the athlete‟s back. The exact positions were:

1. Lower arms, medial surface just far enough from the wrist joints to allow free movement.

2. Medial surface of the upper arm.
3. Immediately inferior to the Sternal Notch
4. Rear of the helmet, approximating the base of the skull (Figure 6.4).
5. Between the posterior superior iliac spines.
6. Lateral surface of the thigh midway between the femoral condyle and the greater trochanter.
7. Shanks on a flat section of the tibia just below the knee.
8. Heels of ski boots, just above the binding, in a protective waterproof casing.

For the purposes of this analysis the ski and boot were modelled as a single rigid body and the IMU for each ski was placed on the heel of each ski boot above the binding but on the part of the boot that was assumed to be rigidly attached to the ski (Figure 6.3).

Figure 6.3: IMU placement behind the ski boot, in a waterproof protective casing.

Figure 6.4: The author modelling the GPS and IMU attached to the helmet

Other measuring equipment

An RS-Scan pressure measurement system was used to determine plantar pressures and the ratio of loading between the skis. Video from a hand held digital camera, panned from a fixed position on the skiers left side of the course was used as an external reference, and to help confirm the validity of the data. A GPS receiver was attached to the athlete‟s helmet and a local GPS base station was positioned near the course.

Equipment list

- 13 x IMUs (XSens Technologies Limited) - Specified accuracy from the manufacturers Kalman filter algorithm in dynamic situations ±3º RMS, **www.xsens.com**.
- 2 x GPS SiRFstar2, single frequency USB receivers, one base station and one rover - 1 Hz output, specified accuracy ±15m RMS in 2D, 0.1m.s^{-1} 95% CI for velocity. Additional information is available at **www.sirf.com**, on the accompanying CD (**Appendices\GPS_Manual.pdf**) and in the reference manual (SiRF Technology Inc, 2005)
- 1 x Sokkia Theodolite, Japan, **www.sokkia.co.jp**
- 2 x Sony DCR-TRV 730E Digital Video Cameras 25fps, **www.sony.net**
- RS-Scan Foot Scan insole system, 100 Hz output, **www.rsscan.com**.

Data logging and synchronisation

Data were logged onto a laptop carried in a backpack by the athlete. This was not ideal but for the prototype system it worked. A program was written in C$^{\#}$ to synchronise and log data simultaneously from two Xbus units and the GPS receiver. Seven IMUs were attached to the first Xbus and six to the second. Data were logged at both 25Hz and 50Hz depending on which laptop was used. Three minutes of logging resulted in about 2.5 mega-bytes of binary data for a typical ski run. Several laptops had to be used because the batteries did not last long in the cold climate and it was easier to replace the laptop than the laptop batteries while on the snow.

Unfortunately the IMU/GPS software synchronisation mechanism was faulty and the two data streams had to be re-synchronised by post processing the data. A synchronisation point was found that minimised the residual between the GPS velocity and integrated global acceleration from the IMUs (Figure 6.5). This was the same method used to synchronise the Coronet Peak data in 2005 described in Chapter 3. Because the GPS data were at 1Hz and the IMU data were at 25 or 50 Hz, the mean IMU velocity over sliding one-second windows was used to get the mean IMU velocity in the synchronisation procedure. Although this method was successful, the minimum residual point was a broad trough and therefore the synchronisation error could be up to two data points or 0.08 seconds at 25Hz. This level of synchronisation error could effect global trajectory but should have no effect on local limb orientation measurements. It would be more reliable in the future to synchronise the data streams directly through hardware coupling.

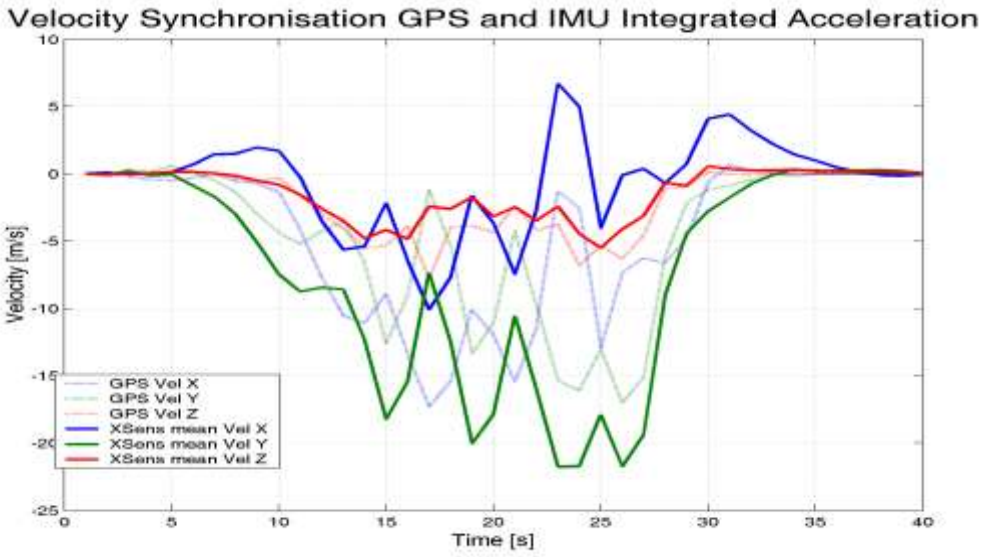

Figure 6.5: Velocity synchronisation of GPS and IMU data

Figure 6.6: System diagnostics using a laptop (Brodie, et al., 2008c)

6.1.2. Experimental

The IMUs were mapped to the athlete‟s body segments through a calibration procedure described in Chapter 4 on page 70. The athlete was instructed to ski at race pace through the course. At the end of each run data was extracted from the athlete‟s data logger for post processing, which is described in detail in the following sections from 6.2 to 6.7. Data from the athlete were then used to drive animations based on the biomechanical man avatar, an accurate anatomical and inertial representation of the athlete.

6.2. The Global Positioning System

In this section ways to improve GPS data accuracy are investigated along with the nature of the measurement noise in the GPS data. GPS data are required to calculate the athlete‟s global trajectory during ski racing. Experiments from Coronet Peak ski area in 2005 showed that the GPS data collected was not accurate for the biomechanical analysis of alpine ski racing and therefore significant improvements were required to the prototype FMC system.

Previously at Coronet Peak, in Chapter 3 in 2005, the GPS chip‟s internally computed location and velocity data were used in a fusion algorithm to estimate the athlete global trajectory but this was found to be unreliable. The values provided by the GPS chip‟s algorithm were inaccurate when the athlete changed direction rapidly. The GPS data were also noisy and contained systematic errors that made the mean error not equal to zero. Global trajectory errors of greater than 15m were observed for a run through a giant slalom race course, which made it difficult to analyse the athlete‟s race performance from the FMC data.

The GPS data is fused with the IMU data to get an accurate estimate of the athlete‟s global trajectory through the giant slalom race course. More details about the fusion process used are provided in Section 6.5, the principals of the algorithm are the same as in Chapter 5 for inline skating. The work done in Chapter 5 showed that the resulting global trajectory error of 0.05m was less than the simulated GPS accuracy of 0.18m based on estimated gate passing times. It is therefore expected that the fusion process will produce data that will be more accurate than either the GPS or IMU data alone.

The accuracy of the measurements of the athlete‟s global trajectories will depend on the accuracy of the underlying GPS data. The fusion algorithm will also perform better if the statistical distributions of noise in the GPS data are known and relatively symmetrical about the mean value. Both the accuracy of the GPS data and the nature of GPS data noise are therefore now investigated. A summary of the findings are presented in section 6.2.3.

The use of the raw GPS pseudo-range and carrier-frequency data as described in sections 6.2.1 and 6.2.2 are now investigated, with respect to producing more accurate estimates of location and velocity. A differential correction is implemented using base station data to correct for systematic atmospheric errors in the pseudo-range and carrier-frequency data. The pseudo-range and carrier-frequency can then be used to compute a differentially corrected GPS receiver location and velocity which are then input into the fusion algorithm. Alternatively the differentially corrected pseudo-range and carrier-frequency data can be directly input into the fusion algorithms. The correction was done because the differentially corrected pseudo-range and carrier-frequency data should have more symmetrical error distributions than the internally computed GPS location and velocity data and so the accuracy of the global trajectory measurements should improve from the previous experiment at Coronet Peak.

GPS pseudo-range and carrier-frequency data were extracted from the SiRF2 receiver using the manufacturers binary communication protocol (SiRF Technology Inc, 2005) and all default internal data smoothing was switched off. The raw binary data were converted to floating point numbers using the vendor‟s protocol. All calculations were post processed using algorithms written by the author in MATLAB.

The raw data were available in the Earth Centred Earth Fixed coordinate system (ECEF), which rotates with the earth. In the ECEF system the origin is the Earth‟s centre. The Z-axis refers to a north-pointing vector through the geographic poles of the earth. The X-axis intersects the Greenwich meridian (where longitude = 0°) and the XY plane makes up the equatorial plane (latitude = 0°).

6.2.1. Pseudo-range and calculating receiver location

Pseudo-range is a pseudo distance measurement between a satellite and a receiver (commonly known as a GPS). If the pseudo- ranges from four satellites to the receiver are known and the satellite locations are known, then it is possible to calculate a unique location for the receiver by a process commonly termed triangulation (Figure 6.7).

The GPS chip pseudo-range (*PR*) data are extracted by serial communication and are contained within the messages with an ID of 28 (Message ID, MID 28). Pseudo-ranges, one for each satellite in view, are based on time-of-flight information from each satellite. The pseudo-ranges are normalised to a distance inside the chip by multiplication with the speed of light. But they are not the actual distances between the satellites and the receiver because time of flight information contains the satellite and receiver clock biases and the path from the satellite to the receiver is curved due to atmospheric effects. The clock biases are due to the fact the internal clocks of the satellites and the receiver are not synchronised. In addition the biases are not stable and drift with time (known as clock drift).

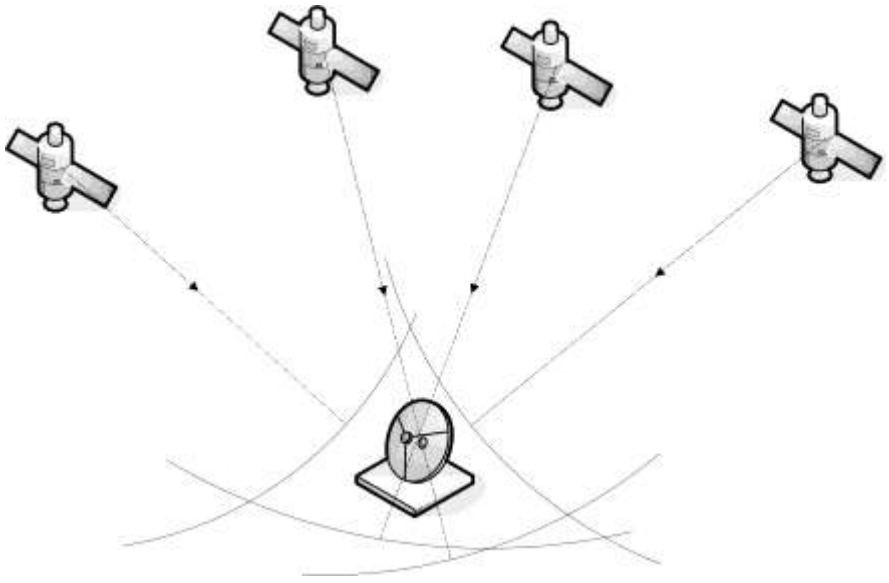

Figure 6.7: Triangulation for receiver location from four satellites

Accuracy of GPS location can be improved by differential correction of the pseudo-range data. To do this a stationary base station at a survey location is required. The base station data is used to remove systematic errors from the pseudo-range data due to changing atmospheric effects. If the base station is located within the vicinity of the rover (GPS receiver attached to the athlete) then the atmospheric effects are assumed to be the same.

The first step to obtaining a differential corrected location measurement is to remove the clock biases. The best estimate of the measured range (*Range*, Equation 6.1) was calculated for each satellite (n=1 to N) for both the GPS receiver attached to the athlete"s helmet (Rover) and the stationary GPS on a tripod beside the course (Base). The effects of satellite and receiver clock bias were accounted for (*Sat_Bias*, extracted from MID 30 and *Bias*, extracted from MID 4). Because of the data format the satellite clock bias was scaled by the speed of light (c=299792458 ms^{-1}) and the receiver clock bias was scaled by $c*10^{-9}$.

Equation 6.1 $$Range_n = PR_n + Sat\_Bias_n * c - Bias * c * 10^{-9}$$

The Range data (Equation 6.1) contained large errors from local atmospheric effects which can be removed. To remove the atmospheric effects the base station data were used to estimate a differential correction (*Range_Corr,* Equation 6.2) for each satellite at each point in time. Before the corrections could be estimated the location of the base station was required. As there were no surveyed points nearby on the ski area, the base station location (*BLX, BLY, BLZ*) was estimated from the median of the GPS location data produced by the GPS base station chip. Estimates of the satellite locations were also required (*SLX, SLY, SLZ*), and were either extracted from the GPS data (MID 30) or were modelled to further improve accuracy.

Equation 6.2

$$Range\_Corr_n = \sqrt{(SLX_n - BLX)^2 + (SLY_n - BLY)^2 + (SLZ_n - BLZ)^2} - Range_{Base_n}$$

Example pseudo-range corrections for six satellites visible from the ski area are shown in Figure 6.8. The corrections were large and fluctuated. The pseudo-range differential corrections (*Range_Corr,* Equation 6.2) were then applied to the GPS rover data from the receiver attached to the athlete (Equation 6.3). The unexplained terms in Equation 6.3 are the GPS rover range data (*Range_R* from Equation 6.1), and the rover location (*RLX, RLY, RLZ*). MATLAB"s non-linear least squares function[3] was used to minimise the residual range error (ε, Equation 6.3) by optimisation the rover location (*RLX, RLY, RLZ*). At least four satellites

[3] By default MATLAB"s nonlinear least squares minimisation chooses the large-scale algorithm. The algorithm is a subspace trust region method and is based on the interior-reflective Newton method described by (Coleman & Li, 1994, 1996).

were required to get a fix, three degrees of freedom for the rover location and one for a new estimate of the receiver clock bias (*Bias*, Equation 6.3).

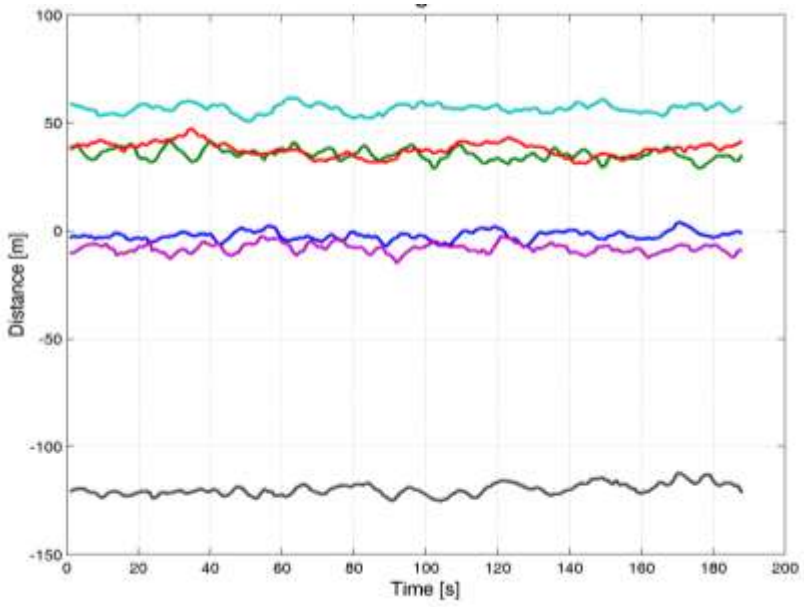

Figure 6.8: Example pseudo-range corrections (six satellites) from skiing

The new clock bias (*Bias*) was assumed to be the mean residual error, found by taking the mean of the residual error (ε, Equation 6.3) for all the satellites in view. After the mean value for residual error was removed there were still small residual errors. The additional residual errors were a result of:

- Instabilities in the receiver and satellite clocks.
- Noise in the signal processing.
- Rapidly changing inconsistent atmospheric conditions.
- Multipath errors because the GPS rover on the athlete"s helmet was not always held at a constant orientation with a clear view of the sky. (Parts of the signal reached the receiver indirectly after reflecting off different surfaces, and therefore the signal contains a bias.)
- The base station was not perfectly synchronised to the rover.

Equation 6.3

$$\sum_{N}^{1}\left(\begin{array}{l}\sqrt{(SLX_n - RLX)^2 + (SLY_n - RLY)^2 + (SLZ_n - RLZ)^2} \\ -Range\_R_n - Range\_Corr_n - Bias - \varepsilon\end{array}\right) = 0$$

Static accuracy of differential GPS location

If GPS data were used to survey gate positions of the race course then it would be important to know the static accuracy of the GPS data. The accuracy of the differentially corrected GPS location data were tested by using two GPS receivers placed on top of a geodetic mark near the top of Mt Victoria, (details of the survey mark are available from the Land Information

New Zealand **http://www.linz.govt.nz/** mark #8106). Eight satellites were visible and the GPS receivers reported ideal conditions (DOP <1m) [4].

However, even under these ideal stationary conditions, at least 20 minutes of data were required for the mean solution to converge to within a metre of the true solution (Figure 6.9, **Blue** X-Axis, **Green** Y-Axis, **and Red** Z-Axis in the ECEF coordinate system). Skiing racing is a dynamic activity with each run lasting less than two minutes and so the single frequency differentially corrected GPS location data alone are unsuitable for its motion capture. The GPS data are also unsuitable for race course gate surveys.

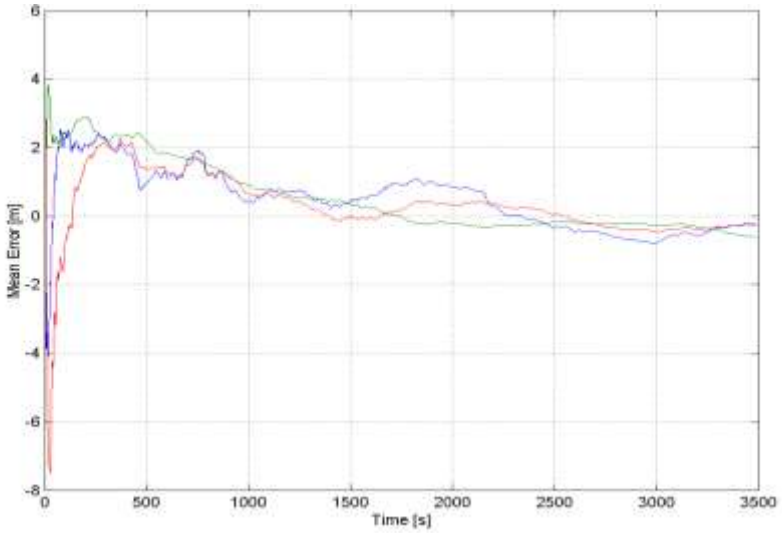

Figure 6.9: Convergence of differentially corrected GPS range data to true location

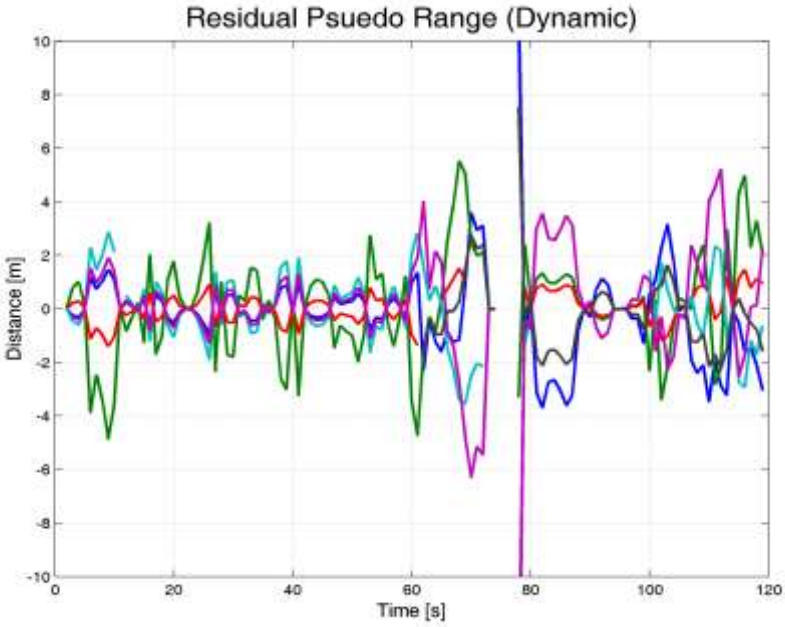

Figure 6.10: Residual pseudo-range (during skiing) used to estimate error

[4] DOP means dilution of precision, a term used by GPS chip manufacturers, 50% off all measurements are expected to fall within the stated DOP.

Dynamic accuracy of differential GPS location

The expected accuracy of the differentially corrected GPS location during skiing was further tested using the residuals from Equation 6.3. It was assumed that because the systematic errors were removed by differential correction the residuals of the pseudo-range data should give an indication of the expected accuracy of the calculated location. Pseudo-range data were collected from a GPS receiver attached to an athlete during an alpine ski run. The pseudo-range data were processed as previously described and a differentially corrected location estimated. The residuals for this solution from Equation 6.3 were then plotted (Figure 6.10).

Figure 6.10 shows that the magnitudes of the differentially corrected pseudo-range residuals are generally between 1m and 5m during skiing. Errors in the calculated location are also expected to be of similar magnitudes as the errors in the residuals and should be have a 95% confidence interval of ±3m. There is signal loss (not enough satellites visible to calculate a fix and with no fix there can be no residuals) around seventy five seconds into the measurement. Before and after the signal loss the residuals increase, probably because the shape of the terrain caused the reception to deteriorate and also caused multipath effects.

In Figure 6.10 the skiing takes place between 30 and 80 seconds and apart from when the signal is lost at the end of the run, the residuals are not affected by the athlete‟s dynamics. Therefore during skiing the GPS location accuracy is not likely to deteriorate. Therefore, it was expected that the differentially corrected location would be more accurate than the GPS chip specification of 15m RMS for horizontal location during normal operation. The residuals also provide additional information about signal noise and will be used to optimise the FMC algorithm.

6.2.2. Carrier-frequency and calculating receiver velocity

Carrier-frequency is used to obtain a measurement of relative velocity between the GPS receiver and each satellite. Relative velocity can then be used to calculate receiver velocity which provides useful information about the athlete‟s trajectory. Alternatively, the carrier-frequency data can be fused with the pseudo-range data, using a Kalman filter, in order to improve receiver location accuracy.

The expected carrier-frequency of satellite signals received by the GPS chip was F=1,575,420,000 Hz (SiRF Technology Inc, 2005). The Doppler Effect was used to convert frequency shifts in the carrier frequencies from the satellites to relative velocities. The carrier-frequency shifts (CF) reported by the GPS chips were scaled internally to give units of velocity. The frequency shifts were multiplied by the speed of light (c=299,792,458ms^{-1}) the constant used by the SiRF2 GPS chip (SiRF Technology Inc, 2005) and divided by the expected frequency (F). The reported carrier-frequency (CF) was not the relative velocity because even though the units were velocity, further processing was required to remove the receiver and satellite clock drifts. The drift was the rate of change of clock bias in hertz.

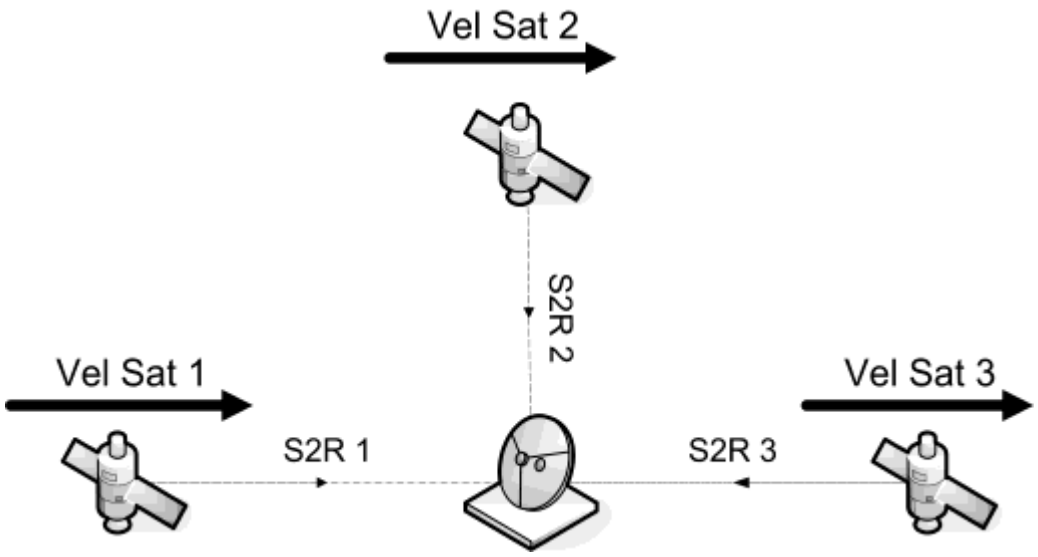

Figure 6.11: Calculation of velocity from carrier-frequency data

To calculate relative velocity the Doppler Effect is used. Doppler Effect explains why an ambulance when travelling towards you appears to have a higher pitched siren than when travelling away from you. As the ambulances approaches the perceived wavelength of the siren is compressed, making it sound higher. As it passes the perceived wavelength of the siren is stretched and the pitch drops. The actual velocity of the ambulance is unchanged as is the actual siren frequency. To calculate receiver velocity, carrier-frequency data from at least four satellites are required. Also required are the satellite to receiver relative location vectors (**S2R,** Figure 6.11) and the satellite velocity vectors. Figure 6.11 shows how the relationship between relative location vector and satellite velocity vector affects the carrier-frequency. When the two vectors are perpendicular (satellite 2) there is no changes to the carrier-frequency. When the two vectors are aligned, the carrier-frequency increases (satellite 1). When the two vectors are opposed, the carrier-frequency decreases (satellite 3).

The scaled carrier-frequency shift data (*CF*, with units of ms^{-1}) was acquired from both the base and rover to calculate a differentially corrected receiver velocity. The first step was to converted the carrier-frequency data into a measured relative speed (*Speed,* Equation 6.4) by subtracting the estimated scaled receiver clock drift (*Drift,* with units of Hz, extracted from MID 4). The clock drift was scaled by the speed of light (c=299,792,458ms^{-1}) over the frequency (F=1575420000 Hz). It was not necessary to remove the satellite clock drift because it was negligible.

Equation 6.4 $$Speed_n = CF_n - Drift * c / F$$

The second step was to calculate the normalised relative location vectors from the satellites to the receivers (|**S2R**|, Equation 6.5) between each satellite location (**SL**= [*SLX, SLY, SLZ*]) and the GPS receivers (**RL** = [*RLX, RLY, RLZ*]). These vectors affect the measured frequency shifts (see Figure 6.11).

Equation 6.5
$$|\mathbf{S2R}|_n = \frac{[SLX_n - RLX \quad SLY_n - RLY \quad SLZ_n - RLZ]}{\sqrt{(SLX_n - RLX)^2 + (SLY_n - RLY)^2 + (SLZ_n - RLZ)^2}}$$

The expected relative speed (*Speed_Exp,* Equation 6.6) is the calculated relative speed between each satellite and the receiver. It is found by the dot product of the normalised relative location vectors (|**S2R**|) with the relative speed vectors. The relative speed vectors are found by subtracting the satellites velocities (**SV** = [*SVX, SVY, SVZ*]) from the GPS receiver velocity (**RV** = [*RVX, RVY, RVZ*]). For the base station this calculation was simplified because the base station was stationary (**RV** = [0 0 0]). The estimates of satellite velocity (**SV**) were either extracted from the GPS chip (MID 30) or were modelled for improved accuracy.

Equation 6.6
$$Speed\_Exp_n = |\mathbf{S2R}|_n * \begin{bmatrix} SVX_n - RVX \\ SVY_n - RVY \\ SVZ_n - RVZ \end{bmatrix}$$

The required differential correction (*Speed_Corr,* Equation 6.7) was then calculated using the base station data. The correction for each satellite was the difference between the expected relative speed (*Speed_Exp*, calculated in Equation 6.6) and the measured relative speed (*Speed*, calculated in Equation 6.4).

Equation 6.7
$$Speed\_Corr_n = Speed\_Exp_n - Speed_n$$

Example differential carrier-frequency corrections for a skiing run are presented in Figure 6.12. The carrier-frequency corrections are between 0ms^{-1} and 0.04ms^{-1}. The units of carrier-frequency are metres per second because as explained at the beginning of this section the carrier-frequency is pre-scaled within the GPS chip. The carrier frequency corrections when scaled by dividing by the athlete‟s velocity through a giant slalom race course of approximately 20ms^{-1} are much smaller than the previous pseudo-range corrections (between 0m and 150m, Figure 6.8) when scaled by the typical giant slalom gate spacing of 20m. It is therefore expected that measurement of the athlete‟s velocity will be more reliable than measurement of the athlete‟s position.

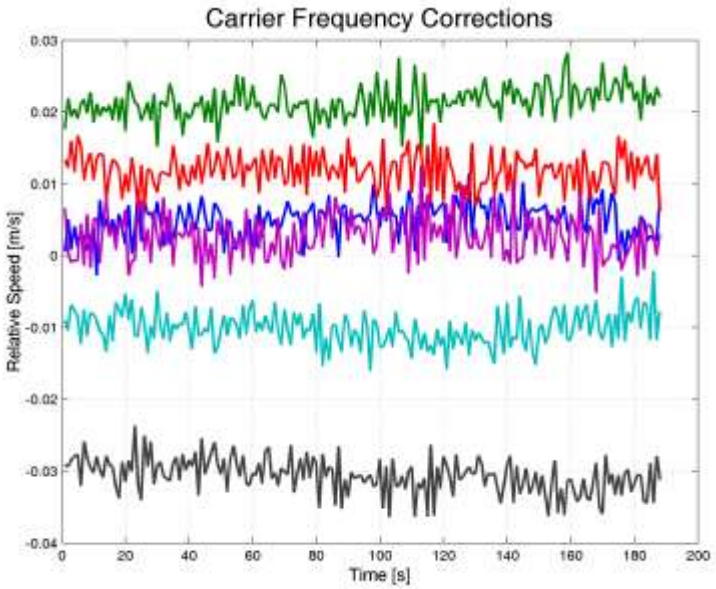

Figure 6.12: Differential carrier-frequency corrections

The differentially corrected GPS velocity of the rover receiver, attached to the athlete, was then calculated. MATLAB"s non-linear least squares function was used to minimise the residual carrier-frequency error (η, Equation 6.8) by optimising of the rover velocity vector. Receiver velocity (**RV**) is incorporated into Equation 6.8 by the term (*Speed_Exp*) that is calculated in Equation 6.6. The term (*Speed_R*) is calculated from the rover data using Equation 6.4. At least four satellites were required to get a fix, three degrees of freedom for the rover velocity vector and one for a new estimated of the receiver clock drift (*Drift*).

Equation 6.8 $$\sum_{N}^{1}\left(Speed\_Exp_n - Speed\_R_n - Speed\_Corr_n - Drift - \eta\right) = 0$$

Differential GPS - integrated velocity accuracy

The accuracy of the integrated GPS velocity data to determine location relative to a base station was tested (Figure 6.13). Integrated velocity could be used to determine athlete location relative to the known position of the start gate with more accuracy than GPS location data alone. Two GPS receivers were used. The GPS base station was attached to a 1.5 metre tripod in the middle of a large car park with an unobstructed view of the sky. The subject then took the second GPS receiver (rover) and walked a loop, stopping at two points marked with cones. The subject started and finished with the GPS rover next to the GPS base station.

The rover velocity was integrated to get a position relative to the base station. Because the ECEF coordinates were used the total distance travelled is the most informative parameter (black line, Figure 6.13). By the time the rover returned to its original position beside the base station the accumulated integration error was 40cm. This was over a period of about 90 seconds. This was more accurate than estimation of relative location based on the

differentially corrected pseudo-range data (Figure 6.9). From this data it appears during ski runs (less than a minute) if the integrated velocity data were used location errors of around 40cm would be expected by the end of the run.

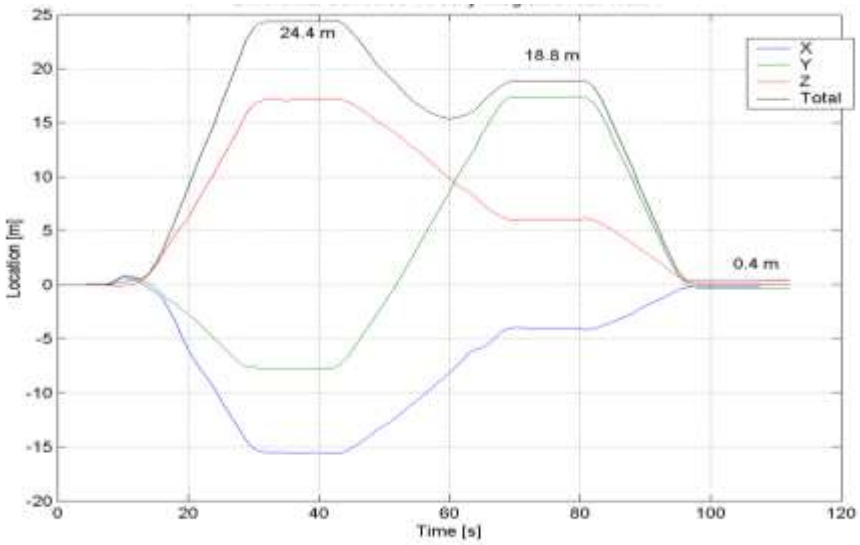

Figure 6.13: Integrated velocity while walking though a loop using ECEF coordinates

Differential GPS - test gate survey

Could the GPS location data be used to correct for the small drift (up to 40 cm) in the integrated GPS velocity during the survey of a typical ski course? The correction is required because it takes several minutes to survey the gate positions on a race course in which time the integrated velocity error is likely to increase to an unacceptable level. In this case the rover stopped at five marked cones for a minute each in order to gain a more accurate fix on each cone location.

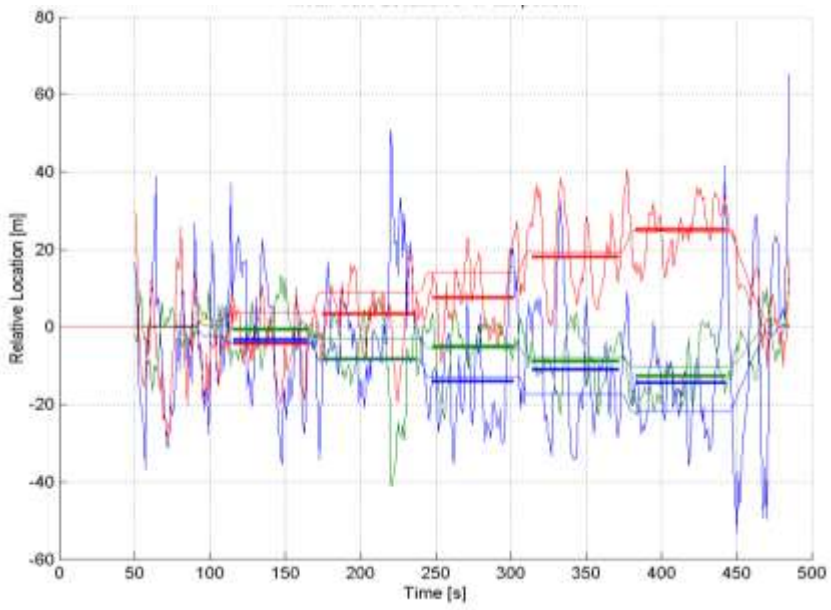

Figure 6.14: Test surveying of the cones making up a simulated racecourse

In Figure 6.14 the noisy lines represent the GPS location based on the differentially corrected pseudo-range data, the smoother lines represent the GPS location based on the integrated velocity data, and the thick lines represent the mean location based on the pseudo-range data for each stationary period. The graph shows that the mean GPS location error is too large to be usefully used to correct for integrated velocity error over the short measurement periods. Therefore, it was not possible to accurately survey the gate location using only a single frequency GPS receiver and instead a theodolite in addition to the GPS will be used to survey the ski run.

Dynamic accuracy of differential GPS velocity

How accurate will the calculated velocity of the athlete from the GPS data be? The expected accuracy of the differentially corrected GPS velocity during skiing, based on the residuals from Equation 6.8, was tested. It was assumed that because the systematic errors were removed by differential correction, the residuals of the carrier-frequency data should give an indication of the expected accuracy of the calculated velocity. Carrier-frequency data were collected from a GPS receiver attached to an athlete during an alpine ski run. The data were processed as previously described and a differentially corrected velocity obtained. The residuals to this solution from Equation 6.8 were then plotted (Figure 6.15).

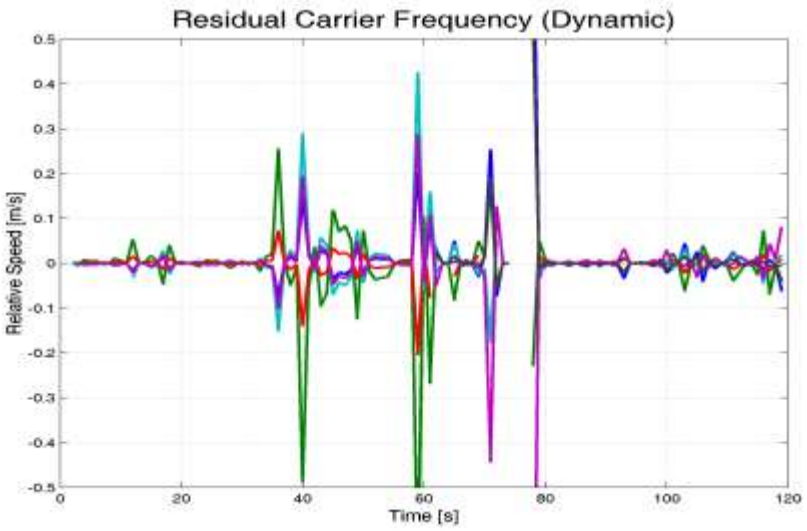

Figure 6.15: Residual speed from carrier-frequency during skiing

The actual skiing in Figure 6.15 takes place between 30 and 80 seconds. During this dynamic period the carrier-frequency residuals increased dramatically from less than 0.01ms^{-1} during the stationary periods to up to 0.5ms^{-1}. It is therefore expected that the GPS velocity 95% confidence interval during skiing giant slalom and rapidly changing direction will be around ±0.3ms^{-1}. This is both less accurate than the GPS chip specification (0.1ms^{-1}, 95% CI, at constant speed) and the experimentally determined stationary accuracy of less than 0.01ms^{-1}.

6.2.3. Summary of GPS accuracy

The summary of results is based on data from a SiRF2 single frequency GPS receiver with good reception and at least five satellites in continuous view.

	Specification	Differential correction	Static and Walking	Dynamic skiing
Pseudo Range		<150m	1-5m	up to 5m
Location	15m RMS		~1m after 20 minutes	±3m 95% CI
Carrier Frequency		<0.04ms^{-1}	<0.01ms^{-1}	up to 0.5ms^{-1}
Velocity	0.1ms^{-1} 95% CI constant speed		<0.01ms^{-1}	±0.3ms^{-1} 95% CI
Integrated velocity			0.4m after 90 seconds	

Table 6.1: Summary of SiRF 2 GPS receiver expected accuracy

Table 6.1 shows that in any fusion algorithm, during quasi-stationary periods much more weight should be given to the GPS velocity than given to the GPS location. During dynamic activities, however, GPS velocity data should be weighted only around an order of magnitude more important than the GPS location. This is because the estimated velocity error during skiing (up to 0.3ms^{-1}) when scaled by the athlete's velocity (~20ms^{-1}) is around an order of magnitude less than the estimated location error (up to 3m) when scaled by the distance between course gates (~20m). The residuals also provide additional information about signal quality and should be used to optimise any fusion algorithm.

In Chapter 3 the global trajectory error of an athlete skiing through a giant slalom race course was reported to be greater than 15m. The table shows that the differentially corrected GPS data should be capably of producing better global trajectory accuracy than 15m.

6.3. Gate survey

The gate locations were surveyed using both GPS and measurements from a theodolite positioned at the bottom of the course. The GPS data in the Earth Centred Earth Fixed (ECEF) coordinate system was transformed into the coordinate system of the theodolite and then the two measurements were fused together to make a best estimate of gate location.

Figure 6.16: Alan Walmsley manning the theodolite to measure gate location

6.3.1. Aligning the GPS and theodolite coordinate systems

The GPS gate locations were based on integrated velocity data (as discussed in Section 6.2.2) and in the Earth Centred Earth Fixed (ECEF) coordinate system. The theodolite data were based on the magnetic coordinate system, with the origin at the theodolite.

Z-axes alignment

The first step was to rotate the GPS data until the GPS Z-axis was aligned with the theodolite Z-axis. The theodolite Z-axis was defined by the gravity vector and was approximated over the race course in the ECEF coordinates by a normalised vector heading from Earth‟s centre to the median GPS gate location. By definition the GPS Z-axis is in ECEF coordinates is [0 0 1];

The GPS data were rotated by an angle (θ) degrees about a vector normal to both the GPS and theodolite Z-axes ($\mathbf{Z}_{\perp}$, Figure 6.17). The normal vector ($\mathbf{Z}_{\perp}$) was found by the cross product of the two Z-axes and the angle (θ) was found by trigonometry.

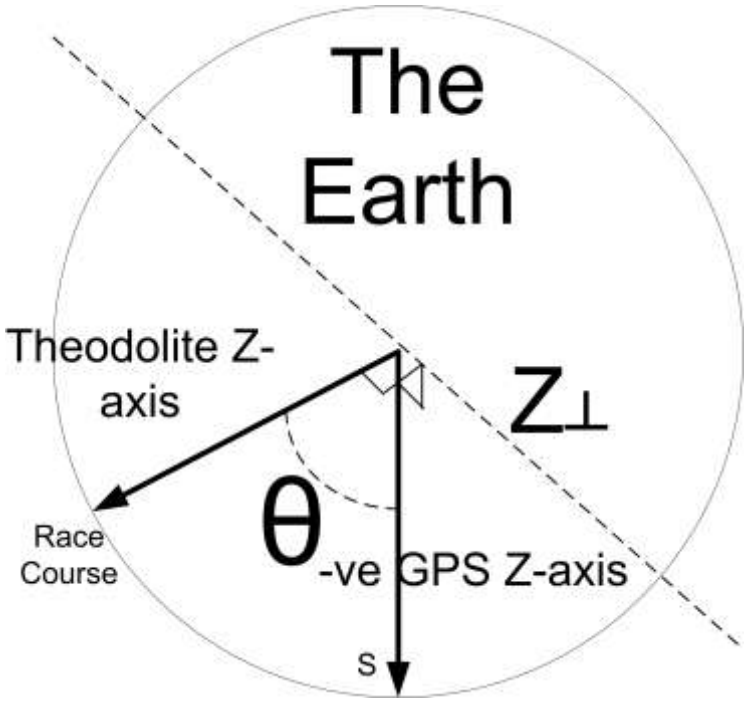

Figure 6.17: Rotation from GPS to theodolite coordinate systems

Heading Alignment

The GPS gate measurements were then rotated about the vertical (the theodolite Z-axis) to align them with the theodolite gate measurements. MATLAB"s non-linear least squares function[3] was used to find a single heading correction that minimised the residual location error between the GPS and theodolite gate locations. The mean residual location error was used as the offset to align the origins of the two coordinate systems.

6.3.2. Data fusion

After the alignment of the two coordinate systems the GPS gate measurements were not exactly the same as the theodolite gate measurements as shown in Table 6.2. The average gate position discrepancy was 2.3 metres with a standard deviation of 0.9 metres.

Mark	*X [m]*	*Y [m]*	*Z [m]*	*Total*
1	-0.23	-0.15	1.00	1.04
2	-1.24	-0.67	0.92	1.68
3	0.43	0.52	1.05	1.25
4	1.44	0.40	0.75	1.67
5	-0.77	-1.82	-2.30	3.03
6	NA	NA	NA	NA
7	0.56	0.57	-2.91	3.02
8	-0.40	-1.69	2.10	2.73
9	-1.03	1.04	2.20	2.64

Table 6.2: Difference between GPS and Theodolite survey after alignment of coordinate systems

In order to obtain the most accurate estimated of gate location the two measurements were fused together, the theodolite measurements were used to remove the integral drift error associated with the GPS gate measurements. It was assumed that the sequential theodolite measurements were essentially accurate but overlaid with some normally distributed error. It was also known that the GPS gate measurements suffered from increasing error with time because they were based on the integrated GPS velocity data but the relative changes between the gates were likely to be more accurate than the theodolite data. Finally it was assumed the missing theodolite gate measurements from gate 6 could be filled from the fused data and the overall accuracy would improve by fusing the two sets of gate measurements. Even with these measures the gate positions could contain significant error (up to ±2m).

6.4. A simple model of the course terrain

In Chapter 5 the athlete‟s contact surface (gymnasium floor) in inline skating was modelled as a flat surface. In alpine skiing the terrain is variable and so for a first estimation, the terrain slope was estimated based on the measured gate locations.

The first step in creating the simple snow surface model (Figure 6.18) was to rotate the gate locations about the vertical axis until the global X-axis represented the average heading of the fall line through all the gates. This meant that the gates could be represented uniquely as a function of X-axis position (the X-axis value of any part of the course is never repeated).

The height of the snow surface was then found by a piecewise cubic Hermit interpolating polynomial (PCHIP in MATLAB). The new unique X-coordinates and the unchanged Z-coordinates of the gates were used as inputs to interpolate the snow surface height (Z-value) between the gates (at different X-values). The PCHIP solution works better than a normal cubic spline in this case because there is less overshoot when the gate is located near a change in slope, which is often the case.

The snow surface was rendered by creating 30-metre wide contour lines perpendicular to the fall line at each one-metre change in height. The snow surface was then defined by grey rectangles connecting subsequent contour lines (Figure 6.26) or by grey triangular faces (Figure 6.18). Triangles are better in animations because three vertices uniquely describe the surface and it is easier for the computer to render triangular faces than rectangular faces defined by four points that may not represent a single flat surface.

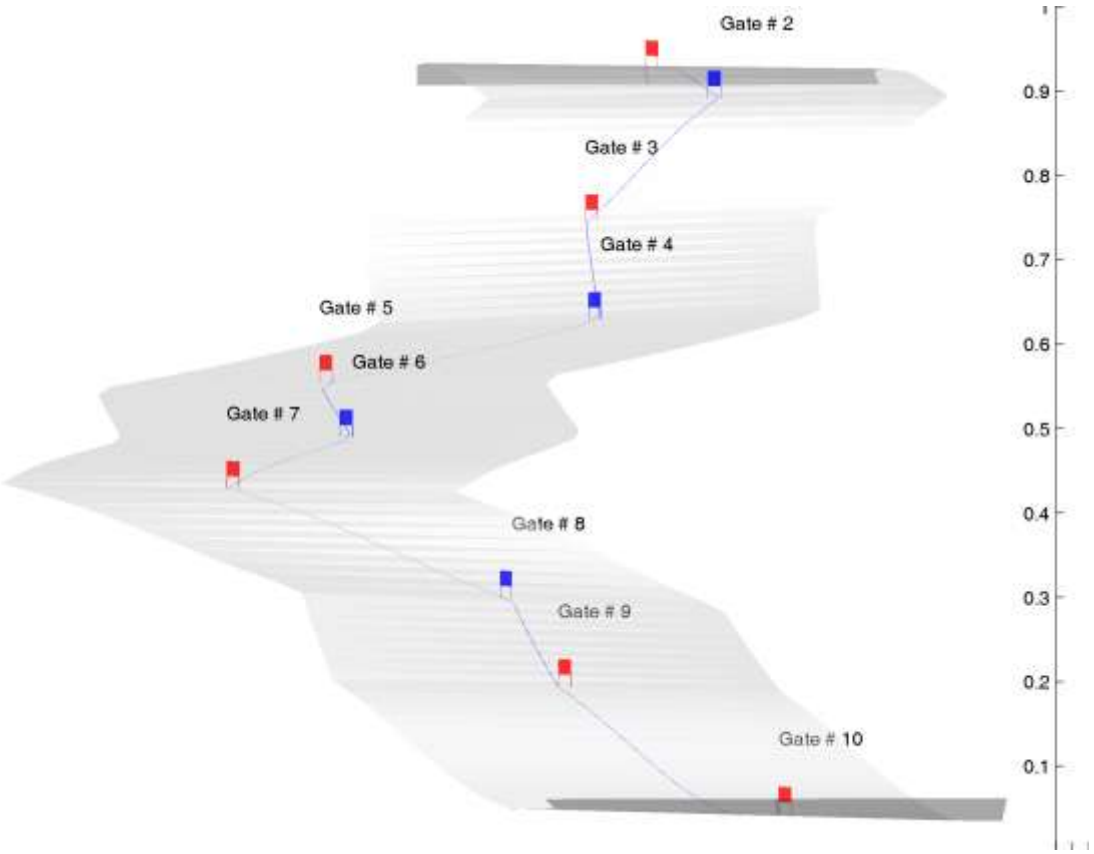

Figure 6.18: Computer model of the ski racecourse based on gate measurements

It was not possible from the limited data collected to estimate the cross slope on the course, but generally course setters try to position the gates down the fall line in order to minimise cross slope in the course. There were several limitations with this simple terrain model and in the future plans a more sophisticated method to measure the changing snow surface contours will be developed. For future terrain measurements a purpose built sled will be skied through the course capable of measuring global location, slope and cross slope at 50Hz.

These limitations together with the reported error for the surveyed gate positions (of up to 2m) could have resulted in the propagation of error into the terrain model. Without additional measurements it was not possible to measure this error and so the error reported for the survey gate positions was adopted. Errors in the terrain model would cause errors in the athlete‟s calculated trajectory because the terrain model is used in the fusion algorithm. The terrain model errors, however, should not affect any comparative analysis between runs because for each run the effects will be very similar.

6.5. Fusion Motion Capture algorithm: Version four

The FMC algorithms used to determine athlete motion was similar to that used for the inline skating experiment in Chapter 5. Except, instead of gate timings, post processed and differentially corrected GPS data (pseudo-range data and carrier-frequency) were used as inputs (Figure 6.19). The snow surface model from Section 6.4 was also used to improve the

estimation of athlete vertical location. More information about the workings of the fusion algorithm was presented in Chapter 5.

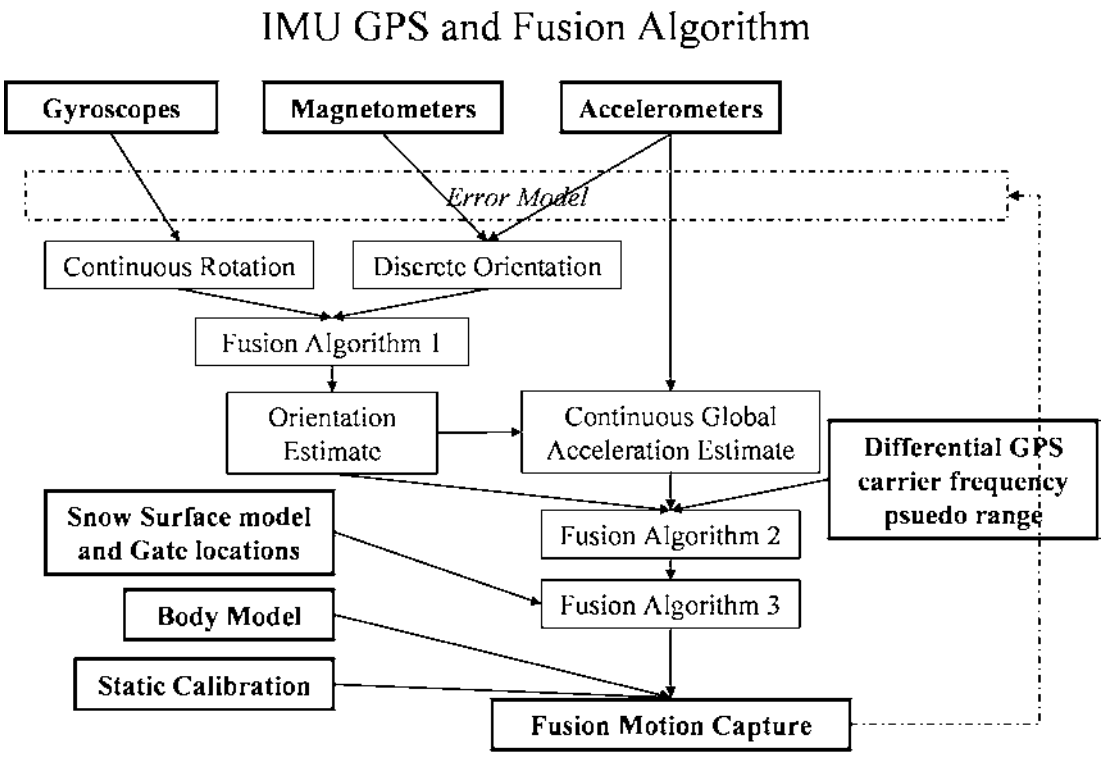

Figure 6.19: Fusion algorithm Version Four

6.5.1. Global trajectory

The first step was to calculate the global trajectory of the athlete"s helmet from the attached GPS receiver and IMU. Unfortunately neither the GPS location calculated from the pseudo-range data nor the GPS location calculated from the differentially corrected integrated velocity data were accurate enough, especially in the vertical axis. Three additional constraints were required to improve the accuracy of the results to a satisfactory level:

1. The athlete remained in contact with the modelled snow surface.
2. The athlete started at the start gate and finished at the end gate.
3. The athlete passed outside each gate.

The snow contact constraint was applied in the same way as the floor contact constraint in the inline skating experiment described previously by Figure 5.5, except this time the snow slope varied according to the model (Figure 6.18).

The first estimate of the athlete"s GPS trajectory was made by integrating the differentially corrected GPS velocity (green line, Figure 6.20). The second estimate was made by constraining the trajectory to start and finish at the boundary gates (blue line, Figure 6.20). There was a surprising amount of GPS location error based on the integrated velocity,

especially in the vertical axis. The correction required (5 metres) was around eleven times as large as the accumulated error of the walking experiment (0.4m, Figure 6.13) and more than would normally be expected for such a short duration (~16s). However, the accumulated error (around 5 metres) agrees with the expected velocity error for GPS velocity based on residuals to the carrier-frequency data during skiing (up to 0.3ms^{-1}, Table 6.1).

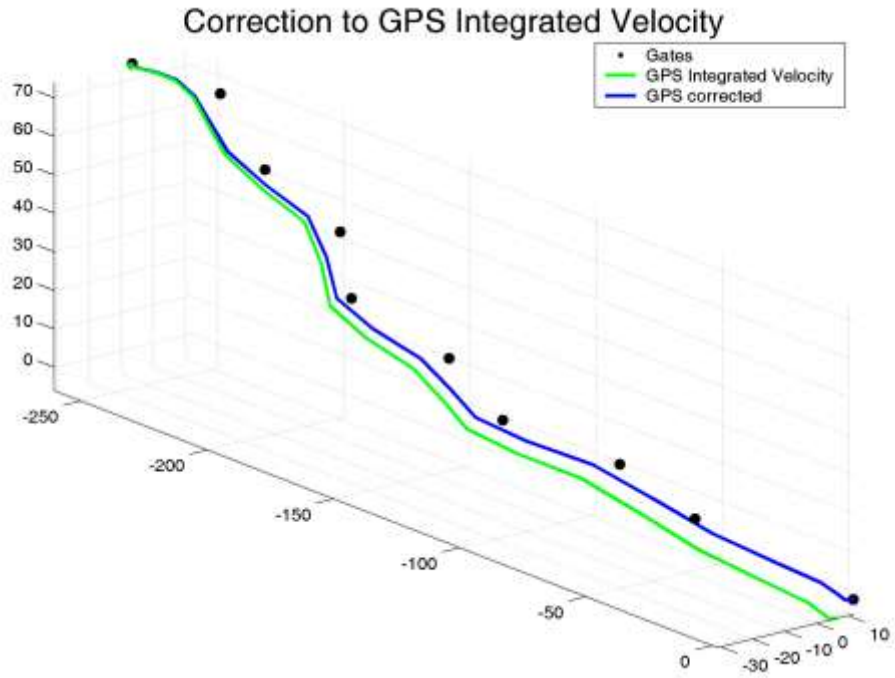

Figure 6.20: Athlete location found by integration and correction of the GPS velocity

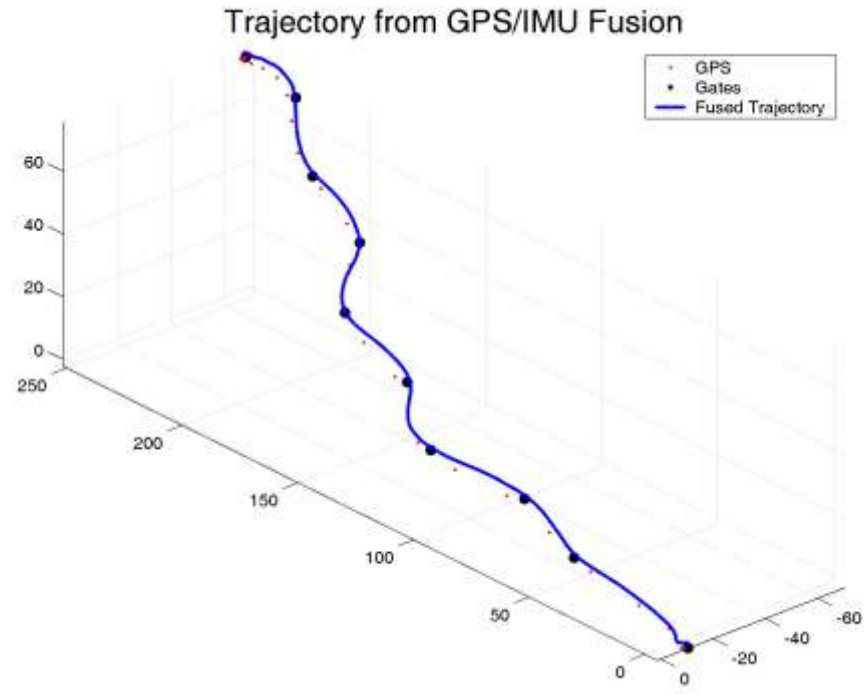

Figure 6.21: Run 3 trajectory by GPS/IMU and gate fusion

After this correction the GPS trajectory does not appear to pass within the gate constraints (blue line, Figure 6.20). However, by fusing the GPS pseudo-range and carrier-frequency data with the IMU data (the [Fusion Algorithm 2] process in Figure 6.19) and then application of the snow surface model and gate passing constraints (the [Fusion Algorithm 3] process in Figure 6.19), a more accurate trajectory was obtained (Figure 6.21). In Figure 6.21 the athlete‟s helmet trajectory (blue line) passes outside each gate and the athlete‟s trajectory remains close to the snow surface. The gates are represented by black dots located at the bases of the inside poles.

The gate passing constraint was applied to make the athlete‟s trajectory consistent with the gate locations, which raised the following issue: The survey gate locations also contained error (up to 2 metres, Table 6.2). It was unfortunately not known which was more accurate, the athlete‟s trajectory, or the gate locations.

The gate passing constraint was applied by shifting the closest point on the athlete‟s trajectory to each gate outside that gate if required. In general a correction from skier‟s right to skier‟s left over the course was required (Figure 6.20). This solution was not ideal, but the only practical one available at the time. The resulting accuracy of the global trajectory is discussed later in section 6.9.

6.5.2. Limb orientation and gyroscope overload

Next the individual limb segment orientations were calculated. After the head segment orientation the location of the C7 neck joint centre was obtained using the body model and processes already described in Chapter 5 on page 84. From the neck joint centre the remaining body segment orientations were obtained by working sequentially from superior body segments to inferior body segments.

However, when calculating the orientation of the thigh segment, it appeared that the thigh IMU attached to the lateral aspect of the thigh (midway between the greater trochanter and lateral femoral epicondyle) was subject to rotations that exceeded the gyroscope linear range. This was probably because of soft tissue and muscle vibrations (wobbling mass) from the ski/snow surface induced vibrations and/or a result of gate contacts.

When the gyroscope linear range (900°/s) was exceeded (at around data point 500, Figure 6.22 top panel) it resulted in a discontinuity error in the IMU orientation. The IMU orientation error can be observed by a step change in the IMU calculated global magnetic field (around data point 500, Figure 6.22 bottom panel). Over the ski course such a large step change in the measured global magnetic field is highly unlikely so it indicates an IMU orientation error was caused by gyroscope overload. The linear ranges of the gyroscopes used were 0-900°/s which was insufficient for the shock loadings that occasionally occur in skiing on some body segments. If uncorrected such a shock loading could cause transient orientation errors of up to 45 degrees in measured thigh body segment orientation.

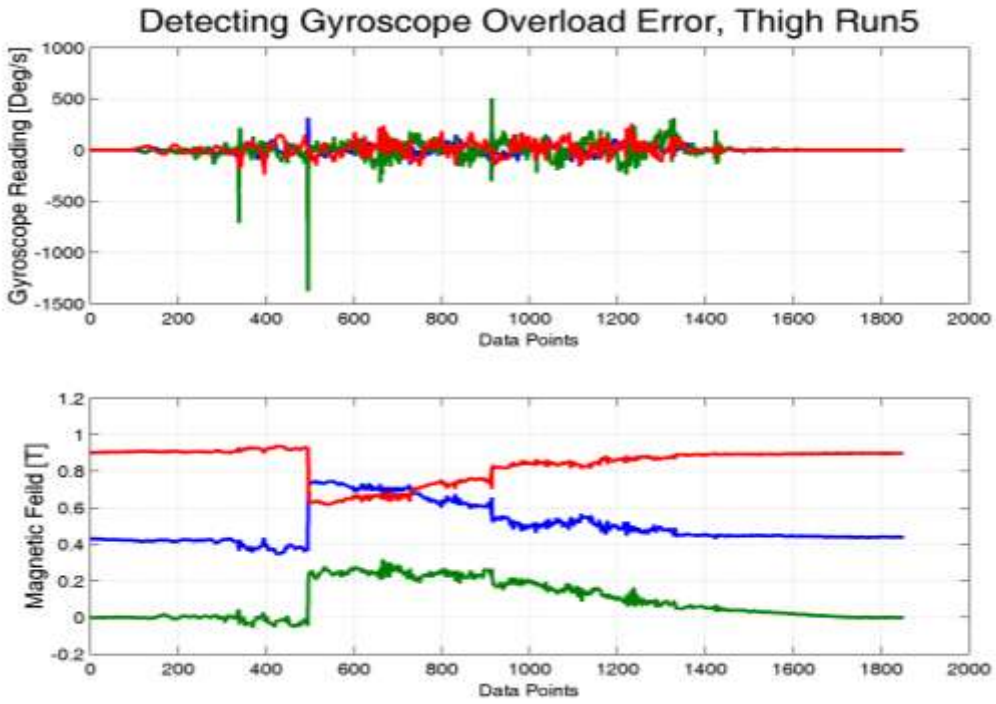

Figure 6.22: Gyroscope overload (around data point 500) causes a step error

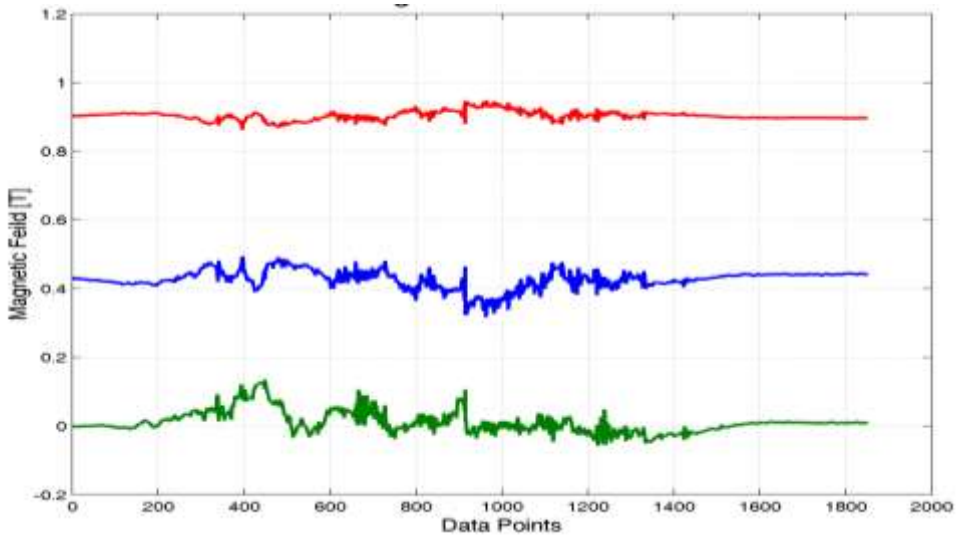

Figure 6.23: Global Magnetic field recalculated after the fusion process

To reduce orientation error caused by gyroscope overload the fusion algorithm checked the gyroscope channels for overload (ω>900°/s) and applied a correction during the overload periods based on assumption that both the measured global magnetic field and measured gravitational acceleration before and after the overload period were approximately equal. The validity of such a correction was determined by examining the IMU measured global magnetic field after the fusion process (Figure 6.23). The new graph shows the original step error at around data point 500 has been reduced markedly. It is surprising to observe that the measured global magnetic field is still variable over the course of the ski run. The residual

variation may be caused by local magnetic effects of the athlete‟s equipment, poor calibration of the IMU magnetometers, iron rich volcanic rock deposits on the ski area, ski area infrastructure, and/or fusion algorithm errors resulting in IMU orientation error.

6.6. Measurement of Earth's magnetic field

How accurate are the IMUs‟ measurements of the Earth‟s magnetic field? How variable is the Earth‟s magnetic field across a ski course? What caused the fluctuations seen in Figure 6.23? In the section the variability of Earth‟s magnetic field in a biomechanics laboratory is investigated, this is a step towards answering the questions above. It is also important to know the variability of Earth‟s magnetic field in indoor situations because the IMU to body segment mapping using the calibration frame presented in Chapter 4 was done indoors.

Magnetic field variability and magnetometer reliability has already been investigated. The local magnetic field effects discussed below would be exacerbated by any additional variability in Earth‟s magnetic field. In Chapter 2 on page 36, the role of the IMU magnetometers in defining sensor heading and orientation was discussed. Previous experiments also demonstrated that the number of IMU‟s connected together affected the magnetometers‟ data, creating a heading error of up to 15°. This effect was termed the „daisy chain effect‟ (Brodie, et al., 2008d) where the additional current drawn when several IMUs were connected together affected the IMU magnetometers. The solution employed to resolve this issue was to recalibrate the IMUs‟ magnetometers in daisy chains exactly how they would be wired to the athlete in the field.

The athlete‟s skis (attached to the feet) and data logging equipment (attached to the torso) contain magnetic material. Previous experimental work by the author (unpublished) suggests that mild magnetic material within 25cm of an IMU affects the magnetometer output. The skis and data logger would not only affect the IMUs attached to the skis and torso, but also IMUs on other body segments as the athlete‟s limbs moved relative to the magnetic material.

6.6.1. Measuring Earth's magnetic field

A protocol to investigate variability in the Earth‟s magnetic field was developed for use in a typical measurement environment, a biomechanics lab. Five IMUs were attached to a (non-ferromagnetic) aluminium square section rod at the follow heights from the floor; 20, 40, 100, 140, & 180cm (Figure 6.24). Prior to performing the survey the IMUs were statically calibrated in a daisy chain using a method previously described to remove any accelerometer and magnetometer biases (Brodie, et al., 2008d). Aluminium is paramagnetic, but the aluminium rod was found not to affect the IMU‟s magnetometers.

The rod was rigid and the sensors were all aligned with the rod to within 1°. When the rod was held vertically the measured projection of the local z-axis of each sensor on the global

XY plane was the same, unless there was variation in the labs magnetic field. The rod was held vertically during measurements using a corner spirit level for alignment.

The rod with attached IMUs was positioned vertically in 25 different locations over a five by five metre grid located in the middle of the laboratory and at least 1.5 metres from the walls and any metallic objects. To ensure the consistency of rod heading between different measurements, the rod handle was aligned with strings of constant heading that traversed the laboratory (Figure 6.24). Three seconds of stationary data were collected after the IMU heading data had stabilised and the rod was stationary.

Figure 6.24: Calibration rod with IMUs aligned with a string of constant heading

MATLAB was used to collect and process the data from each of the 25 different positions. Five sensors were used making a total of 125 measurements locations. The measurements were used to map the magnetic variation within the laboratory.

From each static measurement a rotation matrix $\mathbf{R}_{LG}$ describing the static orientation of the sensor was formed as previously described (Brodie, et al., 2008d). The heading (the projection of the local z-axis on the global XY plane) was then calculated by Equation 6.9. The dip of the earth's magnetic field was found from the IMU magnetometer output (**mag**). First the normalised local measured magnetic field vector (**h,** Equation 6.10) was calculated then it was rotated into global coordinates (**H**, Equation 6.11). The dip could then be calculated by Equation 6.12.

Equation 6.9 $$Heading = \arctan(\mathbf{R}_{LG}(1,3)/\mathbf{R}_{LG}(2,3))$$

Equation 6.10 $$\mathbf{h} = \frac{\mathbf{mag}}{|\mathbf{mag}|}$$

Equation 6.11 $$\mathbf{H} = \mathbf{R}_{1,G}\mathbf{h}$$

Equation 6.12 $$Dip = \arccos(\mathbf{H}(1))$$

6.6.2. Results

Table 2 below summarises the variation in the heading and the dip of Earth's magnetic field in our laboratory. At each height the range of both heading and dip is displayed.

Heading [°]	Max °	Min °	Range °	Dip [°]	Max °	Min °	Range °
All	41	-3	44	**All**	72	51	21
20 cm	33	-3	36	**20 cm**	72	52	20
40 cm	35	8	27	**40 cm**	69	51	18
100 cm	39	13	26	**100 cm**	68	53	15
140 cm	49	18	21	**140 cm**	67	55	12
180 cm	41	19	22	**180 cm**	67	56	11

Table 6.3: Variability of the Earth's magnetic field through an XY plane at each height (Z)

A contour map shows the variation in magnetic field heading one metre from the ground (Figure 6.25).

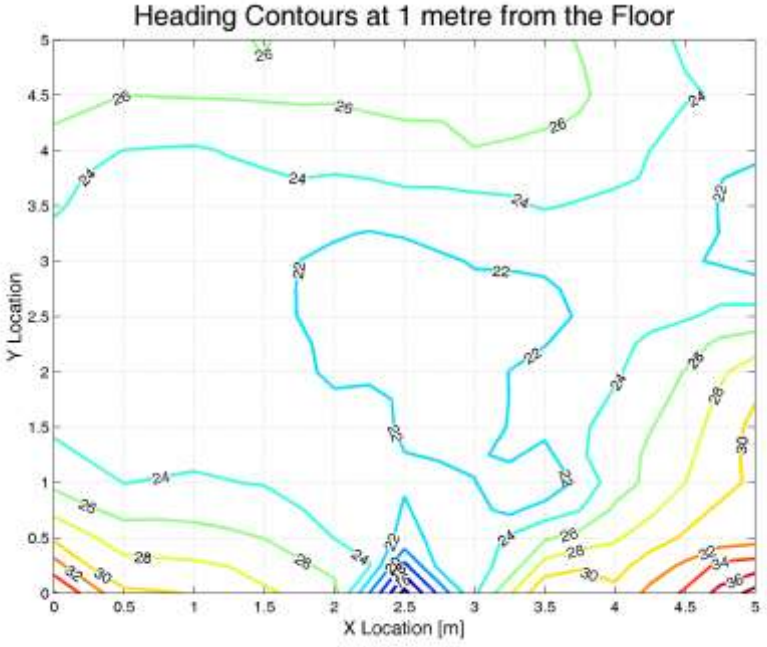

Figure 6.25: Contour heading map at 1 metre from the floor

6.6.3. Discussion

The results show that the variation of the magnetic field in our laboratory can not be ignored (Table 6.3). The high variability in heading at 20cm from the floor (36°, Table 6.3) compared to the variability at 140cm from the floor (21°) supports a theory that concrete reinforcing steel used in buildings has a significant influence on the measured heading. However the size of the effects were large considering measurements were made at least 1.5m from any wall or metallic object. As the construction of our laboratory is probably typical of many sport-biomechanics laboratories, these results show that using the magnetometers in IMUs to correct heading drift, and this is how the vendor supplied software operates (XSens, 2004a), is unlikely to be successful at producing results accurate enough for most biomechanists in such laboratory spaces. This also raises the question how useful will the magnetometer data be during a skiing because the IMUs will be moving relative to magnetic equipment carried by the athlete. Fortunately the fusion motion capture algorithm presented in section 6.5 is unaffected by magnetic field variations through the ski race course.

The high variability in heading reported in Table 6.3 (up to 44°) accounts for the heading correction required to the left shank segment (25°, Chapter 5) during the inline skating experiment. It that chapter it was hypothesised that the correction was a result of a non-homogeneous magnetic field during the IMU to body segment mapping procedure and this is confirmed by the results presented here.

6.7. Thigh soft tissue artefacts

Soft tissue artefacts affect the orientation of the IMU relative to the thigh body segment. Knee bending causes the IMU attached to the thigh to move relative to the thigh creating „phantom“ abduction and adduction of the thigh. The phantom movements cause errors in the knee position, which is propagated through the shank and ultimately causes errors in the location of the skis relative to the athlete“s centre-of-mass (CoM). This is a problem because the ski location defines the athlete“s base of support and so will affect the future analysis of external torques and postural balance during skiing.

It was difficult to find a good location to attach the IMU to the measure the thigh segment orientation. The lateral surface of the quadriceps, over the tendinous sheath, midway between the femoral condyle and the greater trochanter was chosen (see Section 6.1.1 on page 117). This location provided a relative flat surface to attach the IMU but unfortunately the surface was found to move considerably with flexion and extension of the knee. The reader can verify this by placing their hand on the lateral aspect of the thigh and performing slow squats. The athlete had well developed thigh muscles so the soft tissue artefact was likely to be substantial.

The thigh soft tissue artefact is an issue for the dynamic analysis of alpine ski racing because it has an effect on the athlete“s measured base of support. Flexing the knees will artificially widen the measured stance and extending the knees will narrow the stance. While cornering the outside leg is extended relative to the inside leg and this will erroneously move the

measured base of support inwards. The thigh segment is approximately 0.40m long and so a soft tissue artefact of 10° could change the stance width by 0.07m.

6.7.1. Removing thigh skin artefacts

In order to reduce the skin artefacts, the knee was assumed to be a single axis joint hinge joint with a small adduction angle of 12° (based on measurements from the athlete‟s static calibration posture). Therefore, the IMU attached to the shank could be used to define the abduction/adduction and internal/external rotations of the thigh. The thigh body segment flexion/extension was still defined by the IMU attached to the thigh.

These modifications successfully removed the soft tissue artefacts but also removed measurements of independent rotation of the shank segment about its long axis when the knee was flexed. In skiing subtle rotations may play a role in regulating the ski/snow carving angle so both versions of the data should be kept. For whole body kinetic analysis the modified data should be used, but for analysis of the knee motion the original data complete with artefacts should also be considered.

In the future experiments could be completed with using multiple IMUs attached to different aspects of the thigh to reduce skin artefact measurements. Soft tissue artefacts are also present for the upper arm body segments, and shoulder movements, but the arm movements are less important in skiing than the leg movements so mitigation of the arm and shoulder artefacts are considered beyond the scope of this thesis.

6.8. Results: Data driven animations

The FMC data were used to visualise the local motion data from several angles. These data driven animations were developed in order to assist with athlete feedback. The data driven animations build on the substantial developments made in Chapter 5 and based on the visualisation of inline skating data. The reader is invited to now view the run 5 local limb movements (Video 6.2). With the distractions of the global motion removed the ski technique is viewed as an abstract envelope of movements and the athlete can focus on how his limbs are coordinated together.

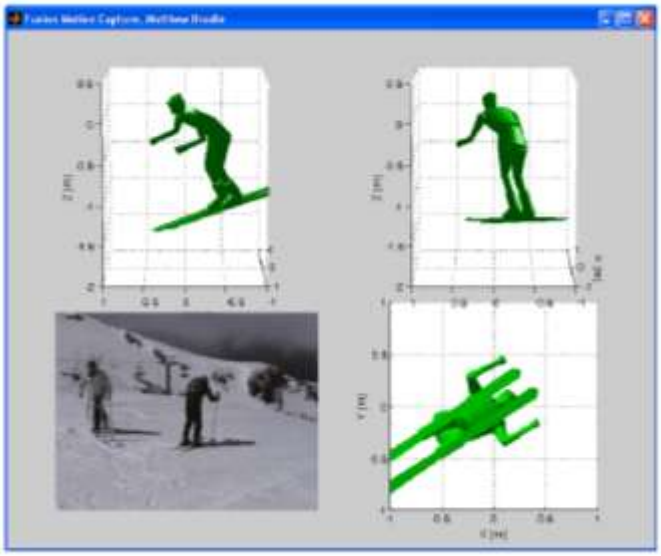

Video 6.2: Appendices\FMC Video\Ruapehu_R5_Relative.avi

The global data driven animations required additional GPS measurements (Section 6.2), the surveyed gate locations (Section 6.3) and a snow surface model (Section 6.4). To estimate the accuracy the FMC data driven animations, they were visually compared to the video feed (Figure 6.26 and Video 6.3).

Figure 6.26: FMC data top left and bottom panels, video feed top right panel
Video 6.3: Appendices\FMC Video\Ruapehu_R5_Contours.avi
Video 6.4: Appendices\FMC Video\Ruapehu_R5_FMC_Video.avi
Video 6.5: Appendices\FMC Video\Ruapehu_R3_Contours.avi

6.9. Orientation and trajectory errors during skiing

Many enhancements to FMC were presented in the chapter which have resulted in significant improvements in accuracy. The first time the FMC system was taken onto the snow was in 2005 at Coronet peak and some results were presented in Chapter 3. In 2005 the limb orientation accuracy was acceptable and the error was estimated to be less than 5° but the global trajectory error for a giant slalom course was unacceptable high and estimated to be greater than 15m. The motion of inline skating was later captured in Chapter 5 and the FMC system incorporated many improvements. For the inline skating experiment the global trajectory accuracy was significantly improved and the error while skating between gates was estimated to be less than 0.05m. It was however not known if the improvements made in Chapter 5 and the additional improvements made in this chapter would perform well on the snow because forces experienced in skiing are much higher than the forces experienced in skating.

The results were a success. They show it is possible to capture the motion of giant slalom skiing. The accuracy of FMC limb orientation and global trajectory measurements are discussed below:

Limb segment orientation

Manual corrections were required to narrow the athlete‟s ski stance; the athlete‟s right ski heading was rotated inwards by 7°. After this correction the local limb angles all appeared plausible (Video 6.3) and the ski angle improvements can be verified against FMC output before the correction (Video 6.4). This type of subjective visual assessment of the accuracy of the FMC data was discussed in detail in Chapter 3 and 5. The heading corrections required were similar but much smaller than those required previously to the inline skater‟s skates (25°, Chapter 5). They were likely a result of variability in the magnetic field during the IMU to limb calibration process. This sensitivity of Earth‟s magnetic field to magnetic interference was highlighted in Section 6.6. In hindsight, the IMU to limb calibration was done too close to a metal table and television.

The soft tissue artefacts of the thigh were removed in Section 6.7 using an assumption that the knee acted like a hinge joint.

Video 6.6: Appendices\FMC Video\Ruapehu_R5_Artefacts.avi

With the soft tissue artefacts suppressed the skis remain a reasonable distance apart even when the athlete extends his knees (Video 6.6). The reader is invited to compare Video 6.6, with no artefacts to Video 6.4, with artefacts paying close attention to the ski spacing.

The final limb orientation error in the data driven animation (Video 6.6) is unlikely to exceed 6° because if larger errors were present then the FMC data visualisation would appear implausible and visual artefacts would be present such as the skis crossing. The 6° estimated

limb orientation error also agrees with the findings of Chapter 4 where the 3° estimate of body model error was added to the 3° estimate of body segment error. The estimated error also agrees with the findings from Chapters 3 and 5.

The most accurate body segment orientation measurements are likely to be from the head and thorax body segments because of their larger mass, slower movements and distance from the vibrating skis. The measurement of sacrum body segment orientation measurement is likely to contain higher body model error due to soft tissue artefacts. The distal body segments such as the forearms, shanks and skis were subjected to highly dynamic movements and so the IMU data is likely to be less accurate. Both the thigh and upper arm body segments suffered from soft tissue artefacts as the IMU moved relative to the underlying bone structure. In addition the thigh body segment occasionally suffered from gyroscope overload introducing transient errors in orientation that were corrected for.

Global Trajectory

An estimate of global trajectory error and/or gate surveying error was made by comparing the gate times from FMC with the nearest frame of the Video (Table 6.4). The reader can check these measurements using the provided data driven animations (Run 3, Video 6.5 and Run 5, Video 6.3). The video frame rate limited the temporal resolution to 0.04 seconds. The temporal error was converted to an estimated spatial error by multiplication by the athlete's mean velocity of about 17ms^{-1} to give a conversion of approximately 0.70m error per frame.

Table 6.4: Estimated number of frames separating video and FMC gate passing

Gate	1	2	3	4	5	6	7	8	9	10
Run 3	NA	1	NA	-2	-2	-5	0	NA	NA	NA
Run 5	NA	1	0	NA	NA	NA	NA	0	-1	NA

Not all gates could be compared for both runs and it was very difficult to pick the gate passing exactly because of the limited quality of the video. The largest error (-5 frames, -0.20 seconds, or 3.4 metres Table 6.4) occurred about gate 6 in run three, at this point the FMC data were ahead of the video data. Inaccurate gate surveying of gate 6 may have contributed to this high error because gate 6 was not visible from the theodolite when the course was surveyed and the missing gate position had to be filled using the GPS data. The gate survey errors were estimated to be around 2 metres (Section 6.3) and so the source of the gate timing errors could either be a poorly surveyed gate or errors in the global trajectory.

The run 3 trajectory error (±5 frames) was much higher than the run 5 error (±1 frame, 0.04s or 0.70m). The difference might be because the sample rate of FMC in run 5 (50 Hz) was twice the sample rate of run 3 (25 Hz) and so it is possible the accumulated integration errors of FMC were reduced by the higher sample rate. Alternatively the difference could be explained entirely by gate survey errors and the fact that because the camera was positioned differently for each run the same gates could not be compared. The following trajectory separation analysis was therefore required in order to further investigate the trajectory error.

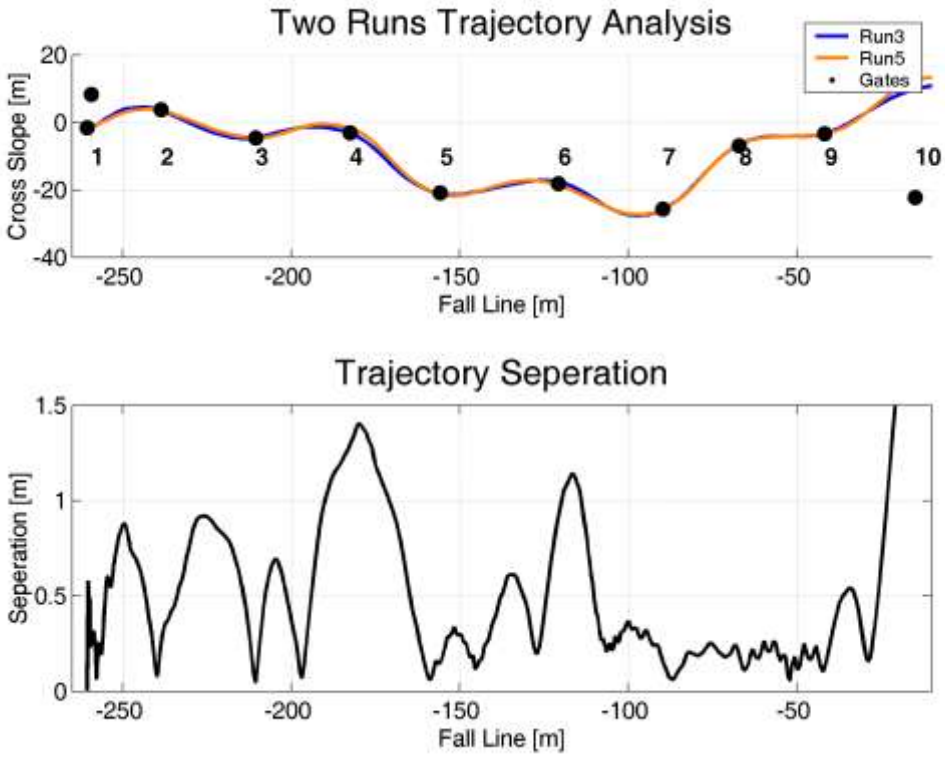

Figure 6.27: Trajectory separation in giant slalom

In Chapter 5 a variability analysis was used on the inline skating trajectory data. That analysis showed that, for inline skating, the trajectory variability through the course (less than 0.05m through the last two gates) was much lower than the estimated error (0.18m) based on video frame rate. It was therefore assumed that 0.05m was a more probable error estimate for inline skating. A variability analysis could not be carried out on the skiing data because only two runs were captured. Instead the separation between the two trajectories was analysed (Figure 6.27) and the analysis shows through the course the trajectories rarely exceed 1.0m. In fact there is a stretch of over 70m, through gates 7, 8 and 9, where the trajectory separation is well below 0.5m. This new evidence suggests that the higher trajectory error recorded in run 3 was the result of gate survey errors and therefore the measured error for run 5 (0.7m) should be adopted for both runs.

The athlete‟s trajectories are calculated relative to the modelled snow terrain. Any errors in the gate positions could therefore have caused additional undetectable errors in the athlete‟s absolute global trajectories as discussed in Section 6.4 on page 135. These undetectable errors are likely to be the same for both trajectories and therefore should not have significant effect on the comparative analyses presented in later chapters. A more sophisticated and more accurate way of measuring the terrain has been developed and will be used in the future to reduce this additional source of error.

Summary of expected errors

Following the investigations in this chapter the estimated accuracy of the FMC system is within 6º for the measurement of body segment orientation and 0.7m for the measurement of global trajectory. Overall the accuracy was a huge improvement on the first racing data gathered at Coronet Peak in Chapter 3 on page 50 using the first version of FMC. The accuracy was also an improvement on the reported GPS receiver accuracy (±15m RMS). The implication of these results is that the prototype FMC system is capable of meeting the first thesis milestone:

To accurately capture the motion of ski racing over a complete race course

A direct comparison of errors between the two different motion capture systems is difficult because the nature of the errors is different. So long as the nature of the error is understood then the FMC system is accurate enough to uncover many general trends from the large data sets. FMC has the additional advantage that multiple runs through race courses can be quickly captured and analysed, providing a data rich environment from which to draw conclusions.

The nature of the error present in FMC data is different from nature of the error resulting from traditional optical analysis. Both global trajectory error and body segment orientation error in FMC data are derived measurement and therefore manifest as low frequency accumulation of integrated error over several seconds. Positional measurements obtained from optical motion analysis systems also contain error, but of a different nature, the error is usually a combination of both systematic error and high frequency noise. In FMC, however, the high frequency content of the motion is derived principally from accelerometer and gyroscope data and should therefore contain less high frequency error except for errors caused by soft tissue artefacts, a problem common for both types of motion capture systems. Compared to the millimetre level errors reported to be achieved by laboratory motion capture systems, the 0.7m error reported for FMC may appear to be large. It would be however impractical to achieve millimetre accuracy of skiing through complete giant racecourses slalom because, as discussed in the introduction, too many synchronised cameras would be required.

7.Forces in Giant Slalom

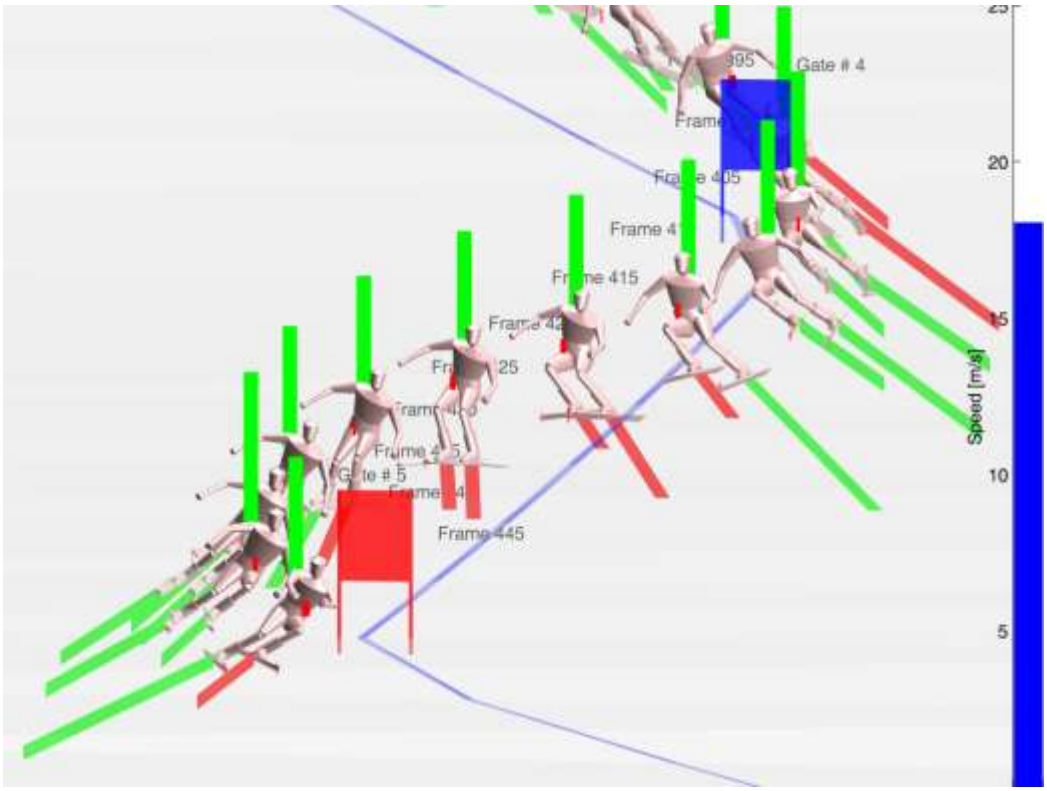

Figure 7.1: Screen shot from of run 3 using the visualisation software

The question is no longer: "How to accurately capture the motion of ski racing over a complete race course?", the question has moved to be closely aligned to the second, third and forth milestones:

"Measure or model the different forces exerted on the athletes through their interactions with their environment"

"To analyse complex whole body motion through a large 3D volume"

"To present the analysis in a way intuitive to the athlete"

In alpine ski racing because style is not judged, the external forces acting on the athlete decide the race outcome. Therefore, measuring, modelling and understanding how the external forces act on the athlete and affect performance is very important.

This is a technical chapter in which the external forces acting on the athlete of wind drag, snow resistance and ground reaction force are measured, modelled and investigated. As discussed in the introduction to this thesis, it is not possible to measure all of these forces directly in alpine ski racing with the equipment available. Instead the forces of wind drag and snow resistance are modelled. The athlete"s FMC and anthropometric data are used to fit optimal parameters to the models of dissipative forces. The results include data driven animations, colour coded force vector analyses and graphs of the external forces. The relative importance of each external force is also investigated using energy and power analyses.

7.1. Accuracy of FMC data and the analysis of forces

What is the accuracy of the forces calculated in the chapter? Is the FMC data good enough to provide useful information to the athletes? Unfortunately without making an independent measurement of force using miniature force plates attached to the athlete"s skis it is not possible to determine the level of accuracy achieved by the calculations presented in this Chapter. However, so long as multiple turns are studied for trends, rather than single turns for absolute values (which is the traditional practice because of the limitations of optical motion capture systems) and so long as it is understood there may be many possible sources of error, then useful information from the analyses may be extracted.

Unlike optical methods that are often employed for motion analysis, FMC makes use of direct accelerometer data. It was discussed in Chapters 3 and 5 that if the derived FMC reconstruction of the motion is constant with a video recording of the motion then the underlying acceleration and rate data, used to calculate the forces, are likely to be relatively free from errors. Many improvements were made to the FMC system in Chapter 6 and the estimated limb orientation and global trajectory errors for giant slalom was reported to be 6º and 0.7m respectively. This was an improvement on the global trajectory accuracy for giant slalom skiing previously reported (>15m, Chapter 3) but larger than the errors for global trajectory reported for inline skating (0.05m, Chapter 5). The gate spacing used in giant

slalom (~30m) was six times as large as the gate spacing used in the inline skating experiment (~5m) and so the forces calculated from the skiing data are likely to be of similar relative accuracy as the forces calculated from the inline skating data. It is useful to remember also that the forces calculated from FMC data do not require any low-pass filtering unlike the forces calculated from the inverse dynamics of optical motion capture system data.

Possible sources of noise in the forces calculated from FMC data were discussed in Chapter 5 on page 102. Forces are calculated from the athlete‟s centre-of-mass trajectory, which in turn is calculated from the GPS data, the helmet IMU accelerometer data and the changing orientation of the body segments. Body segment orientation measurements are principally based on the IMU gyroscope data and the body model.

Resultant forces calculated from FMC data of ski racing are most dependant on the helmet IMU accelerometer and GPS data because the global trajectories of the athletes can be assumed to be large compared to any small orientation errors of the body segments. A theoretical sensitivity analysis shows: The smallest observable error in body segment orientation is around 6º for the skis, which would result in the ski tip position changing by around 0.08m and would cause the skis to cross at some stage through the course. In skiing the athlete experiences rapid changes in acceleration while travelling in the vicinity of 20m/s over a 200 metre course and so 0.08m changes in ski position are at least three orders of magnitude less than the global trajectory and are likely to have very little effect on either the forces or other parameters in the analyses presented in this Chapter. Parts of the analysis in this Chapter could in principal have been done with just differential corrected GPS and single IMU attached to the athlete‟s sacrum to approximate the centre-of-mass trajectory.

The following error calculation for global acceleration and force measurements are based on data from the IMU and GPS units attached to the athlete‟s helmet. The accuracy of the GPS velocity data used in the fusion algorithm was determined in Chapter 6 to be 0.3ms^{-1} for giant slalom skiing. The GPS velocity data at 1Hz can be differentiated to get GPS acceleration and so the error for GPS acceleration (0.4ms^{-2}) is estimated by combining the likely errors in subsequent GPS velocity data using Equation 7.1. The equation is used when the errors are uncorrelated.

Equation 7.1 $$E = \sqrt{E_1^2 + E_2^2}$$

Additional errors might also be caused by the accelerometer bias of 0.02ms^{-2} and accelerometer nonlinearity error of 0.2% (XSens, 2004a). The nonlinearity error could be up to 0.04ms^{-2} for accelerations of 20ms^{-2} experienced by the IMU attached to the helmet. The largest source of acceleration error however is the possibility of a 3° measured orientation error for the IMU attached to the athlete‟s helmet. A 3° error in IMU orientation would cause a 5% error in the measured global acceleration, an error of up to 1.0ms^{-2} (calculated by taking the sine of 3° and then multiplying the result by the maximum acceleration, of 20ms^{-2}, experienced by the IMU attached to the athlete‟s helmet).

The effect of all the different uncorrelated acceleration errors is then calculated using Equation 7.1; the acceleration error is estimated to be up to 1.2 ms^{-2}. The force error is found by multiplying the acceleration error by the athlete and equipment mass of 96.2kg. Based on these calculations and assumptions, the estimated error in the resultant forces calculated from FMC data could be up to 110N. The main sources of this error are proportional to the measured acceleration and so during slower movements when the measured acceleration is less the force error should also reduce.

The estimated acceleration error (1.2 ms^{-2}) is four orders of magnitude less than the unfiltered acceleration error reported for skiing data (10,000m/s^2) from an optical analysis system (Nachbauer, et al., 1996). Why was the force data several orders of magnitude better than that achieved with an optical analysis system? FMC uses relative velocity (GPS carrier frequency data) angular velocity (gyroscope data) and acceleration (accelerometer data) directly. FMC exploits the properties of the signals from IMUs and GPS, fusing them without the need for post low-pass filtering and so ensuring maximum derived signal bandwidth.

The estimated resultant force error for giant slalom skiing of 110N is greater than the estimate of force error reported for inline skating, of 25N, discussed in Chapter 5. The forces experienced by the athlete in skiing (shown in Figure 7.2) are also greater than the forces recorded for inline skating and so it is unlikely that the increased error will have any significant adverse effects on the analysis.

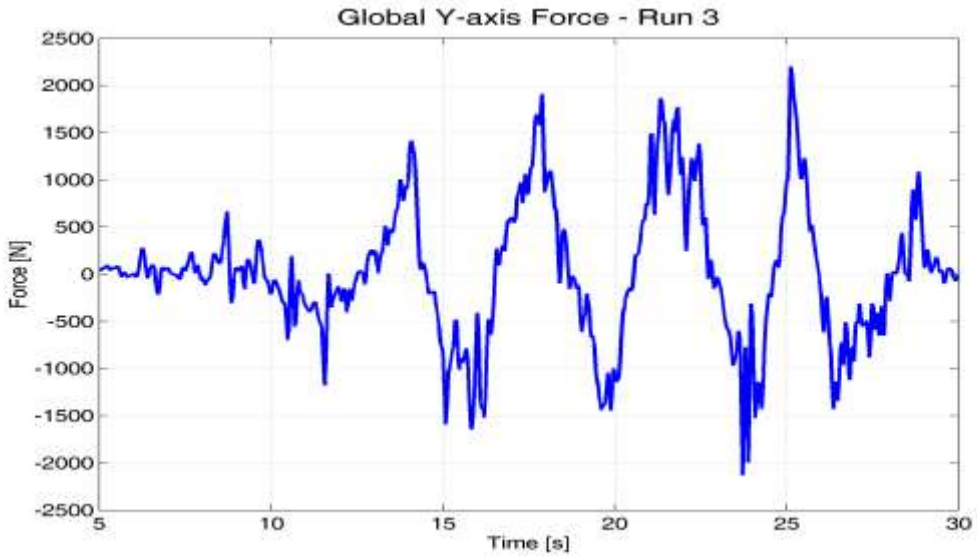

Figure 7.2: Resultant force across the ski slope in Run 3

Figure 7.2 shows there is considerable high frequency content in the resultant forces acting on the athlete‟s centre-of-mass, especially at the turn apex, for example around 15 seconds. The high frequency content is greater than the estimated force error of 110N and this is expected because the athlete‟s skis do not run smoothly across snow surface. The high frequency acceleration of the right ski is shown in Figure 7.3. The maximum acceleration, of nearly

$80ms^{-2}$, is around four times as large as the acceleration experienced by the athlete‟s centre-of-mass. This confirms the skis are not running smoothly across the snow surface. The athlete uses his technique to control perturbations in the ski motion and to transform the high frequency ski motion into a smooth, centre-of-mass trajectory through the gates (visualised in Figure 7.4). It is possible a skilled athlete might be considered, on an abstract level, a low pass filter and this could have some interesting implications for further research.

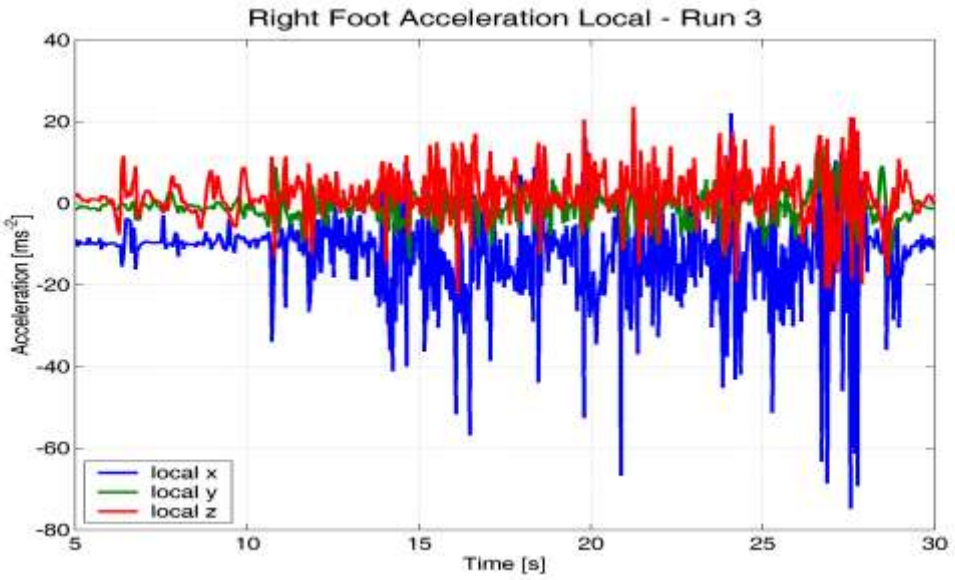

Figure 7.3: Local acceleration of the right ski

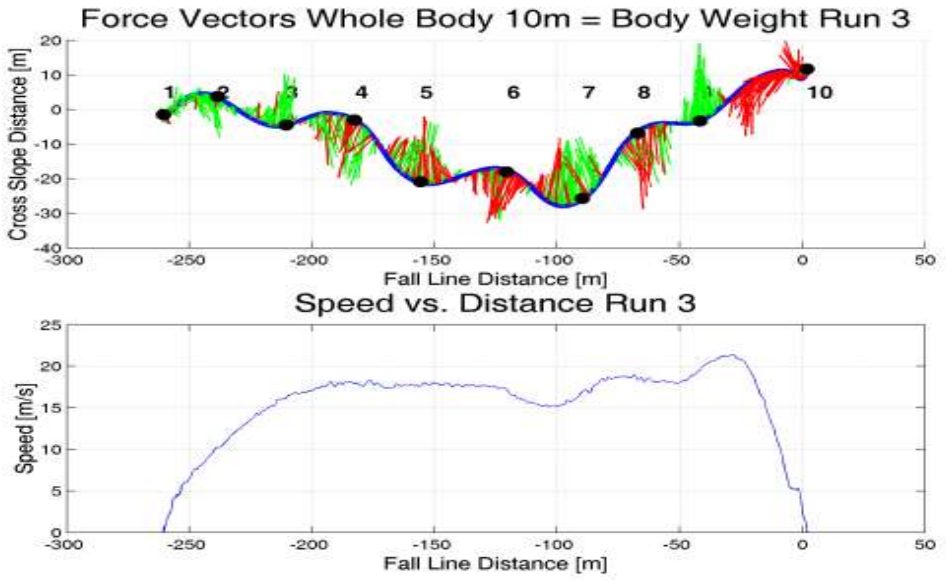

Figure 7.4: Force vector diagram of resultant forces for run 3

In Figure 7.4 the force vector analysis, top panel, shows the calculated resultant forces are consistent with the athlete‟s motion through the gate set, the forces are directed into the turns and there are distinct periods of acceleration or braking. This confirms 110N is a reasonable

estimate of the resultant force error and that this level of error in the data should have no significant effect on the analyses. The bottom panel in Figure 7.4 shows very little noise in the velocity data and so confirms that $0.3ms^{-1}$ was a reasonable estimate of velocity error.

These findings also agree with previous sensitivity analyses. In Chapter 4, during the wand trial, scaled Gaussian noise was added to the simulated GPS data to investigate the effects of GPS noise on FMC measurements of global trajectory and body segment orientation. In that chapter, the simulated GPS noise was shown to have a detrimental effect on the measured wand location but very little effect on the measured wand velocity data. Forces are partly derived from the velocity data and partly from the IMU measured accelerations and so the addition of a small amount of noise to the GPS velocity data should only have a small effect on the derived forces. A sensitivity analysis was also done on the 3D anthropometric frame data to determine how errors in bony landmarks position measurement might affect limb orientation measurements. It was determined that the IMU to body segment mapping error was less than 3º for all body segments accept the sacrum. These mapping errors should not significantly affect the measured forces.

In this chapter, section 7.5, a further sensitivity analysis is performed to investigate the extent of velocity effects on wind drag and snow resistance coefficients, which reveals some interesting findings. It is unlikely any further analyses of errors using the data available would yield any additional information other than speculation about what the errors might be. It should be re-enforced, however, that because this is a prototype system that is still undergoing testing and development, other errors might exist and when it becomes practical the results presented in the following chapters should be verified by additional data.

7.2. Models for dissipative forces

In alpine ski racing both the dissipative forces of wind drag and snow resistance act to decelerate the athlete and significantly increase course time. Although the forces tend to be small compared with the ground reaction forces, they always oppose the motion and hence over the duration of a run cause a significant amount of the available gravitationally potential energy to be dissipated. Ultimately these dissipative forces limit the athlete‟s maximum velocity. The dissipative forces therefore form an important part of the biomechanical analysis of alpine ski racing. The dissipative forces are considered important by athletes and money is spent tuning skis, buying waxes and wearing speed suits in a direct effort to reduce them.

During a ski race it is not possible to measure wind drag directly. Snow resistance could be measured with miniature force plates attached to the athlete‟s skis but at this stage such force plates are expensive and unacceptable to many athletes because of perceived performance loss and reduced safety. The wind drag force and snow resistance force therefore are modelled in skiing. This section follows on from the information about snow resistance and wind drag presented in the introduction.

7.2.1. Wind drag model

At high-speed wind drag in skiing is mainly due to pressure drag and is modelled by Equation 7.2. In the past wind drag has been estimated from measurements made using different stationary poses in wind tunnels (Kaps, et al., 1996). Wind drag during athlete performance through a race course was also estimated by fitting measurements of joint angles that could be filmed in the sagittal plane to data from wind tunnel tests (Barelle, et al., 2004).

Equation 7.2 $$F_{Drag} = \frac{1}{2}\rho A_c C_d V^2$$

In Equation 7.2 the symbols have the following meanings: (ρ) Density of air, (V) Relative wind velocity between the athlete‟s centre-of-mass (CoM) and the surrounding air, (A_c) Cross sectional area normal to the relative wind velocity, (C_d) The coefficient of wind drag.

Previous papers often measure wind drag in terms of the drag coefficient (C_d) or drag area (A_c*C_d, the drag coefficient multiplied by the cross sectional area). Reported values for drag area range from 0.15m^2 for the „egg posture“ in skiing at 28ms^{-1} (Barelle, et al., 2004) to 0.73m^2 for an upright posture in cross country skiing at less than 11ms^{-1} (Spring, et al., 1988). Reported values for wind drag coefficients (C_d) are subject, posture, and speed dependant. For ice skaters measured in a wind tunnel in coaching poses at 12ms^{-1}, C_d is subject dependant between 0.79 and 0.99. But at low velocities (~5ms^{-1}) C_d is reported to increase 2-3 fold for the same subjects (van Ingen Schenau, 1982). For the same subject different postures can also result in different drag coefficients, 0.6 for semi squatting to 1.0 for an upright position.

The high variability in wind drag coefficient highlights a problem for the accepted model of wind drag in skiing. This high variability is thought to be a consequence of skiing generating variable turbulent airflow in the boundary layer around the skier with a Reynolds number in the range 10^5 and 10^6 (Equation 7.3). In this Reynolds number range the airflow characteristics change rapidly as does the wind drag coefficient. In engineering this is termed the second critical flow region. A discussion of this is provided by Spring (Spring, et al., 1988). Over the second critical region turbulence builds up in the boundary layer close to the athlete‟s surface causing a sudden drop in the cross sectional area of the turbulent wake behind the athlete, and therefore a drop in wind drag coefficient.

Equation 7.3 $$\mathrm{Re} = \frac{LV}{\nu}$$

Reynolds number (Re, Equation 7.3) is dependent on the characteristic length (L) of the immersed object, fluid (in this case air) velocity (V) and the kinematic viscosity of air (υ=14.93*10^{-6} at standard conditions). Unfortunately, in skiing the characteristic length of the athlete perpendicular to the airflow is not fixed; it is different for each body segment, and

depends on the interaction between the body segments. If we take ($0.2<L<0.5$) the critical period starts at velocities between $3ms^{-1}$ and $8ms^{-1}$ and finishes between $30ms^{-1}$ and $75ms^{-1}$. A Reynolds number of $2.8*10^5$ is reported as the critical Reynolds number for cylinders, but depending on the characteristic length, this corresponds to velocities anywhere between $9ms^{-1}$ and $20ms^{-1}$.

Schenau showed that surface roughness also decreases the critical Reynolds number and hence moves the onset of a sudden decrease in wind drag coefficient to lower velocities. Probably due to this phenomenon, it was reported tight fitting woollen suits are better for skating at slow speeds <7 ms^{-1} than smooth suits (van Ingen Schenau, 1982).

How do the measurements made on static poses relate to wind drag when the athlete is moving between gates? This might destabilise the flow causing transient effects. Are the air flow characteristics of wind tunnel experiments where the subject blocks a significant proportion of the tunnel cross sectional area and hence the air must be squeezed past the subject the same as the air flow characteristics where the athlete moves over an undulating surface through still air? What about the aerodynamic lift force, a force perpendicular to relative wind velocity and which has been assumed is negligible because the athlete appears to adopt a posture with very little angle of attack relative to the wind velocity. It seems that any model used to estimate instantaneous wind drag is going to have inherent errors, but the trends observed over complete ski runs may be useful in the biomechanical analysis of alpine ski racing.

Fortunately most of the reports suggest that the airflow characteristics stabilises at relatively low wind speeds. Spring showed that wind drag area stabilised from $5ms^{-1}$ (Spring, et al., 1988) and Schenau showed wind drag coefficient stabilised around $16ms^{-1}$ (van Ingen Schenau, 1982). Above these velocities the wind drag coefficient can be approximated by a constant. In giant slalom athletes travel faster than $16ms^{-1}$ through most of the course and so wind drag could be estimated using a constant drag coefficient. The issue of subject specificity is controlled by optimisation of a wind drag coefficient for the subject. Later on in Section 7.4 the instantaneous cross sectional area (A_c) is measured to control the effect of postural changes on wind drag.

The value used for air density (ρ = $1.15kgm^{-3}$) was calculated from the measurements of air pressure (946mbar) and temperature (14°C) on the field. This was lower than the standard air density normally used (ρ = $1.20kgm^{-3}$). The air humidity of 28% was found not to significantly affect the dry air density at this relatively low temperature.

7.2.2. Snow resistance models

Three equations are commonly used to model ski/snow interaction; the Coulomb model (Equation 7.4), the viscous model (Equation 7.5), and Kap"s empirical model (Equation 7.6, Kaps et al., 1996). Laboratory measurements of the friction coefficient in the Coulomb model

range from (μ=0.003-0.007) for ice and (μ=0.04-0.2) for snow (Shimbo, 1971) and (van Ingen Schenau, 1982). More background information is contained in the Introduction (Chapter 1).

Equation 7.4 $$F_{Frict} = \mu F_N$$

Equation 7.5 $$F_{Viscous} = \frac{\eta A_c V}{d}$$

Equation 7.6 $$F_{Snow} = F_N(\mu_F + \mu_V V)$$

In the above equations; μ is the friction coefficient, F_N is the normal force, η is the fluid viscosity, A_c is the contact area, V is the ski velocity, d is the fluid depth, μ_F is the static friction coefficient and μ_V is the dynamic friction coefficient.

In giant slalom neither the Coulomb model nor the viscous model are able to estimate the forces retarding the skis motion as they move through the snow surface. In giant slalom the ski does not sit flat on the snow surface, but moves from edge to edge between gates. The ski bends and the snow is displaced as it compresses and fractures. Federolf showed that this is a non-linear threshold process (Federolf, et al., 2007).

If snow compression and displacement are significant then ski speed also needs to be incorporated into the model. Logically the faster the ski travels through the snow the more snow is displaced and the quicker the athlete‟s kinetic energy is dissipated. Instinctively Kaps has tried to incorporate velocity effects into a simple model and predicted some average coefficients (Kaps, et al., 1996), Equation 7.6). Kaps‟ empirical equation was used in this thesis and from this point on the retarding force as a result of the ski travelling through the snow, will be referred to as snow resistance.

Equation 7.6 also makes theoretical sense. The static coefficient (μ_F) models the ski/snow sliding friction ($F_N \bullet \mu_F$) that increases with increased normal force (F_N). The dynamic coefficient (μ_V) models the force required to compress the snow ($F_N \bullet \mu_V \bullet V$) as the ski moves forward through the top snow layer. The force required to compress the snow depends on how fast the snow is compressed (V) and how deep the ski penetrates. Ski penetration depth is included in the model by including the normal force (F_N).

Running in a straight line Kaps predicted low coefficients of friction (μ_F~0.008, similar to that of ice skating rinks) with very little dependency on velocity (μ_V~0.00009sm^{-1}). This may be because he attempted to solve for the coefficients of snow resistance and wind drag simultaneously. Kaps did not discuss the inherent negative correlation between the variables in this mathematical solution. For example as the optimum solution for the wind drag coefficient goes up the solution for the snow resistance coefficients must go down, but the residual from the optimisation may remain relatively unchanged. Hence, an infinite number of dependent solutions for wind drag coefficients and sliding friction coefficients exist that fit

the data equally well. It is possible in their solution they overestimated wind drag and underestimated sliding friction. The low dependency on velocity for the straight running experiment may also be because less snow is displaced going straight relative to turning.

Kaps then completed some traversing experiments but only solved for the static friction term (μ_F = 0.060 – 0.171) for velocities between 0.6ms^{-1} and 16.6ms^{-1}. These results apparently show an increasing snow resistance with increasing velocity, but could also (as discussed by Kaps) be a result of the snow softening through the day.

7.3. Biomechanical Man Version Two with solid limbs

A volumetric model of the athlete was needed to estimate changing cross sectional area more accurately (Section 7.4) and therefore estimate the wind drag more accurately (Section 7.5). Each segment of the athlete was rendered by an elliptic cylinder, with end caps (Figure 7.5). The dimensions of the ellipses were determined about each joint centre from calliper measurements of the athlete. End caps were both convex and concave. For the terminal segments such as the hands and head the terminal end caps‟ centres were offset, which allowed better visualisation of 3D orientation. Between 16 and 128 faces were used to render each elliptical surface; more faces smoothed the appearance but required more memory.

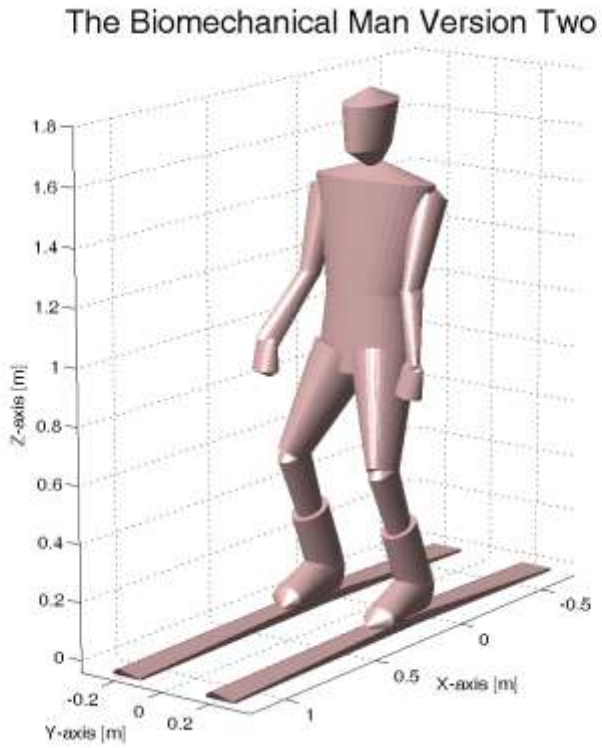

Figure 7.5: The Biomechanical Man Version Two, solid elliptical surfaces with end caps

The code to render the athlete avatar into a solid form was written in MATLAB. Because the same language and protocol was used for the original triangular body segments it was immediately possible to use the new avatar to animate data from the athlete‟s motion. In fact

the FMC data could easily be used to drive any avatar. Unfortunately, in version one of the MATLAB code a small bug resulted in the faces of each body segment not being rendered correctly. This resulted in some abstract art (Figure 7.6) and demonstrates the complexity of developing a visualisation system from scratch.

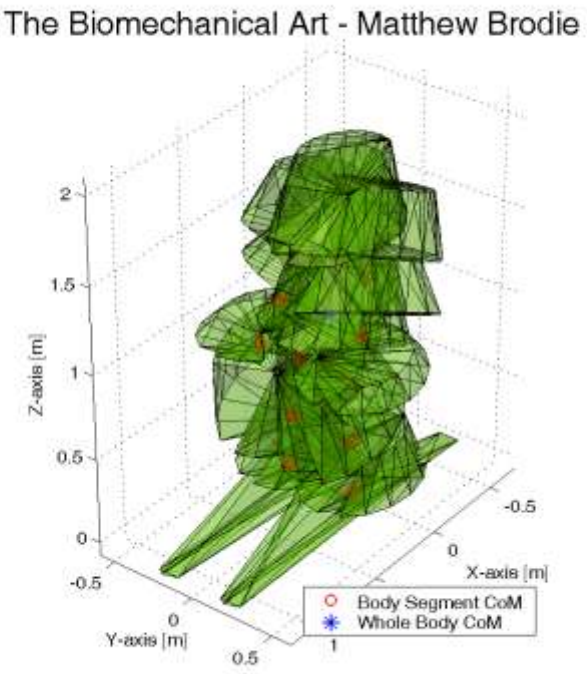

Figure 7.6: Version one of the new rendering algorithm contained some bugs

The volumetric model body segment limb lengths were based on measurements of the athlete in the anthropometric frame. Any potential error in the limb lengths could propagate into error in the athlete"s volumetric body model. In Chapter 4 on page 76, the relative error of lengths between bony landmarks from subjects in the anthropometric frame were analysed and the body segment orientation error estimate was 3%. Additional errors of 4% in segment limb lengths may have resulted from the error between bony landmark measurements and the calculated joint centre locations as discussed in Chapter 4 on page 74. The Biomechanical Man Version Two model is therefore estimated to contain up to 7% error in limb lengths, which may propagate into the following cross sectional area calculations.

7.4. Dynamic cross sectional area and wind drag

Ideally athletes would like to reduce their wind drag in giant slalom skiing. One approach is to reduce the drag coefficient (*Cd*) by using aerodynamic suits and slight adjustments to static postures based on wind tunnel measurements and/or intuition. The biggest reduction in wind drag, while moving dynamically between course gates, should be a result of the athletes adopting a technique that reduces their cross sectional area. The changing cross sectional area

of the athlete was measured using FMC data and the revised biomechanical man model and so it then became possible to estimate dynamic changes in wind drag through the course.

7.4.1. Method of measuring cross sectional area

FMC data were used to drive the biomechanical model in an animation and the athlete was rendered as a white avatar on a black background. The motion was viewed from a virtual camera positioned a fixed distance from the athlete and coincident with the athlete's CoM velocity vector. An orthographic (parallel) projection was used to render the avatar and so the measured area did not depend on the distance of the athlete's body segments from the virtual camera.

For each frame the cross sectional area was estimated by counting the number of white pixels in the figure. The measurements were then scaled to area by dividing by the number of pixels in a square metre patch. A white square patch with metre long sides was rendered normal to the virtual camera and at the same fixed distance as the avatar. The scale used was 29,241 pixels per square metre, which should have resulted in an accuracy of better than 1cm^2, assuming rather optimistically that the body model was accurate to this level, which is unlikely since in the previous section the body model limb segment error was estimated to be up to 7%.

7.4.2. Results of cross sectional area in skiing

The method appeared to work, Figure 7.7 shows a negative image of the avatar taken as a snapshot during the analysis. An animation of several turns from run 3 is also provided to allow the reader to validate the principals behind the proposed method (Video 7.1).

Figure 7.7: Screen capture: A silhouette of the athlete's cross sectional area

Video 7.1: Appendices\FMC Video\Silhouette.avi

The athlete‟s changing cross sectional area normal to the velocity vector was then measured by pixel counting and plotted in Figure 7.8.

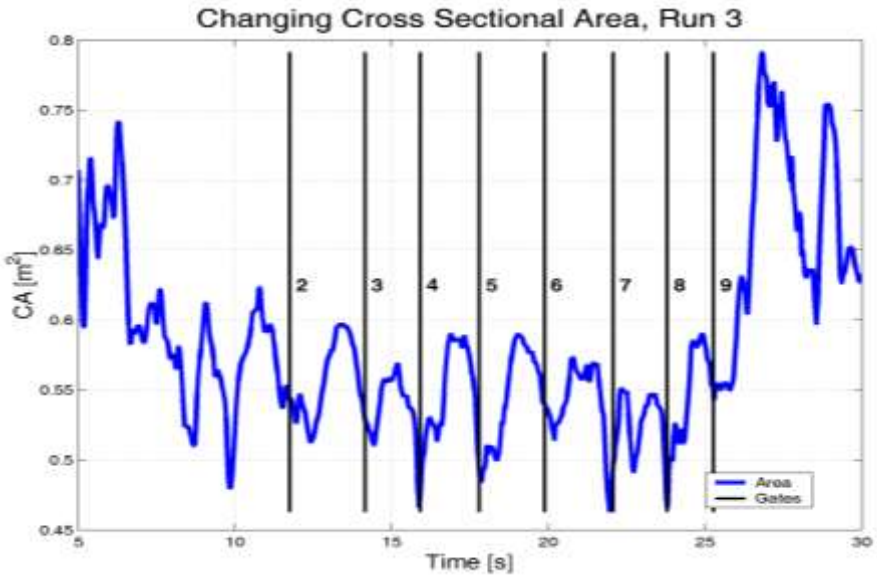

Figure 7.8: Changing cross sectional area between gates 2 and 9 on run 3

7.4.3. Discussion about changing cross sectional area

There was an apparent relationship between the athlete‟s average cross sectional and his speed; compare Figure 7.8 with his velocity profile produced later on in Chapter 8 on page 196. On average the smaller the athlete‟s cross sectional area the faster he went. Gravity provides the main propulsive force so it is logical that the athlete might think that „reducing wind drag by reducing cross sectional area will increase speed‟. However, energy analyses of skiing presented later in this chapter show that these small changes in posture had little effect on outcome because at the speeds the athlete was travelling the wind drag force was apparently the least significant force.

Between gates 2 and 9 in Figure 7.8, the higher speed sections of the course, his area changes rhythmically with gate location. Cross sectional area is as high as $0.6m^2$ during upright stances, from the cross over point to the gate approach, but reduces to as low as $0.46\ m^2$ at and just after each gate. As a consequence of stance changes, the athlete‟s calculated wind drag force was approximately 25% lower near the turn apexes compared to between the gates. The reduction in cross sectional area as speed increased may have also been a result of the athlete inclining more at the turn apexes, and therefore, bending more at the waist in order to pass outside each gate.

The body model limb segment error of up to 7% was adopted for the cross sectional area measurements, therefore in absolute terms the cross sectional area error is approximately $0.04m^2$. The changes in cross sectional area between gates (around 25%) are larger than the estimated error (up to 7%) and so the estimated error should have no significant effect on the

wind drag force analysis between the gates, especially because the choice of wind drag coefficient is likely to be inversely proportional to the mean calculated wind drag area.

The cross sectional area was largest (up to 0.78m^2) when parts of the ski bases lost contact with the ground, such as during a skating stroke (t~6s, Figure 7.8) and during the skidding stop (t~27s, Figure 7.8). When velocity was low during the skating start, even with the high cross sectional area, the drag force was low, but during the skidding stop where velocity was high, the increased cross sectional area produced a significant increase in drag force.

7.5. Calculating model coefficients

This section covers how the wind drag and snow resistance coefficients were calculated from the FMC data of the athlete skiing. The coefficients were required to estimate the external forces of wind drag and snow resistance on the athlete.

The residual of a force balance (for the athlete‟s movements, Equation 7.7) was minimised by using MATLAB algorithms to select the coefficients of wind drag (C_d) and sliding friction (μ_F). This is similar to the method introduced for inline skating in Chapter 5 on page 95. The optimisation was completed many times with different windows of data to investigate the robustness and potential velocity dependency of the coefficients.

Equation 7.7 $$\mathbf{Residual} = m * \mathbf{A}_{\mathbf{CoM}} - \mathbf{F}_{\mathbf{g}} - \mathbf{GRF}_{\mathbf{L}} - \mathbf{GRF}_{\mathbf{R}} - \mathbf{F}_{\mathbf{Drag}} - \mathbf{F}_{\mathbf{Drag}}$$

Improvements were made in the selection of wind drag and snow resistance coefficients from the previous inline skating experiment. Unchanged from the work in Chapter 5 was the process of calculating CoM acceleration ($\mathbf{A_{CoM}}$), weight force ($\mathbf{F_g}$), and the ground reaction forces under each foot ($\mathbf{GRF_L}$ + $\mathbf{GRF_R}$). The first estimation of ground reaction forces are defined as the forces normal to the ski bases and hence can be estimated from the FMC data, the resultant forces (Figure 7.4, top panel) and the orientation of the skis. Enhancements included incorporating the athlete‟s changing cross sectional area (A_c) into the model. To find the wind drag and sliding friction coefficients the problem was re-written in the form of a linear equation (Equation 7.8), which required some new variables to be defined.

Equation 7.8 $$\mathbf{Ax} + \mathbf{b} = \mathbf{0}$$

First a matrix called **Wind_Slide** (n by 3 matrix, Equation 7.9) was created. It contained three element vectors of combined wind drag and snow resistance vectors over n time steps.

Equation 7.9 $$\mathbf{Wind\_Slide} = \mathbf{F}_{\mathbf{g}} + \mathbf{GRF}_{\mathbf{L}} + \mathbf{GRF}_{\mathbf{R}} - m * \mathbf{A}_{\mathbf{CoM}}$$

Because friction opposes the direction of motion, trigonometry was used to keep only the components of **Wind_Slide** parallel to the athlete"s motion (**WS_Parr**, Equation 7.10 and Equation 7.11). In these equations | | denotes the magnitude of a vector at each time step, and ($\mathbf{V_{CoM}}$) denotes the athlete"s velocity vector.

Equation 7.10
$$\cos\theta = \frac{\mathbf{Wind\_Slide}}{|\mathbf{Wind\_Slide}|} \bullet \frac{\mathbf{V_{CoM}}}{|\mathbf{V_{CoM}}|}$$

Equation 7.11
$$\mathbf{WS\_Parr} = \frac{\mathbf{V_{CoM}}}{|\mathbf{V_{CoM}}|}\left(\cos\theta|\mathbf{Wind\_Slide}|\right)$$

Next wind drag was accounted for by combining the elements of the wind drag equation (Equation 7.2) into a matrix variable **VA2** (n by 3 matrix, Equation 7.12) This variable represents the combined effects of air density (ρ = 1.15 kgm^{-3} @ 946mbar and 14°C), the measured changing cross sectional area (A_c, Section 7.4) and velocity, on wind drag. The matrix **VA2** contained one row of data for each time step. Each row contained the X, Y and Z-axes contributions to wind drag, before being scaled by the unknown coefficient (C_d).

Equation 7.12
$$\mathbf{VA2} = \frac{\mathbf{V_{CoM}}}{|\mathbf{V_{CoM}}|}(0.5A_c\rho|\mathbf{V_{CoM}}|^2)$$

Next the effects of snow resistance were included. To prevent under specification of the problem, the ground reaction forces were assumed to act mainly normal to the ski base surface. The snow resistance therefore was assumed to act only in the plane of the ski base (local x and z axes of the ski). The velocity of each ski ($\mathbf{V_{Global}}$) was extracted from the FMC data. The velocity of the ski in the plane of its base ($\mathbf{V_{Ski\_Base}}$, Equation 7.14) was then calculated in the global coordinate system. The measured orientation of the skis (rotation matrices $\mathbf{R_{LG}}$ and $\mathbf{R_{GL}}$) was used to move between the global and local coordinate systems.

Equation 7.13
$$\mathbf{V_{Local}} = \mathbf{R_{GL}}\mathbf{V_{Global}}$$

Equation 7.14
$$\mathbf{V_{Ski\_Base}} = \mathbf{R_{LG}}\begin{bmatrix}\mathbf{V_{Local\_X}} & \mathbf{0} & \mathbf{V_{Local\_Z}}\end{bmatrix}$$

The magnitude of the ground reactions forces (|**GRF**|) was then combined with the components of the left (L) and right (R) ski velocity vectors coincident with the athlete"s centre-of-mass velocity vector to get the effective normal force (**N**, Equation 7.16). The effective normal force was required to estimate the snow resistance.

Equation 7.15 $$\cos\beta_L = \frac{\mathbf{V}_{\text{Ski\_Base\_L}}}{\left|\mathbf{V}_{\text{Ski\_Base\_L}}\right|} \bullet \frac{\mathbf{V}_{\text{CoM}}}{\left|\mathbf{V}_{\text{CoM}}\right|}$$

Equation 7.16 $$\mathbf{N} = \frac{\mathbf{V}_{\text{CoM}}}{\left|\mathbf{V}_{\text{CoM}}\right|}\left(\cos\beta_L\left|\mathbf{GRF}_{\text{L}}\right| + \cos\beta_R\left|\mathbf{GRF}_{\text{R}}\right|\right)$$

With all the preparation done the matrices **WS_Parr**, **VA2** and **N** were re-shaped into row vectors, each now three times the original length, and put into linear equation form (Equation 7.8). Finally the data from each run were used to find the coefficients of wind drag (C_d) and snow resistance (μ_F) that minimised the equation for residual forces from Equation 7.7 parallel to the athlete"s centre–of-mass velocity (Equation 7.17). Because of its simple form, it took less than 0.5 seconds to solve Equation 7.17 hundreds of times for different windows of data. MATLAB was used to solve the over determined simultaneous equation. Because **A = [VA2 N]**, (from Equation 7.8 and Equation 7.17) is not a square matrix but is full, Householder reflections were used to compute an orthogonal-triangular factorization, which sped up obtaining a solution. MATLAB called LAPACK algorithms written in FORTRAN to solve the linear equation.

Equation 7.17 $$\begin{bmatrix} C_d & \mu_F \end{bmatrix} = \begin{bmatrix} \mathbf{WS\_Parr} \end{bmatrix} / \begin{bmatrix} \mathbf{VA2} & \mathbf{N} \end{bmatrix}$$

7.5.1. Choosing the coefficients

Using the procedure described in Section 7.5 the coefficients of wind drag (C_d) and snow resistance (μ_F) were calculated over different windows (lengths) of data (Figure 7.9) for Run 3. The data windows included all data above an increasing cut-off speed. Eventually when the cut-off speed was above 16ms^{-1} the solution became unstable because the number of data points used was too small. The snow resistance coefficient was multiplied by ten so both coefficients could be viewed on the same graph.

Figure 7.9 shows a strong negative correlation between the optimised solutions of the two different coefficients making it very difficult to obtain a robust or accurate solution. The negative correlation is probably because both coefficients have a strong dependency on velocity as discussed in Sections 7.2.1 and 7.2.2. Systematic errors therefore could have been introduced into the data through the erroneous selection of model coefficients.

Any systematic errors in modelled forces could be exacerbated by the method used to model the ground reaction forces (as two forces acting nearly perpendicular to the ski bases). The athlete polling, crashing through the course gates or the ski flexing could produce ground reaction forces with components parallel to the ski base that do not fit the model and therefore could produce extreme statistical outliers. These extreme statistical outliers could cause, for example, the mean horizontal ground reaction forces acting on the athlete to be over-

estimated. This in turn could cause error in the selection of mean wind drag or snow resistance coefficients. Similarly the snow resistance force coefficient could be overestimated and the wind drag force coefficient underestimated. The model coefficients are interdependent because the calculation of forces is a closed loop constrained by the athlete"s centre-of-mass trajectory.

Between 10ms^{-1} and 16ms^{-1} on the horizontal axis, the solution appears to stabilise. The athlete generally skied faster than 15ms^{-1} so it was decided to reduce the complexity of the problem by assuming a fixed wind drag coefficient based on all data above 15ms^{-1}. More reasoning behind this choice is found in Section 7.2.1. The calculated wind drag coefficient chosen was C_d=0.52 (see Speed=15ms^{-1} in Figure 7.9) it was assumed to be constant and independent of velocity. The analysis shows the wind drag coefficient could well have been as high as C_d=0.60 or as low as C_d=0.48 for the athlete.

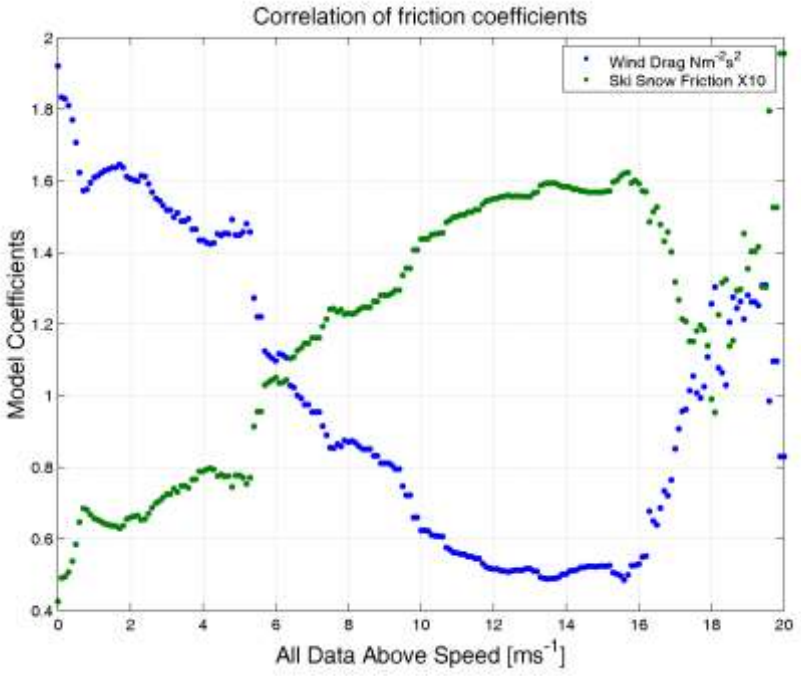

Figure 7.9: Changes in optimised friction coefficients with velocity

After assuming the wind drag coefficient was constant over the majority of the racecourse it was then possible to investigate further the effects of velocity on the snow resistance. First, the data were ordered based on speed and selected large windows of data (>8 seconds) with different mean velocities. Snow resistance only was then solved for (μ_F, Equation 7.17).

It appeared from the data that snow resistance in giant slalom increased with velocity (Figure 7.10), but the relationship is not linear. There was not enough data to develop a more complex model and so a linear model was fitted to the section of the data between 3ms^{-1} and 18ms^{-1}. Below 3ms^{-1} the athlete may have used his poles, which were not accounted for in the force balance, and above 18ms^{-1} the reduced data window size increased the noise in the motion.

The snow resistance model Equation 7.6 was the same as the linear model used to fit the athlete‟s data in Figure 7.10. The y-intercept in Figure 7.10 defined the static term for snow resistance (μ_F=0.042) and the slope of the line in Figure 7.10 defined the velocity dependant term (μ_V=0.0061sm^{-1}). If however a different wind drag coefficient had been chosen then the snow resistance coefficients would also be different. Further analyses are therefore required to confirm these results.

Equation 7.6 $$F_{Snow} = F_N(\mu_F + \mu_V V)$$

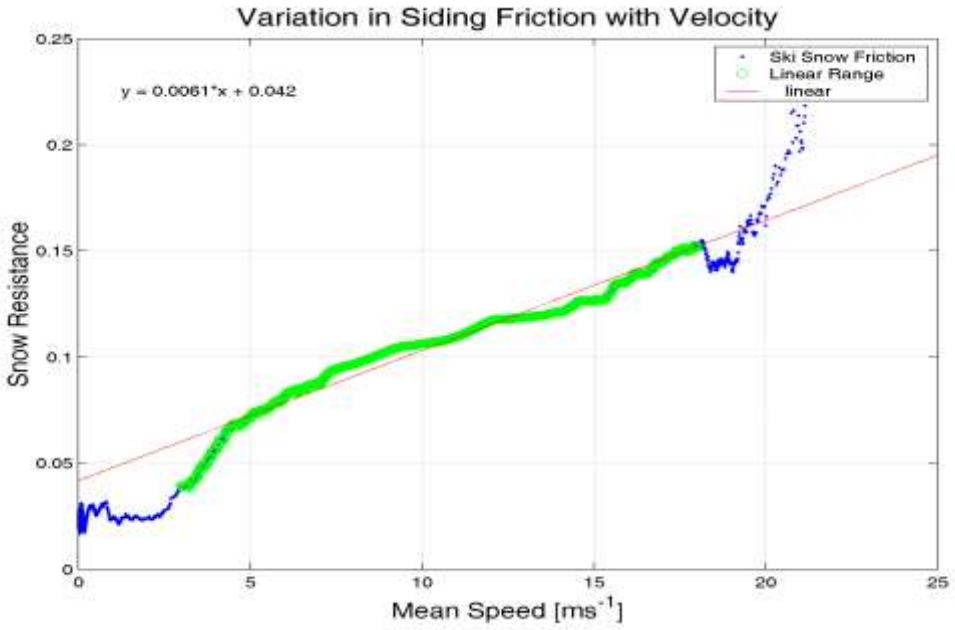

Figure 7.10: Snow resistance coefficient versus Mean speed - fitted with a linear model

7.5.2. Discussion about wind drag and snow resistance

How do the model coefficients for wind drag and snow resistance compare with previous research?

The snow resistance model (linear fit of Figure 7.10) predicts a total snow resistance coefficient ($\mu=\mu_F+\mu_V V$) at slow speeds of around 0.04 but at high speeds the total coefficient increases to 0.2, these values are within the range suggested in literature for hard and soft snow respectively (μ=0.04-0.2, (Shimbo, 1971). The model used to fit the data also agrees with data from Kaps (μ=0.060–0.171) for velocities between 0.6ms^{-1} and 16.6ms^{-1} (Kaps, et al., 1996), but it seems Kaps may have done his experiments on slightly softer snow as his values are slightly higher at slower speeds.

The snow resistance model coefficients used and therefore the calculated snow resistance agree with miniature force platform measurements of forces parallel to ski bases (Lüthi, et al., 2005). Lüthi showed, for his athlete and snow conditions skiing at 13m/s, between 7% and

10% of the ground reaction forces were parallel to the ski bases. The model predicted at 13m/s about 12% of the ground reaction forces should parallel to the ski bases (Figure 7.10). The difference might be because of softer snow conditions, different skis, different course setting and/or different wax used for ski preparation.

The athlete‟s wind drag area (C_dA_c) was calculated based on C_d=0.52 (Figure 7.11). While the athlete was running both skis smoothly over the snow the wind drag area varies between 0.24m^2 and 0.33m^2. This is in agreement with previous experiments conducted in wind tunnels. It is not as low as values for the „egg posture‟ (C_dA_c=0.15). But it sits nicely between semi squatting (C_dA_c=0.2) and upright poses (C_dA_c=0.35, (Barelle, et al., 2004).

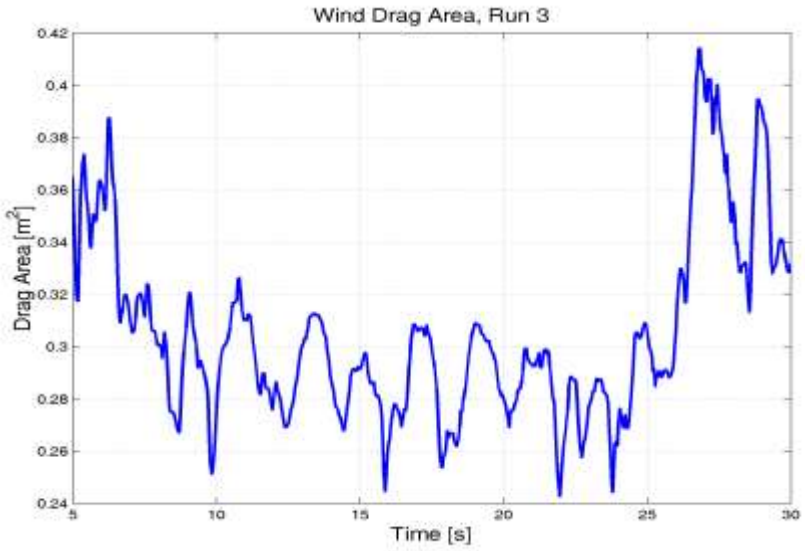

Figure 7.11: Instantaneous wind drag area from FMC

How accurate is the fixed wind drag coefficient? The model incorporates the effect of changing posture cross sectional area on wind drag force. Because there was not sufficient data, the model does not incorporate the effects of changing velocity and characteristic posture length on Reynolds number and therefore drag coefficient (C_d).

Springs data (Spring, et al., 1988) can be re-arranged to show there may be a correlation between characteristic posture length (L) and drag coefficient (C_d). If Spring‟s measured wind drag area is divide by the measured projected area a wind drag coefficient is obtained. Spring‟s data show moving from a crouched posture (long length parallel to the wind and higher Reynolds number) to an upright posture (short length parallel to the wind and lower Reynolds number) increases the wind drag coefficient by 20% to 40%. The optimisation used in this thesis selected an average value for the wind drag coefficient so the results may have underestimated the effect of stance changes on wind drag force from standing to crouching.

To reduce the effect of stance changes on drag coefficient error some sort of mean characteristic length of the athlete‟s stance could be estimated by his silhouette as viewed perpendicular to the wind velocity. In the future the changing characteristic lengths (L) of the

athlete and the changing velocity (V) could be used to estimate changes in Reynolds number and the effects on the drag coefficient. However at this stage there was not have enough data to build such a detailed model and so it was decided that this approach was beyond the scope of this thesis.

The analyses of wind drag and snow resistance based on the FMC data have produced some interesting results. Because of the high correlation between the different optimised coefficients, the data were windowed by velocity using all data greater than 15ms^{-1} to predict a constant coefficient of wind drag. A linear model was then used to predict the change in snow resistance coefficient with velocity. Neither assumption was perfect, but it was the best that could be done with the data available. In the future, if the analysis was repeated, 3D force plates could be used under the athlete"s feet to separate snow resistance from wind drag. The athlete could ski through the course several times at different speeds and with different stance heights. This would hopefully provide enough data to improve the understanding of the dissipative forces in giant slalom skiing.

The results of this analysis are surprising: It appears that over the course snow resistance was generally larger than wind drag (Figure 7.12). This contradicts some previous research based on laboratory measurements of ski/snow friction (Barelle, et al., 2004). The snow resistance was higher than expected for the relatively hard and fast snow. The high snow resistance coefficients at high speeds were probably caused more by the displacement, compression and ploughing of the snow, especially while cornering. At slow speeds the traditionally Coulomb ski/snow sliding friction predominated.

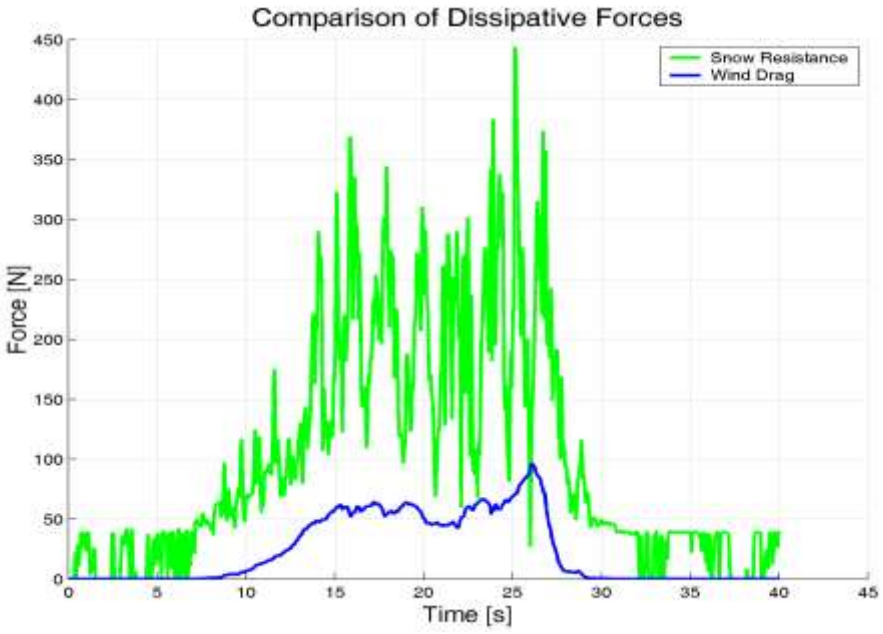

Figure 7.12: Comparison of dissipative forces through the course

There is a small possibility that some error exists in these results, a consequence of statistical outliers in the motion capture data combined with analysis error, and exacerbated by the high

negative correlation between the dissipative force coefficients. In the future the results should be confirmed by additional data from multiple runs of multiple athletes on similar and steeper terrain with different snow conditions.

7.6. Ground reaction forces

The new models of wind drag and snow resistance made it possible to make a better estimate of the ground reaction forces normal to the ski bases (**GRF**). The calculations for **GRF** are similar to the calculations used in Chapter 5 but in this section estimates for the resistive forces parallel to the athlete"s velocity ($\mathbf{F_{Drag}} + \mathbf{F_{Snow}}$, Equation 7.18) are available from the previous section. Therefore, it was possible to use the total forces normal to the ski bases instead of only the projection of the total forces perpendicular to the athlete"s velocity.

1. First the total forces normal to both ski bases (**GRF**) were calculated by a force balance on the athlete"s centre-of-mass (Equation 7.18). In this case wind drag ($\mathbf{F_{Drag}}$) and snow resistance ($\mathbf{F_{Snow}}$) had previously been estimated in Section 7.5 and ($\mathbf{F_{CoM}}$) was the net force acting on the athlete"s centre-of-mass found from the FMC data.

Equation 7.18
$$\mathbf{GRF} = \mathbf{F_{CoM}} - \mathbf{F_{Gravity}} - \mathbf{F_{Drag}} - \mathbf{F_{Snow}}$$

2. The forces normal to the ski bases (**GRF**) were then attributed to the left ($\mathbf{GRF_L}$) and right skis ($\mathbf{GRF_R}$) according to the estimated foot loading ratio and the orientation of the vectors normal to the bases of each ski (Equation 7.19 to Equation 7.22).

Equation 7.19
$$\left|\mathbf{GRF_R}\right| = \frac{\left|\mathbf{GRF}\right|}{\cos\theta_R + \cos\theta_L \frac{Ratio}{1-Ratio}}$$

Equation 7.20
$$\left|\mathbf{GRF_L}\right| = \frac{\left|\mathbf{GRF}\right| - \left|\mathbf{GRF_R}\right| * \cos\theta_R}{\cos\theta_L}$$

Equation 7.21
$$\mathbf{GRF_R} = \left|\mathbf{GRF_R}\right| * \mathbf{Ski}\perp_{\mathbf{R}}$$

Equation 7.22
$$\mathbf{GRF_L} = \left|\mathbf{GRF_L}\right| * \mathbf{Ski}\perp_{\mathbf{L}}$$

Where: *Ratio* is the foot loading ratio, θ_L and θ_R are the angles subtended by **GRF** and the vectors normal to the bases of each ski respectively and $\mathbf{Ski}\perp_{\mathbf{R}}$ and $\mathbf{Ski}\perp_{\mathbf{L}}$ are the unit vectors normal to the bases of each ski.

3. The estimated ground reaction force ($\mathbf{GRF_{Est}}$) was rotated to the match the supplied force normal to the ski bases (**GRF**). The correction was applied separately to the left and right feet.

   The sum of the estimated ground reaction forces ($\mathbf{GRF_{Est}} = \mathbf{GRF_L} + \mathbf{GRF_R}$) resulted in a vector that ends on the plane normal to **GRF** and projects exactly onto the **GRF** vector. However $\mathbf{GRF_{Est}}$ and **GRF** may not be exactly the same vector because:

   - The foot loading ratio may be incorrect.
   - The athlete‟s GRF may be projected either inside the vector normal to the ski base during turning by a „gripping of the snow‟ due to the longitudinal grain etched into the ski base.
   - The athlete‟s GRF may be projected outside the measured vector normal to the ski base during turning due to off centre ski loading, ski bending and/or rotational slack between the boot and ski. The ski/boot/foot segment was assumed to be a rigid body.
   - There may be drift errors in the ski orientation measurements as a result of the fusion algorithm performing poorly.

7.7. Residual forces, power and energy

After the ground reaction force analysis there were still residual forces unaccounted for in the athlete‟s force balance (Equation 7.7). The existence of these residual forces shows there is scope to improve the FMC system accuracy further. The causes may have been:

- Noisy FMC data (discussed in Section 7.1) producing a resultant force error of up to 110N.
- The ski/boot/foot segment was not rigid and the ski was bending about multiple axes as it vibrated rapidly through the snow surface, such that the ski moved and bent relative to the IMU attached to the ski boot heal.
- Movement between the athlete‟s helmet and the athlete‟s head. The IMU and GPS used to calculate the global trajectory were attached to the helmet movement of the helmet relative to the head could be misinterpreted as whole body movement by the FMC system.
- Neither of the models of wind drag nor snow resistance could accurately predict the instantaneous forces.
- Errors in the inertial parameters of the athlete‟s body model.
- The athlete poling and crashing through gates, which creates addition horizontal ground reaction forces which are not perpendicular to the ski bases.

The remaining residual forces were accounted for by scaling them to each foot according to the foot-loading ratio and adding them to the ground reaction forces. This might reflect the instantaneous bending of the ski, the possible effect of elastic energy stored in the ski, and

rapid changes in orientation between the ski base and the IMU measured orientation of the boot base.

In Figure 7.13 the combined ground reaction forces and residual forces are plotted about gate six.

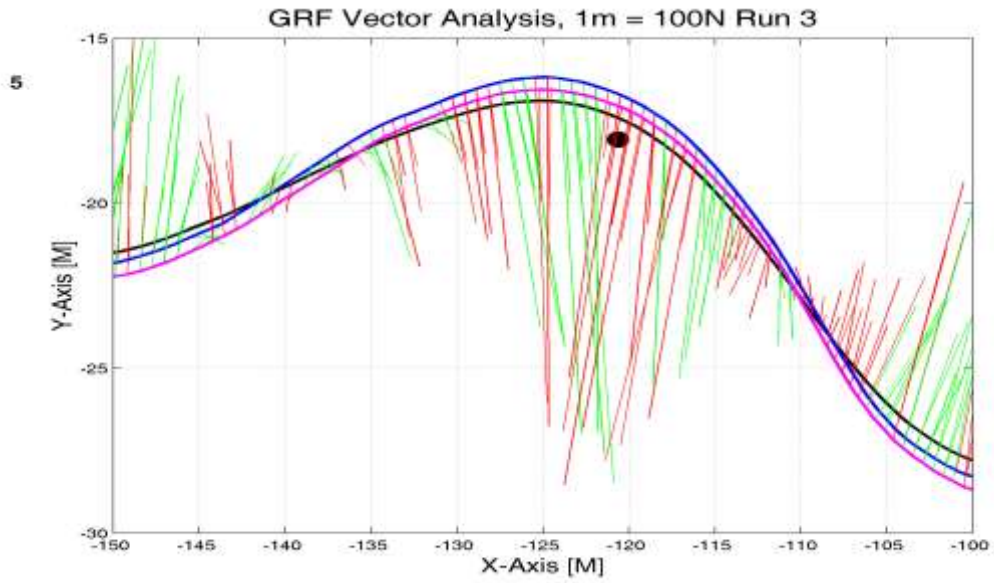

Figure 7.13: Ground reaction force vector analysis about gate 6 in run 3

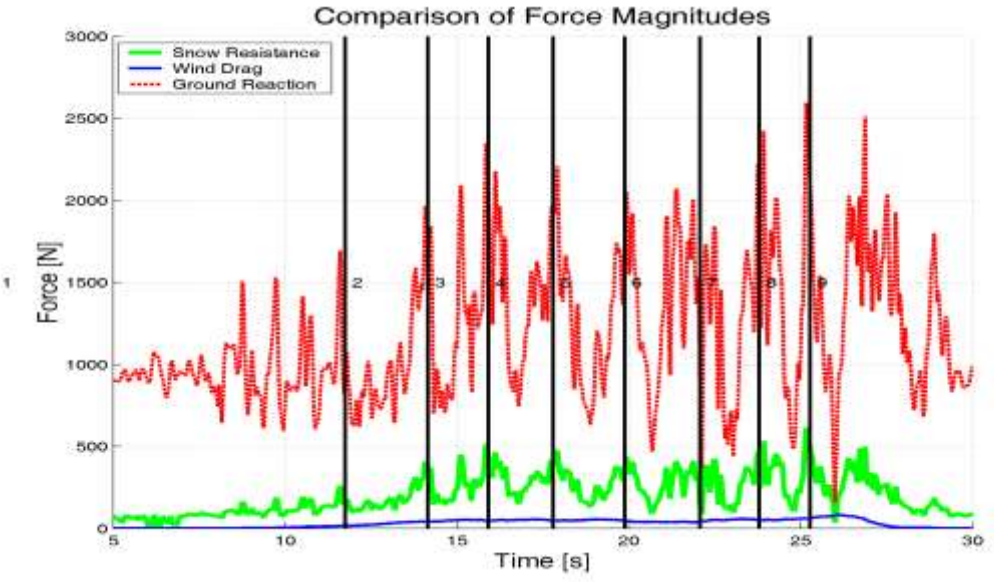

Figure 7.14: Comparison of ground reaction force to dissipative forces

Figure 7.13 shows the athlete's CoM trajectory (black line), right ski trajectory (magenta line), and left ski trajectory (blue line). The ground reaction forces are plotted as vectors originating from points on the ski trajectories and colour coded (green for forces acting to increase speed and red for forces acting to decrease speed). The combined ground reaction forces are likely to contain 110N of error, a direct result of error in the calculated resultant

forces. Figure 7.13 shows that this level of error has not significantly affected the analysis of ground reaction forces. In the figure the forces are directed into the turn, do not fluctuate randomly, and show distinct periods of positive and negative work.

Figure 7.14 shows a comparison between the ground reaction forces, snow resistance and wind drag from run 3. The ground reaction forces generated by the athlete were much larger in magnitude than either snow resistance or wind drag. In summary, because of the calculation methods used, most of the high frequency noise in the force analysis will be in the ground reaction forces. All three forces could contain unknown systematic mean error, the result of error introduced during the selection of the model coefficients. The model coefficients that were selected agreed with literature values as discussed in Section 7.5.2 and so it was assumed that any systematic error was not large enough to significantly affect any future analyses.

The combining of the ground reaction force with residual force worked well for the colour coded force vector analysis. Unfortunately, for a power analysis, combining the two forces did not work well because the ground reaction force power became swamped with high frequency signal content. This can be seen by comparing power analyses when the residual forces are separate (Figure 7.15) and when the residual forces are combined with ground reaction forces (Figure 7.16). Therefore, to improve the clarity the residual forces were kept separate because this made it easier to observe the trends in the ground reaction force power. In Figure 7.15 trends in the ground reaction force power are easier to observe, compare the positive ground force power about gates 5, 7 and 9 versus the neutral ground reaction force power about gates 6 and 8. The positive power about gates 5, 7 and 9 corresponds to increased speed (kinetic energy) and increased ground reaction force work in the energy analysis (Figure 7.17).

The energy analysis shows that the residual forces had little effect on the athlete‟s overall performance compared to the other forces (purple line, Figure 7.17) and so leaving the residual forces out of any future power analyses is unlikely to affect the results. In future energy analyses, the residual forces will be added to the ground reaction forces, but it is equally possible that some residual forces should be added to the wind drag force to simulate the non-steady state air flow about the athlete (or „buffeting“) as he moves between stances and causes eddies to develop. Perhaps some residual forces should also be added to the ski/snow resistance to simulate the rapid fracturing of the snow surface. This highlights the difficulties in estimating ground reaction forces. In the future the accuracy of this analysis of forces should be tested with force plate data from skiing.

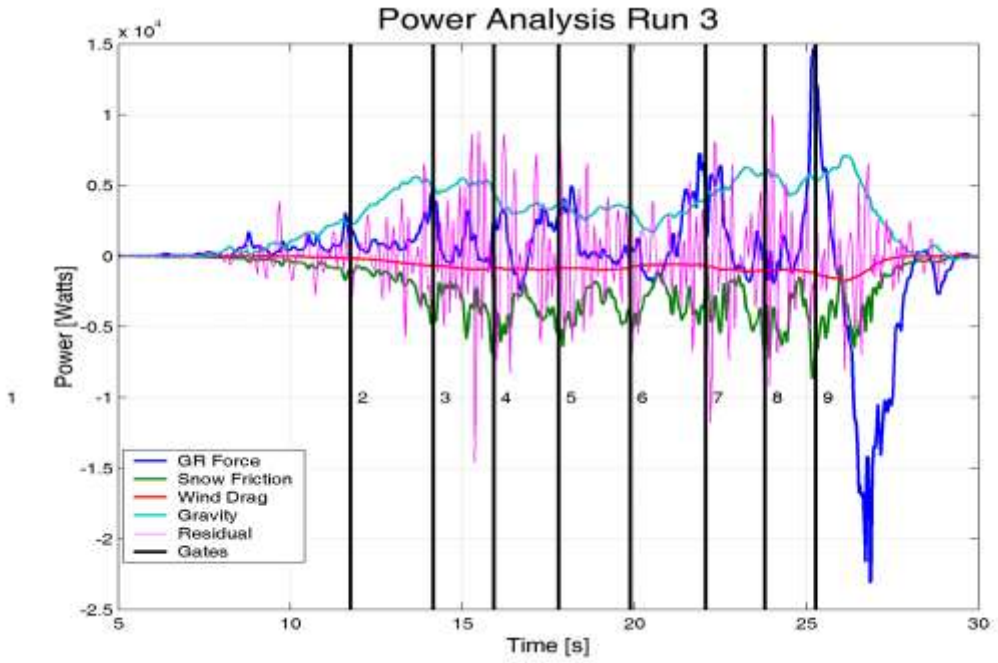

Figure 7.15: Power analysis run 3 with residual forces separated

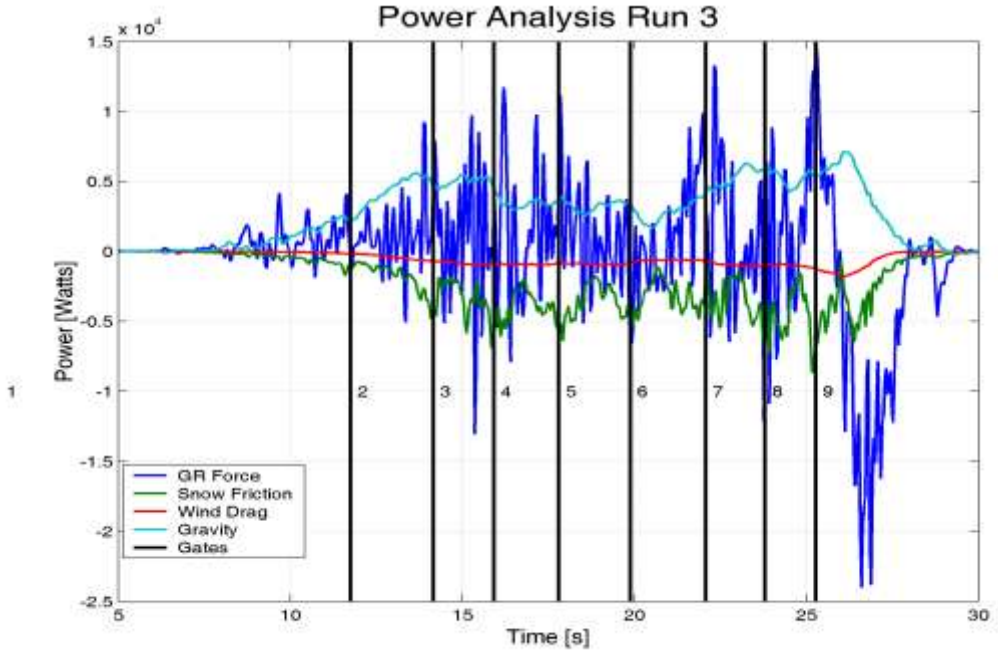

Figure 7.16: Power analysis run 3 residual forces and reaction force combined

Any noise error in the ground reaction forces (up to 110N) is magnified in the power analyses. The relative error for the ground reaction force power (7.5%) is calculated by combining the relative velocity error ($0.3ms^{-1}/20ms^{-1}$ = 1.5%) with the relative acceleration error ($1.2\ ms^{-2}/20ms^{-2}$ = 6%). Because the two relative errors are correlated they are combined by addition. This corresponds to a noise error in the ground reaction force power of up to 1,500W compared to the measured power is 20,000W and should not significantly affect the analysis. Any noise error is suppressed in the energy analysis by the integration process used

in its derivation. Unknown systematic errors in the selection of the wind drag and snow resistance model coefficients could have affected the relative magnitude of the different external forces in both the power and energy analyses.

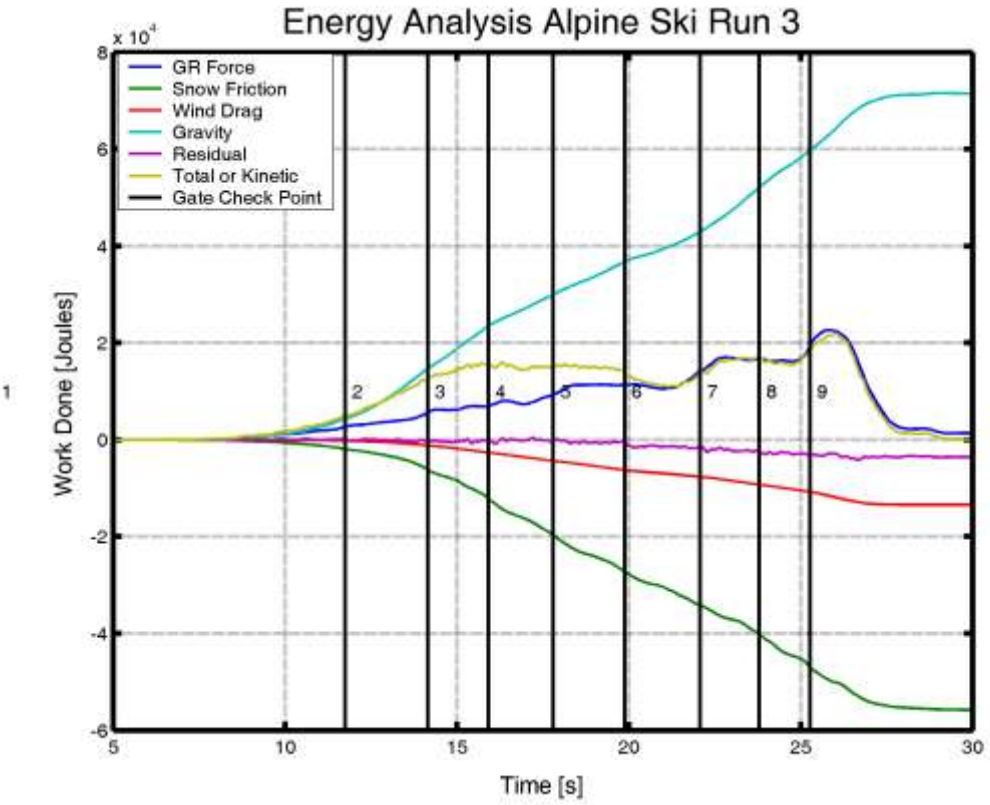

Figure 7.17: Energy analysis of run 3 with residual forces separated

7.8. Foot loading ratio

Skiing is predominately a bipedal stance activity so RS-Scan insoles were used to measure the foot loading ratio. Unfortunately the RS-Scan system was inherently unreliable at measuring this force ratio, as discussed previously for the inline skating experiment in Chapter 5 on page 94. On the snow RS-Scan insole measurements were obtained for Run 3, but the data were corrupted for Run 5, possibly because of insufficient battery power. An estimate of foot loading ratio for Run 5 therefore was attempted from inverse dynamics.

The left/right foot loading ratio was found by minimising the residual between the externally applied torque and rate of change of angular momentum. By selection of the foot loading ratio the effective point of application of the force under the skis was changed and the calculated externally applied torque also changed. The calculations used are similar to those described in Appendix B for inline skating data. But because the interaction between the snow and the ski was more complicated than the interaction between the skate and gymnasium floor and so several changes were made to the algorithm as described below.

7.8.1. Inertial properties of equipment

The inertial properties of the skis and were modelled and combined with the inertial properties of the athlete‟s feet. The combined weight of the skis and boots were 13.8kg, which was a significant proportion of the athlete + equipment mass (96.2kg). The skis were long (1.88m), heavy and located some distance for the athlete‟s CoM and so also contributed significantly to the athlete‟s angular momentum.

The mass of each boot (2.9kg) was added to the mass of the athlete‟s foot segments. The scaled inertial parameters used for the feet were then recalculated with the modified mass according to Dumas and Reed (Dumas, et al., 2007) and (Reed, et al., 1999).

The ski was modelled as a uniform density cuboid (Equation 7.23) with dimensions 1.88 by 0.08 by 0.01 metres and mass 4kg. The ski was attached to the toe of the boot at the location of the front binding, approximately one metre from the tail of the ski.

Equation 7.23
$$I = \frac{mass}{12}\begin{bmatrix} y^2+z^2 & & \\ & x^2+z^2 & \\ & & x^2+y^2 \end{bmatrix}$$

The new centre-of-mass of the foot/boot/ski segment was found by adding the weighted CoM of the ski to the weighted CoM of the foot/boot segment. The internal tensor of the ski was added to the inertial tensor of the foot/boot assuming that the ski axes were aligned with the foot/boot axes. Because of its length and mass, the moments of inertia of the skis were far greater than that of the feet.

7.8.2. Inertial properties of helmet and backpack

The mass of the backpack containing data logging equipment was 5.4kg. This mass was accounted for by modelling it as a uniform density cuboid and adding it to the inertial properties those of the thorax body segment. The mass of the helmet was 0.6kg and it was accounted for by adding its mass to the mass of the head segment and the inertial parameters were recalculated according to Dumas and Reed (Dumas, et al., 2007) and (Reed, et al., 1999).

Errors in the inertial parameters were based on the analysis presented by Dumas and Reed and discussed in Chapter 4 on page 74. The estimated errors in body segment centre of mass location were 6%, in inertial tensors were 6% and in body segment masses were 10%.

7.8.3. Algorithm for determining foot loading ratio in skiing

Run 3 FMC data was used to estimate foot loading ratio (estimated ratio) from inverse dynamics and compared it to the measured foot loading ratio based on the RS-Scan data (measured ratio). The calculations are explained later in this section and involve using MATLAB to minimise the residual to Equation 7.26.

Unfortunately the skis are not point contacts and the athlete can apply pressure over the base of the ski well beyond the base of the boot by applying a torque through the semi rigid ski boot. There are three unknown parameters; the foot loading ratio and the centre-of-pressure under each ski. Because the data were noisy moving windows of 11 data points were used to estimate the optimised parameters at each time step.

Two iterations through the entire process were required for the estimated coefficients of wind drag and snow resistance to converge. The following calculations required an initial estimate of wind drag and snow resistance force, based on an estimate of the ground reaction forces, which ultimately was dependant on the FMC data, the foot loading ratio and measured ski orientation. Therefore for the first iteration it was arbitrarily assumed an equal distribution of weight between the feet to estimate the coefficients of wind drag and snow resistance. The second iteration used the foot loading ratio estimated during the first iteration, at which point the two solutions converged.

If each parameter was solved sequentially, MATLAB‟s non-linear minimisation tool for one variable (**`fminbnd()`**) was used to determine the foot loading ratio. The foot loading ratio was between 0 and 1 and was calculated to minimise the residual between the internal change in angular momentum and the externally applied torque attributed to forces between each ski and the snow. A ratio of 1 corresponds to 100% left foot loading and a ratio of 0 corresponds to 100% right foot loading.

The optimisation algorithm (**`fminbnd()`**) is based on golden section search and quadratic interpolation. A FORTRAN program implementing the same algorithm is available (Forrsythe, Malcolm, & Molar, 1976).

If the centre-of-pressure (CoP) under each foot and the foot loading ratio were solved together, the optimisation algorithm (**`lsqnonlin()`**) was used. This algorithm is a subspace trust region method and is based on the interior-reflective Newton method described by (Coleman & Li, 1996) and (Coleman & Li, 1994).

The user supplied function

The optimisation algorithm minimised the residual from a supplied function that evaluated the sum of residuals squared between the rate of change of angular momentum and the externally applied torque based on an estimated foot loading ratio and ski centre-of-pressure. The residuals were summed over the three axes using a moving window of 11 data points.

The rate of change of angular momentum ($\mathbf{T_{Internal}}$) was not affected by the loading ratio and was pre-calculated according to the method used for the inline skating experiment in Appendix B (**Appendices\Inline skating supplement.pdf**).

The external torque for any given estimated ratio was then calculated in the following way:

1. The total forces normal to the left and right skis bases ($\mathbf{GRF_L}$+ $\mathbf{GRF_R}$) were estimated for a given foot loading ratio using the procedure outlined in Section 7.6 (Ground reaction forces).

2. The location of the centre-of-pressure under each ski ($\mathbf{COP_L}$ & $\mathbf{COP_R}$) in the global reference frame was calculated, using the ski orientation ($\mathbf{R_{Ski}}$), the supplied estimated centre-of-pressure under each ski in the local reference frame (**cop**), and the global location of the ski tail (**Ski_Tail**).

Equation 7.24 $$\mathbf{COP_L} = \mathbf{Ski\_Tail_L} + \mathbf{R_{Ski\_L}cop_L}$$

3. The external torque acting on the athlete's centre-of-mass was calculated using cross products (Equation 7.25).

Equation 7.25 $$\mathbf{T_{External}} = \left(\mathbf{CoP_{Right}} - \mathbf{CoM}\right) \times \mathbf{F_{Right}} + \left(\mathbf{CoP_{Left}} - \mathbf{CoM}\right) \times \mathbf{F_{Left}}$$

4. The residual error for the foot loading *ratio* and centre-of-pressure data was calculated as the sum of the squared difference between the internal rate of change of angular momentum and the calculated external torque (Equation 7.26).

Equation 7.26 $$\mathbf{Residual} = \sum \left(\mathbf{T_{External}} - \mathbf{T_{Internal}}\right)^2$$

7.8.4. Results of foot loading ratio and CoP measurements

For a 1000 data point run, the estimated ratio took less than 30 seconds to solve sequentially and around 5 minutes to solve for all three parameters simultaneously. A comparison of the measured ratio from RS-Scan and the estimated ratio by torque balance (Figure 7.18) shows that at the start of the run 3, during the skating motion, the two measurements are in very good agreement. Generally the estimated ratio was noisier, but mostly it predicted correctly that the outside foot was supporting most of the load through each turn. There are only two occasions when the estimated ratio was completely different from the RS-Scan measured ratio, just after gate 6 and during the skidding stop at the end of the run. Neither error is surprising. At the start of the skidding stop the athlete almost becomes airborne and so the ground reaction forces were very small. Any error in the torque calculations would have been

magnified by the small denominator in the calculation of CoP. About gate 6 there is a gate collision that would have caused an unstable result because of horizontal ground reaction forces acting on the athlete, but not acting through the ski bases.

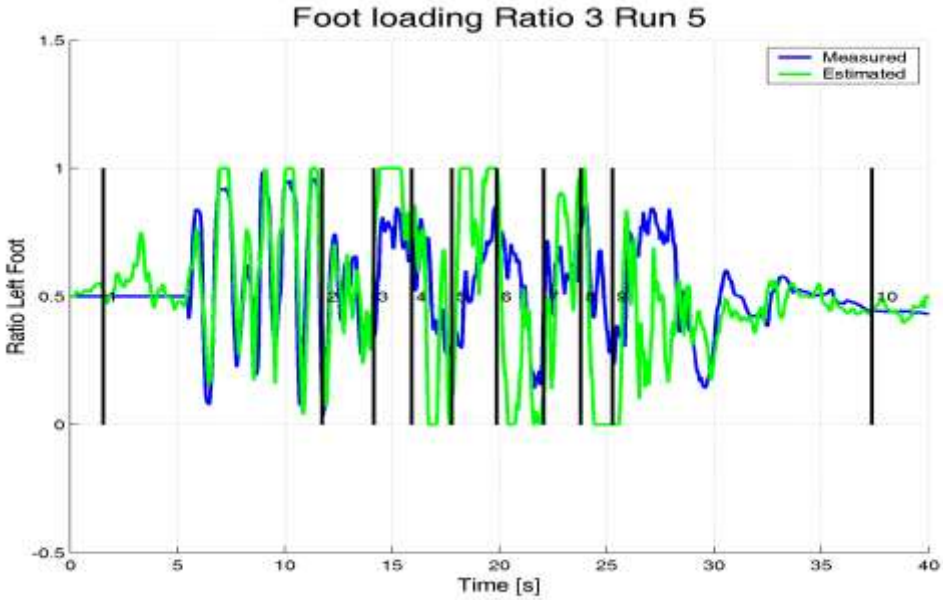

Figure 7.18: Measured and estimated foot loading ratio from Run 3.

The RS-Scan insole system suffered from hysteresis issues as discussed in Chapter 5 on page 94. The RS-Scan insole system also suffered from preloading in the tightly fastened boot, which made underestimations of measured ratio highly likely. Lüthi showed pressure sensitive insoles are less sensitive to rapid changes in loading than miniature force platforms and underestimate the peak forces (Lüthi, et al., 2005). All of these factors could account for the difference between the RS-Scan measured ratio and the estimated ratio by torque balance.

The error in external applied torque ($\mathbf{T}_{\mathbf{External}}$) was estimated to be up to 18%. The error was estimated by the addition of a 6% error in ground reaction forces with a 6% error in body segment centre-of-mass location and a 6% body segment orientation error. A similar level of error was assumed for the rate of change of angular momentum ($\mathbf{T}_{\mathbf{Internal}}$). It was not known how this level of error would affect the foot loading ratio and centre-of-pressure calculations that minimised the residuals over multiple data points in an attempt to reduce the measurement noise. In addition it was more difficult to predict the foot loading ratio for skiing than inline skating, because in skiing:

- The centre-of-pressure under each ski moved over a large area.
- The skiing FMC data were noisier
- The skiing was predominantly bipedal
- The athlete used poles and collided with gates that created additional external forces and torques not accounted for by the contact between the skis and the snow.
- The skis bent.
- It was difficult to determine accurately the point of application of the snow resistance force.

The ski bending meant that the IMU measured ski orientations (from IMUs attached to ski boots) may not have been always representative of the orientations of ski bases. The athlete poling or colliding through gates would have produced horizontal ground reaction forces not applied at the ski bases and may have produced unstable results. In addition, the pressure sensitive insoles could not measure centre-of-pressure movement beyond the boot base. However, some useful information can be extracted from this analysis. The measured longitudinal (local foot x-axis) centre-of-pressure movement measured by the RS-Scan insoles was compared with the estimated centre-of-pressure using the torque balance.

The RS-Scan insole measurement of centre-of-pressure showed some interesting trends (Figure 7.19). The centre-of-pressure was measured in millimetres along the length of the foot from the calcaneus. The measured centre-of-pressure movements ranged from 70mm to 140mm, a range well within the boundaries of the ski boot base of support. In general the centre-of-pressure moved very slightly from toe to heel through each turn. For the even numbered gates, which are right turns and the outside foot was the left foot; the centre-of-pressure is moved towards the toe of the outside foot and heal of the inside foot. During tuning the outside foot is slightly behind the inside foot so this observation is not surprising. In this way the centre-of-pressure remained close to the projection of the athlete‟s CoM on the base of support. This trend was not observed for the right left turns, maybe because there was a slight cross slope on the course, or the athlete‟s techniques were different for left and right turns.

It is interesting to note that when the estimated ratio (see Figure 7.18) produced the greatest errors, the measured centre-of-pressure separations between the feet were high (see Figure 7.19).

The estimated centre-of-pressure from the torque balance was too noisy to be useful (Figure 7.20). In Figure 7.20 a centre-of-pressure of zero centimetres corresponds to the athlete‟s calcaneus. The range of estimated centre-of-pressure movement was an order of magnitude greater than the RS-Scan measured centre-of-pressure movement. This was probably a result of noise in the system, but it could also be a result of moments transmitted through the semi rigid boot that were not being recorded as centre-of-pressure movements by the RS-Scan system.

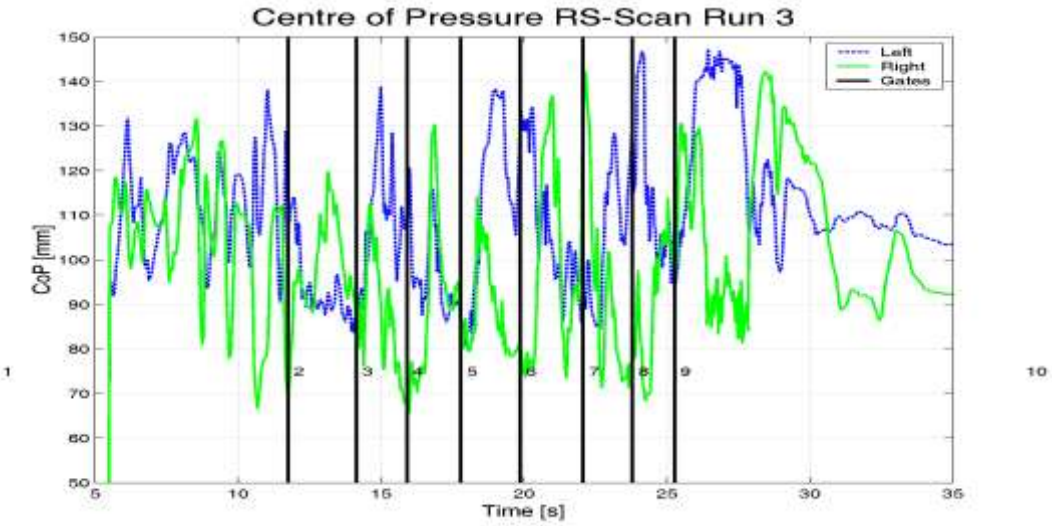

Figure 7.19: Measured CoP movement using RS-Scan insoles

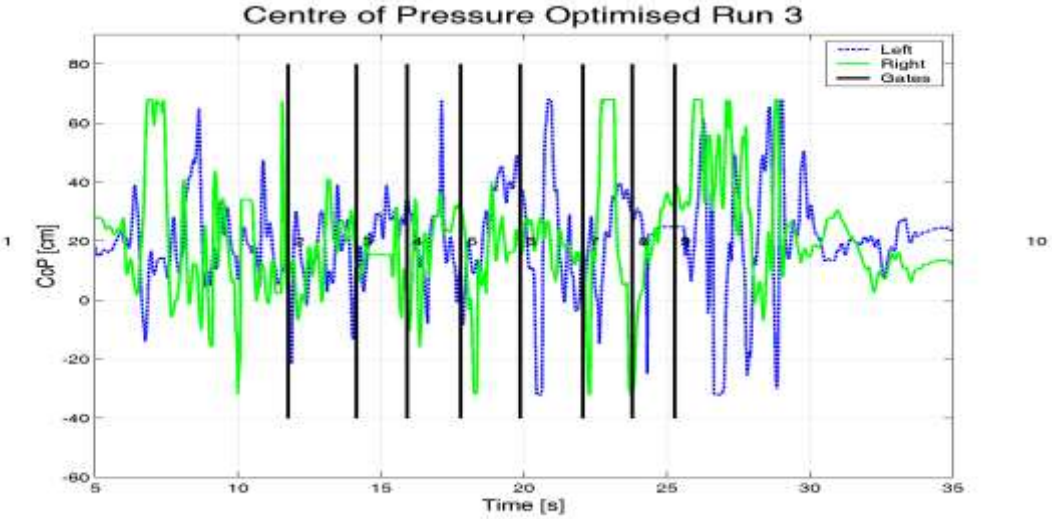

Figure 7.20: Estimated CoP movement using a torque balance

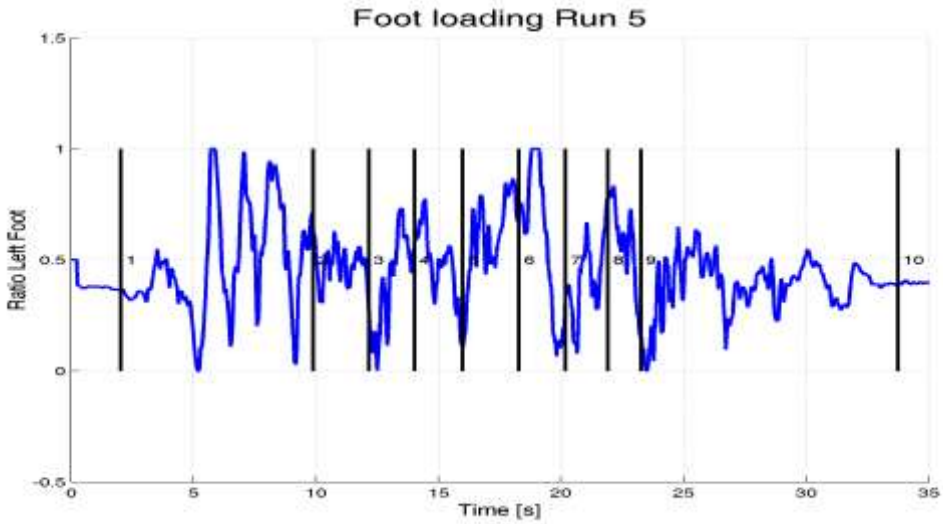

Figure 7.21: Estimated foot loading ratio from change in angular momentum for Run 5

The estimated centre-of-pressure was reasonable when the athlete was stationary at the end of the run and generally predicted the centre-of-pressure to be between 10 and 20 cm forward of the athlete‟s calcaneus.

Despite these results the inverse dynamic estimate of foot loading ratio was repeated for run 5 (Figure 7.21). It appeared the run 5 data produced better results because during the ski run, between gates 2 and 10, when the athlete is not skating, the estimated loading ratio only went out of range (meaning it estimated the weight was entirely on one ski) three times, at gate 3, 6 and 9. Compared to the run 3 estimated foot loading ratio (Figure 7.18) where the estimated ratio was much more erratic. It may be the run 5 data were more reliable because the run 5 data were recorded at 50 Hz (instead of 25 Hz for run 3), which may have reduced the accumulated integral error as discussed in Chapter 6 on page 148. The snow was softer in run 5 and so vibrations were also reduced. Unfortunately, it was impossible to compare the estimated ratio in run 5 to the measured ratio because the RS-Scan equipment failed to record the data in run 5.

7.8.5. Conclusions of foot loading ratio optimisation

There is no substitute for using three component force plates under the athlete‟s feet to accurately measure the ski/snow interaction. In the absence of such data it appeared that reasonable estimates were possible using the RS-Scan insole system and the calculations presented in this chapter, even though the RS-Scan system suffered from hysteresis and preloading.

In the absence of any data from the athlete‟s feet the optimisation, based on the laws of physics, was able to provide a reasonable estimate of foot loading ratio. Because the estimates might contain error, trends over many turns should be given more weighting in an analysis than individual data points. The optimisation was not so good at estimating centre-of-pressure movement. The noisy results indicated that there were still errors in the FMC data and/or the solution for estimated foot loading ratio and centre-of-pressure movement in skiing is difficult to obtain from a torque balance. The run 5 data were promising but the accuracy was unconfirmed.

7.9. Results and Implications

7.9.1. Visualisation of external forces

Skiing takes place in three dimensions and several external forces act on the athlete including; gravity, ground reaction forces under each ski, snow resistance forces and wind drag. Colour coded force vector diagrams were developed to convey to the athlete the resulting effects of all the forces at different stages of the racecourse (Figure 7.4). If only one of the external forces is of interest then the colour coded force vector diagrams can be adapted to show the external force of interest Figure 7.13, but if multiple forces are of interest then two

dimensional figures displaying the three dimensional forces in skiing quickly become cluttered and are difficult to understand.

Data driven animations were developed to visualise the external forces. The external forces of gravity, ground reaction forces under the skis, wind drag and snow resistance are visualised and colour coded using algorithms written by the author in MATLAB (Figure 7.1 and Video 7.2). The forces are colour coded; green if the force has a positive power (acting to increase speed) and red if the force has a negative power (acting to reduce speed). Data driven animations display complex scientific data that might be conveyed in a way that is understandable to the athletes and coaches.

Video 7.2: Appendices\FMC Video\Ruapehu_R5_Force_Optim.avi

Without the development of these data visualisations it would be difficult to analyse the large data sets provided by the prototype FMC system. Also it should be noted that the estimated ground reaction force error (up to 110N) and any error in the wind drag force and snow resistance force model coefficients does not significantly affect these data visualisations.

7.9.2. Energy and work of external forces

Energy is computed from the integral of power and power is computed from the dot product of velocity and force. The powers of the external forces acting on an object are positive if some components of the forces act in the same direction as the object‟s velocity. In skiing an external force, such as wind drag, has a negative power because it is acting to decrease speed and reduce kinetic energy. Overall the wind drag force in skiing always does negative work. Therefore, energy analyses may be useful to determine the importance of different forces acting on the athlete over complete sections of race courses.

The energy analysis (Figure 7.22) also shows both wind drag and snow resistance forces did negative work and acted to decelerate the athlete. The snow resistance was about five times more important than wind drag. Gravity always acted to accelerate the athlete and hence did positive work as the athlete descended the slope.

Ground reaction force normal to the ski bases can do both positive and negative work and depends more than any of the other forces on the athlete‟s technique (Figure 7.22). For example after gate 9 when the athlete skids to a stop ground reaction forces were used for braking and hence the sudden decrease in both ground reaction force work done and kinetic energy after gate 9. About gate 7 the athlete was able to accelerate using his ground reaction forces normal to the snow surface and hence the increase in work done by the ground reaction forces and also the kinetic energy about gate 7. Some possible reasons for this accelerative ski technique are discussed later in Chapter 8.

The interaction between the ski and the snow is a combination of the ground reaction force normal to the ski surface and the snow resistance force. If the work done by both of these forces is combined it is always negative (Figure 7.23). The combined total ground reaction force does not accelerate the athlete in skiing. The ground reaction force component that is approximately normal to the ski base, which is mostly a reaction to the athlete‟s technique, can sometimes act to accelerate the athlete. The similarity between the shapes of the total or kinetic energy curve and the ground reaction force work curve demonstrates; the athlete ultimately controls his speed through ski techniques that regulate his ground reaction forces.

The energy analysis (Figure 7.22 and Figure 7.23) shows that from the start until about gate 4 the athlete was accelerating. During this period the increase in speed is the result of work done by gravity and some ground reaction force work. After gate 4 the athlete reaches quasi steady state where the work done be gravity is almost equally consumed by the dissipative forces of wind drag and snow resistance. From gate 4 until the end of the course gravity is still the most important accelerating force but it is the ground reaction force work, a result of the athlete‟s technique, which mainly shapes transient changes in the athlete‟s kinetic energy.

In giant slalom large changes to the snow resistance and wind drag are not under the immediate control of the athlete, but depend on the snow conditions, the equipment and choice of wax. The FIS regulations ensure that all athletes use similar ski designs and so how the athlete regulates the ground reaction forces by technique may be the most important factor in deciding race outcome. Therefore, energy analyses are potentially very useful in the analysis of the effects of different alpine ski racing techniques and strategies.

Energy analysis is also very useful for analysing noisy force data. The integration process used to obtain work done from power suppresses most of the high frequency noise in the data. The energy analyses presented are however susceptible to any systematic force errors present which might have resulted from systematic errors in the wind drag force and snow resistance force model coefficients. It is possible, in Figure 7.22, that snow resistance force might be slightly over estimated and wind drag force slightly underestimated for example.

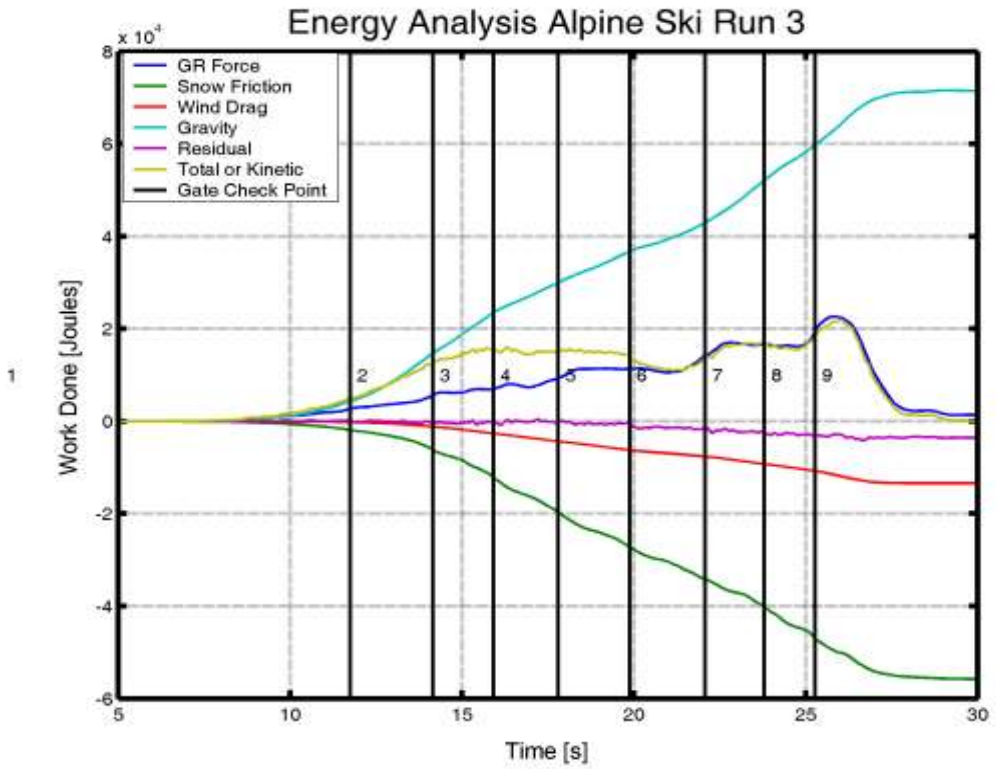

Figure 7.22 Energy analysis with forces separated

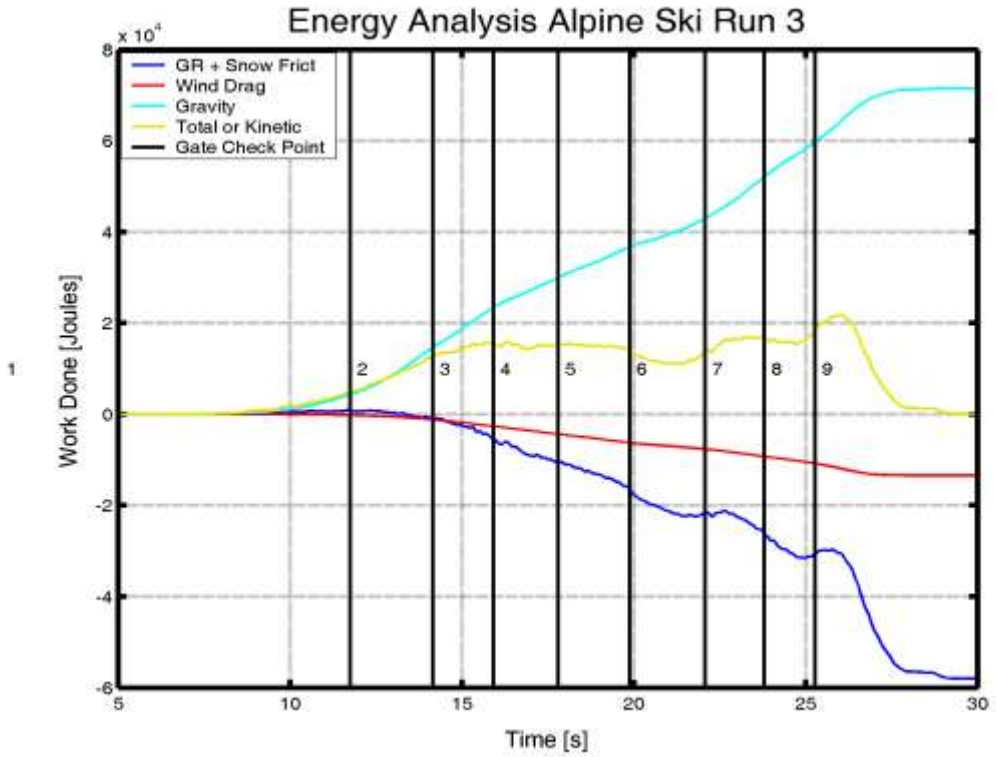

Figure 7.23: Energy analysis with ground reaction and snow resistance combined

7.9.3. Visualisation of external torques

The net joint torques show rotating forces at each joint centre. They are a measure of the combined effect of muscles, tendons and ligaments acting across joints such as the knees. Net joint torques together with joint range of motion and joint velocities can give very useful information for injury prevention, the design of sport specific strength programs and equipment such as ski boots or safety release bindings.

The net joint torques were calculated from the athlete‟s FMC data according to the method set out in Appendix B. This could be the first time it has been practical to calculate the net joint torques in 3D for a complete ski run. Custom-built visualisation software (implemented in MATLAB) was used to present the information as data driven animations.

The net joint torques for run 5 are visualised by a data driven animation (Video 7.3). In the video the torques are defined according to the right hand rule; if the right hand thumb is placed along the vector starting at the joint centre, the curled fingers indicate the direction of action on the distal body segment. The scale is 1 metre equals 200 Nm. Magenta is for isometric torques defined as a joint velocity of less than $20°s^{-1}$. Dark blue for concentric torques (where the torque is aligned with the joint movement) and light blue for eccentric torques (where the torque is opposed to the joint movement). For variation this time the virtual camera is positioned on the opposite side of the athlete from the previous data driven animations displaying the ground reaction forces (Video 7.2).

Video 7.3: Appendices\FMC Video\Ruapehu_R5_Torque.avi

The net joint torques about the flexion/extension axes of the knee and ankle joints are visualised in Figure 7.24. Only the flexion/extension torques are plotted. This representation shows how the knee and ankle joint torques worked together in the sagittal plane. In Figure 7.24 the predominately negative ankle torque represents plantar flexion and the predominately positive knee torque represents knee extension. Predominantly these knee and ankle torques are working together to prevent the semi crouched stance from collapsing against both the force of gravity and the high ground reaction forces experienced while cornering. The ankle and knee torques allow the transmission of high ground reaction forces to athlete‟s upper body and therefore, effective control of the CoM trajectory through the ski run.

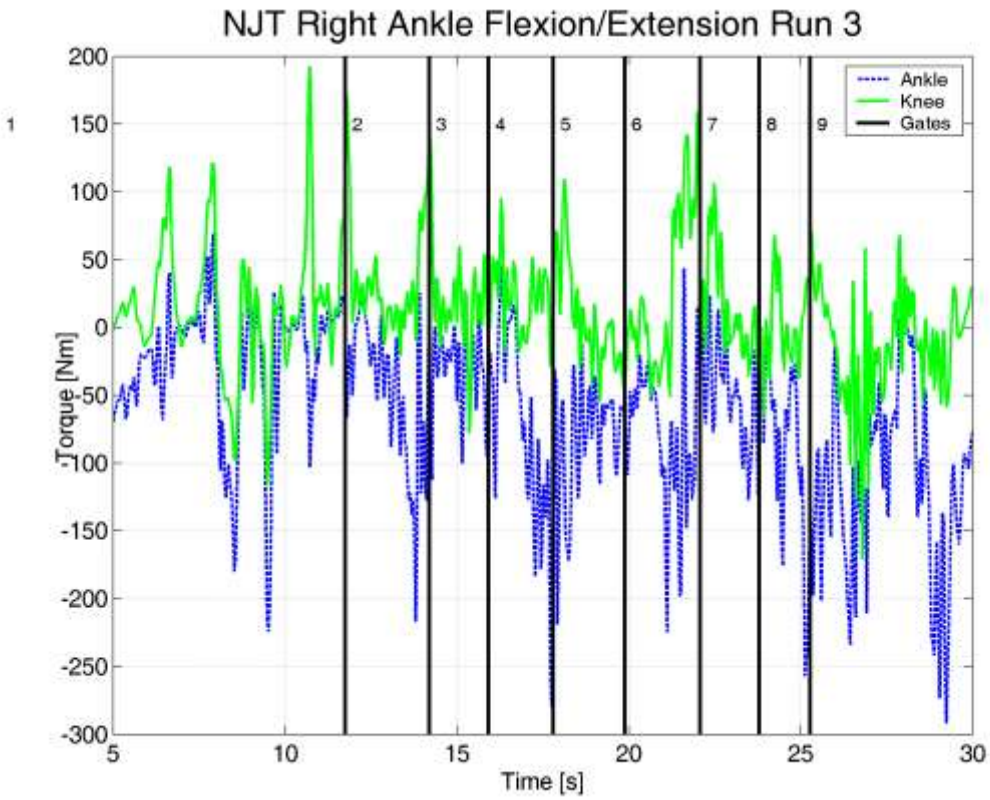

Figure 7.24: Flexion/Extension torques of the knee and ankle during giant slalom

Similar to the analysis of inline skating net joint torques (Appendix H), the data driven animation (Video 7.3) shows the high joint loading in the lower body and lumbar joint centre relative to the upper body. However, in comparison to the inline skating, there is a much less clearly defined pattern of torques. In the skating experiment there were identifiable periods of eccentric loading and concentric push off through the skating stroke. In this skiing experiment by comparison, the net joint torques fluctuated rapidly about all axes (flexion/extension, abduction/adduction and internal/external rotation) and modes of action (isometric, concentric and eccentric), probably because of the rapidly changing loads experienced by the athlete.

There were significant net joint torques about all three axes of the local limbs. This indicates that athlete training could benefit from a variety of different exercises that require the athlete to maintain postural balance while performing lifts, therefore creating net joint torques about multiple axes during the lifts.

The net joint torques about the knee and ankle are mainly a result of the high ground reaction forces and so the error calculated for the external torque (18%) in Section 7.8.4 was adopted from the net joint torques. Given the scale of the net joint torques the error was estimated to be up to 40Nm.

Figure 7.24 shows the net joint torques acting to flex and extend the right knee and right ankle. The magnitude of the knee torques experienced by the athlete during skiing were about a third of the maximum torques reported in previous studies for ski jump landings (Herzog &

Read, 1992; Nachbauer, et al., 1996). The maximum knee extensor torque experience by the athlete (<200Nm) were well within the maximum isometric extensor torques of Herzog‟s subjects (300-600Nm) and so the athlete was probably not in danger injuring his knees when he ran the course.

The higher net joint torques observed at the ankles relative to the knees were in part due to the passive support of the rigid ski boot. This may have moved much of the athlete‟s active response to the external loading partially from his ankles to his knees. It is not surprising that knee injuries in skiing are very common. Future work could further analyse the net joint torques in order to reduce knee injuries in skiing.

8. Optimisation of Ski Race Technique

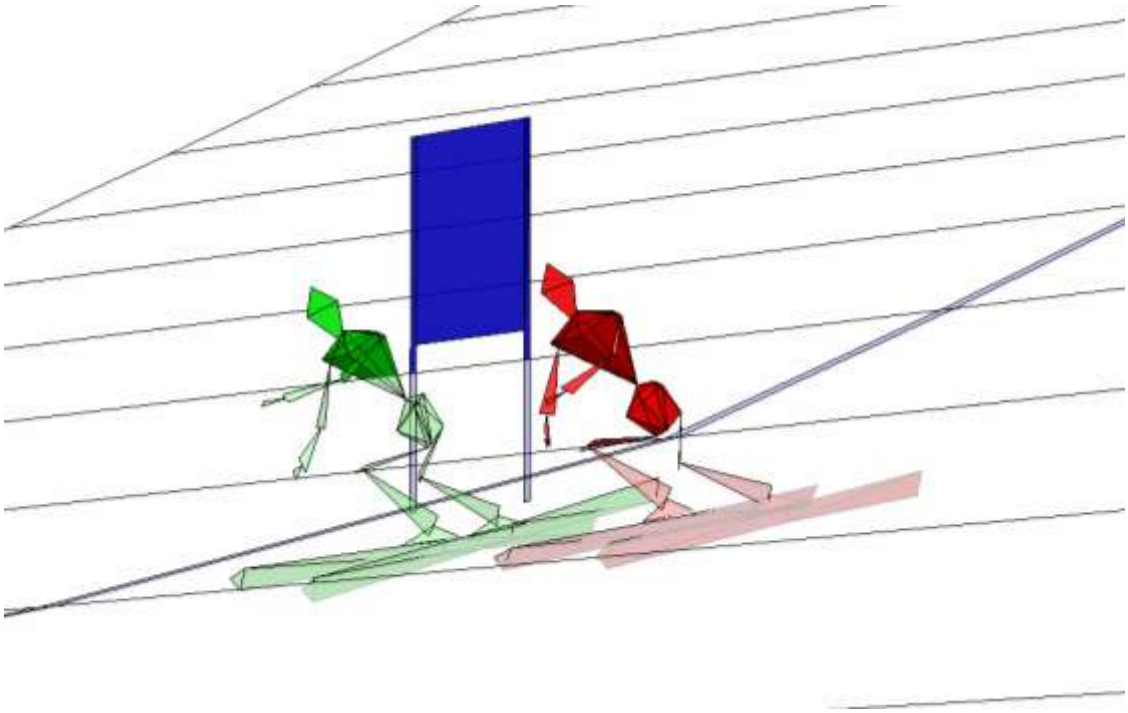

Figure 8.1: Two runs by the same athlete, green has an early lead...

What makes one athlete the fastest? In this chapter two giant slalom training runs by a skilled athlete (<20 FIS points) are compared. The analysis focuses on the external forces (gravity, wind drag, snow resistance, and the round reaction forces normal to the ski bases), acting on the athlete and how those external forces affected race outcome.

The athlete may be considered as an element of an over determined redundant system; meaning many different combinations of local limb movements could produce a similar global trajectory and overall performance. This chapter therefore focuses on the whole body movements and external forces acting on the athlete. As discussed in the introduction, in alpine ski racing because style is not judged and therefore the external forces acting on the athlete explicitly decide the race outcome. The majority of the analyses presented in this chapter provide additional useful information to ski race athletes, coaches, and equipment manufacturers, which could not practically be provided by any other means. Force, power and energy analyses over complete race courses could not be completed by a coach with a hand held video camera or, as discussed in the introduction, practically with conventional optical motion capture systems.

The focus is on the analysis of the athlete‟s whole body motion. First presented are traditional analyses. Two runs, run 3 and run 5 are visualised in Section 8.1, followed by gate split times and global trajectories. FMC data can provide far more information than is traditionally available for alpine ski athletes and opens up the opportunity to optimise the athlete‟s technique. Force, power and energy analyses are used to pinpoint the differences between the two runs (Section 8.4). The athlete‟s changing turn radius and changing inclination (leaning angle) into each turn are measured (Section 8.6). Accelerative turn technique and how the athletes and coaches might use the information in this chapter to ski faster is discussed (Sections 8.7 and 8.8).

Limitations of the analyses

The analyses in this chapter are from two giant slalom runs of a single athlete down moderately sloping terrain. The differences between the two runs are sometimes smaller than estimated errors in the data. A chronological analysis is presented in Section 8.1.2. The analysis shows that; the fastest time through the course was 13.38s, the time difference between the two runs was only 0.14 seconds, and the time differences between gate splits were sometimes as little as 0.04 seconds. These differences are getting very close to the temporal resolution of the hand held video camera (0.04s) used to help investigate the accuracy of the results. This leads to the question: Are the data accurate enough for the following analyses to be useful?

Estimated errors for the current FMC system for giant slalom skiing are presented in Table 8.1. The errors and the implication of errors on the analyses have already been discussed in Chapters 5, 6 and 7. The analyses presented in this chapter examine the two performances by the athlete using many different parameters. The parameters measured (temporal, spatial, kinematic and kinetic) all draw non-contradictory conclusions about the

athlete‟s performances and so suggest the data are reliable. The following trends observed are from multiple turns providing a data rich environment from which to draw conclusions. This gives the following analyses more credibility than if data from only a single turn or point in time had been analysed. The balance of the evidence suggests that the data presented are accurate enough to distinguish between two very similar ski runs and therefore can provide useful information.

Table 8.1: Summary of estimated FMC errors for giant slalom

Quantity	Estimated Error	Typical Value	Relative Error
Time [s]	0.04	2.0 - between gates	2.0%
Location [m]	0.7	30 - between gates	2.3%
Velocity [ms^{-1}]	0.3	18	1.6%
Acceleration [ms^{-2}]	1.2	20 for CoM	6.0%
Force [N]	110	1,800	6.0%
Power [W]	1,500	20,000	7.5%
Work [J]	Error reduced by integration of power		
Body Orientation [º]	6	up to 180	3.2%
Torque [Nm]	40	200	18.0%

To the author‟s knowledge there were no comparable analyses available in literature with which to compare most of the findings presented in this chapter. Some previous work on the simulated optimum trajectory in skiing focused on a single turn and therefore produced results different from this research (Hirano, 2002; Reinisch, 1991). Additional data should be collected in the future in order to confirm the initial findings, confirm the accuracy and also determine how the results compare to the performances of other athletes under different course conditions.

8.1. Race Analysis

Two complete runs (run 3 and run 5) through a 10-gate giant slalom training course over 250 metres in length were captured. In run 5 the athlete ran the course 0.14 second faster than in run 3, why? The video footage of run 3 is provided (Video 6.1).

Video 8.1: Appendices\FMC Video\Ruapehu_R3_Video.avi

8.1.1. Visualisation

A Ski X is a race where up to six athletes race simultaneously through a course that resembles a terrain park. The two ski runs by the same athlete (blue biomechanical man – run 3 and orange biomechanical man – run 5) can be simultaneously viewed in a single data driven animation, a virtual Ski X (Video 8.2).

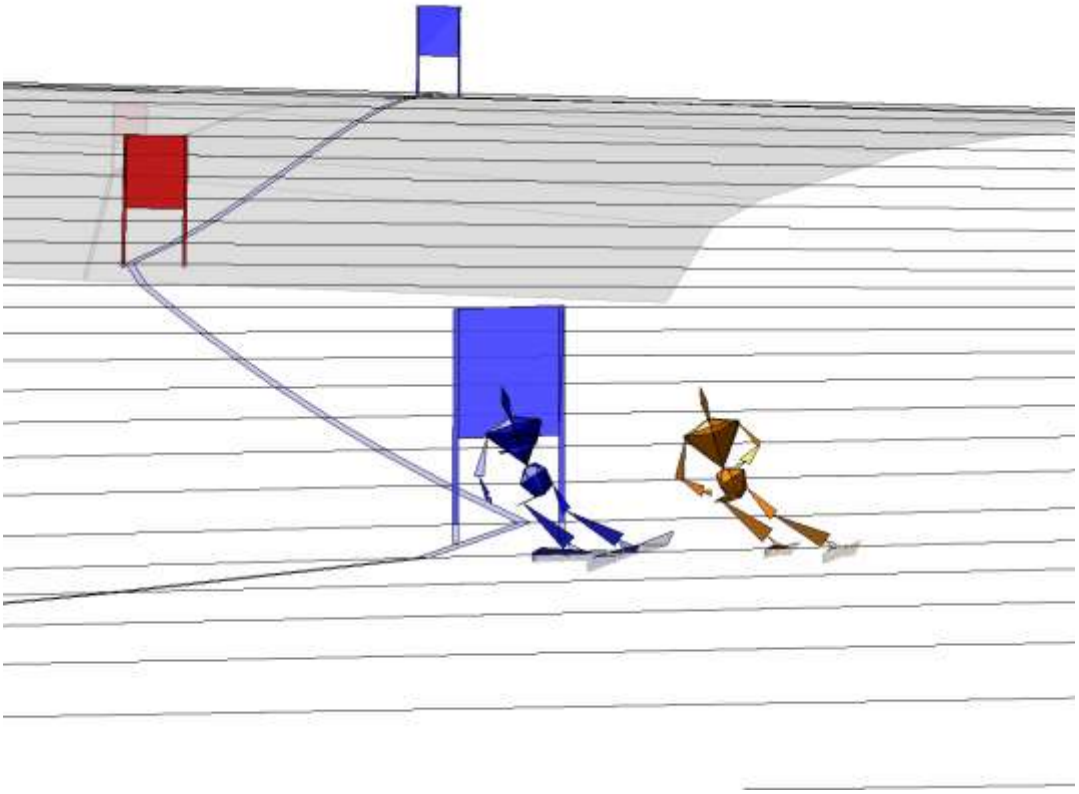

Figure 8.2: The blue man, run 3, takes the inside line about gate 4 in a virtual ski X

Video 8.2: Appendices\FMC Video\SkiX_Final.avi

Timing for virtual Ski X starts at gate 2, a blue gate, and ends at gate 9. The two runs were synchronised at the point of passing gate 2. Data from run 5 were down sampled to 25Hz to match the data rate from run 3 to ensure consistent visual representation. The orange man (run 5) won the race, passing gate 9 around four frames or 0.14 seconds ahead of the blue man (run 3). Video 8.2 demonstrates the power of FMC to provide different types of feedback to alpine ski racing athletes.

8.1.2. Chronological analysis

Course times are usually measured using timing gates. With FMC data it is possible to produce virtual gate splits, the time difference taken to pass between sequential gates. The gate splits show that if gate splits 4, 5 or 6 had been analysed in isolation it might have been erroneously concluded that run 3 was the better run (Figure 8.3). Run 5 was faster by 0.14 seconds but the lead changed several times over the course.

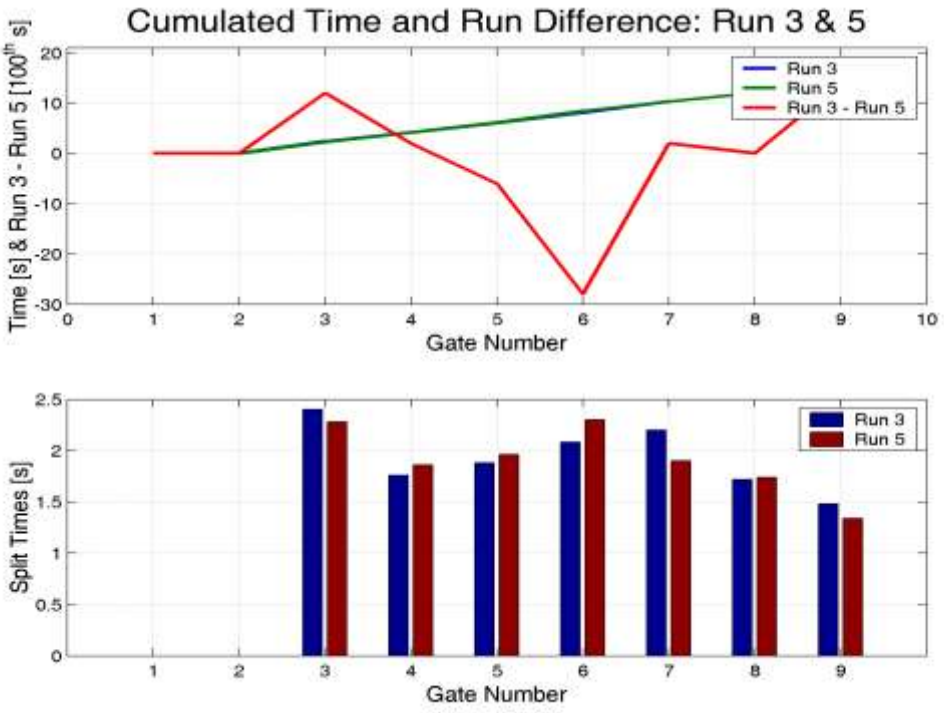

Figure 8.3: Chronological analysis using FMC

8.1.3. Course line

During the „virtual" Ski X the lead changed twice (Video 8.2). Initially the orange biomechanical man poles more aggressively to take an early lead, then the blue biomechanical man regains the lead with an inside line about gate 4, but the orange man wins. The question is why?

The athlete's centre-of-mass (CoM) trajectories in both runs was investigated. The first lead change occurred about gate 4 when the blue avatar (run 3) took an inside line (Figure 8.4 and Figure 8.2) which resulted in a shorter path. Because the athlete was travelling at similar speeds in both runs the shorter line resulted in a faster time and blue took the lead. This strategy is in agreement with the simulated optimum trajectory calculated from the inline skating data, whereby tighter turns resulted in a 20% faster time (Chapter 5, page 114).

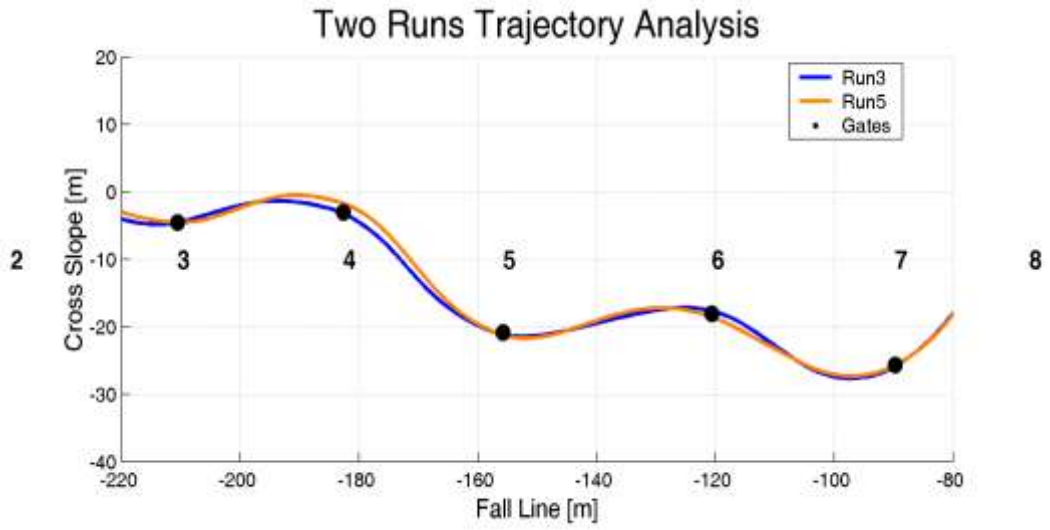

Figure 8.4: Comparison of Trajectory between gates 3 and 7

The next lead change just after gate 8 but the cause can be traced back to differences in technique about gate 6. About gate 6 in Figure 8.4 the apex of run 5 (orange line) was before the apex of run 3 (blue line), but there is very little length difference between these two trajectories. So why did the orange man win? In order to answer this question further analysis is required.

8.1.4. Speed

Examination of the speed profiles (Figure 8.5) from the two different runs shows that about gate 6 the athlete looses speed in run 3 (blue line) but gains speed in run 5 (green line). This indicates something interesting happened about gate 6.

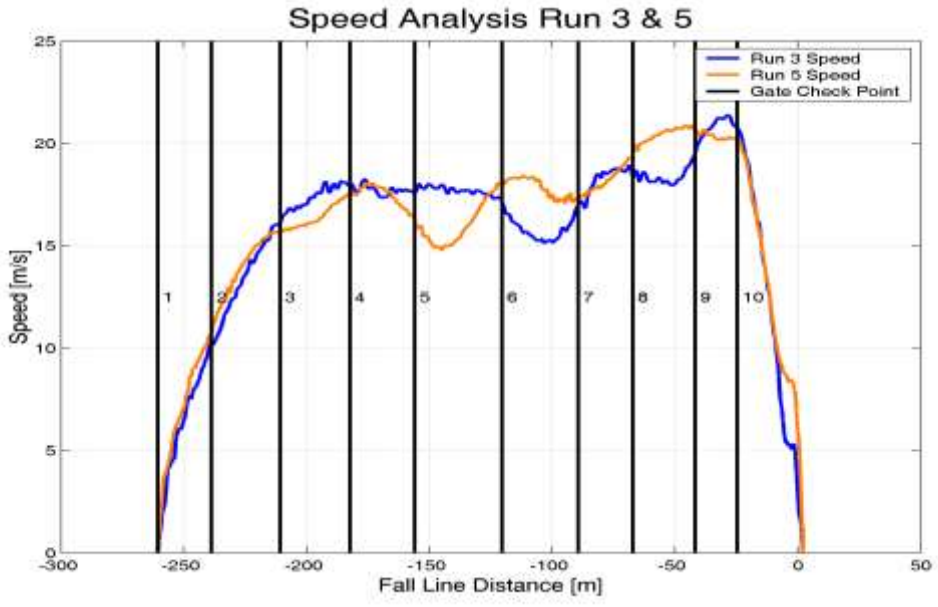

Figure 8.5: Speed profile of Run 3 (blue line) and Run 5 (green line)

8.1.5. Resultant Forces

The close up force vector diagram shows the athlete"s CoM trajectories about gate 6 for run 3 (top panel, blue line, Figure 8.6) and run 5 (bottom panel). The resultant external forces acting on the athlete are also visualised (red vectors for periods of braking and green vectors for periods of acceleration). The CoM trajectories about gate 6 reveal that in run 3 the athlete took a „pinch" line; going straight for the gate and then turning sharply. In contrast to the performance about gate 4, the straighter trajectory about gate 6 resulted in a slower overall time. Why?

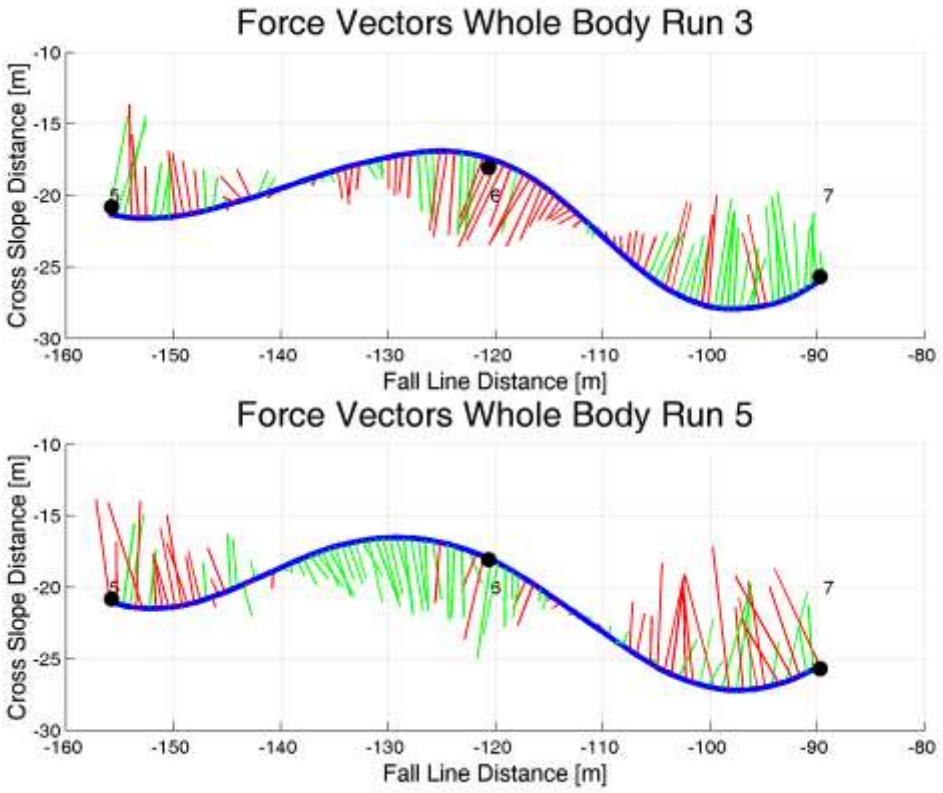

Figure 8.6: Close up force vector diagram, top panel run 3, and bottom panel run 5.

Before gate 4 the athlete was still accelerating from the start, which made the shorter radius turn of run 3 about gate 4 faster. About gate 6 however, the slightly longer radius turn of run 5 was faster (Figure 8.6, bottom panel). In run 5 the athlete generated more green accelerating forces through the turn, by leaning into the turn early and by using a clean „carving" ski trajectory. In run 5 the gain in speed from turn 6 was maintained to the end of the course and was a major contribution to the 0.14 second lead by gate 9.

Another possible reason for the better turn about gate 6 in run 5 was, counter intuitively, the slower speed about gate 5 (Figure 8.5). Did the slower speed in run 5 allow the athlete time to increase the inclination angle earlier and shift his turn apex before gate 6 in run 5? It is also interesting to note that the about gate 4 the terrain was steeper than about gate 6 which suggests anecdotally that tighter turns might be better in steeper terrain.

Figure 8.6 shows the resultant forces acting on the athlete, but which of the external forces (gravity, wind drag, snow resistance, or ground reaction force) were most responsible for the difference in performance between the two runs? Run 5 was also completed later in the day did this contribute? In order to answer these questions further analysis of the complete racecourse is required.

8.1.6. Ground reaction forces

Ground reaction forces in this analysis exclude the snow resistance forces parallel to the ski bases. The ground reaction forces are approximately normal to the bending ski bases. The athlete skied faster in run 5 than in run 3 because he generated more green accelerating ground reaction forces normal to the ski bases about gate 6 (Figure 8.7 and Figure 8.8).

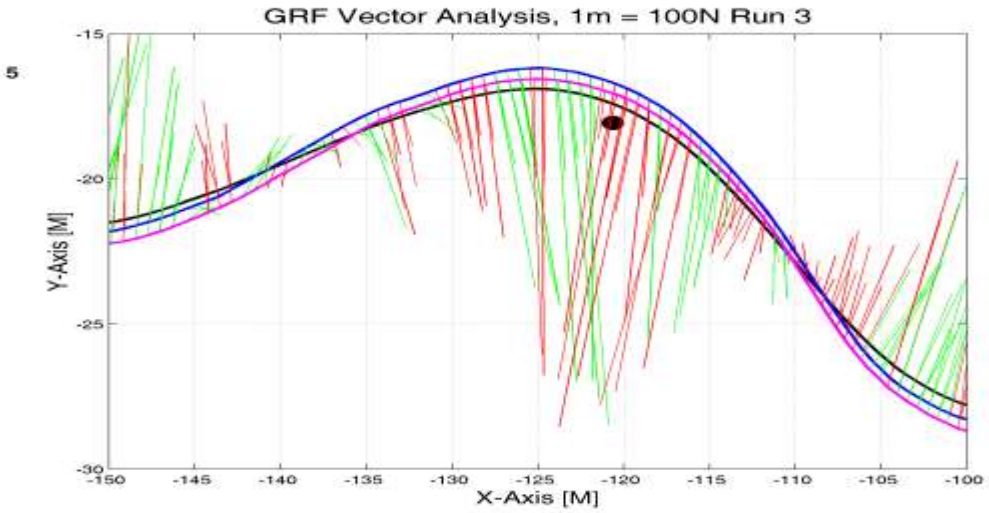

Figure 8.7: Ground reaction force vector analysis run 3

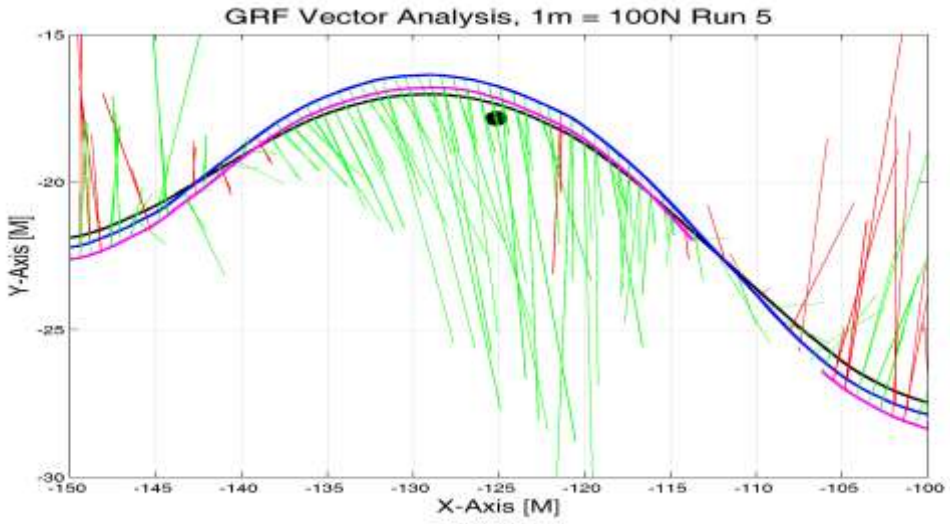

Figure 8.8: Ground reaction force vector analysis run 5

In these figures (Figure 8.7 and Figure 8.8) both skis and CoM trajectories are visualised; black for the CoM, blue for the left ski and magenta for the right ski. The ground reaction forces and residual forces (excluding snow resistance) are visualised by vectors originating at the instantaneous centre-of-pressure (CoP) of each ski. Green vectors indicate an accelerating effect (positive power) and red vectors indicate a braking effect (negative power).

Run 5 data were collected at 50 Hz, twice the frequency of run 3, which has been down sampled to 25Hz to ensure consistent visual representation. Green vectors in these analyses do not necessarily mean the athlete was accelerating, only that his ground reaction forces were acting to accelerate him. This is in contrast to a resultant force vector diagram where a green resultant force indicates the athlete was accelerating (Figure 8.6).

In run 5 the turn about gate 6 is characterised by a smooth and early build up of green accelerating ground reaction forces (Figure 8.8). In run 5 the force build up starts at around negative 138 metres and peaks near the gate. By contrast in run 3 the ground reaction build up begins later, around negative 130 metres, and develops more quickly (Figure 8.7). In run 3 the turn is characterised by short periods of braking „red" ground reaction forces interspersed with periods of accelerating „green" ground reaction forces. The fluctuating forces indicate the athlete did not carve a smooth arc through the snow and may have slipped sideways in the turn.

In run 5 the apex of the turn was about 5 metres further from the gate than in run 3. The crossover point (where the centre-of-mass passes over the skis) before gate 6 is also earlier in run 5. This resulted in a longer path in run 5, but it also gave the athlete more room to set up the ski edges for a smooth „carving" arc about gate 6 and it allowed him to accelerate through the turn.

Video 8.3 is a data driven animation from gate 5 to gate 7 with the ground reaction forces visualised. In run 5 the athlete is an orange avatar, in run 3 he is a blue avatar. The avatars are based on anthropometric measurements of the athlete.

Video 8.3: Appendices/FMC Video/SkiX_GRF_567.avi

After viewing the data driven animation about gate 6, it is apparent the athlete maintained better contact with the snow in run 5 (orange avatar). In run 5 he was able to engage his ski edges earlier creating more positive work through regulation of ground reaction forces. Kinematic (visual) differences between the athlete's body segments during the two runs are subtle. Close inspection shows that in run 5 after engaging the ski edges the athlete quickly abducted his outside (left) hip creating a more acute ski/snow angle. In run 3 this type of hip action occurred later on in the turn after passing the gate.

8.2. Resultant force vector analyses

The FMC data from two runs was used to create resultant force vector analyses of the athlete‟s performance through the complete racecourse. The analyses are very useful in determining where the athlete lost and gained speed in each run through the course. There are interesting differences between the two runs which are now presented (Figure 8.9 and Figure 8.10).

Figure 8.9 shows in run 3 the athlete lost speed about gates 6, 8 and 10. About these gates there is a predominance of red retarding forces. What is not clear at this stage is why? Without more information it cannot be ruled out that (among other things) course gradient was less about gates 6, 8 and 10, in which case there was nothing the athlete could do.

Figure 8.10 shows in run 5 a different pattern; speed was lost about gates 5, 7 and 9. If the athlete had combined of the best aspects from both runs 3 and 5 it appears he could have improved his performance; from 13.38s in run 5 to a theoretical minimum time of 12.96s, a further improvement of 0.42s or 3% and larger than the 0.14s difference between the two runs. The theoretical minimum time was estimated by combining the minimum split times for each gate plotted in Figure 8.3 and the simplicity of this estimation does not account for how the athlete‟s performances through sequential course gates might be interrelated. In any case, the right turns were better in run 5 and the left turns were better in run 3. But which of the external forces were most responsible for the observed differences gate-to-gate and run-to-run? Wind drag, snow resistance or ground reaction forces?

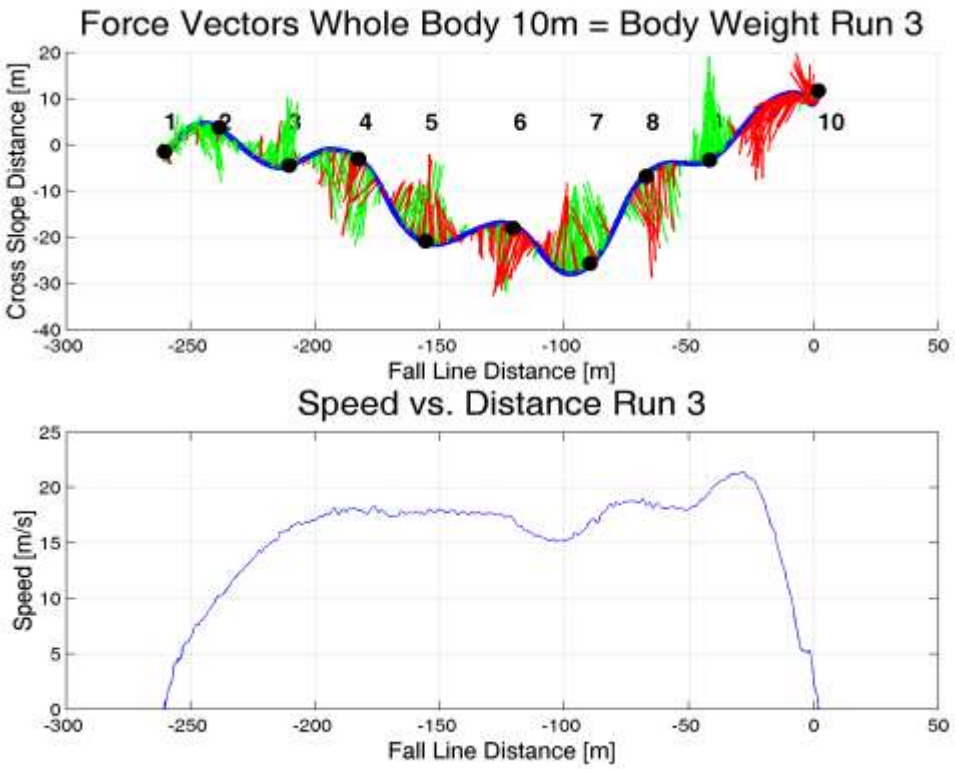

Figure 8.9: Force vector diagram resultant forces run 3

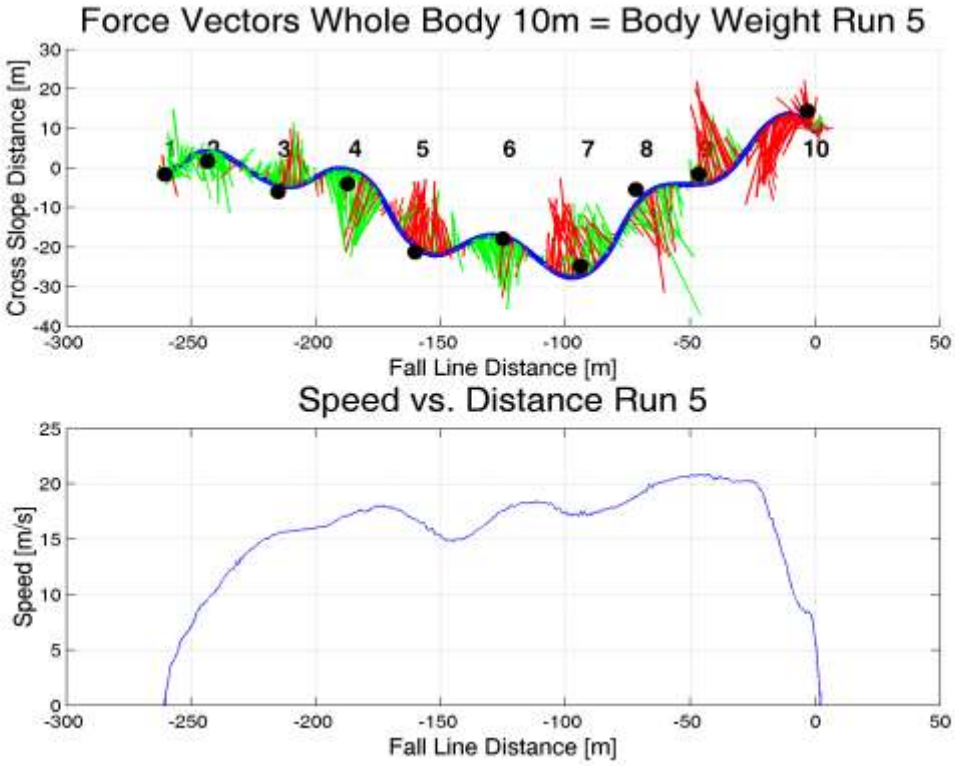

Figure 8.10: Force vector diagram resultant forces run 5

8.3. Wind drag and snow resistance

Wind drag area

Between the two runs there were only small differences between the wind drag areas, therefore it is unlikely wind drag affected race outcome (Figure 8.11 and Figure 8.12).

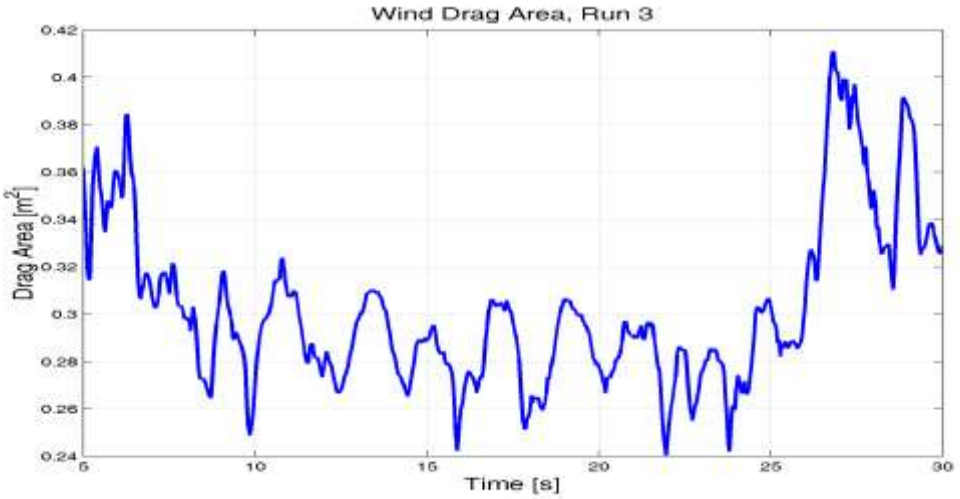

Figure 8.11: Drag area run 3, coefficient of friction *Cd* = 0.52

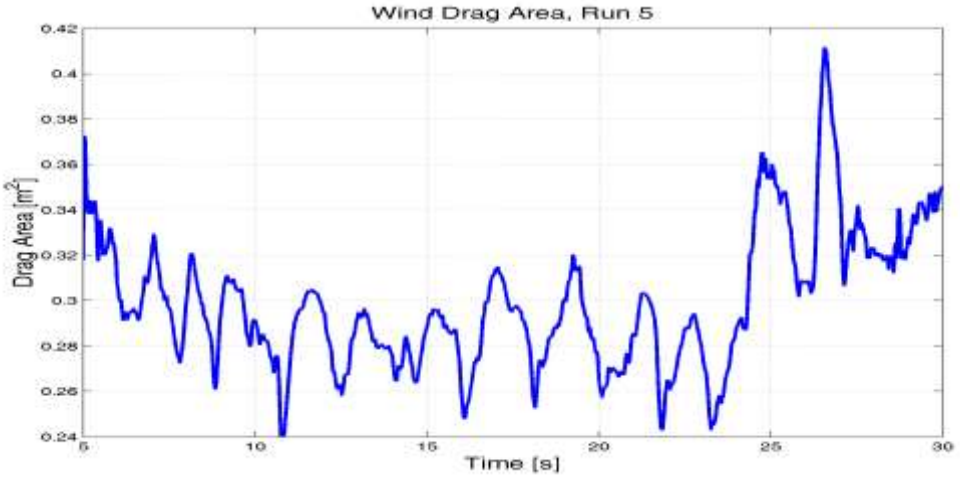

Figure 8.12: Drag area run 5, coefficient of friction *Cd* = 0.52

Hard and soft snow

There were small differences in snow resistances between runs 3 and 5 (Figure 8.13 and Figure 8.14). In both figures snow resistance appears to increase with increased velocity. The softer snow in run 5 had less resistance to displacement at high speeds but more resistance to sliding at slower speeds than the harder snow in run 3.

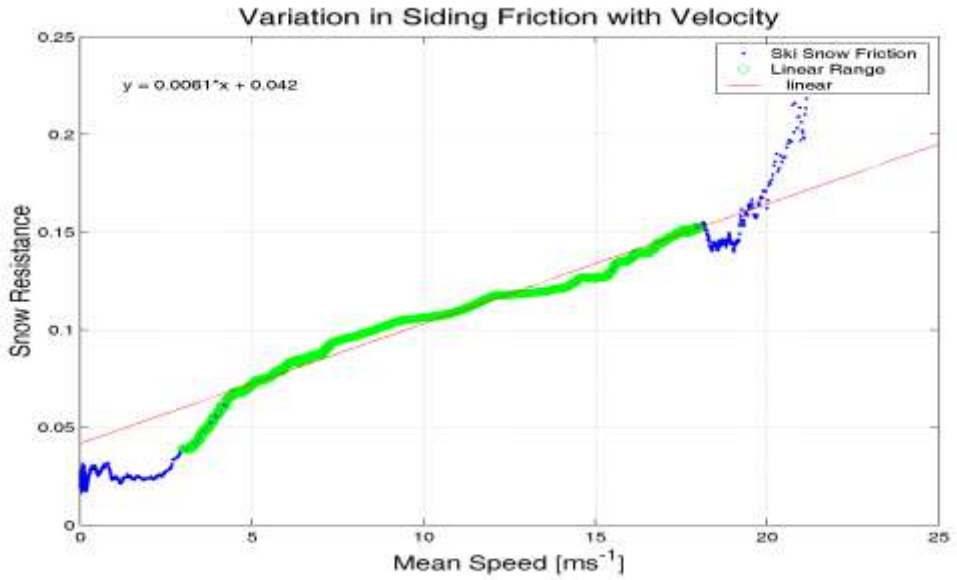

Figure 8.13: Snow resistance, the hard snow of run 3

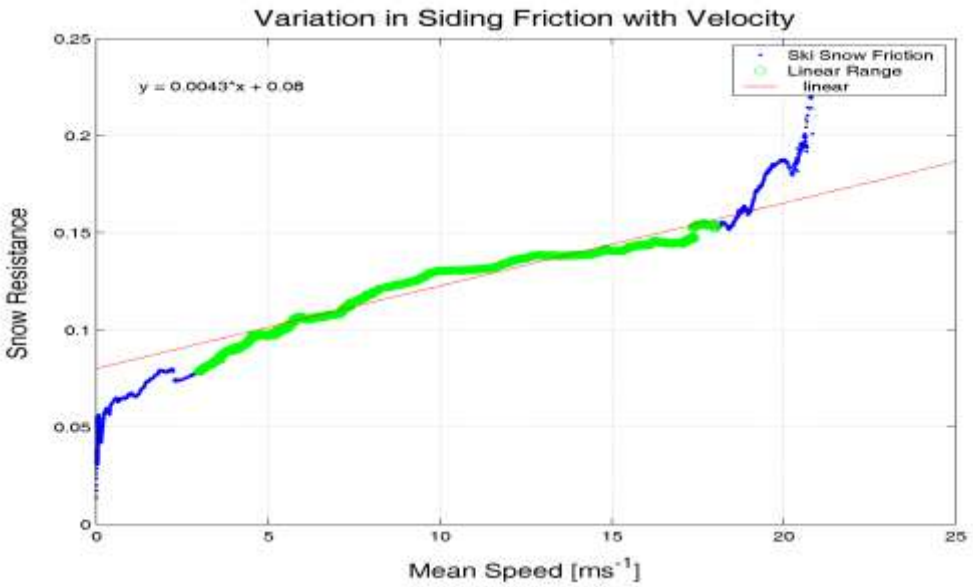

Figure 8.14: Snow resistance, the softer snow of run 5

A linear model was fitted to the experimental data to estimate the snow resistance using the procedures developed in Chapter 7 (Equation 7.6 on page 159). The static snow resistance in run 5 (μ_F~0.08) was twice that of run 3 (μ_F~0.042) indicating the snow was softer. Unexpectedly, the velocity dependant snow resistance was greater for run 3 (μ_V~0.0061sm^{-1}) on harder snow than run 5 (μ_V~0.0043sm^{-1}) on softer snow, which may indicate that it took more work to displace the harder snow in run 3 at higher velocities than it did to displace the slightly softer snow in run 5. If the linear models used provided a reasonable estimate of the true snow resistance, then at a speed of 22ms^{-1}, the snow resistance was approximately equal for both runs.

8.4. Power, energy and work

The energy analyses of runs 3 and 5 show the effects of the different external forces on the athlete‟s kinetic energy (Figure 8.15 and Figure 8.16). The analyses also provide useful information about where the and how the athlete increases speed because kinetic energy is proportionally to the athlete‟s speed squared. In the analysis of alpine skiing a force has a positive power and does positive work if it is acting to increase the athlete‟s speed. More calculation details are available in Chapter 5 on page 97. An introduction to the use of energy analysis for alpine ski racing was also presented in Chapter 7 on pages 172 and 184.

Power is measured in Watts and calculated from the dot product of the force and velocity vectors. Work in joules is the integral or sum of power with time. If an external force shows an energy increase about a gate then it has done positive work and acted to increase the athlete‟s total kinetic energy, and hence velocity. In summary, positive power and work are good, the athlete will go faster if the positive work done by the external forces can be increased.

Figure 8.15 and Figure 8.16 show that in runs 3 and 5 gravity acted to increase the athlete‟s kinetic energy (turquoise lines) and hence acted to accelerate him while wind drag and snow resistance acted to retarded him (red and green lines). In both runs the work done by gravity was the same, and snow resistance (green lines) had a larger negative effect than wind drag (red lines). The snow resistance acted to retarded the athlete more in run 5, so why then was 5 was faster?

In Figure 8.15 and Figure 8.16 the shape of the total kinetic energy (yellow lines) and the work done by the athlete‟s ground reaction forces (blue lines) were very similar. The similar shapes suggest that the primary differences between the two runs resulted from differences in ground reaction forces. A good technique that used the reaction forces normal to the ski bases to maintain kinetic energy and therefore maintain speed was an important difference between the two runs.

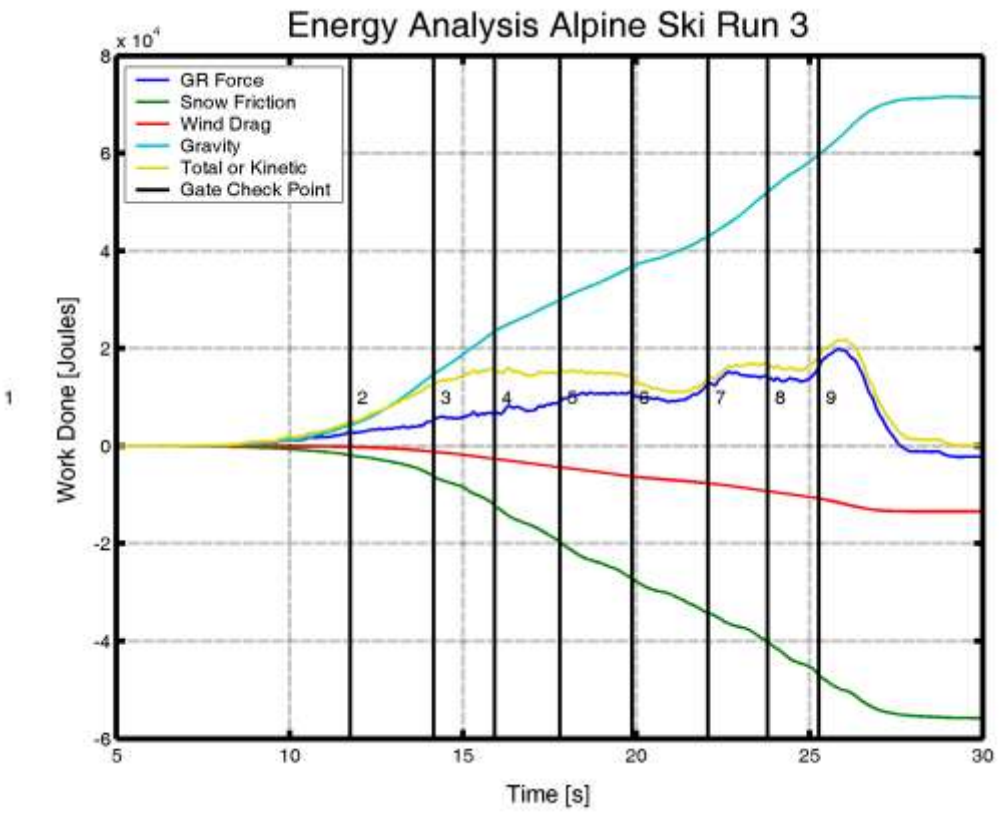

Figure 8.15: Energy Analysis of external forces for run 3

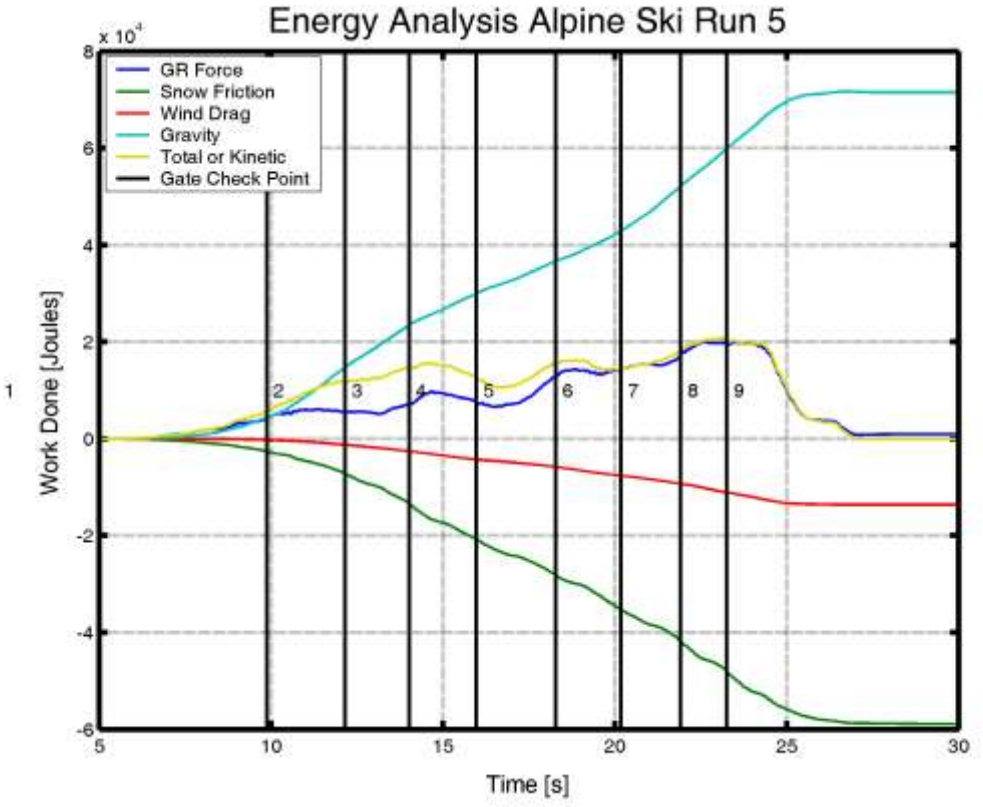

Figure 8.16: Energy Analysis of external forces for run 5

Component power analysis identifies the poor turns in both runs by negative ground reaction force powers and good turns by positive ground reaction force power.

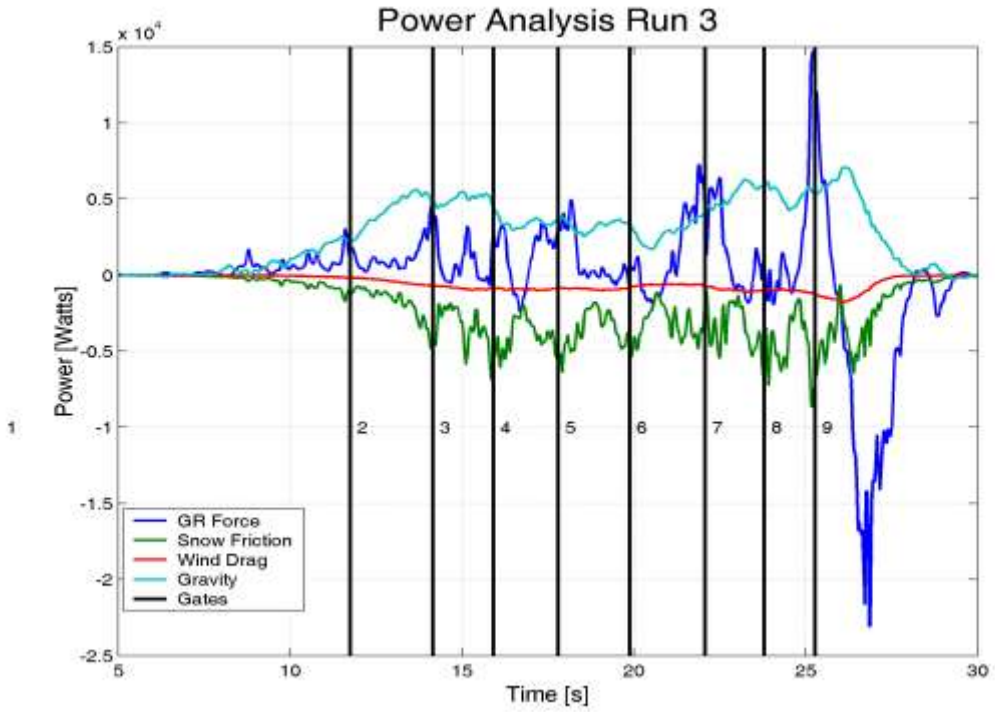

Figure 8.17: Power analysis of run 3

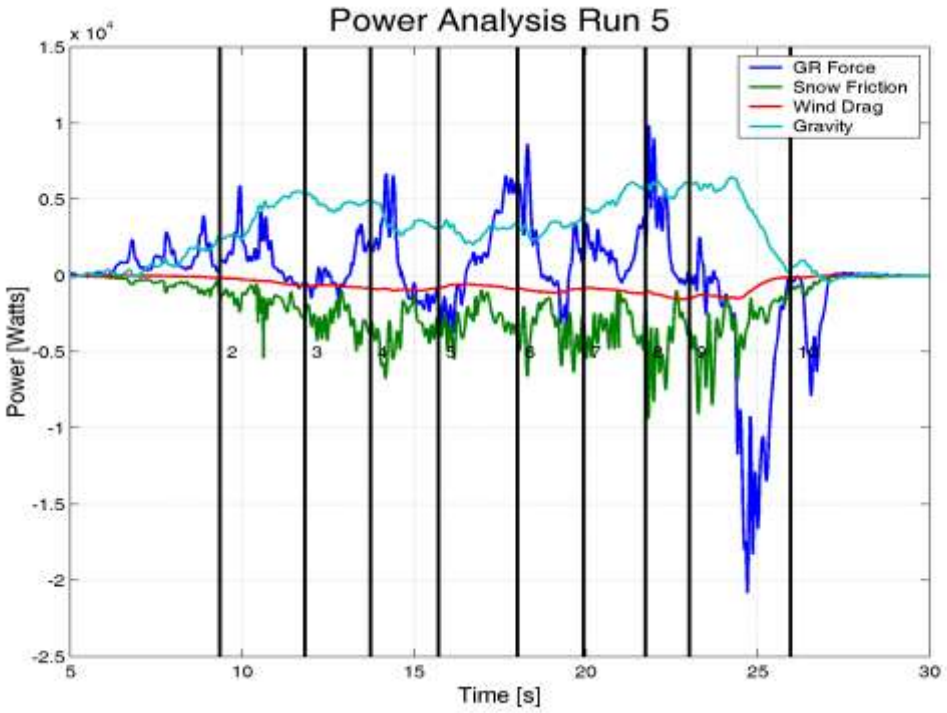

Figure 8.18: Power analysis of run 5

The poor turns (6 and 8 in run 3 and turns 3 and 5 in run 5) can be identified by negative ground reaction force power (blue lines, Figure 8.17 and Figure 8.18). The athlete's

aggressive skating and pole action before gate 2 is visible as four spikes in the ground reaction force power of run 5 (Figure 8.18). The snow resistance power is generally negatively correlated to the ground reaction force power because an increase in force normal to the ski base about each gate also increases the snow resistance force.

Figure 8.19 and Figure 8.20 show the work done by the athlete using either his left or right ski.

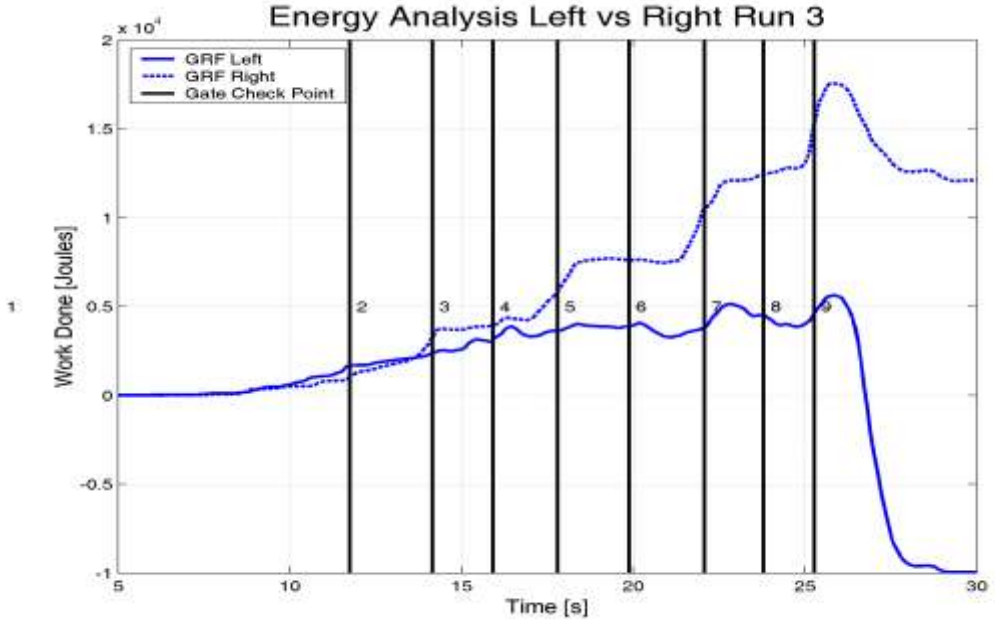

Figure 8.19: Energy analysis the work done by the left and right skis in run 3

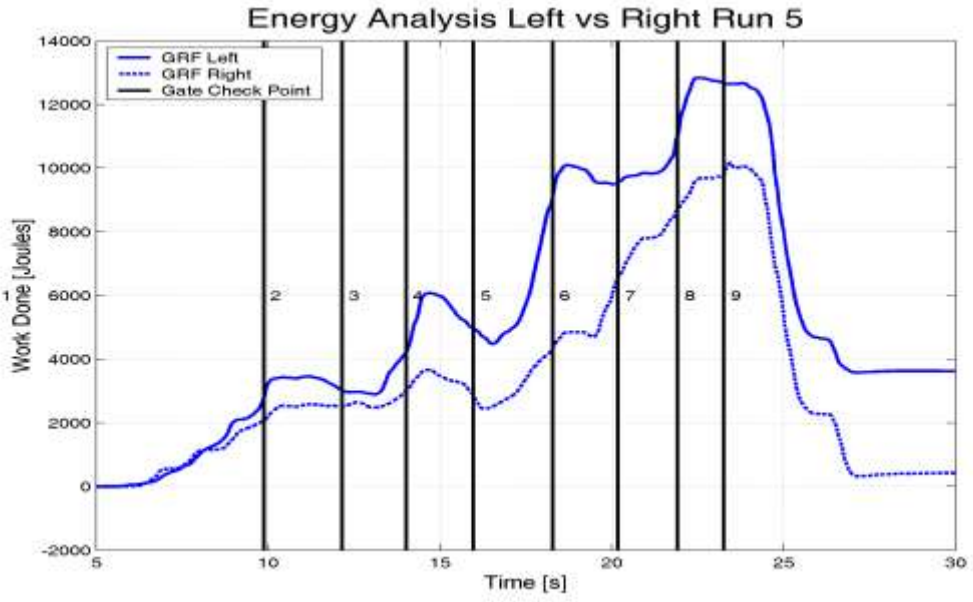

Figure 8.20: Energy analysis the work done by the left and right skis in run 5

In run 3 he did more work with his right ski. In run 5 he did a similar amount of work on both skis in the softer snow conditions, but slightly favoured his left ski. The athlete predominately

used his outside leg while turning and so the component foot energy analysis accounts for the better left turns in run 3 and the better right turns in run 5 (see the previous force vector diagrams Figure 8.9 and Figure 8.10).

8.5. Data driven animation with forces

How can the information in this chapter be presented intuitively for audiences of athletes and coaches? Forces, work, energy and power could seem too esoteric and too far removed from the athlete‟s perception of performance. Data driven animations were used to present the complex data in a way intuitive to the athlete.

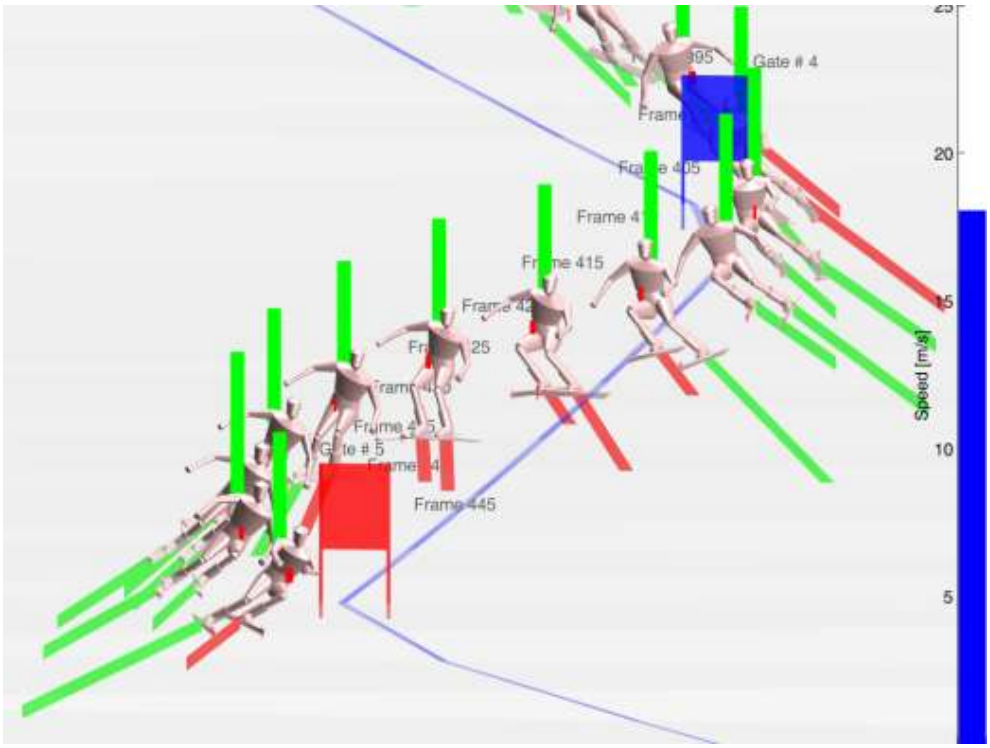

Figure 8.21: Screen shot from of run 3 using the visualisation software

The athlete‟s movement data were animated and the external forces of gravity, wind drag, snow resistance and ground reaction forces approximately normal to the ski bases were superimposed as colour coded vectors (Figure 8.21 and Video 8.4). This is possibly the first time the biomechanical analysis of a complete giant slalom training run has been performed successfully and also the first time the data from giant slalom have been visualised in this way. Data driven animations were also good way to qualitatively validate the results because if there were large errors in the animations the athletes (who are experts in the movements of skiing) were able to pick them up. The software used to visualise the data was written by the author in MATLAB. Much of it is similar to the code used for visualising the inline skating experiment.

Video 8.4: Appendices\FMC Video\Ruapehu_R3_Force_RScan.avi
Video 8.5: Appendices\FMC Video\Ruapehu_R5_Force_Optim.avi

In these data driven animations (Video 8.4 and Video 8.5) the external forces have been visualised by vectors that represent magnitude, direction, point of contact and power. If the external force has a positive power it is acting to accelerate the athlete and it is colour coded green. Red vectors are for braking forces.

The data driven animations contain a large amount of useful information for an athlete and give a good „feeling" for the relative effects of different external forces during different parts of the course. With this type of feedback the athlete can concentrate on technique improvements that reduce the amount of red braking forces. The animations show the ground reaction forces were most important to race outcome because these varied the most over the course.

The data driven animations show the differences between the foot loading ratio and ski"s centre-of-pressure movements measured by the RS-Scan insoles for run 3 and estimated using a torque balance for run 5. In Chapter 7 on page 176 methods were presented for estimating both the foot loading ratio and the ski centre-of-pressure movements from the FMC data, but the results could not be independently validated. Video 8.5 shows however that the estimated ratio and centre-of-pressure are plausible. The estimated centre-of-pressure in run 5 moved beyond the boot sole and travelled along the length of the ski base. The measured centre-of-pressure in run 3 (Video 8.4) remained well within the boot sole. Centre-of-pressure movements beyond the boot sole and along the ski base are plausible and are a result of the transmission of torque through the semi-rigid boot shank.

8.6. Technique optimisation

The optimal ski racing technique is athlete, course and equipment specific. The fastest possible course time depends on both local turn technique and global race strategy. The ideal athlete executes „perfect" turns and selects the optimum places to make the turns. In this section FMC data are used to investigate how turn radii and inclination (leaning angle) might contribute to the execution of perfect turns.

Inclination measures how far the athlete leans into the turns from a vector normal to the snow slope. The minimum inclination is 0º and corresponds to an upright stance used when running straight down the fall line. The maximum inclination angle is 90º and corresponds to the athlete lying flat on the snow, but athletes seldom incline more than 70º during races. Inclination is important in giant slalom turn technique where the athletes use inclination to maintain postural balance while cornering. The higher the inclination angles the more horizontally directed ground reaction forces (GRF) are produced and the faster or tighter the athletes can turn (as discussed Section 8.1.6 in the GRF force vector analyses of run 3 and 5, Figure 8.7 and Figure 8.8).

In Chapter 5 several ways to measure the inline skate athlete‟s ability to incline (lean into turns) were investigated. Inclination was identified as a performance-limiting factor by the use of friction cones. It was also one of the constraints used in the athlete‟s simulated minimum time trajectory. The simulated inline skating trajectory suggested the athlete might reduce course time up to 20% by selecting different optimum turn radii for different parts of the course. Finally, in Section 8.1.6 the ability to maintain sustained ski/snow-edging angle by abduction of the outside hip in combination with inclination was also identified as a key component of the athlete‟s best turn.

8.6.1. Friction Cones

Friction cones provide estimates of how far the athlete inclined while turning about the course gates (Figure 8.22 and Figure 8.23). Friction cones are important because the ability to incline is a performance-limiting factor. In the analysis of inline skating the friction cones provided an estimate that combined the static friction limit (between the skate wheels and the floor perpendicular to the skates rolling motion) and the athlete‟s perception of a safe inclination angle. In skiing the friction cone provides an estimate of maximum leaning angle from the vector normal to the snow surface. While turning the front edge of the ski cuts into the snow and makes a banked curve that the rear of the ski runs on. Subtracting the friction cone inclination angle from 90º provides an estimate of the minimum ski/snow surface angle possible before the snow fractures and the ski edge slips out of the turn.

Figure 8.22 shows in run 3 the athlete was able to incline up to 53° from the vector normal to the snow surface 95% of the time. In run 5 he inclined up to 59° from the vertical 95% of the time (Figure 8.23). What effects did the increased inclination have on his performance? More analysis, presented in the next section, is required to answer this question.

Compared to the inline skating friction cone (95% limit 31°, Figure 5.16), in skiing the athlete was able to incline much further into each turn. The friction cone for skiing also contains more outlying data points than the friction cone for inline skating because the ski cuts a path in the snow that dynamically fractures the snow surface. This is a much more complicated interaction to model than the skate wheels running smoothly and gripping a gymnasium floor. The athlete also used his poles and collided with the course gates, which produced additional forces parallel to the snow slope that did not fit the friction cone model.

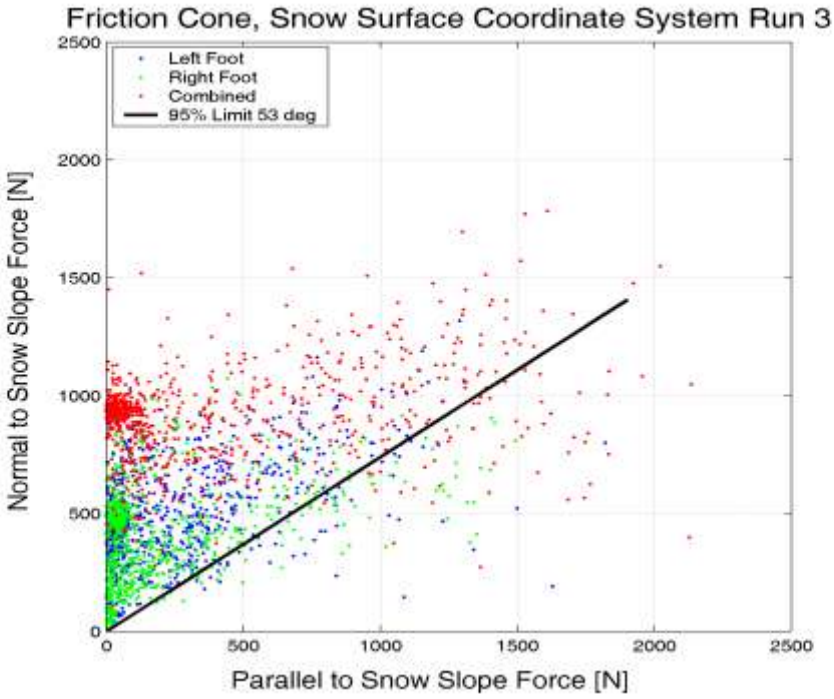

Figure 8.22: Friction cone for run 3

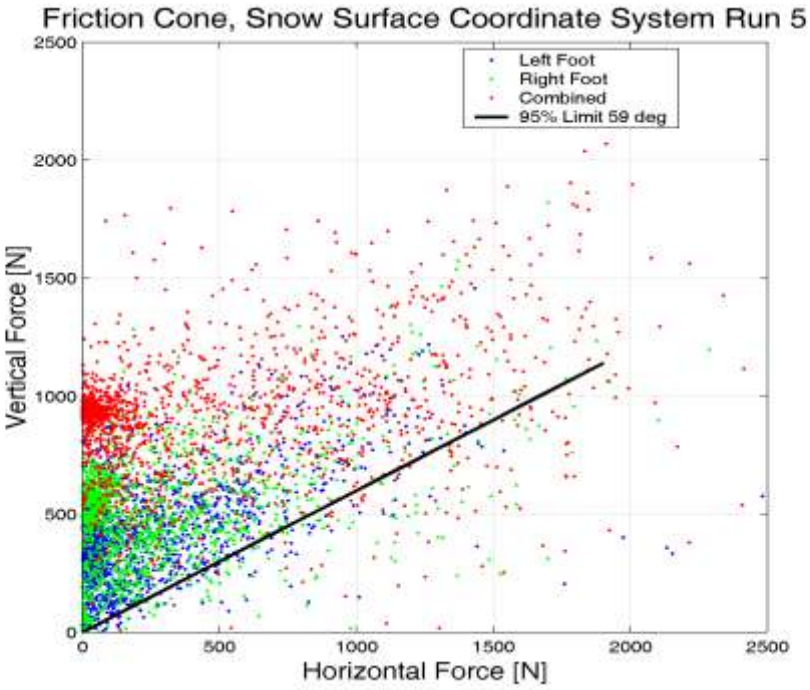

Figure 8.23: Friction cone for run 5

The friction cone data were rotated into the athlete centred coordinate system (Figure 8.22). In the athlete centred coordinate system the global Z-axis is rotated from the vertical vector to the vector normal to the changing snow slope and the X and Y-axes are rotated into the changing plane of the snow surface with the X-axis heading coincident with the athlete‟s velocity vector heading. The GRF normal to the snow surface was plotted against the GRF

parallel to the snow surface and projected in the plane normal to the athlete‟s velocity vector. Because the snow slope changes, the modelled changing snow slope described in Chapter 6 was used to rotate measurements from the global coordinate system into the athlete centred coordinate system.

8.6.2. Leaning angles

To run a giant slalom at speed the athlete must incline or lean into each turn. The first way to measured inclination was physical inclination using the athlete‟s CoM location relative to his base of support (Figure 8.24 and Figure 8.25). The athlete‟s physical inclination was measured by an angle between a vertical vector (global Z-axis) and a vector connecting the skis centre-of-pressure with the athlete‟s CoM projected into the plane perpendicular to the athlete‟s velocity vector.

In run 5 (Figure 8.25) the athlete physically inclined between 5º and 10º further into each turn than in run 3 (Figure 8.24), which confirms the findings of the previous friction cone analyses. The turn about gate 6 was previously identified as a key factor in race outcome (Figure 8.6). In run 5 the peak inclination angle about gate 6 was slightly earlier relative to the gate than in run 3 and this may have contributed to the better performance in run 5.

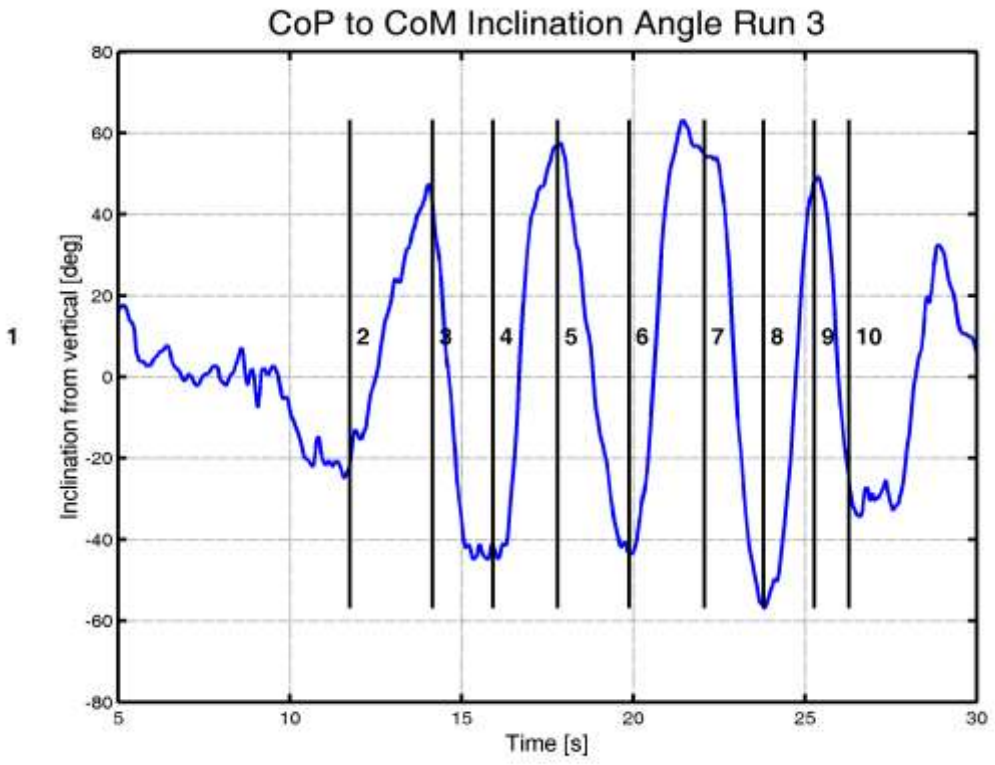

Figure 8.24: Physical Inclination angle in run 3

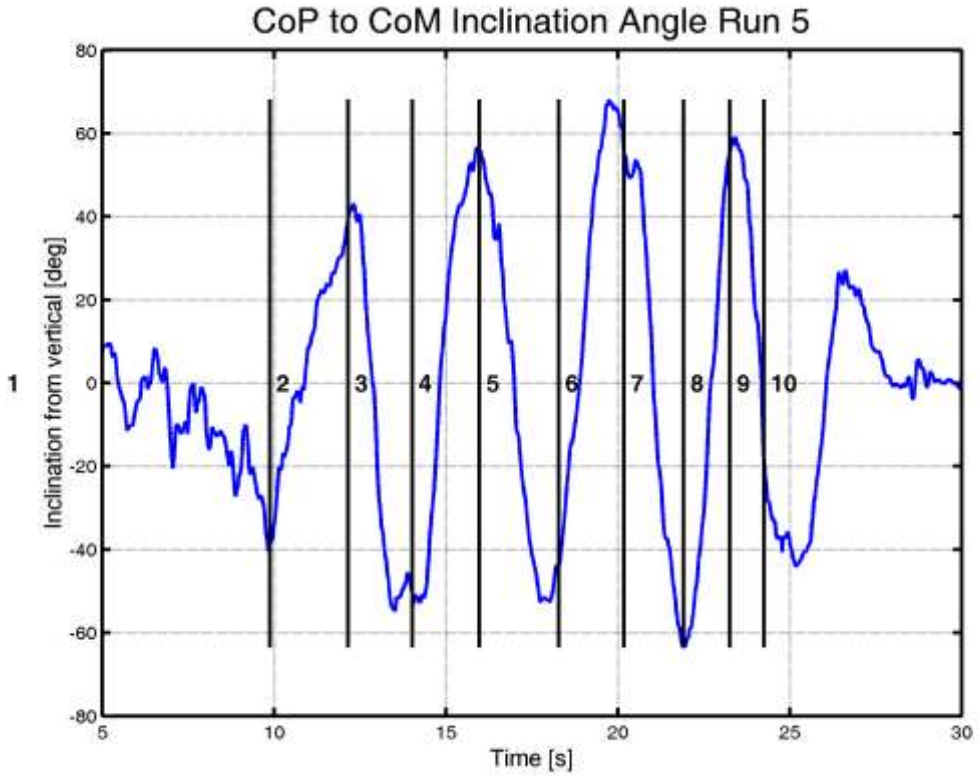

Figure 8.25: Physical Inclination angle in run 5

8.6.3. Force angles

The second way to measured inclination angle was force inclination, using the ground reaction forces visualised in Figure 8.21. The angle between the vertical vector and the ground reaction force vector projected onto the plane perpendicular to the athlete"s velocity vector was measured (Figure 8.26 and Figure 8.27).

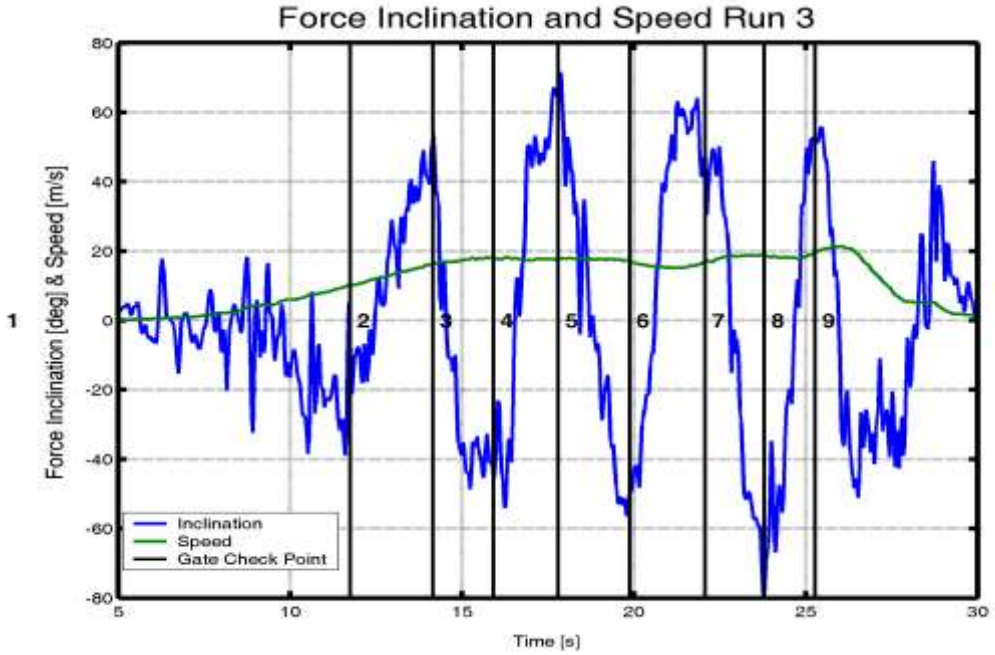

Figure 8.26: Force inclination angle in run 3

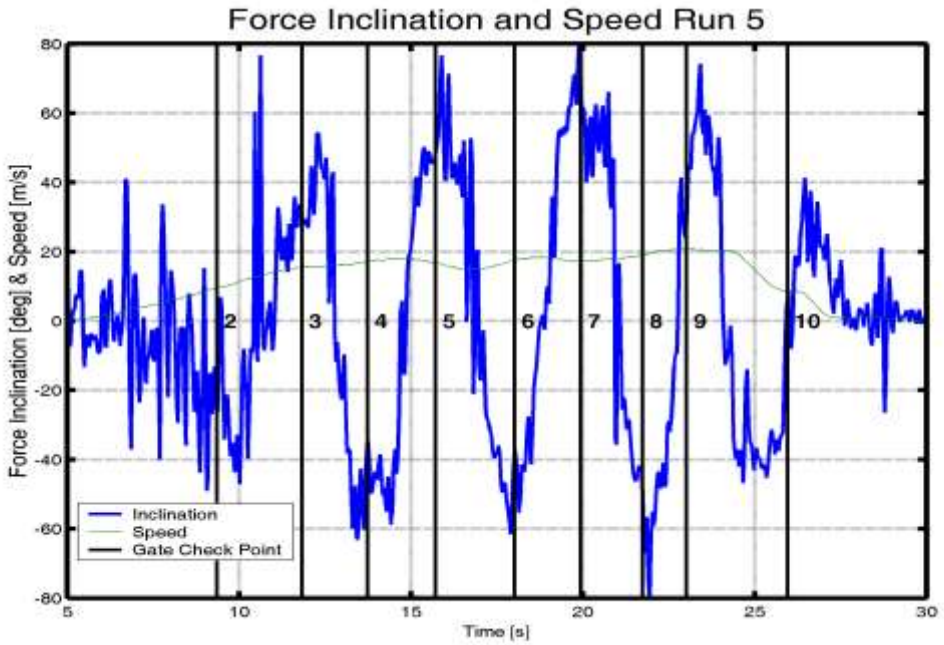

Figure 8.27: Force inclination angle in run 5

The force inclination graphs (Figure 8.26 and Figure 8.27) are very similar in shape to the physical inclination graphs (Figure 8.24 and Figure 8.25) except there is more high frequency information in the force inclination graphs. Because the athlete has a certain amount of rotational inertia, changes in the physical inclination angle occur more slowly than changes in the force inclination angle.

Force inclination and physical inclination are not the same. The athlete controlled changes in his physical inclination angle by momentarily moving the force inclination angle away from the physical inclination angle. The separation between the force inclination and physical inclination created external torques that affected his whole body rotation. Rotations included; edge-to-edge (about the anterior-posterior axis) between turns, forward-and-back (about the medial-lateral axis) to maintain balance and regulate centre-of-pressure movement, and twists (about the superior-inferior axis) to control the ski and body alignment relative to the direction of travel.

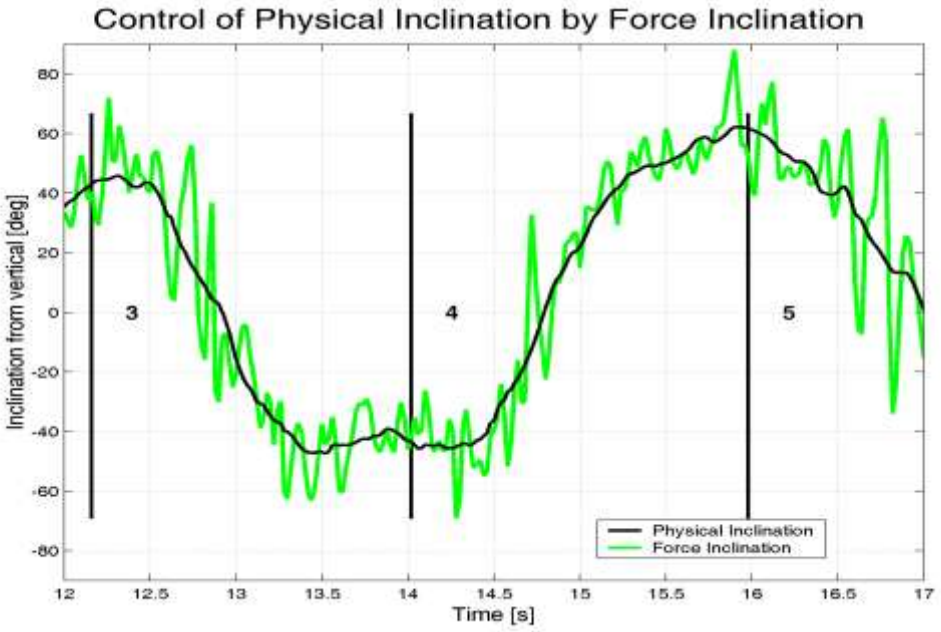

Figure 8.28: Close up of physical and force inclination at gate 4 in run 5

Figure 8.28 shows the physical inclination and force inclination angles about gate 4 in run 5. Throughout the run the athlete rotated from edge-to-edge between turns. When entering turn 4 the athlete"s physical inclination magnitude increased as he rotated maintaining angular velocity about his anterior-posterior axis (from 12.75s to 13.25s, Figure 8.28). Before the apex of the turn the athlete created a torque that reduced his angular velocity to zero and stabilised his physical inclination angle (the peaks in force inclination before gate 4 from 13.25s to 13.5s). Through the turn apex the athlete created instantaneous torques to maintain his postural balance and to make fine adjustments to his trajectory (the fluctuating force inclination from 13.50s to 14.25s). After the apex the athlete created additional torques to increase his angular velocity and so enable rotation from edge-to-edge out of turn 4 and into turn 5 (from 14.25s to 14.50s). This use of external torque created from ground reaction

forces to control inclination angle explains why the force inclination angle contained more power in the higher frequency components than the physical inclination angle and why there was generally time lag between the low frequency components of the physical and force inclination angles.

8.6.4. Turn radii

In this section optimum turning radius for the course is investigated. Based on the athlete‟s CoM acceleration the instantaneous radius of curvature projected onto the plane of the snow surface is calculated for runs 3 and 5 (Figure 8.29 and Figure 8.30). More details about the calculations used are available in Appendix H.

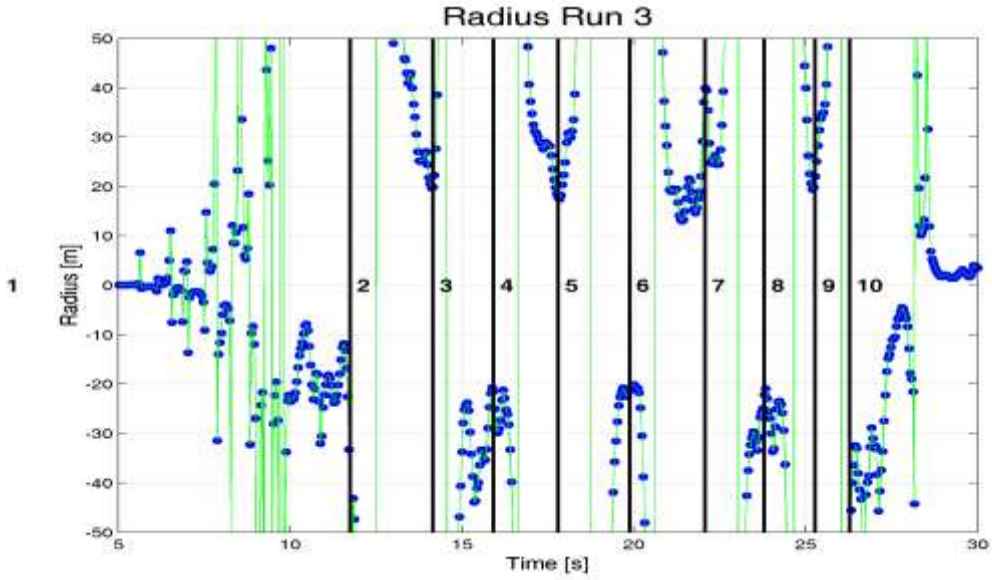

Figure 8.29: Instantaneous turn radii in run 3

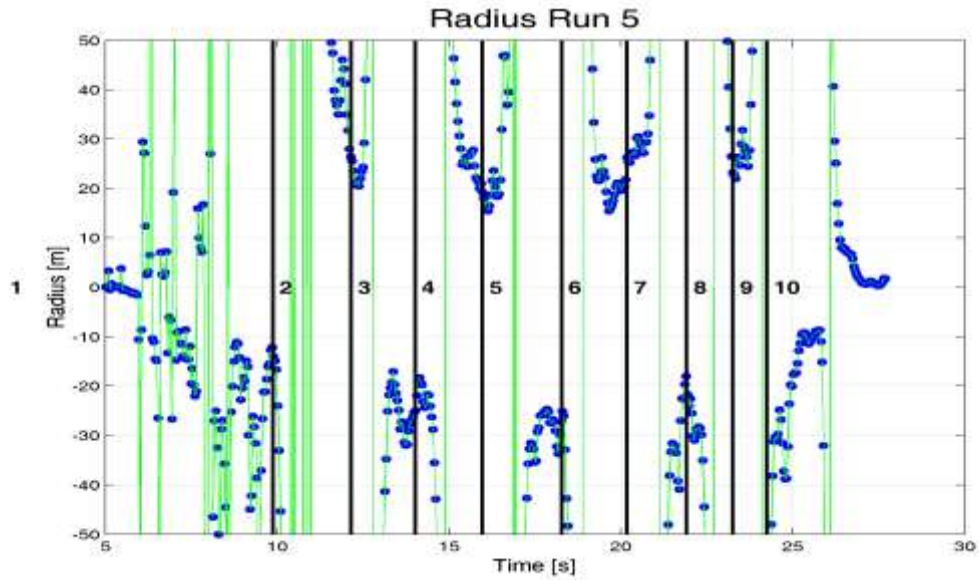

Figure 8.30: Instantaneous turn radii in run 5

Figure 8.29 and Figure 8.30 show the athlete did not make constant radius turns. Two extremes of turn technique and therefore turn radius evolution were observed during the runs. About gate 4 in both runs 3 and 5 a double minimum is observed in the graphs of turn radius, the minimum radius is observed once before the turn apex and once after the turn apex. The athlete therefore entered gate 4 with a tight turn, which set him up so he could pass safely through the gates with a more open turn, and some room for error. The strategy may also have provided the athlete with more time to control external torque about the anterior posterior axis in order to rotate between the turns and is similar strategy to the open radius turn strategy used by the inline skater and discussed in Chapter 5. About gate 8 however the minimum turn radius was observed once, near the gate and probably represented a more aggressive turning strategy with less room for error.

Table 8.2: Minimum turn radii in metres

	Gate 2	Gate 3	Gate 4	Gate 5	Gate 6	Gate 7	Gate 8	Gate 9
Run 3	11.8	19.7	20.8	17.4	20.1	14.6	20.9	19.4
Run 5	11.8	20.5	18.3	15.4	23.9	15.5	18.0	22.0

In general the left turns about gates 5, 7 and 9 (mean minimum radius 17.4m) were tighter than the right turns about gates 4, 6 and 8 (mean minimum radius 20.3m) indicating a cross slope and/or a difference in technique between the left and right turns.

The course line analysis (Section 8.1.3) identified that turn 4 was better in run 3 than in run 5 because of a shorter trajectory and therefore it was assumed that in run 3 a tighter turn had been used. The „tighter turns are better" hypothesis might be just another way of phrasing the „going straight turning short" (GSTS) strategy discussed by David Lind (Lind & Sanders, 1997). New information from the turn radius analysis however shows that the minimum turn radius about gate 4 was unexpectedly greater in run 3 (20.8m, Table 8.2) than in run 5 (18.3m). These turn radii data contradict the going straight turning short race strategy and suggests for some gates an optimum turn radius exists, which dose not result in the tightest practical paths between the gates. The hypothesis is also supported by the turn data from gate 6. About gate 6 the performance in run 5 was better than the performance in run 3 (see Section 8.1 Race Analysis) and the minimum turn radius of the „better" turn (23.9m, run 5) was again greater than the minimum turn radius of the „lesser" turn (20.1m, run 3). It was possible the larger radius turns allowed for higher speeds with similar inclination angles.

Table 8.3: Turn length in seconds and metres

	Gate 4 [s]	Gate 4 [m]	Gate 6 [s]	Gate 6 [m]
Run 3	1.60	28.0	1.00	17.3
Run 5	1.56	26.3	1.26	21.3

Figure 8.29 and Figure 8.30 show the more open turns, gate 4 in run 3 and gate 6 in run 5 resulted in the turn being sustained longer. Turn length for these two turns was measured by

the length travelled while maintaining a turn radius of less than 50m (Table 8.3). These data suggest that open and sustained turns through some sequences of gates may be better than tighter shorter turns. The broader sustained turns through some of the racecourse gates may have been better because the technique resulted in the athlete spending relatively more time travelling closer to the fall line (about the gates) than travelling across the fall line (between the gates). Using more open turns, the athlete might sometimes be able to reach the mid point between the gates faster even though the path length is longer.

About other gates however the tighter turns were better. About gate 7 the technique used in run 3 has previously been identified by both the resultant force vector analysis (Section 8.2) and the power analysis (Section 8.4) as superior to the technique used in run 5. In this case the tighter turn of run 3 (14.6m minimum radius) was better than the performance in run 5 (15.5m minimum radius). The results suggest the optimum turn radius for each gate is a trade off between tighter turns that result in shorter path lengths and more open turns that allow for faster turning speeds and also result in more acceleration earlier in the turn while travelling closer to the fall line.

8.7. Accelerative turn technique

Turn 6 of run 5 demonstrates how the athlete might use ground reaction forces to create positive power and increase speed through a turn (Figure 8.18). Previously David Lind hypothesised how the athlete might theoretically do this (Lind & Sanders, 1997) in his book, *"The Physics of Skiing"*. Lind compares the athlete‟s motion to the motion of a child on a swing or the motion of an imaginary cart on frictionless tracks making fixed radius turns. The data show that the athlete did not make fixed radius turns (Figure 8.29 and Figure 8.30) so a more general theory is required:

Athletes can increase speed through additional muscle work when their centre-of-mass and ski trajectories are diverging.

The theory comes with the caveat, „provided there is little snow resistance and there is not too much ski skidding‟. The work done by ground reaction forces normal to the ski bases excludes the work done by snow resistance forces, which are parallel to the ski bases and are always negative. Gravity did much more work than ground reaction forces in the experiments (Figure 8.16) but the athlete had no influence on the work done by gravity. The ground reaction force work therefore was largely responsible for the experimental race outcome because the athlete directly influenced it through race technique.

8.7.1. Acceleration from diverging ski and CoM trajectories

The CoM and ski trajectory may diverge as indicated by the location of green arrows in Figure 8.31. The Figure 8.31 is a schematic of the athlete‟s ski and CoM trajectories. Because the motion takes place in three dimensions, the CoM and ski trajectory may diverge in both

the top and profile planes of view. The diagram is only a schematic and is not an accurate representation of the actual athlete‟s technique.

Figure 8.31 shows two opportunities to use ground reaction forces to increase speed. In each case the ski and CoM trajectories are diverging and so the ground reaction force vector normal to the ski bases may have a small component in the direction of the athlete‟s velocity vector. A force component in the direction of travel is required for the ground reaction force to have a positive power and act to increase speed.

The first opportunity to increase speed using ground reaction force work might occur during the entry phase of the turn if the athlete runs smoothly on the ski edges with appropriate physical inclination. The athlete could then use internal muscle forces to push his CoM away from his skis. The resulting motion may vaguely resemble a double footed skating stroke as the skis and CoM trajectory are diverging in the horizontal plane as viewed from the top. This type of motion can be termed „lateral projection“. If the lateral projection is perpendicular to the CoM trajectory, then by definition it does no work and therefore does not affect speed. The lateral projection defined here, however, is perpendicular to the ski trajectory and therefore some component of acceleration is in the direction of travel and so changes speed.

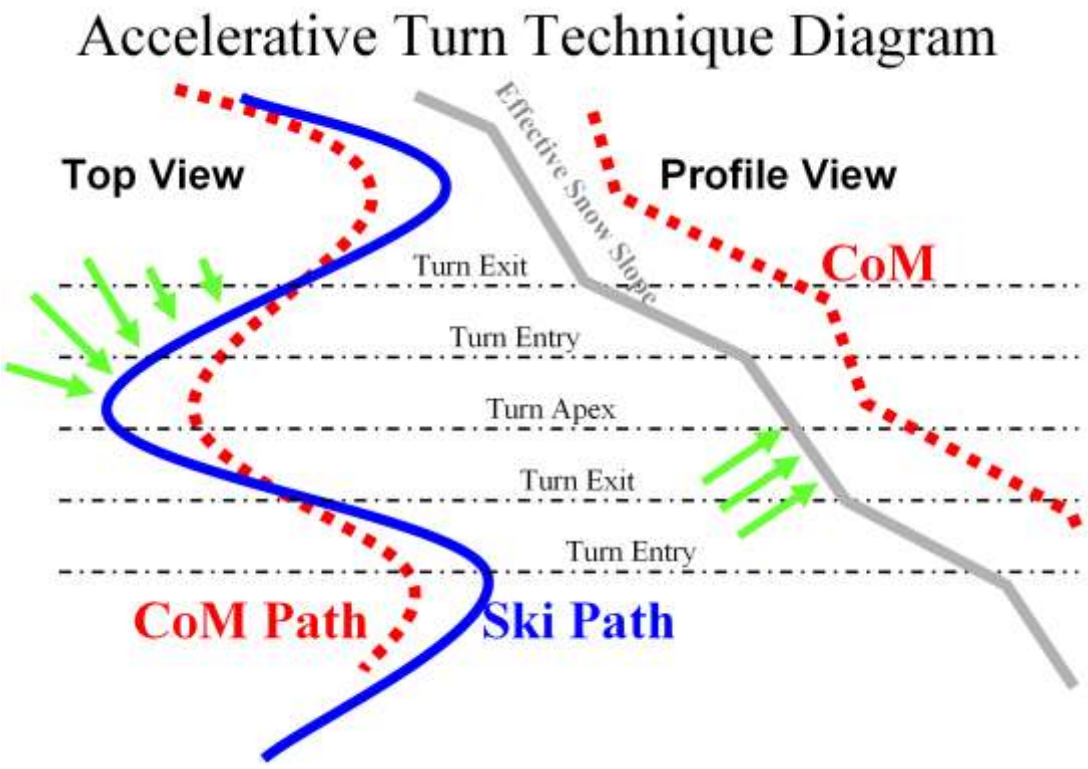

Figure 8.31: Schematic of how ground reaction forces might accelerate the athlete

In order to investigate accelerative turn technique The relative distance from the centre-of-mass (CoM) to the ski centre-of-pressure (CoP) was plotted in the athlete centred coordinate system for run 5 (Figure 8.32). In the athlete centred coordinate system the athlete‟s

measurements are rotated differently at each time point depending on the changing CoM velocity vector and the snow slope orientation.

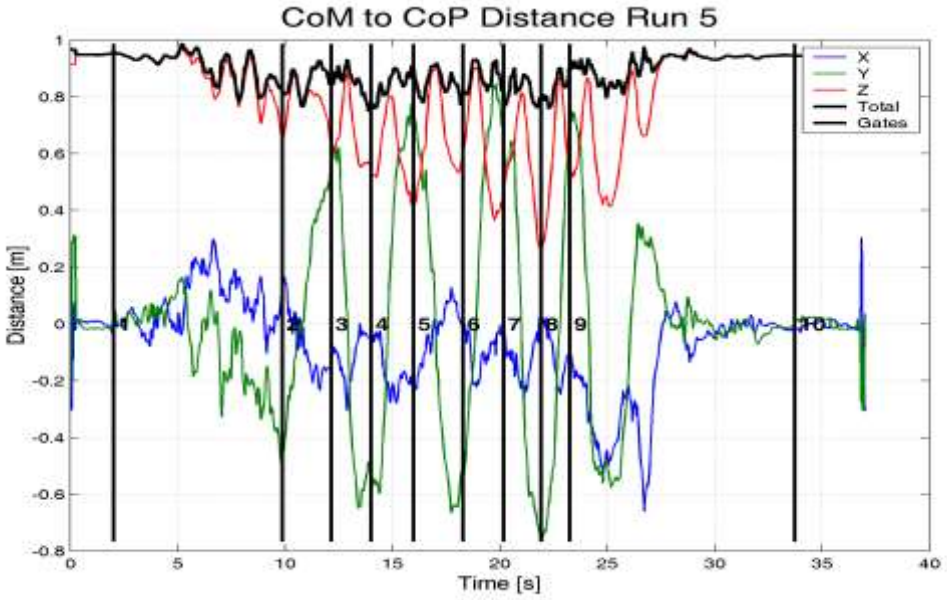

Figure 8.32: CoP to CoM distance in run 5

In Figure 8.32 the Z-axis (red line) shows movement normal to the changing snow slope, the Y-axis movements (green line) show movement perpendicular to the athlete‟s CoM motion, and the X-axis movements (blue line) show movement coincident with the athlete‟s velocity vector projected on the snow slope. The largest movements between the athlete‟s skis and CoM were a result of the athlete moving from edge-to-edge in order to maintain postural balance while making consecutive turns. These movements (Y-axis) by definition were perpendicular to the athlete‟s CoM trajectory and therefore did not affect speed.

The turn about gate 6 in run 5 was previously identified as an exceptional turn. In run 5 about gate 6 the turn apex occurred before gate 6 and the athlete‟s CoM moved forward relative to the skis in the direction of motion for the first part of the turn (blue line, positive slope, between 16 and 17.5 seconds, Figure 8.32). This confirms that lateral projection was used to accelerate the athlete before gate 6. In the second half of the turn however the CoM moved backwards relative to the skis and any increases in kinetic energy had the potential to be lost through negative ground reaction force work. The Figure 8.8 shows that additional work was also done in the later half of the turn after the gate.

In the later half of the turn 6 in run 5 the athlete‟s CoM moved away from the skis in the direction normal to the snow slope as the athlete stood up (red line, positive slope from gate 6, Figure 8.32). This represents the second opportunity to increase speed from internal muscle work (green arrows profile view, Figure 8.31). This time the gains were made normal to the snow surface. This type of motion may be called „pumping“ and resembles the technique an athlete might use to gain additional speed in a half pipe.

8.7.2. Acceleration from effective snow slope changes

Pumping might increase speed through a course if the athlete is able to create higher ground reaction forces near the turn apex where the effective snow slope is greatest and then almost becomes airborne through the transition between turns, where the effective snow slope is least. Pumping may also be used in combination with pre-jumping as the snow slope changes. By pre-jumping the athlete jumps slightly before a roll over into steeper terrain and the flight distance is decreased. He lands on the steepest part of the slope just after the roll over and can then accelerate off the steeper slope.

To investigate if the athlete used pumping the effective snow slope was plotted based on the skis centre-of-pressure trajectory (Figure 8.33).

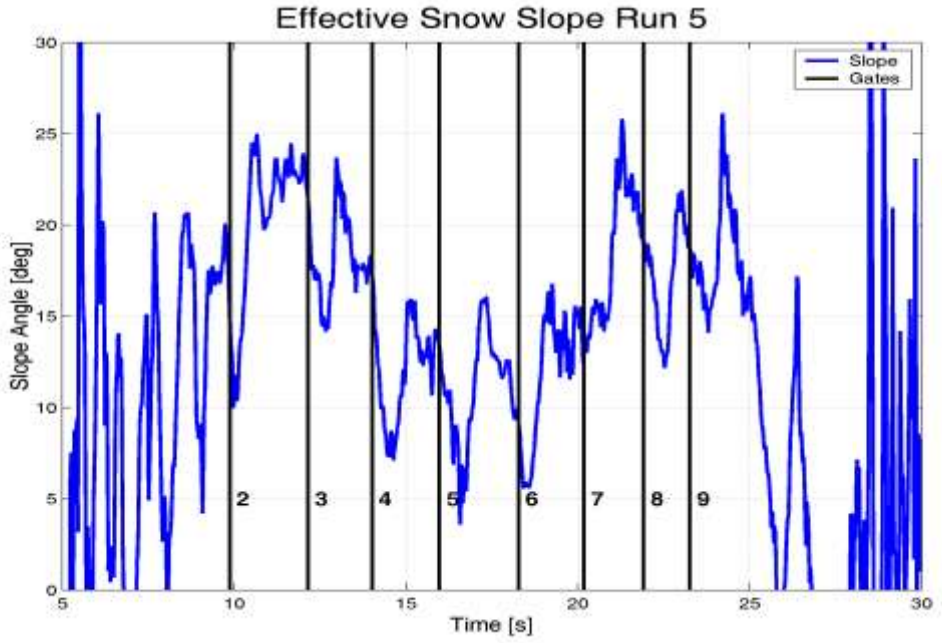

Figure 8.33: Effective snow slope changes due to athlete trajectory in run 5

Figure 8.33 shows that even though the actual snow slope (from the terrain model) was constant between the gates, the effective snow slope (as plotted) was reduced as the athlete skied across the fall line between turns. The changes in the effective snow slope were generally around 10° between gates. The time spent travelling across the fall line (between gates) is visualised by the troughs of Figure 8.33 where the effective snow slope is least and the time spent travelling down the fall line (round the gates) is visualised by the peaks. In order to increase speed the athlete should spend more time travelling down the fall line relative to the time spent travelling across the fall line.

If the effective snow slope is compared against the ground reaction force power graph for run 5 (Figure 8.18) then about some gates, such as gate 6 in run 5, there is an apparent correlation between positive ground reaction force power and the increasing effective snow slope. About other gates, such as gate 5 in run 5, there is no correlation between ground reaction force

power and the increasing effective snow slope. About gate 6 the athlete may have used additional internal muscle work to push away from the slope (pump) where the effective snow slope became steeper. The athlete‟s technique about gate 6 was better than about gate 5.

In summary, by using additional muscle work to regulate the ground reaction forces the athlete effectively skied on a steeper slope. Lateral projection, pushing the CoM away from the ski trajectory was also effective. The athlete used lateral projection in the early part of the turn to increase speed, and during skating starts (see the three spikes in ground reaction force power before gate 2, Figure 8.18).

Increasing ground reaction forces however also increases snow resistance forces, which always act to reduce speed. The combination of snow resistance work and ground reaction force work over a complete racecourse is always negative (See Figure 7.23 on page 186). After the first gate the question „how to gain energy in some parts of a turn cycle?“ could probably be rephrased to „how to minimise energy loss in a complete turn sequence?“ At high speed there is far more potential to lose energy through skidding than there is to gain energy through pumping and lateral projection. Nearly all of the athlete‟s speed comes from the conversion of gravitational potential energy into kinetic energy, but ultimately it is how the athlete generates additional ground reaction forces that decides race outcome.

8.8. Discussion about race strategy

The analyses presented in this chapter have shown there are many factors that might affect performance in a race, but what are the most important factors that define race strategy? Here it is discussed that athletes may be able to improve performance by focusing on only three aspects of race strategy; choosing the optimum turn radius, turn entry point and inclination angle for each gate. These three parameters depend on multiple factors including among other things speed, terrain slope, gate setting and ski design. Using the fusion motion capture data it is possible to investigate some general trends in these parameters and start to develop an optimum race strategy.

8.8.1. General trends

Figure 8.34 shows that the minimum turn radius generally increased with the athlete‟s speed. At race pace (between $15ms^{-1}$ and $21ms^{-1}$) the minimum turn radius ranged from 14m to 24m and was principally limited by the maximum inclination of the athlete (how far he was able to lean into each turn, Figure 8.35). At race pace the athlete‟s maximum physical inclination angle (between 45° and 70º) did not increase as speed increased and so speed increases resulted in turn radius increases. The athlete‟s maximum inclination angle was limited by the maximum ski/snow angle the athlete could sustain before the snow surfaces beneath the ski bases fractured and also the athlete‟s ability to rotate from edge-to-edge quickly between the turns. These factors were further dependant on the athlete‟s strength, agility, balance and the

ski equipment design. Maximum inclination angle however may not have produced the optimum turn radius and further analysis is required to determine the optimum performance.

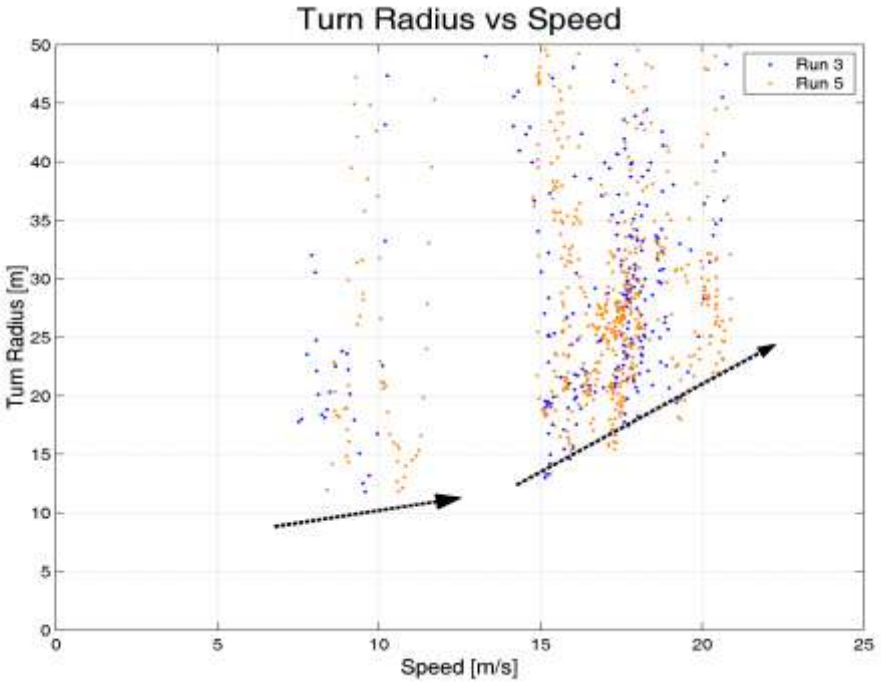

Figure 8.34: Increasing turn radius with speed

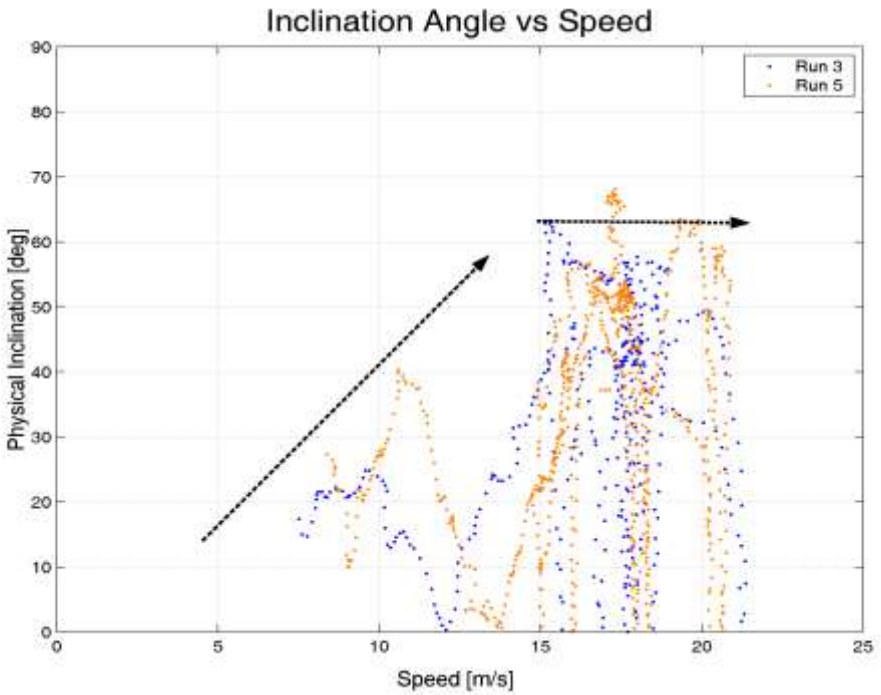

Figure 8.35: Physical inclination reaches a limit at race pace

The general trends presented in this section do not describe the optimum performance through the racecourse, this discussed later on. The graphs use a window of the athlete‟s data starting from one second before gate 2 and finishing one second after gate 9. The trend lines overlaid on the data are based on the apparent visual trends in the data. More data are required to confirm these initial findings and to complete statistical analyses.

8.8.2. Ski selection and design

The ski should be designed by the manufacturer and/or selected by the athlete to match the specific requirements of the racecourse. Unlike inline skates, a single alpine ski design can not perform turns of all radii at all speeds equally well. Ski trajectory is a result of the ski side cut radius, the ski flex and the ski/snow angle. The theoretical relationship between ski side cut, edging angle and ski trajectory has been documented by others (Erich Müller & Schwameder, 2003). They show that theoretically the ski should carve tighter turns if it has more shape and if the ski/snow angle is increased.

The ski turning radius data from the race course was plotted against the ski edging angle data (see Figure 8.36). The ski design should be selected to best match the performance required during the turns, which generally corresponds to the area of Figure 8.36 with higher ski/snow angles (between 40° and 80°). The mean properties of the „optimum‟ ski (side cut radius and flex) may, for example, be determined by the trend line, while the spread of the data may determine the optimum versatility, the extent that the properties of the ski should vary along its length.

The ski/snow edging angle has been plotted over the course for run 3 (Figure 8.37) where 0º corresponds to the ski sitting flat on the snow. In the figure the skating start, one stroke from the right ski and two strokes from the left ski are visible as peaks near the second gate. The figure also shows that the outside ski was edged between 10º and 20º more around each gate than the inside ski.

If the peak ski edging angles in Figure 8.37 are compared with the minimum turn radii in Figure 8.29, it becomes apparent that the peak ski edging angles occur sometime after the minimum turn radii about turn. This observation explains the large spread of data in Figure 8.36: Ski turn radius vs. ski edging angle. On steeper terrain, at the top half of the turn, the ski/snow angle was too small to allow the athlete‟s skis to carve tight trajectories and a skidding technique may have sometimes been used to approach the gates (the skidding zone, Figure 8.36). Through the bottom half of the turn the ski/snow angle was larger and the ski flexed more as a result of the ski side cut. The ski, if poorly designed, might therefore have tried to carve a turn that was too tight and this could cause loss of control (the wobble zone, Figure 8.36).

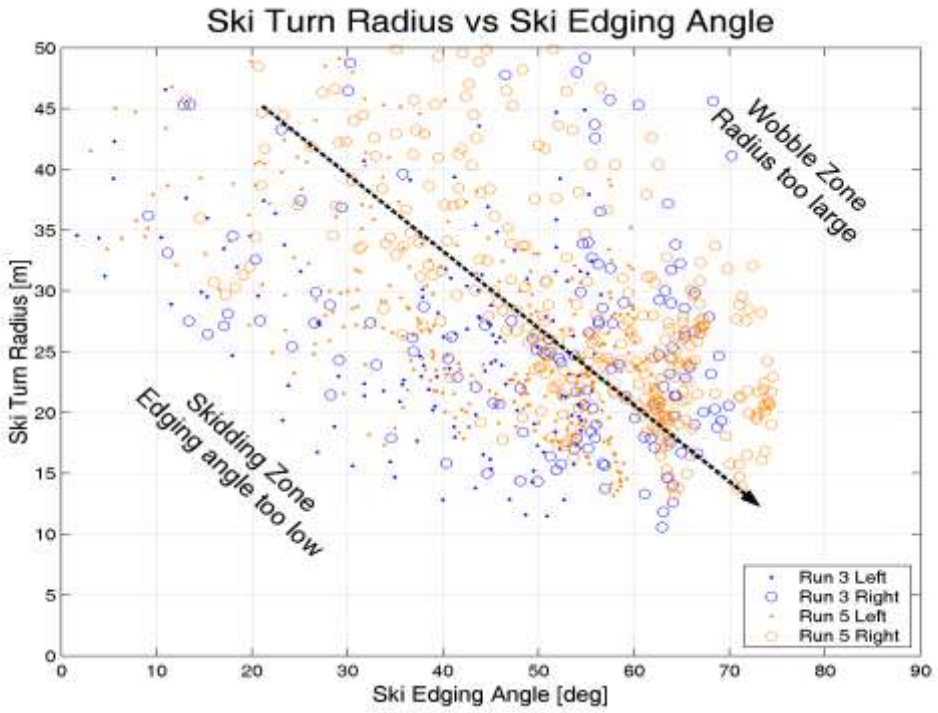

Figure 8.36: Ski turn radius vs. ski edging angle

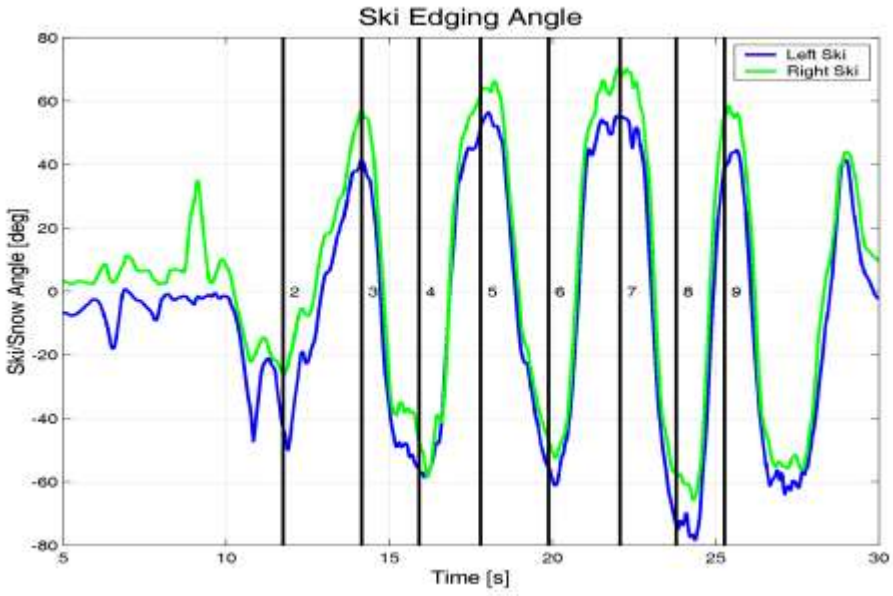

Figure 8.37: Ski/snow edging angle for run 3

To improve the versatility of the ski design the rear section of the ski is generally stiffer and straighter than the front section of the ski. The athlete therefore may move his centre-of-pressure along the ski base in order to effectively change the ski properties. In the skidding zone of Figure 8.36 the athlete should reduce skidding and therefore snow resistance by moving his centre-of-pressure forwards on the ski. This type of centre-of-pressure movement was previously observed in the insole data from run 3 (Figure 7.19, on page 182). The correct

ski design selection for a course and an athlete should result in both a faster and safer performance.

8.8.3. Optimum race strategy

The data presented in this thesis suggest that the optimum race strategy is a trade off between tighter turns, that result in shorter path lengths and more open turns that allow for more acceleration and faster turning speeds. The athlete must at least select for each gate, a point on the turn approach arc, the target turn radius, and the target inclination angle.

The optimum race strategy probably is different for each gate and sits between two extreme strategy boundaries. The first strategy (the tight turn strategy) is to take the shortest practical path between the gates without losing speed. The tight turn strategy is generally limited by the athlete‟s maximum inclination angle and the turn apex should be located next to the inside gate. A shorter path length at similar speeds takes less time to complete.

The second boundary strategy (the open turn strategy) is to make the longest most open turns practical while still passing between the gates. The open turn strategy is limited by the gate locations. The open turns can be run at higher speeds and provide the opportunity to accelerate earlier and over longer distances while travelling closer to the fall line about the gates. The turn apex depends on both the terrain and the future gate locations, therefore, the turn apex is not always located next to the inside gate.

Figure 8.38 shows another general trend, the athlete‟s minimum turn radius increased with increasing snow slope angle. Snow slope was not strongly correlated to speed through the racecourse and so Figure 8.38 presents an additional relationship to Figure 8.34: Increasing turn radius with speed.

The trend line in Figure 8.38, if extrapolated, predicts an optimum turn radius of zero metres on flat terrain. The extrapolated result is impractical for alpine skiing, but suggests that when the snow slope decreases the tight turn strategy may become more suitable. As the terrain steepens the open turn strategy may become more suitable because gravity is able to provide more acceleration. Using an open turn, the athlete is able to accelerate faster about the gate by travelling closer to the fall line both earlier on and for longer distances. Using more open turns on steeper terrain, the athlete may reach the midpoint between the gates earlier, even though the path length is increased.

The open turn strategy agrees with some parts of previous research based on simulations of optimum trajectory through single turns discussed in Chapter 1, Figure 1.5 (Hirano, 2002; Reinisch, 1991). Their analyses showed that quicker paths between two points were achieved by heading closer to the fall line at the start of the run and therefore accelerating faster. The open turn strategy discussed here however results in a very different trajectory between gates because the athlete is required to pass through multiply gates,

Alternatively, the relationship between increasing turn radius and increasing snow slope (Figure 8.38) may be partially explained by the athlete‟s maximum ski/snow edging angle limit. The same ski/snow edging angle on steep terrain results in less inclination from the vertical and therefore results in a more open turn.

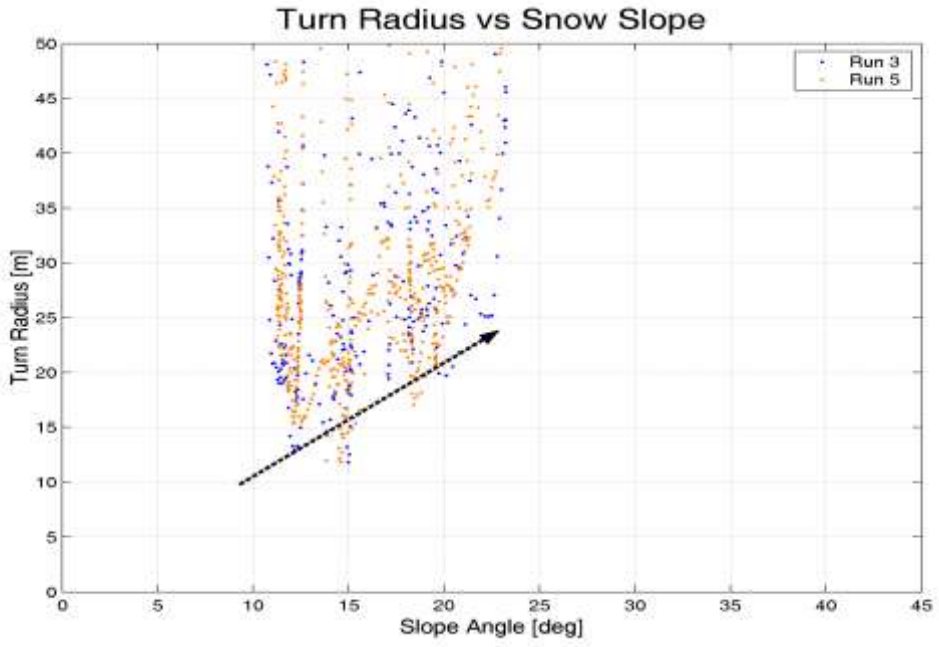

Figure 8.38: Turn radius vs. snow slope

Finally, it appears the athlete preferred at some level, symmetry between turns. In run 5 the athlete consistently inclined between 5° and 10° more (see Section 8.6.2) perhaps in an attempt to ski faster, however the athlete might have skied faster if he had been able to incline less about the left turns while inclining more about the right turns. This hypothesis is supported by Figure 8.36: Ski turn radius vs. ski edging angle and suggests the athlete‟s skis may have influenced his race strategy. Turns generally favoured the outside ski and so the left turns were made by the right ski and the right turns were made by the left ski. Figure 8.36 shows the data points corresponding to the right ski (left turns) were on average above the trend line (closer to the wobble zone) and so perhaps less ski/snow edging angle and inclination should have been used for the left turns. The data points corresponding to the left ski (right turns) were on average below the trend line (closer to the skidding zone) and so perhaps more ski/snow edging angle and inclination should have been used for the right turns. Most athletes do not have access to a large selection of different ski designs and so the naturally turning properties of their ski equipment may affect their race strategy. If the naturally turning properties of the ski equipment match the race strategy it might be interpreted by the athlete as a „good feeling“ because less effort should be required to control the ski and also the ski should create less resistance as it moves through the snow.

The fact the optimum solution is likely to be asymmetric may have been the result of a slight cross slope through the course. The simulated optimum solution for inline skating calculated

in Chapter 5 was also much more asymmetric than the athlete‟s measured trajectories. This could mean elite athletes may be able to improve by specifically training on asymmetrical gate sets with visual markers to guide their trajectory choice.

In conclusion, the optimum race strategy is influenced by complex interactions between many variables including; gate locations, snow slope, ski equipment, athlete ability, and speed through the course. The optimum strategy for each gate is a trade-off between tighter turns that result in shorter path lengths and more open turns that allow for more acceleration and faster turning speeds. The minimum turn radius (approximately between 15m and 25m) generally increased with both speed and snow slope. The athlete‟s physical inclination angle (approximately between 45° and 70°) was generally independent of speed at race pace. This discussion was based on data from two runs by a single athlete. Additional data and computer simulations are required to confirm the initial results and provide more specific guidelines to athletes.

8.8.4. Simulating the optimum trajectory

A simple model of the athlete‟s global race strategy could be defined by three control parameters for each gate, a target location for the turn apex, a target inclination angle, and a target turn radius. In Chapter 5 the inline skating athlete‟s optimum trajectory was simulated using two control parameters for each gate, turn radius and turn apex location. Alpine ski racing requires at least one additional control parameter if not more to account for the ski angle of attack and therefore, the ski skidding to some extent rather than carving a perfect line through the snow. If the athlete inclination angle is greater than required to make the target turn radius then the ski will skid. The ski will also skid if the radius the ski carves as a result of ski/snow angle, ski flex and ski side cut radius does not match the radius the athlete‟s centre-of-mass makes, with some slack allowed for relative movement between the ski and CoM trajectories.

On the local turn level additional degrees of freedom might also be required to model how the athlete might increase his speed by additional internal muscle work. Additional degrees of freedom might also be required to model how and when the athlete uses the separation between force inclination and physical inclination to rotate about the anterior posterior axis from edge-to-edge between gates. These additional degrees of freedom should also describe if each turn is an aggressive turn with the peak inclination angle at the turn apex or if less aggressive open radius gate passing strategy is used.

9. Conclusions

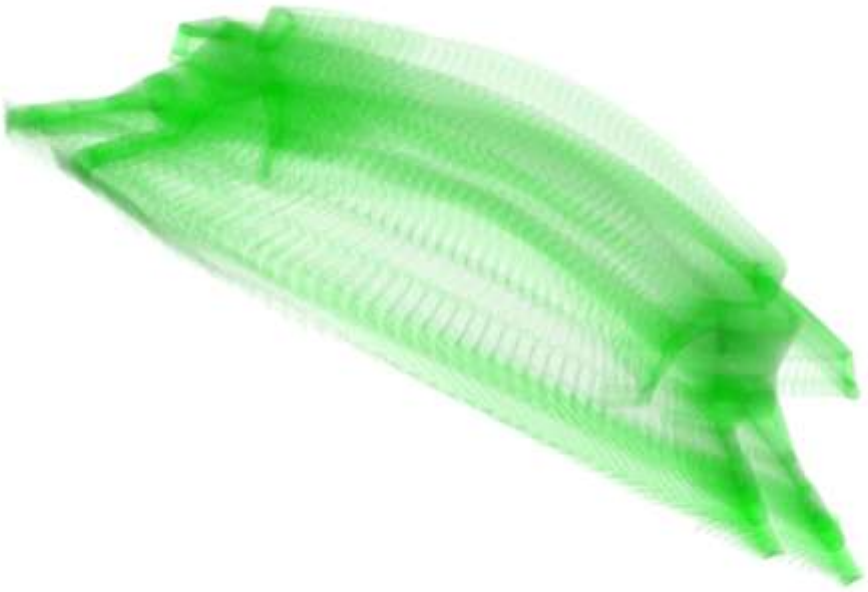

Figure 9.1: Visualisation of athlete speed in giant slalom skiing from FMC data

What makes one athlete the fastest, is it science or art? In the introduction it was discussed that the optimum strategy for passing through a series of gates was unknown. The optimum ski design for a particular gate set was unknown. The optimum envelopes of athlete movements through complete gate sets were also unknown. Steps towards finding these answers required measurements, models, and estimations of the external forces acting on the athlete. Simulations of performances during a ski races based on estimations of the athlete‟s physical limitations were also required. These and other questions became part of the thesis objective:

"Optimisation of athlete movement in alpine ski racing"

The principal thesis objective was not completely achieved. If the wearable motion sensors had performed to the manufacturers specifications out of the box, if the single frequency global positioning system (GPS) receiver had provided reliable trajectory information without the need for custom fusion algorithms to be developed, and if the pressure sensitive insoles had not suffered from hysteresis, then more progress may have been made towards satisfactorily answering the thesis objective.

However, every cloud has a silver lining. The problems encountered provided many opportunities. A new prototype motion capture system was developed, a camera-less motion capture system called Fusion Motion Capture (FMC) that combined GPS and inertial measurement units (IMUs) attached to the athlete and pressure sensitive insoles. The FMC development and analyses presented throughout the thesis provide a novel contribution to the body of knowledge at both the theoretical and practical level.

Practically it has now become possible to capture the performance of an athlete through an entire ski racecourse. Theoretically and experimentally the new fusion algorithms show there may be more suitable alternatives to the popular Kalman filter style signal processing commonly used to try and achieve accurate measurements from wearable motion capture system data. Furthermore, the research from both inline slalom skating and giant slalom ski racing has provided a framework and some measured physical boundary constraints during a performance, such as the maximum inclination angle of an athlete. In the future, with additional development and more race data, the work in the thesis could be used to progress closer towards the optimisation of athlete movement in alpine ski racing.

The research has resulted in the development of novel methods, such as data-driven animations and colour coded force vector analysis that were successful in communicating the research results to athletes and coaches as well as biomechanists. The research has provided some useful practical conclusions, but these conclusions come with two caveats. They are largely based on data from only two runs by a single elite athlete using the FMC system. Also the accuracy of the FMC system has yet to be explicitly determined on snow.

The practical conclusions for coaches and athletes are:

- The optimum turn radius range for passing between the gates on the giant slalom racecourse is between 15 metres and 25 metres. The optimum turn radius increases with both increasing speed and snow slope. .
- Optimum physical inclination angles from the vertical are generally between 45º and 70º. Postural balance is maintained by leaning into the turns and so more inclination is required as speed increases.
- A good match between the ski design, the course, and the athlete should result in both a faster and safer performance.
- The optimum race strategy is a trade off between tighter turns that result in shorter path lengths and more open turns that allow for faster turning speeds and also result in more acceleration earlier in the turn while travelling closer to the fall line.
- Athletes may prefer to make identical turns in different parts of the course but this does not produce the fastest course time. Athletes might improve through practise dedicated to taking each course gate differently.
- Reduction of snow resistance is of similar importance as the reduction of wind drag.
- At moderate speeds (<20m/s) and on moderate terrain (<25°) athletes may use internal muscle work, through the techniques of lateral projection and pumping, in order to increase speed.
- Dry land training should include exercises that require athletes to maintain postural balance while both subjected to both destabilising perturbations and performing lifts.

9.1. A critical review of the research achievements

The conciseness of the research objective disguised the complexity of the objective and so it was separated it into five milestones that could be used to assess overall progress.

1. To accurately capture the motion of ski racing over a complete race course

The first research milestone was satisfactorily achieved. The solution was a new wearable motion capture system called Fusion Motion Capture (FMC). FMC combines inertial measurement units (IMUs) and pressure sensitive insoles with a global positioning system (GPS). The validation process was not straightforward because both body segment orientation and global trajectory had to be investigated and there was no practical *gold standard* available for comparison.

In the introduction, Chapter 1, it was discussed that traditional 3D optical motion capture and analysis systems may not be the most suitable tool for the biomechanical analysis of alpine ski racing. Some of the papers researched raised various issues including the requirement for data smoothing (Förg-Rob & Nachbauer, 1988) and the extensive post processing time required for manual digitisation (Yeadon, 1989). In addition, using the available video

technology it was only practical to capture the motion through parts of a course. Even though the relationship between consecutive turns has been acknowledged (Supej, et al., 2005) and the author of this thesis has also suggested that the outcome of a race depends on the performance of multiple sequential turns through the entire course (Brodie, et al., 2008b).

„What measurement accuracy is sufficient for ski racing?" For a modern laboratory based 12 camera motion analysis system, the 95% confidence interval for thigh segment flexion/extension angle is approximately ±6º (Schwartz, et al., 2004). On snow measurements are likely to be less accurate than measurements made in a controlled laboratory and so 6° RMS was chosen as the benchmark. Until the development of FMC there was no practical alternative to optical motion capture for alpine ski racing.

A commercial wearable motion capture system based on inertial measurement units (IMUs) containing multiple accelerometers, gyroscopes and magnetometers was compared to optical motion capture in a laboratory in Chapter 2. The tests revealed the commercial system in 2005 was probably unsuitable for the motion capture of alpine ski racing. Among other issues, orientation errors of over 30º were observed for a simple pendulum swing and so custom data fusion algorithms were developed. The new data fusion algorithms gave an error of less than 2° RMS for the same rapid pendulum swings using the original system sensors in the laboratory. This was similar to the accuracy reported for trunk inclination during slow movements (Luinge, 2002) and well within the 6° benchmark. The development of these custom data fusion algorithms was a significant step towards meeting the first research milestone.

GPS data were then fused with the IMU data in order to obtain a more accurate global trajectory and also more accurate body segment orientation measurements. In Chapter 3 results were reported from tests of the prototype FMC system at Coronet ski area, in New Zealand, in 2005. It was the first time the motion of an athlete through a complete free ski run had been captured and it was another significant step forward. The initial validation process by subjective visual comparison of FMC data to video frame data was discussed. Using this method the accuracy of the first prototype FMC system was estimated to be less than 5° for body segment orientation. The visual comparison was made principally by observation of the ski motion. A 5º error in ski orientation measurement would cause the ski tip to be displaced around 0.08m and would be expected to manifest in some visual artefact such as the ski"s crossing. No such visual artefacts were observed in the FMC data. It was however discovered that the global trajectory error for an athlete skiing through the giant slalom course was both greater than the course gate spacing and greater than the specified accuracy of the receiver (15m RMS). Further work therefore was required to obtain an accurate global trajectory..

The second version of the FMC algorithm was developed and tested using a wand with three markers attached to it in Chapter 4. The tests were scaled to a laboratory situation using simulated GPS data. The fusion process was able reduce the simulated GPS noise three fold, which, if scaled up to the ski area corresponded to an estimated RMS location error of between 3 and 4m. Compared to the gate spacing of around 30m, the relative error for

location was estimated to be around 13%. This was another step forward, but the estimated location error from the simulated GPS noise appeared to still be too large for ski racing and so further work was still required.

The motion of an athlete inline skating through an indoor slalom course was captured with the prototype FMC system in Chapter 5. GPS data were unavailable and so approximate gate timings, recorded using frames from a handheld video camera, were used as a substitute. A variability analysis of the athlete‟s global trajectory revealed that it was likely the error in trajectory while skating between the course gates was less than 0.05m, which was much lower than the resolution of the simulated GPS data (0.18m) based on the video frame rate. The improved accuracy highlighted how the fusion algorithm produced results that were significantly more accurate than the raw data. The encouraging result suggested that future skiing data collected by FMC might be accurate enough for a meaningful biomechanical analysis of alpine skiing. The FMC algorithm was able to exploit the properties of the signals from IMUs and simulated GPS, fusing them without the need for post-processing low-pass filtering and so ensured maximum derived signal bandwidth.

In 2006 the revised prototype FMC system was taken to the Turoa ski area, Mount Ruapehu New Zealand, where the motion of a New Zealand national team athlete racing through a giant slalom course was captured. FMC estimates of gate contact times were compared with video estimates of gate contact times. The estimated error for global trajectory was reported to be 0.7m. With additional improvements, it may be possible to further reduce the trajectory error for alpine ski racing as was shown for the inline skating data.

The estimated errors of less than 6º for limb orientation and 0.7m for global trajectory demonstrate that it is now practical to accurately capture the motion of alpine ski racing over a complete race course. Compared to laboratory based optical motion analysis data the global trajectory error may appear large, but on snow field measurements are expected to inherently contain more error. The FMC position data are derived from other information and so are expected to contain more error than the direct FMC velocity and acceleration data. The nature of the error present in FMC data (low frequency drift) is different from the nature of the error expected from traditional optical motion capture analysis (high frequency noise and systematic errors) and so a direct comparison of errors between the two different motion capture systems is difficult. FMC has the additional advantage over optical motion capture system in that multiple runs through race courses can be quickly captured and analysed providing a data rich environment from which to draw conclusions.

2. Measure or model the different forces exerted on the athletes through their interactions with their environment

The second milestone was satisfactorily achieved, but without three-component force platforms between the bindings and skis it was not possible to explicitly determine the accuracy of the forces. For the first time, however, it was possible to investigate

simultaneously all the external forces responsible for ski race outcomes over a complete ski race training course. Four main types of external forces acted on the athlete including; gravity, wind drag, snow resistance and ground reaction forces. The resulting calculated forces were superimposed upon the data driven animation (Video 9.1). The data driven animation shows the calculated forces appear plausible.

Video 9.1: Appendices\FMC Video\Ruapehu_R3_Force_RScan.avi

The current FMC system was not capable of directly measuring all of the forces and so some forces were modelled in Chapter 7. The model parameters were chosen to minimise the residual of a force balance based on the athlete"s measured CoM trajectory. A velocity and normal force dependant equation proposed by Kaps was used for the ski/snow sliding friction (Kaps, et al., 1996). This dissipative force was re-named snow resistance because the equation combined the effects of the ski sliding over the snow and the ski displacing the snow. Wind drag force was modelled using the athlete"s measured changing cross sectional area which improved accuracy.

Both the wind drag and snow resistance models coefficients were unfortunately found to be dependent on velocity and so were highly negatively correlated. The solution to this problem was to optimise first for the wind drag coefficient, then assume it was constant, and finally solve for the snow resistance coefficient over different velocity windows. The optimised wind drag coefficient resulted in a stance dependant wind drag area of between $0.24m^2$ and $0.33m^2$, which agreed with values from literature (Barelle, et al., 2004). The optimised snow resistance coefficients also agreed with values from research (Kaps, et al., 1996).

The results were surprising because they suggested that the snow resistance forces were greater than the wind drag forces through the giant slalom course. This finding contradicted previous research that implemented traditional ski/snow sliding friction models and was based on measurements made in laboratories (Barelle, et al., 2004). The finding however agreed with force plate data from Lüthi (Lüthi, et al., 2005).

There were two types of error present in the calculated forces, high frequency noise error and systematic error. The possibility of high frequency noise in the FMC data propagating into the calculated ground reaction forces was discussed in both Chapter 5 for inline skating and in Chapter 8 for skiing.

The error present in the inline skating data while skating between the gates was assumed to be about 25N based on the high frequency content of the FMC force data. There was a possibility that 25N was an overestimation because the skating motion must have contained some actual high frequency content. The error analysis of skiing was more sophisticated and it was based on the measured GPS velocity residuals, the reported properties of the IMU accelerometers, and the estimated IMU orientation error. The resultant forces calculated from the FMC data of giant slalom was estimated to contain 6% error or up to 110N of noise. This was a significant improvement on the force data of skiing obtained in the past from optical

motion capture systems. The unfiltered acceleration error for FMC ($1.2ms^{-2}$) was four orders of magnitude less than the unfiltered acceleration error reported for an optical analysis system of $10{,}000ms^{-2}$ (Nachbauer, et al., 1996).

The presence of 6% error (up to 110N) in the resultant forces from the skiing data is likely to have very little significance for the analyses presented in this thesis. Inspection of the colour coded force vector analysis (Figure 9.2) shows that the forces were consistent with the athlete"s centre-of-mass trajectory. The forces are directed into each turn and there are distinct periods of acceleration and breaking which appear to be unaffected by any measurement noise.

Figure 9.2: Performance feedback using a colour coded force vector diagram

As well as noise, systematic errors in the derived forces may also have been present in the data. They might have resulted from the wind drag force and snow resistance force model coefficients containing biases. Any systematic force errors would not have affected the analysis of the race outcome presented in Chapter 8, but they could have slightly altered the calculated relative importance of the different external forces.

In summary, the different external forces acting on the athlete were successfully measured and modelled. Errors were present, but appear to have had no significant affect on the analyses of giant slalom ski racing and the conclusions presented in this thesis.

3. To analyse complex whole body motion through a large 3D volume

The third milestone was satisfactorily achieved through the development of methods that reduced the reliance on kinematic obsession. In alpine ski racing style does not decide race outcome, race outcome is decided by the minimum time. The external forces acting on the athlete completely determine trajectory and therefore they explicitly determine the outcomes of races.

In Chapter 8 two runs by the same athlete were compared (run 3 and run 5) through a ten-gate giant slalom training course. The analysis showed that although the virtual SkiX lead changed several times, the athlete was 0.14 seconds faster in run 5 (orange avatar, Video 9.2). Interestingly, gate split times showed that if gates 4, 5 or 6 had been analysed in isolation it would have been erroneously concluded that run 3 was the better run. The key differences between the two runs were determined by a combination of different analyses including; virtual gate split times, speed profiles, trajectory analysis, colour coded force vector diagrams, power analysis and energy analysis.

The final lead change occurred between gates 8 and 9 but the cause can be traced back to differences in technique about gate 6. It was discovered that positive ground reaction force power, about gate 6 in run 5, was the mark of the exceptional turn by the athlete. Positive ground reaction force power meant that the athlete was accelerating though the turn as a result of good technique. In other cases, such as about gate 4 in run 3, where the lead changed, the trajectory analysis showed it was the tighter turn and therefore shorter path that was the key difference.

Video 9.2: Appendices\FMC Video\SkiX_Final.avi

Once the key gates to race outcome had been identified it was possible to drill down and look at both the kinetic and the kinematic differences between the athletes performance. An example of this was done for gate 6, in run 5 (the winning run) where the turn was characterised by a smooth and early build up of ground reaction forces. The athlete engaged his ski edges with the snow surface well before the gate and turn apex, using a combination of high inclination from the vertical and abduction of the outside hip to increase his outside ski/snow angle.

The energy analyses offered insights into the performance outcomes of the athlete‟s complex whole body motion through the race course. An energy analysis showed that:

- Over the course snow resistance did approximately three times more negative work than wind drag.
- Gravity did the most positive work as the athlete descended the slope.
- Ground reaction forces did both positive and negative work depending on the athlete‟s technique.

The energy analyses suggested it was differences in the ground reaction forces balanced with the choice of „optimum" global trajectory, both a direct result of the athlete"s technique, which had the most effect on giant slalom race outcome.

A power analysis of the ground reaction forces suggested that the athlete might be using internal muscle work to increase velocity at some parts of the race course. How the athlete could use the accelerative turn techniques of lateral projection and pumping were also investigated over the changing effective snow slope.

The net joint torques and net modes of muscle action were calculated for the athlete skiing through the giant slalom course. The knee extensor torque experienced by the athlete (<200Nm) were well within the maximum isometric extensor torques (300-600Nm) presented in a study by Herzog (Herzog & Read, 1992). The net joint torques fluctuated rapidly about all axes (flexion/extension, abduction/adduction and internal/external rotation) and all modes of action (isometric, concentric and eccentric). This information could be used to design sport specific strength training programs and equipment such as ski boots or safety release bindings.

The analysis of the complex whole body motion during giant slalom ski racing revealed some interesting findings. Many steps were made towards answering the research objective. There were no apparent comparable analyses available in literature with which to compare most of the research. In the future therefore further experiments should be completed in order to confirm the findings.

4. To present the analysis in a way intuitive to the athlete

The fourth milestone was comprehensively achieved. In the introduction it was discussed that, before FMC, it was not practical to complete the biomechanical analysis of athlete movements through a complete racecourse because of resource and time constraints. There were therefore no templates to use as a basis for presenting the data. Through the research it has become practical to analyse a complete run, and the results may now be presented to the athlete soon after each run.

Throughout the thesis visualisation software was developed in order to present the data intuitively to the audience. The first skiing data were presented in Chapter 3 as a series of stick figures, very similar in appearance to Marey"s photographs of a white heron from 1884 reproduced in Chapter 1. In order to display the forces acting on the athlete during skiing and the effects of the forces, colour coded force vector diagrams were developed in Chapter 3. The colour coded force vector diagrams successfully enhanced the athlete"s ability to distinguish between accelerating and braking turns.

Progress was made in Chapter 5 using the inline skating data. Data driven animations were developed. The first data driven animations were similar in appearance to the animation of a galloping horse produced by Muybridge in 1877. Significant improvements were soon made to the data driven animations that allowed the captured data to be viewed from different virtual camera positions. Camera position and camera movements were chosen to simultaneously communicate both the large scale global movements through the inline skating course and the local limb movements. The external forces of wind drag, ground reaction force, bearing friction and gravity were then superimposed on the data driven animations in order to provide additional information. This may be the first time such a data driven animation has been rendered in an attempt to communicate some of the complex biomechanics associated with inline skating.

The colour coded force vector diagrams were also further developed in Chapter 5. The individual ground reaction forces under each skate were plotted and colour coded in order to distinguish periods of acceleration and braking. Other analyses were also developed for the inline skating data and presented as figures, including; friction cones, power analysis, energy analysis and variability analysis. These figures provided insights into the complex and large data set provided by the prototype FMC system.

In Chapters 6, 7 and 8 the data visualisations from the inline skating experiment were further improved and extended for alpine ski racing. Two examples of the effective visualisation methods developed are colour coded force vector analysis (Figure 9.2) and data driven animations with speed, external forces, and powers displayed (Video 9.1). Other figures produced for the ski racing data analysis include; leaning angles, force inclination, turning radii, changes in effective snow slope and ski edging angles.

Many of the data visualisations presented in this these were developed specifically for the requirements of the biomechanical analysis of alpine skiing, but could also have wider applications. Without the development of these data visualisations it would have been difficult to analyse and interpret the large data sets provided by the prototype FMC system.

5. ***To optimise the athlete's essential movements through simulations based on athlete specific performance parameters***

The fifth milestone was not completely realised, but through the research presented in this thesis the framework has been laid to build athlete specific simulations in the future. Such simulations could be used to calculate the athlete"s optimum trajectory and technique through a course. The simulations could also be used to predict how proposed changes in FIS regulation might affect athlete safety and spectator enjoyment.

In the introduction the question was posed: „What makes one athlete the fastest, is it science or art?" Previous work from literature focused on the brachistocrone problem and showed that

the fastest time between gates was not a straight line, but that the athlete should start out heading down the fall line accelerating early (Hirano, 2002; Reinisch, 1991). These previous works support the „going straight turning short" race strategy but unfortunately produce improbable trajectories because infinite acceleration is required at the turn apex (Figure 1.5).

In Chapter 5 multiple laps through an inline skating slalom course were analysed because of the similarities to slalom skiing. A variability analysis was used to investigate possible control parameters the athlete might use to construct a global trajectory. On the global level the athlete appeared to aim for checkpoints, generally located about a metre before each gate in order to set up for each turn. The global „checkpoint" was combined with either a target turn radius or a target inclination angle, which resulted in the athlete passing safely between the gates.

The FMC data from inline skating were then used to drive athlete specific simulations of the athlete's global trajectory. The only mathematical simulations of optimal global trajectory completed in this thesis. The purpose was to find a minimum time trajectory through the course. The best simulated trajectory was a 20% improvement on the athlete's actual performance and was paradoxically achieved by skating slower, but with tighter turns.

Future simulation of optimum skiing trajectories would require a more complicated model than the model used for the inline skating experiment. The FMC data was used to investigate some limits to possible simulation model control parameters. These general limits also provide useful information to athletes wishing to optimise their race strategy.

- Optimum turn radii for passing between gates in giant slalom are between 15 and 25 metres, increasing with both increasing speed and increasing snow slope.
- Optimum physical inclination angles from the vertical are generally between 45º and 70º. Postural balance is maintained by leaning into the turns and so more inclination is required as speed increases. Once race pace is reached the physical inclination angle appears to be limited by a maximum ski/snow edging angle.
- Ski design may affect optimum race strategy.

The existence of an optimum radii range challenges the traditional race strategy of „going straight turning short" supported by the previous simulation research from literature. The research shows that the athlete's shortest path, although sometimes the fastest path, was not always the fastest path. The findings related to the optimum trajectory through multiple gates in this thesis were different to previous works by Hirano and Reinisch for single turns and so additional experiments should be conducted in order to confirm the results.

9.2. Final conclusions

The research shows Stenmark's comments, „Many skiers do not take advantage of the way modern equipment has been designed to facilitate carving turns" (Stenmark, 1990), do not hold true for today's best athletes. The research demonstrates today's highly skilled athletes

can make use of the way modern skis are designed to facilitate racing turns, but also shows how scientific analysis can be used to improve performance.

Key conclusions from the research are:

1. FMC is more suitable than traditional optical motion capture systems for the biomechanical analysis of alpine ski racing because:
    a. The athlete‟s motion through complete race courses can be captured and used to determine race performance.
    b. FMC exploits the properties of the signals from IMUs and GPS, fusing them without the need for post low pass filtering and so ensures maximum derived signal bandwidth.
    c. FMC is less time consuming as there is no manual digitisation and checking.

2. Laboratory experiments show the accuracy of FMC is stable and relatively independent of both the type of motion and its duration (unlike IMU-based systems that were available in 2005). However, the prototype FMC system accuracy has yet to be explicitly determined on snow and in the future a way of doing this should be devised.

3. FMC directly measures accelerations and velocities which are closely related the forces that affect performance. The forces calculated from FMC data do not require low-pass filtering and contain several orders of magnitude less noise than the unfiltered forces calculated from optical motion capture data.

4. Snow resistance in skiing appears to be at least equal in importance, if not more important than wind drag. The apparent velocity dependency of snow resistance contradicts results from laboratory based ski/snow sliding models.

5. Gravity does the most work in a ski race, acting to increase athlete speed, but it is ground reaction forces (a direct consequence of athlete technique) that decides the outcome of a race.

6. On moderate terrain, when the ski and CoM trajectories are diverging, athletes may increase speed by lateral projection and pumping.

7. During a giant slalom run athletes experience high and rapidly fluctuating torques about all three axes of the lower limbs and lumbar spine. This information might be useful in designing training programs and ski equipment in order to both reduce injuries and improve performance.

8. The data visualisations and data analyses developed are useful tools for presenting complex biomechanical analyses of ski racing in a way that is intuitive to athletes, coaches and biomechanists.

9. The research disproved the „going straight turning short" race strategy. The research showed that for the athlete on the giant slalom course an optimum turning radius range between 15 and 25 metres existed, which corresponded to a physical inclination angle of between 45º and 70º. Generally athletes should use more open turns as the speed increases and as the terrain becomes steeper.

Until more data is collected, it is not known if these results collected from two runs of a single athlete at moderate speeds on moderately sloping terrain can be generalised to all athletes on all terrain. In the future biomechanical analyses of alpine ski racing performance will be able to investigate previously unanswerable questions using multi-dimensional data from complete race courses. In the future it may become possible to ***optimise athlete movement in alpine ski racing***.

9.3. Future research

In October 2007 more racing data were collected from another athlete at Mt Ruapehu with an improved FMC system. Steeper terrain was used and a purpose built rig was skied through the course to complete a more accurate survey of the gates. The purpose built rig was capable of measuring fluctuations in terrain slope between the gates and the cross slope. This research should help to reduce the FMC global trajectory errors and will be presented in the future.

In December 2007 the FMC system was taken to Italy and research was carried out sponsored by Nordica (a ski equipment company) in collaboration with the University of Padova. In this set of experiments electromyography (EMG) and ski bending data were collected simultaneously with the FMC data. The collaboration continues.

Future development of the FMC algorithm could focus on making location as accurate as acceleration and velocity data. In addition a prototype self-calibration procedure has been partially developed to construct more accurate body models. In the future the body segment to IMU calibration might be carried out using a series of set movements on a force platform. The preliminary results suggest this should give enough data to determine both the IMU to body segment calibration and the inertial properties of the athlete"s body segments.

If FMC had additional data from miniature force platforms attached between the skis and boots then it might be possible to separate the ground reaction forces from the snow resistance forces and the wind drag forces. It then might be possible to determine the parameters for more detailed models of snow resistance and wind drag using real race data. The effects of the changing Reynolds number on wind drag coefficient and the affects of ski/snow edging angle and ski bending on snow resistance could also be further investigated.

FMC data could be used to improve safety of ski racing by providing knee loading data for the reduction of knee injuries. Proposed changes in equipment and course regulations could

be analysed to ensure the most accurate information about athlete safety was used in the decision making process.

The algorithms developed for the optimisation of race strategy in inline skating could be improved and adapted for skiing. Firstly, the constant radii turns need to be replaced with a model that incorporates the changing inclination angle of the athlete. Secondly, additional degrees of freedom are required to optimise the angles of attack of the skis. In skiing the athlete often regulates speed by increasing the angle of attack of his skis and skidding. The ski/snow contact is not well modelled by the point contact used for the skating model because the ski trajectory of least resistance depends at least on the side cut radius, the ski/snow angle and the ski angle of attack. However, data collected in this thesis provides a useful set of ball-park parameters that can be used to define boundary conditions in any future simulation work of ski racing.

Appendices

A. Example Code

Example code written and adapted using MATLAB and Excel are available on the supplementary CD in a folder titled Example Code. Three examples of code and one Excel spreadsheet are included. Most of the work was rapid prototyping of the system and some of the code is quite untidy.

The code may be used so long as this thesis and the code source is cited. Any adaptations made to the code should preserve the comments in the header. Under the same conditions the Biomechanical Man avatar may also be used

Example 1, the Excel spreadsheet

Title: 3D Anthropometry

The spreadsheet works through the calculations required to calculate 3D joint centres from the measured locations of a subject‟s bony landmarks. The anthropometric measurements required are from a subject sitting in our custom measurement frame. More details are provided in Section 4.3 on page 65 and on the accompanying CD (**Appendices/Example Code/Biomechanical_Man/More about the Biomechanical Man.pdf**).

Example 2, The Pendulum

This was the first code written in order to track the motion of a pendulum swing over short time periods. Both the code and example data are provided. Data from an IMU attached to the pendulum are provided. The code processes the IMU data using the simple bi-directional integration discussed in Section 2.2 on page 29. The code uses two iterations to solve for the pendulum swing. The output is in quaternions, but global acceleration, estimated from the IMU orientation and the accelerometer data is also plotted. The bi-directional filter removes the drift from the gyroscope bias over short periods of action.

MATLAB is required to run the code. Set the folder Pendulum as the MATLAB current directory and run the m-file titled Pendulum_Example.m. If the code does not work it may be necessary to change the code on lines 16-18 to point to the location of the pendulum folder.

Example 3, Nancy

This code animates a body model called Nancy in real time using ten IMUs attached to a subject to capture the motion data required to drive the avatar. More details about the code development and assumptions made can be found on the accompanying CD (**Appendices\Example Code\Nancy\More about Nancy.pdf**).

To run this code 10 IMUs, an XBus and the COM object supplied by XSens are required; it works with MATLAB 6.5 or later. This code contains the original version supplied by XSens, with some changes made so 10 IMUs could be attached and so the IMUs could be attached to to any part of any body segment.

MATLAB is required to run the code. Set the folder Nancy as the MATLAB current directory and run the m-file titled XM_Nancy_V2.m by typing in the command window Nancy_V2(port), were „port" stands for the serial port number that the XBus is connected to. If the code does not work it may be necessary to attach 10 IMUs to an XBus and then attach the XBus to the computer. The XSens COM object is also required.

Example 4, The Biomechanical Man

When the code is run the biomechanical man will be rendered based on the measurements in the anthropometric frame from the previous Excel spreadsheet. Both body segment centre of mass and whole body centre of mass will be visualised. More details are provided in Section 4.3 on page 65. More details about the code development and assumptions made can be found on the accompanying CD (**Appendices/Example Code/Biomechanical_Man/More about the Biomechanical Man.pdf**).

MATLAB is required to run the code. Set the folder Biomechanical_Man as the MATLAB current directory and run the m-file titled Biomech_Man_Example.m, it may be necessary to change the **`Anthro_File`** to point to the location of the Biomechanical_Man folder on the computer first.

B. Inline Skating

Inline skating supplementary material can be found on the accompanying CD (**Appendices\Inline skating supplement.pdf**). The material may be useful to those readers interested in inline skating biomechanics, or comparing skating to skiing, or more technical details, or extending some parts of the experiments, or further developing wearable motion capture systems. The table of contents of the supplementary electronic material is provided below.

Bibliography

Angeloni, C., Riley, P. O., & Krebs, D. E. (1994). Frequency content of whole body gait and kinematic data. *IEEE Transactions on Rehabilitation Engineering, 2*(1), 40-46.

Bachmann, E. B. (2000). *Inertial and magnetic tracking of limb segment orientation for inserting in synthetic environments.* Unpublished PhD, Naval Postgraduate School, Monterey, CA.

Barelle, C., Ruby, A., & Tavernier, M. (2004). Experimental Model of the Aerodynamic Drag Coefficient in Alpine Skiing. *Journal of applied biomechanics, 20*, 167-176.

Bernstein, N. (1967). *The Co-ordination and Regulation of Movements*. London, England: Pergamon Press.

Brandenberger, H. (1934). *Skimechanik*. Rapperswil: RaVerlad.

Brodie, M. A., Walmsley, A., & Page, W. (2005). *Optimisation of alpine ski race technique using sensor fusion.* Paper presented at the New Zealand Sports Medicine + Science Conference, Queenstown, New Zealand.

Brodie, M. A., Walmsley, A., & Page, W. (2006a). *3D Anthropometry, the Biomechanical Man, and Fusion Motion Capture.* Paper presented at the Sports Medicine + Science Conference, Auckland, New Zealand.

Brodie, M. A., Walmsley, A., & Page, W. (2006b). *3D Anthropometry, the Biomechanical Man, and Fusion Motion Capture.* Paper presented at the 6th Australasian Biomechanics Conference (ABC6), Auckland, New Zealand.

Brodie, M. A., Walmsley, A., & Page, W. (2007). Fusion Integration: COM Trajectory from a Force Platform. *Journal of Applied Biomechanics, 23*, 310-315.

Brodie, M. A., Walmsley, A., & Page, W. (2008a). Dynamic accuracy of inertial measurement units during simple pendulum motion. *Computer Methods in Biomechanics and Biomedical Engineering, 11*(3), 235-243.

Brodie, M. A., Walmsley, A., & Page, W. (2008b). Fusion motion capture: a prototype system using inertial measurement units and GPS for the biomechanical analysis of ski racing. [Research]. *Journal of Sports Technology, 1*(1), 17-28.

Brodie, M. A., Walmsley, A., & Page, W. (2008c). Fusion Motion Capture: Can Technology be used to Optimise Alpine Ski Racing Technique. In F. K. Fuss (Ed.), *The Impact of Technology on Sport 2* (pp. 825-831). Leiden, The Netherlands: Taylor and Francis.

Brodie, M. A., Walmsley, A., & Page, W. (2008d). The Static Accuracy and Calibration of Inertial Measurement Units (IMUs) for 3D Orientation. *Journal of Computer Methods in Biomechanics and Biomedical Engineering, 11*(6), 641-648.

Brown, A. (2005). GPS/INS uses low cost MEMS IMU. *IEEE A&E Systems Magazine*(September), 3-10.

Broxmeyer, C. (1964). *Inertial Navigation Systems*. New York: McGraw Hill.

Casolo, V., Lorenzi, V., Vallatta, A., & Zappa, B. (1997). Simulation techniques applied to skiing mechanics. In E. Müller, H. Schwameder, E. Kornexl & C. Raschner (Eds.), *Science and Skiing* (pp. 116-130). London: E & FN Spon.

Coleman, T. F., & Li, Y. (1994). On the Convergence of Reflective Newton Methods for Large-Scale Nonlinear Minimization Subject to Bounds. *Mathematical Programming, 67*(2), 189-224.

Coleman, T. F., & Li, Y. (1996). An Interior, Trust Region Approach for Nonlinear Minimization Subject to Bounds. *SIAM Journal on Optimization, 6*, 418-445.

Ducret, S., Ribot, P., Vargiolu, R., Lawrence, J., & Midol, A. (2005). *Analysis of downhill ski performance using GPS and grounding forces.* Paper presented at the Science and Skiing 3, Aspen, USA.

Dumas, R., Cheze, J., & Verriest, P. (2007). Adjustments to McConville et al. and Young et al. body segment inertial parameters. *Journal of Biomechanics, 40*, 543-553.

Federolf, P., Scheiber, P., Rauscher, E., Schwameder, H., Luthi, A., Rhyner, H., et al. (2007). Impact of skiers actions on the gliding times in alpine skiing. *Scandinavian Journal of Medicine and Science in Sports*.

Förg-Rob, W., & Nachbauer, W. (1988). Use of Spline-Functions in the Smoothing of Film Data for Slalom Ski Racers. *International Journal of Sports Biomechanics, 4*, 166-177.

Forrsythe, G. E., Malcolm, M. A., & Molar, C. B. (1976). *Computer Methods for Mathematical Computations*: Prentice-Hall.

Giakas, G., & Baltzopoulos, V. (1997). Optimal digital filtering requires a different cut-off strategy for determination of higher derivatives. *Journal of Biomechanics, 30*(8), 851-855.

Giansanti, D., Maccioni, G., Benvenuti, F., & Macellari, V. (2007). Inertial measurement units furnish accurate trunk trajectory reconstruction of the sit-to-stand manoeuvre in healthy subjects. *Medical and Biological Engineering and Computing, 45*(10), 969-976.

Hatze, H. (1966). Die biomechanishe und physikalische Grunglegung der Handschrägfahrstellung in Schilauf. *Leibesübung-Leibeserziehung, 20*(9), 1-3.

Herzog, W., & Read, L. (1992). External Loading at the Knee Joint for Landing Movements in Alpine Skiing. *Journal of applied biomechanics, 8*, 62-80.

Hirano, Y. (2002). Alpine ski racing: Use of optimal control theory to determine the 'quickest' line between two gates. In S. Ujihashi & S. J. Haake (Eds.), *The Engineering of Sport* (pp. 400-407): Blackwell Science.

Howe, J. (1983). *Skiing Mechanics*. Laporte, CO: Poudre.

Ismail, A. R., & Asfour, S. S. (1999). Discrete wavelet transform: a tool in smoothing kinematic data. *Journal of Biomechanics, 32*, 317-321.

Kalman, R. E. (1960). A new approach to linear filtering and prediction problems. *Journal of Basic Engineering*, 35-45.

Kane, T. R., Hayes, W. C., & Priest, J. D. (1974). Experimental determination of forces exerted in tennis play. In R. C. Nelson & C. A. Morehouse (Eds.), *Biomechanics IV* (pp. 284-290). Baltimore: University of Park Press.

Kaps, P., Nachbauer, W., & Mossner, M. (1996). Determination of kinetic friction and drag area in alpine skiing. *Ski Trauma and Skiing Safety ASTM, 10*, 165-177.

Kroll, J., Schiefermuller, C., Birkalbauer, J., & Muller, E. (2005). Inline-skating as a dry land modality for slalom racers - electromyographic and dynamic similarities and differences. In E. Muller (Ed.), *Science and Skiing 3* (pp. 76-86). Oxford: Meyer & Meyer Sport (UK) Ltd.

LeMaster, R. (1999). *The Skiers Edge*. Auckland: Human Kinetics.

Lind, D., & Sanders, S. P. (1997). *The physics of skiing at the triple point*. New York: The American Institute of Physics.

Luinge, H. J. (2002). *Inertial sensing of human movement.* Unpublished PhD, University of Twente, Enschede, the Netherlands.

Luinge, H. J., & Veltink, P. H. (2005). Measuring orientation of human body segments using miniature gyroscopes and accelerometers. *Medical and Biological Engineering and Computing, 43*, 273-282.

Luinge, H. J., Veltink, P. H., & Baten, C. T. M. (1999). Estimating orientation with gyroscopes and accelerometers. *Technology and health care, 7*, 455-459.

Luinge, H. J., Veltink, P. H., & Baten, C. T. M. (2007). Ambulatory measurement of arm orientation. *Journal of Biomechanics, 40*(1), 78-85.

Lüthi, A., Federolf, P., Fauve, M., Oberhofer, K., Rhyner, H., Ammann, W., et al. (2005). Determination of forces in carving using three independent methods. In E. Müller (Ed.), *Science and Skiing 3*. Oxford: Meyer and Meyer Sport.

Macey, K. E. (2000). *Applications of Wavelet Transforms to Analysing Medical Signals.* Unpublished PhD, University of Canterbury, Christchurch, New Zealand.

Margane, J., Trzecinski, L., Babiel, S., & Neumaier, A. (1998). *A mechanical apparatus executing turns on carver skis.* Paper presented at the XVI ISBS Symposium, Konstanz.

Matijevec, V. (2003). *Path of the masters, to ski wisely*. Slovenia: Marbona.

Matsuda, K. (2003). Biomechanical analysis. (Review). *Chronicle of physical education in higher education, 14*(3), 12.

Möser, G. (1957). *Untersuchung der belastungsverhältnisse bei der alpinen skitechnik.* Martin Luther University, Halle-Wittenberg.

Müller, E. (1994). Analysis of the biomechanical charateristics of different swinging techniques in alpine skiing. *Journal of sports sciences, 12*, 261-278.

Müller, E., & Schwameder, H. (2003). Biomechanical aspects of new techniques in alpine skiing and ski-jumping. *Journal of Sports Sciences, 21*(May), 679-692.

Muybridge, E. (1887). *Animal Locomotion*. Phyladelphia: University of Pennsylvania.

Nachbauer, W., & Kaps, P. (1994). Loading at the knee joint for straight running over moguls in alpine skiing. *Journal of Biomechanics, 27*(6), 679.

Nachbauer, W., Kaps, P., Nigg, B., Brunner, F., Lutz, A., Obkircher, G., et al. (1996). A video technique for obtaining 3D coordinates in alpine skiing. *Journal of applied biomechanics, 12*, 104-115.

Pfau, T., Witte, T., & Wilson, A. M. (2005). A method for deriving displacement data during cyclical movement using an inertial sensor. *Journal of Experimental Biology, 208*, 2503-2514.

Pozzo, R., Canclini, A., Cotelli, C., & Baroni, G. (2005). 3-D kinematics and kinetics of G-Slalom in elite skiers at Val Badia World Cup race in 2002. In E. Muller (Ed.), *Science and Skiing 3* (pp. 76-86). Oxford: Meyer & Meyer Sport (UK) Ltd.

Quinn, T. P., & Mote, C. D. (1992). Prediction of the loading along the leg during snow skiing. *Journal of Biomechanics, 25*, 609-625.

Raschner, C., Schiefermuller, C., Zallinger, G., Hoffer, E., Müller, E., & Brunner, F. (2001). *Carving turns versus traditional parallel turns - a comparative biomechanical analysis.* Paper presented at the 2nd International Congress on Science and Skiing, Salzburg.

Reed, M. P., Manary, M. A., & Schneider, L. W. (1999). *Methods for measuring and representing automobile occupant posture.* Warrendale, USA: SAE Technical Paper Series, Society of Automobile Engineers.

Reinisch, G. (1991). A Physical Theory of Alpine Ski Racing. *Spektrum Sportwissenschaft, 1*(27).

Schwartz, M. H., Trost, J. P., & Wervey, R. A. (2004). Measurement and management of errors in quantitative gait data. *Gait & Posture, 20*, 196-203.

Senner, V., Lehner, S., Wallrapp, W., & Schaff, P. (2000). *The boot induced ACL rupture in alpine skiing: current knowledge and feasible solutions.* Paper presented at the 2nd International Congress on Science and Skiing, Salzburg.

Shimbo, M. (1971). *Friction of snow on ski soles, unwaxed and waxed*. Tokyo: Hitachi.

SiRF Technology Inc. (2005). *SiRF Binary Protocol Reference Manual* (No. Revision 1.6). San Jose, CA 95112, USA.

Spring, E., Savolainen, S., Erkkila, J., Hamalainen, T., & Pihkala, P. (1988). Drag Area of a Cross-Country Skier. *Journal of Applied Biomechanics, 4*, 103-113.

Stenmark, I. (1990). Ski Technique in the 1990s. *Snow Country*, p.18.

Supej, M., Kugovnik, O., & Nemec, B. (2005). Advanced analysis of skiing based on 3D kinematic measurements. In E. Muller (Ed.), *Science and Skiing 3* (pp. 76-86). Oxford: Meyer & Meyer Sport (UK) Ltd.

van den Bogert, A. J., Read, L., & Nigg, B. M. (1996). A method for inverse dynamic analysis using accelerometery. *Journal of Biomechanics, 29*(7), 949-954.

van Ingen Schenau, G. J. (1982). The influence of air friction in speed skating. *Journal of Biomechanics, 15*(6), 449-458.

Waegli, A., Skaloud, J., Ducret, J., & Roland, S. (2007). *Assessment of timing and performance based on trajectories from low-cost satellite positioning.* Paper presented at the 4th International Congress on Science and Skiing, Austria.

Winter, D. A. (1991). *The Biomechanics and Motor Control of Human Movement* (2nd ed.). New York: Wiley.

Wood, G. A., & Jennings, L. S. (1979). On the use of spline functions for data smoothing. *Journal of Biomechanics*(12), 477-479.

XSens. (2004a). *Motion Tracker Technical Documentation Mtx-B* (No. 1.03): XSens Technologies B.V. **www.xsens.com**.

XSens. (2004b). *Users Manual MT9 Software* (No. 1.02): XSens Technologies B.V. **www.xsens.com**.

XSens. (2004c). *Users Manual XBus Master B* (No. 1.02): XSens Technologies B.V. **www.xsens.com**.

XSens. (2005). *Technical Documentation XBus Master B* (No. 1.32): XSens Technologies B.V. **www.xsens.com**.

Yeadon, M. R. (1989). A Method for Obtaining Three-Dimensional Data on Ski Jumping Using Pan and Tilt Cameras. *International Journal of Sports Biomechanics, 5*, 238-247.

Zatsiorsky, V., & Duarte, M. (2000). Rambling and Trembling in Quiet Standing. *Motor Control, 4*, 185-200.